architecture and urban planning
physics
chemistry
mechanics
civil engineering
electrical engineering
computer sciences
environmental engineering
mathematics

Technical Transactions

Czasopismo Techniczne

Volume 1
Year 2017 (114)

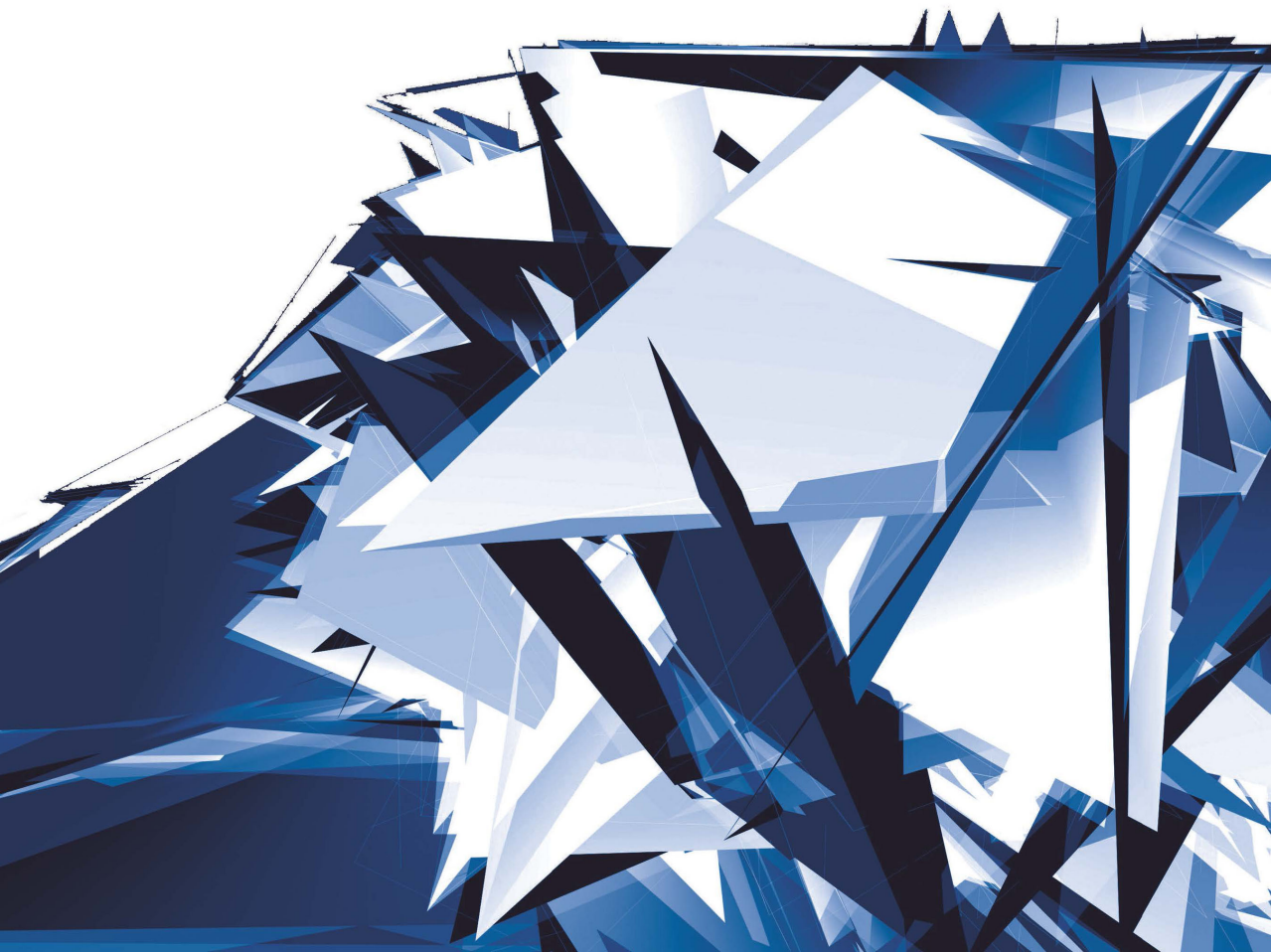

Technical Transactions

Czasopismo Techniczne

Volume 1

Year 2017 (114)

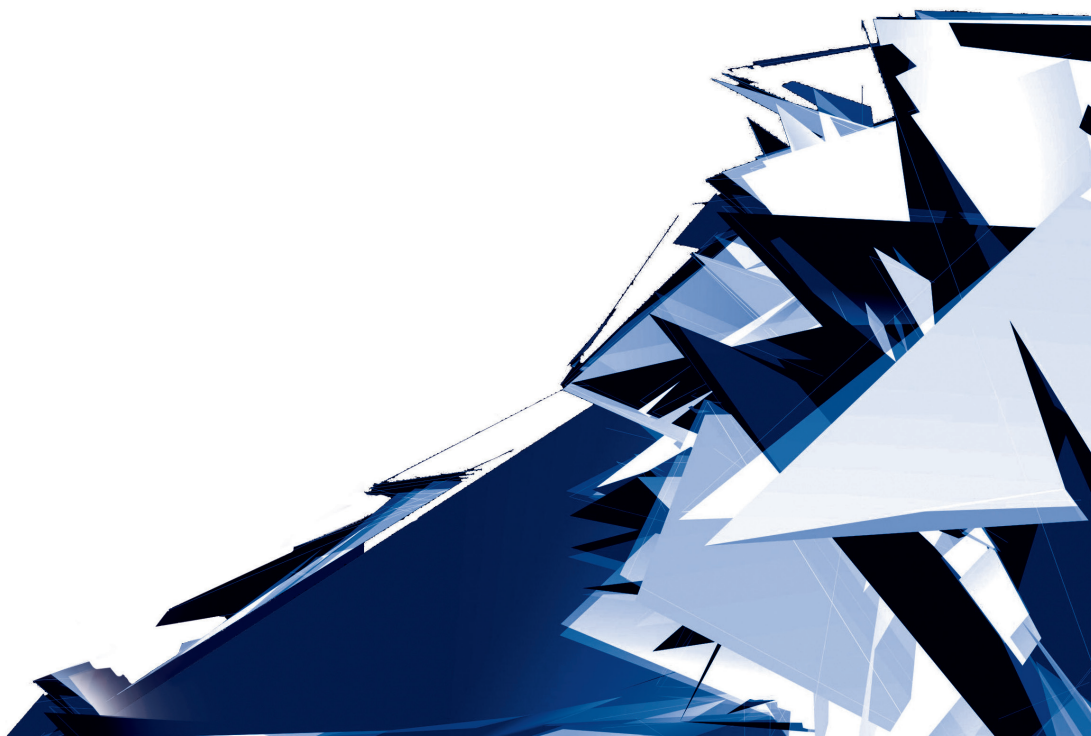

www.ejournals.eu/Czasopismo-Techniczne
www.technicaltransactions.com
www.czasopismotechniczne.pl

ISSN 0011-4561

Basic version of each Technical Transactions magazine is its online version
Pierwotną wersją każdego zeszytu Czasopisma Technicznego jest jego wersja online

Contents

PHYSICS:

TECHNICAL TRANSACTIONS 1/2017
CZASOPISMO TECHNICZNE 1/2017
ARCHITECUTRE AND URBAN PLANNING
DOI: 10.4467/2353737XCT.17.001.6098

Tetiana Kazantseva (enltexa@hotmail.com)
Department of Design and Architecture Fundamentals, Institute of Architecture, L'viv Polytechnic National University

Evolution of the polychromy in L'viv architecture in the period of the second half of the 17th century to the first half of the 19th century

Ewolucja polichromii w architekturze Lwowa od drugiej połowy XVII wieku do pierwszej połowy XIX wieku

Abstract

The article deals with the question of the evolution of polychromy in the L'viv architecture in the period of the second half of the 17th century to the first half of the 19th century. On the base of field and historical research, the author considers polychrome techniques, the colour palette, and the main principles and peculiarities of polychromy use on the façades and interiors of L'viv buildings of the Baroque and Classicism periods.

Keywords: evolution of polychromy in architecture, façades and interiors of the L'viv buildings of the Baroque and Classicism periods, polychromy techniques and the principles of their use

Streszczenie

W artykule przedstawiono ewolucję polichromii w architekturze Lwowa w okresie od drugiej połowy XVII wieku do pierwszej połowy XIX wieku. Na podstawie historyczno-terenowych badań autorka analizuje technikę polichromii, palety kolorów oraz podstawowe zasady i cechy wykorzystania polichromii na elewacjach i we wnętrzach budynków lwowskich okresu baroku i klasycyzmu.

Słowa kluczowe: ewolucja polichromii w architekturze, elewacja i wnętrza budynków lwowskich okresu baroku i klasycyzmu, techniki polichromii i zasady ich wykorzystania

1. Introduction

A certain colour palette, principles, and techniques of polychromy characterize the architecture of each historical period. The city of L'viv is a perfect model for academic research of any phenomenon in the process of stylistic evolution due to large number of extant buildings, which have high architectural and artistic value. Buildings in Gothic, Renaissance and Baroque styles are very interesting because of their unique artefacts and enigmatic general polychromy scheme. Polychromy in architecture of the most recent periods is presented by numerous examples based on L'viv and European prototypes. In this article, we consider the polychromy of L'viv architecture in the period of the second half of the 17th to the first half of the 19th centuries as a remote period, which unites two styles – Baroque and Classicism, characterized with very different attitudes to polychromy and demonstrating the evolution of the phenomenon within the period.

Despite the wide range of issues to research, thorough studies of the polychromy peculiarities of the discussed period do not exist. In the professional literature dedicated to L'viv architecture, the elements of polychrome design of architectural and artistic details of Baroque and Classicism are considered casually, while particular attention is paid to the polychromy of L'viv sculpture [e.g. 1, 3, 6, 7, 9, 10]. In her works dedicated to particular historical periods, techniques and methods (of wall painting execution), the author has already discussed polychromy in L'viv architecture [e.g. 4, 5].

A short review of L'viv architectural polychromy of the previous periods

This paper is an integral part of the comprehensive research on polychromy in L'viv architecture, based on analyses of field and historical research. Briefly summarizing the polychromy of the 14th–17th centuries researched by the author, [5] we can identify that in the Gothic period brick masonry with strongly baked bricks and red mortar were used. In the Renaissance, architectural polychromy of facades with monochromatic (light ochre or red) wall and coloured (red, green, orange) white-stone details was extant. The same phenomenon can be observed in building interiors – red, blue, ochre wall background and blue, green, ochre, red, white and black sandstone and stucco details. Some elements were emphasized with gilding; wooden ceiling beams were coloured in white, blue, black and ochre. Some interiors were decorated with stone veneer using alabaster, marble and sandstone. This polychromy, which can be named as architectural due to the use of bright pure colours and an identical colour scheme was characterized by ease of perception consistent with the philosophy of the Renaissance.

Polychromy in the L'viv architecture of the Baroque period

From the second half of the 17th century, L'viv architects began to build in Baroque style, a record number of sacral buildings appeared that was unattainable either in previous or succeeding styles. Church interiors were decorated with great magnificence, which called for great financial costs and collaborations with famous artists, and naturally could not be reconstructed quickly, which provides preservation of some of them until today. The architectural tastes of the time could no longer be satisfied with Renaissance polychromic methods. If the Renaissance was marked by a loyal attitude to the previous style, shown by the

secondary use of Gothic details, so the Baroque was characterized by a certain intolerance to the previous style, a desire for complete reconstruction and at the very least a change of polychromy. This was the cause of ruination of authentic Gothic interiors of the Latin Cathedral[1] (Fig. 1), the Armenian Church, and the Renaissance interiors of the Bernardine Church[2]. The first feature that had to be changed was the bright colour palette of the Gothic and Renaissance. In the Baroque, the **principle of mixing a few colours** in aim to get a complicated colour became very important. The neighbourhood of such mixed colours gave a special complicated baroque palette. White was used only in exclusive cases, for example to mark highlights (Fig. 2). The conception of a dark Baroque palette is refuted by the results of numerous restorations of Baroque murals, for example in the Bernardine Church (Fig. 3). The architecture of the Ancient Rome, with elegant colouring of finishing materials and illusionistic murals was the prototype of the polychromy of the Italian Baroque. The L'viv baroque obviously was inspired by European examples and inherited their general complicated colouring (Fig. 4).

The colour design of facades also become complicated as we can see in the example of the façade of the house at 28 Market Square. Research shows that in the period of the Renaissance the wall was painted light ochre with vivid polychromic details; in Baroque the façade was repainted in light olive (more than 10 layers) and the sandstone details of the window and door frames and the first floor were repainted in black (Fig. 5). This colour scheme is consistent with the attitude to façade polychromy traditional for the late Baroque. For example, according to Brzezinski's research, the facades of the Late Baroque in Wrocław were painted in complicated background colours with black details [2]. Unfortunately, we have no more evidence about the polychromy of L'viv Baroque facades[3]. On facades, one can find several murals in niches (in St. Benedict's church[4] (Fig. 6), on the Latin Cathedral's wall) with a special golden background and complicated colour palette. The façade`s background in turquoise of the Holy Spirit Church (Kopernyka St.) represented the influence of Kyiv or even Rastrelli Baroque that was rather an exception than the rule for L'viv architecture.

Another feature, which characterized the L'viv version of the Baroque was an attraction to theatricality and illusion as opposed to the tectonic visually clear colour scheme of the Renaissance. Analogically to Italian Mannerism where the tendency towards illusionistic painting appeared, the roots of the illusionistic attitude in L'viv must be sought in L'viv Renaissance architecture, such as the illusionistic painting of the City Arsenal's pillars or the wide spread illusionistic shadows on reliefs or moulding (the Bandinelli Palace). Certainly, the number of such artefacts from the 17th century was higher, but the aggressive Baroque approach to previous styles prevented it.

---

1 Erected in 14th century, in 1761–1776 refurbished in the Baroque style; in 1765–1770s Stanisław and Marcin Stroiński, Józef Chojnicki painted the interior.

2 Erected in 1600–1630 by Paweł Rzymianin, Andreas Bemer, Ambroży Przychylny (arch.). In 1738–1740 Benedykt Mazurkiewicz with L'viv artists R. Bartnicki, Woliński and J. Strochiński painted the interior in *al fresco* technique, than in 1746 Stanisław Stroiński painted the interior.

3 In 1980s the institute "Ukrzakhidproektrestavratsiia" (The West Ukrainian Project Institute of Conservation) and Department of Historic Environment Protection held research of L'viv buildings polychromy. Unfortunately, the materials, which were stored in archive of Department of Historic Environment Protection, were lost.

4 Erected in 1597–1616 by Paweł Rzymianin (arch.), restored in 1623–1627 by Jan Pokorowicz (arch.), restored in 1748 by Marcin Urbanik (arch.).

Fig. 1. Baroque murals of complicated plot and colouring in the gothic interior of Latin Cathedral (Photo by A. Kazantseva)

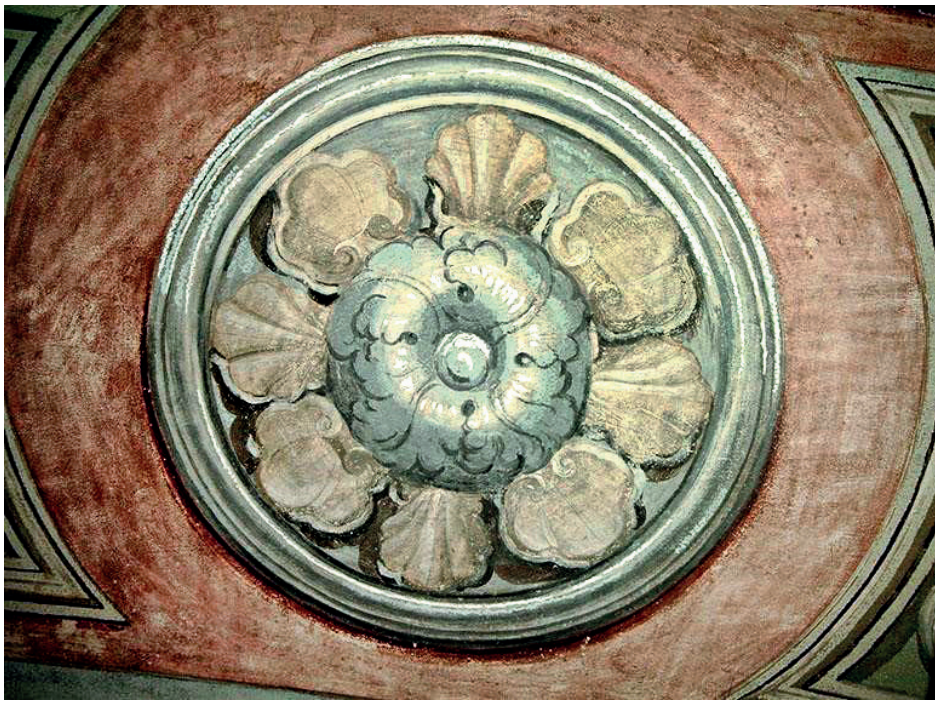

Fig. 2. Limited use of white colour only on highlights, Bernardine church (Photo by A. Kazantseva)

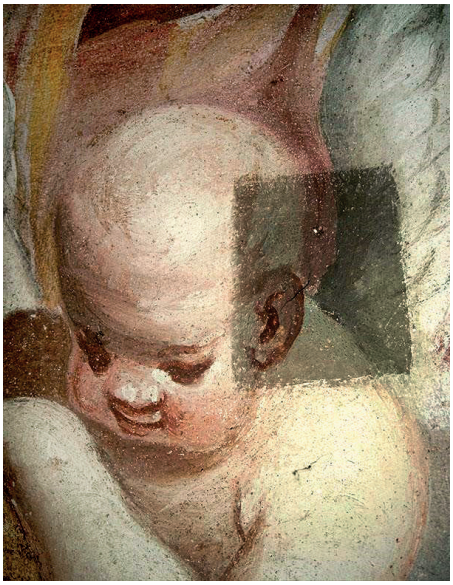

Fig. 3. Dark colouring of Baroque wall painting resulting from air pollution, fragment cleaned during restoration works, Bernardine Church (Photo by A. Kazantseva)

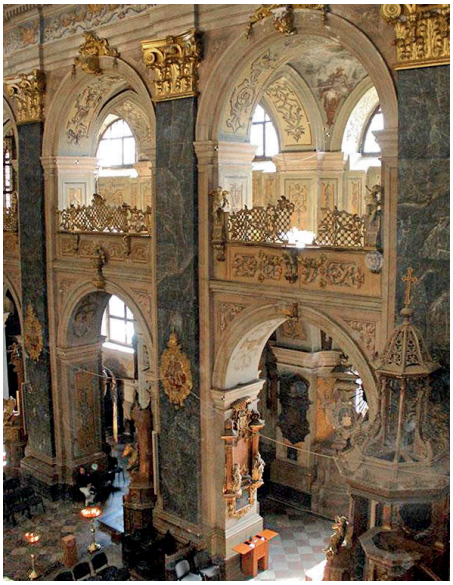

Fig. 4. Elegant colouring of Baroque church interior inspired by ancient Rome interiors, Jesuit Church (Photo by A. Kazantseva)

a)

b)

Fig. 5. Research of painting in Baroque period in 28 Market Sq.: a) black sandstone details, b) olive wall background (soundings of painting layers) (Photo by A. Kazantseva)

Fig. 6. Baroque painting of the niche of the gate of the ensemble of St. Benedict Church (Photo by A. Kazantseva)

Fig. 7. Engraved drawing in wall painting, Jesuit Church (Photo by A. Kazantseva)

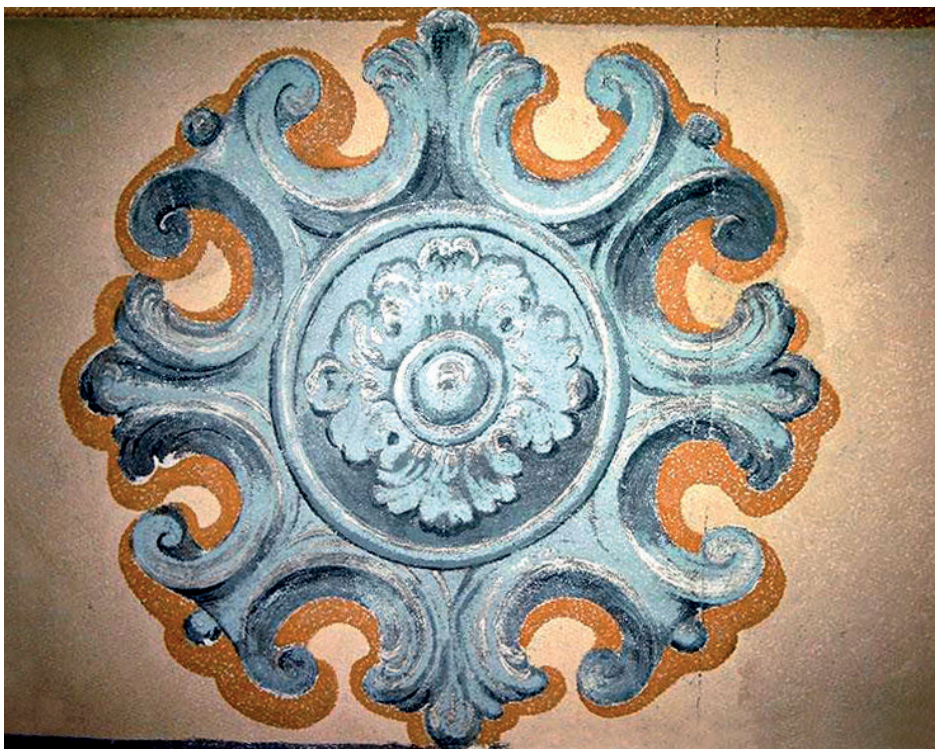

Fig. 8. Combination of cool and warm colours in depicting of detail and background, Bernardine Church (Photo by A. Kazantseva)

However, in the interiors of L'viv sacral buildings, the murals of the 17th–18th centuries are fully represented. The illusionistic painting (trompe l'oeil), or the imitation of architectural and sculptural details by painting, often in grisaille, became the new technique of the time. Grisailles were painted on the base of the combination of white and black with an additional shade of umber, grey and brown, which provide an illusion of stone details. These paintings were made in al fresco and al secco techniques with engraved drawing (Jesuit Church[5], Barefoot Carmelites Church[6]) (Fig. 7). Additional realism and a high artistic effect were achieved with the help of a simple method, namely the combination of warm and cool shades of colour in depicting details and their background (Bernardine Church) (Fig. 8). Depicting architecture in different views and distortions, including fantastic architectural shapes, let us attribute these murals to the fourth (fantastic or Baroque) type (according to the classification of Pompeii paintings). In European terminology, a special classification of illusionistic Baroque paintings exists, namely the "view from below" ("Di sotto in sù"), which is painted according to the author`s imagination (the method of Late Mannerism), and "quaturadra", which consist of precise perspective depicting of sculpture and architecture, combined with thematic painting (pure Baroque method). In L'viv murals, both methods were combined (Fig. 9–12). The method of anamorphosis was traditionally used to combine real and depicted architectural elements. The illusionistic painting was used to imitate fluting on the pilasters (Barefoot Carmelites Church) (Fig. 11), cantilevers of a very complicated configuration, portals, cartouches (Latin Cathedral), rococo ornaments and frames (Jesuit Church). In Bernardine Church through illusionistic portals, one can see the illusionistic landscape or half-opened doors attract to enter, which looks completely realistic and visually widens the space (according to Pompeii paintings). The frontier between illusion and reality becomes unclear, as for the example in the Jesuit Church two balconies (real and illusionistic) are located side-by-side, and the illusionistic shadow from the illusionistic balcony is a mirror copy of the real shadow from the real balcony (Fig. 12). The special topic of research is represented by illusionistic windows, painted with real windows vis-à-vis. These illusionistic windows give us information about the stained glass windows of that time [8]. Through the illusionistic window lattice, one can often see blue sky with clouds.

Sometimes the technique of illusionistic painting lost its realism, gaining illusion and uncertainty just like opening doors to another world. In this manner, the illusory sculptures on the real pilasters of the Barefoot Carmelites Church were painted.

The theatricality of architecture needs the wide involvement of spectators, with God the Creator as the most important one. Therefore, the vaults of Baroque churches (or painted in Baroque period) are illusionistic openings to the heavens – one can see angels and God the Father on the clouds in sunlight surrounded by a fantastic landscape (Fig. 14). In addition to architectural motifs in murals, ships and marine scenes appeared, which show the desire for

[5] Erected in 1610–1630 by Jacopo Briano (arch.); Francis Řehoř Ignaz and Sebastian Ecksteins painted the interior in the 1740s.

[6] First mentioned in 1634, attributed to Jan Pokorowicz (arch.); Italian painter Giuseppe Pedretti and his apprentice, Bernardin monk, Benedykt Mazurkiewicz painted the interior in the 1730s. According to the institute "Ukrzakhidproektrestavratsiia" research, those paintings can be considered to be the unique in Western Ukraine due to their execution completely in *al fresco* technique.

Fig. 9. Illusionistic mural of Baroque interior, Bernardine Church (Photo by A. Kazantseva)

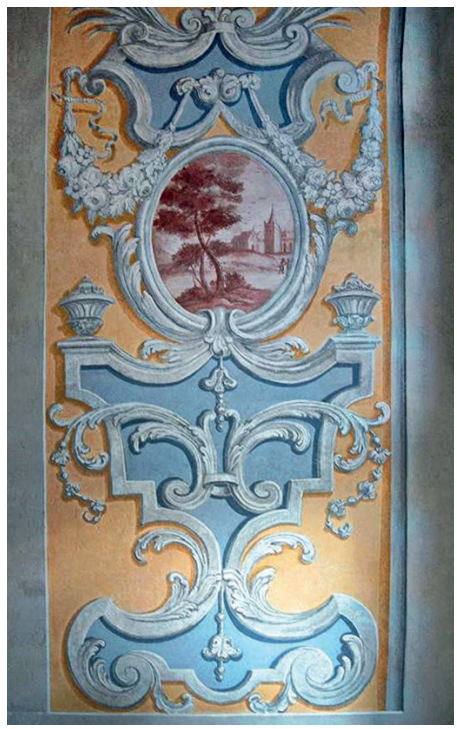

Fig. 10. Illusionistic mural of Baroque interior, Bernardine Church (Photo by A. Kazantseva)

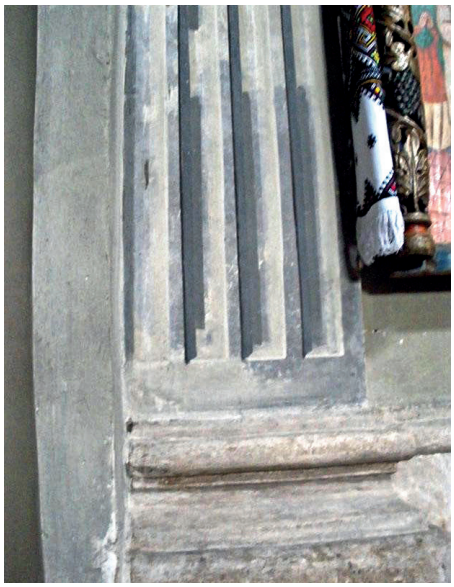

Fig. 11. Combination of illusion and reality – achromatic flutes of real pilasters of Barefoot Carmelites Church (Photo by A. Kazantseva)

Fig. 12. Unclearness of frontier between reality and illusion – shadows of real and illusionistic balconies, Jesuit Church (Photo by A. Kazantseva)

the sea of the L'viv Baroque [7]. The colour of the sky (or vault) is always different, which creates the colouring of church interior: in the Bernardine church – golden, in the Jesuit church – green, in the Barefoot Carmelites Church – light blue.

The desire for illusions also appeared in the widespread method of imitation of finishing materials, which was revealed in a number of versions. Firstly, in the aforementioned illusionistic murals some details (portals, frames, cornices) were painted imitating marble texture (the Bernardine church). Gilding was imitated in the same way. Secondly, real architectural elements can be painted imitating marble (e.g. the pilasters in the Jesuit Church) (Fig. 15). Thirdly, the special material was made by means of a commixture of glue and pigments in different combinations (e.g. the altars in the Latin Cathedral[7], the Dominican Church[8]). This is known as faux marble (scagliola), the production of which was naturally a cheaper method, which satisfied architects` desire for the creation of unique and expressive colour effects. The conservatism of L'viv architecture caused the realism of the created colouring of faux marble, but in other European cities, we can observe unexpectedly clearly decorative colouring designs (e.g. in Vilnius).

In this multicolourness, the entirety and ensemble design of Baroque and Rococo interiors was organized by accenting architectural details (capitals, rococo decoration, keystones etc.) with gilding (Fig. 16). Such an excess of gold was appropriate in the dingy lighting of candles due to additional reflections. Gilding was put over the support base (which could be red or green), giving the elements a respectively warm and cool shade of colour (Fig. 17).

7 1765–1776, Piotr Polejowski authorship.

8 1771–1775, Piotr Polejowski authorship.

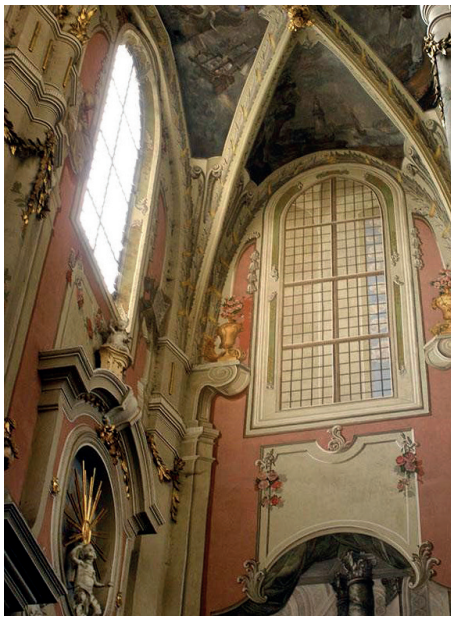

Fig. 13. Illusionistic windows in Gothic style (but with divisions of 18th century) in Latin Cathedral (Photo by A. Kazantseva)

Fig. 14. Opening of heavens or fantastic landscapes on the plafond, Campian`s Chapel (Photo by A. Kazantseva)

Fig. 15. Imitation of marble by painting, Jesuit Church (Photo by A. Kazantseva)

Fig. 16. Emphasizing by gilding of architectural decoration in Baroque and Rococo, Jesuit Church (Photo by A. Kazantseva)

Fig. 17. Traces of red support base under gilding, Jesuit Church (Photo by A. Kazantseva)

Fig. 18. Pastel colouring of rococo façade, 30 Market Sq (Photo by A. Kazantseva)

Fig. 19. Rococo paintings with murals in Dominican monastery (Photo by A. Kazantseva)

Fig. 20. Polychrome façade scheme in Classicism – light yellow background, white details (Vynnychenka Str.) (Photo by A. Kazantseva)

Polychromy in the L'viv architecture of the Rococo period

The Rococo period in L'viv was characterized by the appearance of delicate pastel colours of wall background and white or golden details, which created a light shining colouring scheme (Fig. 18, 19). Illusionistic paintings continued to be used, although without big theme compositions. Marble was also imitated, and reliefs and gilded moulding were supplemented with paintings. Some sacral interiors in L'viv are designed in this style (St. Anthony's Church[9], St. George's Church[10], the Dominican monastery, the Latin Cathedral Chapels). Also some excellent Rococo facades were preserved in L'viv, which are waiting for their field research.

Polychromy in the L'viv architecture of the Classicism period

At the turn of the 19th century, the polychromatic scheme of the Baroque had lost its attractiveness. Classicism as the hierarchical system did not perceive the complex colour palette and illusions of the Baroque, which lost its monumentality at the end of the 18th century. For the beginning of classicism, the discovery of Greek monuments, which had mainly lost their polychromy, played a significant role. The remains of polychromy were attributed to barbarian latest paintings. This conception remained until G. Semper wrote his treatise about the polychromy of the ancient world (1834). Therefore, the Classicism of the beginning of the 19th century is represented with a strict hierarchy of polychromatic means. The walls` backgrounds had to be painted in light yellow with white architectural decoration (Fig. 19). Buildings painted in this way had to create a harmonious urban ensemble similar to other cities built at the beginning of the 19th century. Nevertheless, Classicism for L'viv was the only one page in the book of the history of the city so the appearance of several houses or even streets in the Classicist style did not influence the change of city polychromy. Besides, in L'viv, the Empire Style played as important a role as Classicism but more diverse and picturesque. Facades in the Empire Style were appropriately decorated by high relief located on red (1–3 Svobody Av.[11], 21 Virmenska Str.[12], 8 Vynnychenka Str.[13] (Fig. 21)) or black background (34 Krakivska Str.[14]) (Fig. 22). The interiors of buildings of the first half of the 19th century were decorated with a wide range of polychromatic means, united in a harmonious hierarchical scheme. The most luxurious example in L'viv are the interiors of the Royal Halls[15] in the Korniakt Palace. Pilasters and socles are coated with faux marble, the floor is decorated with various parquetry patterns, different in each room, and the ceiling is entirely covered with white bas-reliefs, which are in several places imitated in grisaille technique – a reflection of Baroque illusions. Wall bas-reliefs are located on a coloured

9 Erected in 1618–1765, including architects Kulczyński and Piotr Polejowski. Interior paintings were executed by Tadeusz Pelcharski.

10 Erected in 1745–1770 by B. Meretyn, K.K. Fessinger. L. Doliński executed interior altar paintings.

11 Erected in 1809–1822 by Fryderyk Bauman, sculptural decoration was executed by Hartman Witwer and Anton Schimser

12 Erected in 1810, sculptural decoration was executed by Hartman Witwer.

13 Erected in 1804–1805, sculptural decoration was executed by Hartman Witwer.

14 Erected in 1830–1840s, sculptural decoration was executed in workshop of Anton and Johann Schimser.

15 Reconstructed in 1793–1820s by Fryderyk Bauman.

Fig. 21. Colouring façade scheme in Empire Style – red background of bas-reliefs, light façade (8 Vynnychenka Str., 21 Virmenska Str.) (Photo by A. Kazantseva)

a)

b)

Fig. 22. Colouring façade scheme in Empire Style: a) black background of bas-reliefs (26 Krakivska Str.); b) red façade background (10 Shevska Str.) (Photo by A. Kazantseva)

Fig. 23. Colouring interior scheme in Empire Style (6 Market Sq.) (Photo by A. Kazantseva)

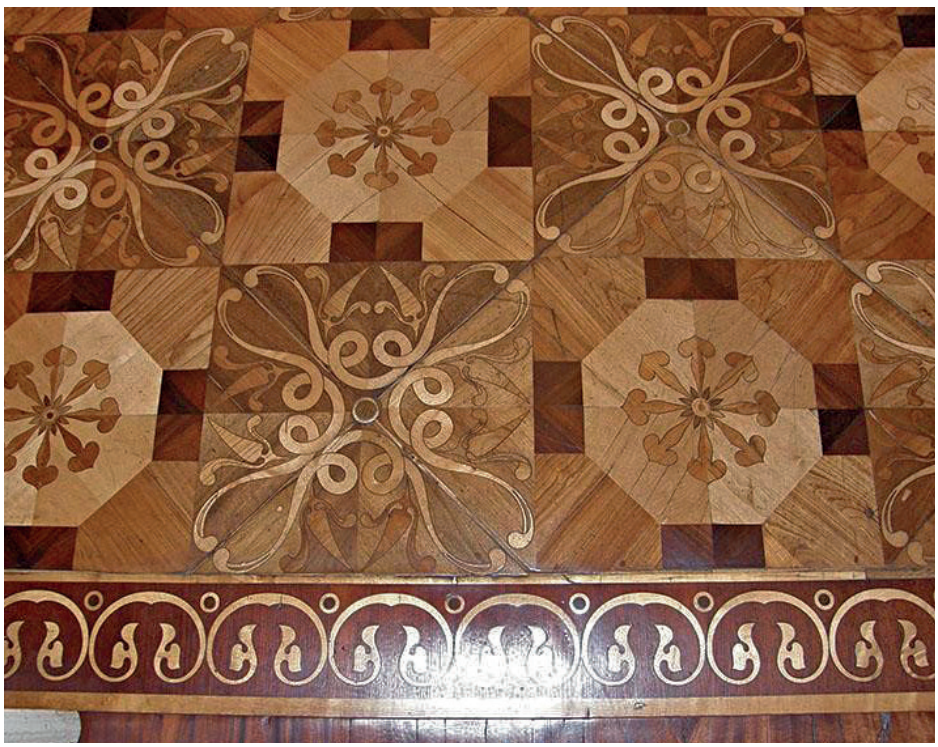

Fig. 24. Parquetry in Classicism interior (6 Market Sq.) (Photo by A. Kazantseva)

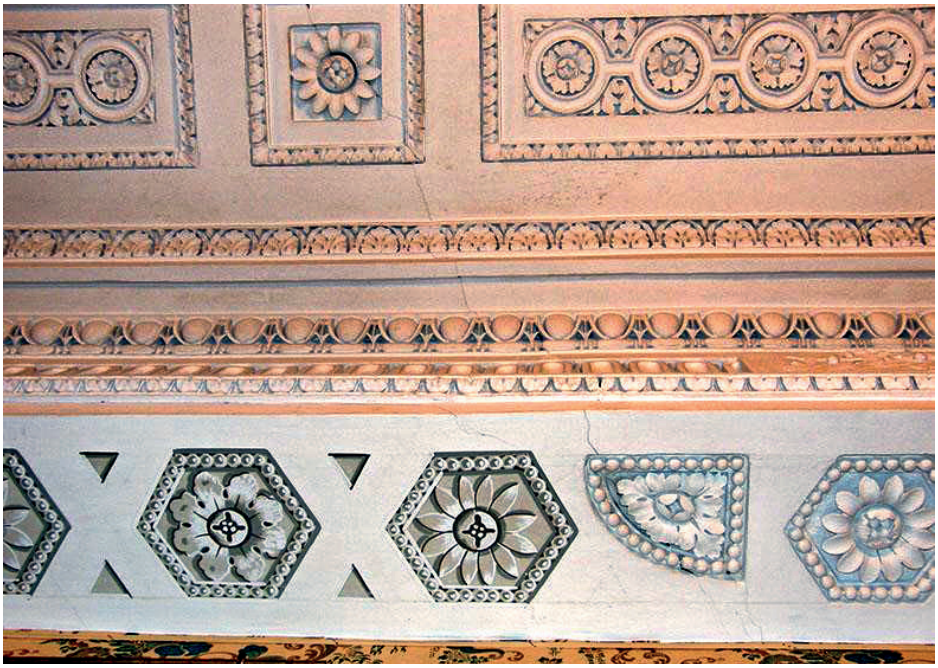

Fig. 25. Parquetry in Classicism interior (6 Market Sq.) (Photo by A. Kazantseva)

background of complicated green colour, the same design we meet in the interiors of Seniavskii`s Arsenal (Baworowski`s palace)[16] and the merely destroyed Besiadetskii's palace[17]. The richness of the interior is supplemented with luminescent materials – bronze lamps, mirrors, black fences, white majolica stoves (Figs. 23–25).

In the middle of 19th century the polychrome Renaissance and Baroque facades of L'viv buildings were not considered to be aesthetic, which caused the cleaning of the surface of the polychrome façade and its covering by grey cement plaster. Such activity led to the destruction of L'viv polychromy, and a loss of interest in colour for decades, which caused the next colour explosion at the end of the 19th century.

2. Conclusions

The polychromy of L'viv architecture of the Baroque and Classicist periods is a unique phenomenon, represented by numerous artifacts, whose principles and methods of use need research and systematization.

In the Baroque, the key ideas that influenced the polychrome design of L'viv buildings were the longing for theatricality, illusion, transmission of the difficulty of being a human being and the unclarity of the frontier between the spiritual and the material. Appropriately,

[16] Anton Schimser executed sculptural decoration.

[17] Reconstructed in 1820–1830 by Fryderyk Bauman.

it caused an appearance of complex colour palette of façades (olive background and black details) and interiors, accenting with gilding of architectural decoration in interiors, the use of illusionistic grisaille murals (imitation of architectural and sculptural details, depicting an open heaven with angels on vaults), and imitation of finishing materials (faux marble scagliola).

In L'viv architecture of the Rococo period, pastel colours of the wall with white or golden details were widespread. In Classicism, the tendency to create a polychrome hierarchy of façade walls by accenting with a yellow background and white or golden details appeared. In the Empire style, high-reliefs were emphasized by the red or black of the background. In the interiors of L'viv building of the 1st half of the 19th century polychrome, the methods of creating a harmonious cosy atmosphere using marble coating of walls, parquetry, moulding, bas-reliefs on the coloured background, bronze lamps, majolica stoves, mirrors were used.

Analysing the evolution of polychromy in L'viv architecture until the 19th century we can conclude that in the Baroque period polychromy gained its primary meaning, becoming an integral means of architectural and artistic expression, which is characterized by a number of common principles, the methods and techniques and creates a unique image of Baroque building.

The colourful decorations in L'viv architecture are unique due to the elegant range of colour (including the scagliola of the colour of natural marble), mix of all possible polychrome techniques in the decoration of one object (with the dominance of the illusionistic paintings of the Italian school of the late Renaissance period), richness and diversity of preserved examples of all styles represented in the architecture in the period of the second half of the 17th century to the first half of the 19th century.

References

[1] Biriulow Ju., *Rzeźba lwowska od połowy XVIII wieku do 1939 roku: Od zapowiedzi klasycyzmu do awangardy*, Neriton, Warszawa 2007.

[2] Brzezowski W., *Faktura i kolorystyka elewacji barokowych na Śląsku*, Politechnika Wrocławska, Architectus 2000, No. 1(7), 61–70.

[3] Cielątkowska R., Onišenko-Švec' L., *Detal architektury mieszkaniowej Lwowa XIX i XX wieku*, Wydział Architektury Politechniki Gdańskiej, Gdańsk 2006.

[4] Kazantseva T., *Evolution of the Polychromy in L'viv architecture / Polichromijos evoliucija Lvovo architektūroje*, [in:] (At)koduota istorija architektūroje (De)Coded History, [in:] Architecture International Interdisciplinary Scientific Conference / Abstracts, Vilnius Academy of Arts, 2016, 60–61.

[5] Kazantseva T., *Ewolucja polichromii w architekturze Lwowa w okresie od XIV wieku do pierwszej połowy XVII wieku/Evolution of the Polychromy in L'viv Architecture of the 14th – the first half of the 17th century*, Przestrzeń i Forma/Space & Form, Instytut Architektury i Planowania Przestrzennego Zachodniopomorskiego Uniwersytetu Technologicznego, 2015 (2), No. 24, 39–50.

[6] Liubchenko V., *L'viv sculpture of the 16th–17th centuries*, Scientific Idea (Naukova dumka), Kyiv 1981.
[7] Prysiazhnyi K., *Do historji koloru w architekturze. On the materials of the research of the institute "Ukrzahidproiektrestawracja"*, [in:] Theses of: "Kolor i faktura w architekturze", Wrocław, Wydział Architektury Politechniki Wrocławskiej 1998.
[8] Prysiazhnyi K., Kazantseva T., Zarechniuk O., *Windows of L'viv buildings*, Scientific Journal of L'viv National Polytechnic University "Architecture", 2013, No. 757, 364–374.
[9] Prysiazhnyi K., *The polychromy of the interior of L'viv dwelling house. The experience of restoration. Dedicated to the memory of Myroslava Maiorchuk*, [in:] Theses and paper of the 1st International Restorers Forum, L'viv, Spolom 2002, 16.
[10] Vuitsyk V., *Selected works. To the 70th birthday anniversary*, Journal of the institute "Ukrzakhidproektrestavratsiia" 2004, No. 14, L'viv.

TECHNICAL TRANSACTIONS 1/2017
CZASOPISMO TECHNICZNE 1/2017
ARCHITECUTRE AND URBAN PLANNING
DOI: 10.4467/2353737XCT.17.002.6099

Andrzej Zdziarski
Marcin Jonak (marcinjonak@wp.pl)
Division of Descriptive Geometry, Technical Drawing & Engineering Graphics, Cracow University of Technology

Anamorphic images on the historical background along with their classification and some selected examples

Obrazy anamorficzne na tle historycznym wraz z klasyfikacją i wybranymi przykładami

Abstract

Art based on optical illusions has accompanied the everyday life of a human being since ancient times, until today. Primarily, it played a specific role as an artistic game and manifested the artists' own mastery, while often playing the serviceable role of an artistic advertisement. This study presents a detailed definition of anamorphic images together with their precise classification, and provides a description of the methods used for their construction. The problems discussed here have been presented on a historical background. The examples of particularly chosen anamorphic images have been presented together with their visualised images. The theoretical background, how one can create such anamorphic images, provides the basis for further design and development of anamorphic images to be created both in an urban space of a town, and in the interiors of public use..

Keywords: transformation, anamorphic image, visualisation of anamorphic images, reflective surfaces

Streszczenie

Sztuka oparta na złudzeniu optycznym istniała od starożytności. Przede wszystkim jako swoista zabawa artystów manifestująca własne mistrzostwo, a często także w roli usługowej, pełniąc zadanie reklamy. Niniejsze opracowanie obejmuje precyzyjną definicję anamorfoz wraz ze szczegółową klasyfikacją i metodami konstruowania obrazów anamorficznych. Zagadnienia te przedstawiono na tle historycznym. Wybrane przykładowe anamorfy zaprezentowano wraz z ich obrazami zrestytuowanymi. Powyższe rozwiązania dają możliwość precyzyjnego projektowania obrazów anamorficznych w zurbanizowanej przestrzeni miejskiej oraz architektonicznych wnętrzach przestrzeni publicznej.

Słowa kluczowe: przekształcenie, restytucja, anamorfa, powierzchnie refleksyjne

1. Introduction

The issue of anamorphism has been extensively described, among others, in the book entitled *Anamorfozy* [2], which presented the problem from the historical perspective, illustrated with prints and painting reproductions. According to the author, "Anamorphosis is not a deviation from the norm, in which reality is tamed by the mind's vision. It is an optical trick, in which the visible covers the real. The elements of this system are ingeniously linked together". Today, anamorphic images are experiencing returns and rebirths. They appear in public as a planar, colourful and surprising compositions, visualised in an appropriate way.

It should be noted that, in 1981, the National Museum in Warsaw opened an exhibition entitled "Perspective, illusion, illusionism." Numerous departments presented different ways of viewing and understanding illusion in art.

Coherent articles related to the topic of anamorphs, published for years, have described a collection of geometric analyses and thoughts associated with their creation and visualisation: [1–9]. They define and record complex rules of geometric transformation of real images into anamorphic images.

This study presents a detailed classification and naming of the distinguished categories in their particular groups.

This paper also aims at broadening the knowledge with methods and simplification of creating complex geometric deformations of anamorphic images and their restoration. The examples of anamorphic images created in a traditional way, both intuitive and using the authors' own digital method, were presented. These studies may be an indication for architects and artists to become interested in this forgotten form of art.

2. Definition and classification of graphic anamorphs

2.1. Definition of graphic anamorphs

Nowadays, the word anamorphosis has become widespread and popular in many areas. For instance, botany and zoology use this term to describe certain shapes and forms of animals that have been transformed under the influence of environmental conditions or organ mutations. In 1970, J.C. Emery gave the name "Anamorphosis" to a collection of literary texts. In music, the word "anamorphosis" is the title of a musical piece called so by F. Morel in 1974. In 20th-century cinema, anamorphosis as a technique allowing to save a good-quality widescreen image on a typical film tape was applied as well. This technique was used for recording and restoring the image with the correct proportions.

Anamorphosis became of high interest of psychoanalysts as well. In the course of time, the perspective transformed with anamorphosis stopped referring only to reality, and became a tool for creating illusions on the border of hallucination [2].

The definition of an anamorph developed by A. Zdziarski [6] is quoted below:

An anamorphic image is an image created through the deliberate, geometric transforming of its proportion in such a way that the correct reading was possible only after looking from a fixed position or in the reflection in the appropriate mirror.

2.2. Classification of graphic anamorphs

According to their ways of visualisation, anamorphic images can be separated into two basic groups:

1) **surface anamorphoses** – the visualisation of which does not require the use of mirrors;
2) **reflective anamorphoses** – the visualisation of which will take place in a suitable mirror surface.

The group of **surface anamorphoses** includes:

1a) flat surface or planar anamorphoses – anamorphic images arranged on the same plane, the visualisation of which requires observation from a particular position.

1b) collapsible surface or collapsible planar anamorphoses – are created on the expanded grid of a specific spatial figure. Their restoration requires the assembly of a specific figure from a given grid and observation from a specific direction.

In the group of **reflective anamorphoses**, the following can be distinguished according to the visualising mirror surface:

2a) **Flat reflective anamorphoses:**
- ▹ **single** – with one visualising mirror;
- ▹ **complex** – with a larger number of flat visualising mirrors;
- ▹ **pyramidal** (pyramid) restoring mirrors having a common point.

2b) **Reflective cylindrical (tubular) anamorphoses,** including:
- ▹ **convex;**
- ▹ **concave.**

2c) **Reflective conical anamorphoses,** including:
- ▹ **convex;**
- ▹ **concave.**

2d) **Reflective anamorphoses implemented using any reflective surface** (sphere, ellipsoid, and others).

Irrespective of the classification above, we can distinguish anamorphoses created:
- ▸ traditionally (intuitive sketches, geometric constructions, mechanical methods – pentagraph);
- ▸ digitally[1].

The classification of anamorphs (open catalogue) in tabular form (with graphical interpretation) is presented below.

[1] Specialized graphic software – yet the Authors of this study specialise in the method of generating anamorphic images created in MS Excel.

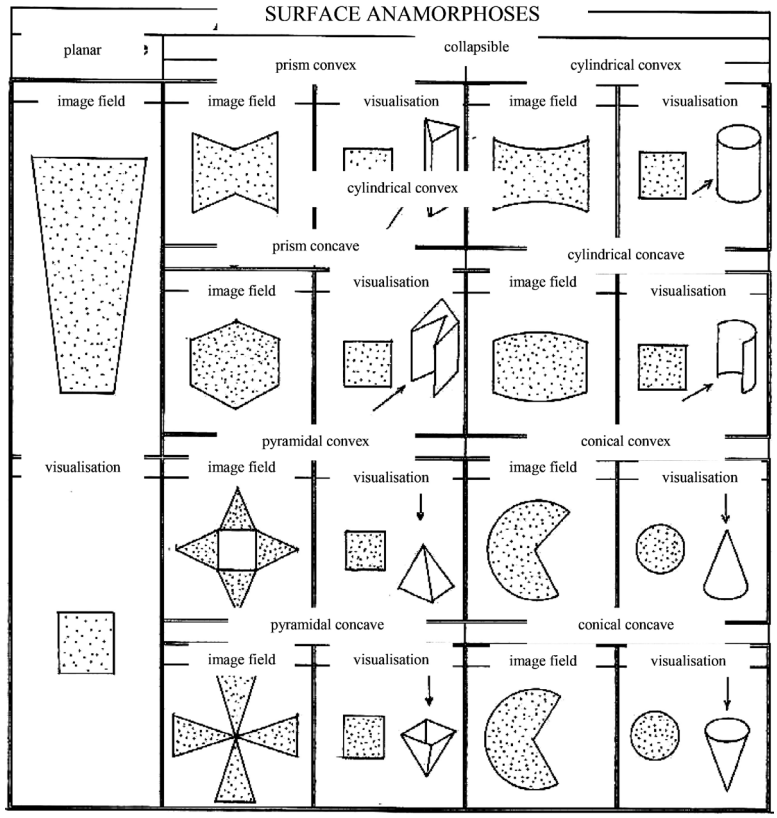

Fig. 1. Surface anamorphs – classification (compiled by A. Zdziarski)

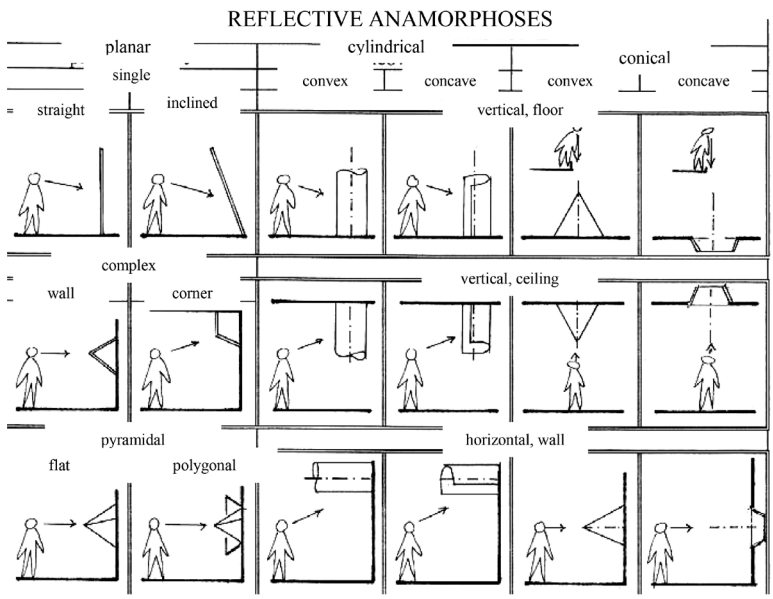

Fig. 2. Reflective anamorphs – classification (compiled by A. Zdziarski)

3. Historical outline of anamorphs

It is known that, in the first decades of the 15th century, Florentine avant-garde artists were trying to find the basics of optics in painting and create a theory of vision in order to raise painting to the status of knowledge. The image could simulate reality on the basis of certain rules. The field of view, as claimed by *Euclid* in the 7th century BC, can be regarded as a pyramid whose apex is in the eye of the observer. It was this principle that architect and art theoretician Leon Battista Alberti based his famous definition of the picture in 1435, according to which **the picture is a cross-section of the pyramid of vision.**

It is likely that it was Leonardo da Vinci and also Albrecht Durer who were the creators or originators of amorphous deformations, yet the very term "anamorphosis" was only coined in the 17th century from the Greek word "to transform". Anamorphosis has its foundations in the classical perspective, which is why its development as an increased knowledge of the perspective is reasonably justified.

In the 16th century, a system of anamorphisms was developed, which was considered "a miracle in art," and its secret was guarded for some time. The first use of the term in the literature dates back to the 17th century in the work of Jean-François Niceron entitled *La perspective curieuse* … (*Curious Perspectives*) [4]. In European painting, anamorphoses were often used as evidence of the artist's craftsmanship and mastery.

Probably the most famous example is a skull used by the German painter Hans Holbein in his painting from 1533, entitled *The Ambassadors* (Figs. 3 and 4). By painting a skull as a symbol of vanity hidden in an anamorphosis, the author introduced a philosophical message to his greatest work. This image probably hung on the staircase in Dinteville's palace. Therefore, while climbing stairs, the recipient was often surprised by the proper content introducing them to reflection and reverie.

Fig. 3. Hans Holbein, 1533, The Ambassadors, oil on panel with an anamorphic image of a skull in the bottom of the image

Fig. 4. The Skull – visualisation of the **flat surface** anamorph from *The Ambassadors*

Difficult to identify from the place where we view the image, a strange object emerges from the floor in Holbein's picture. Reading the meaning of this strange form requires the adoption of a special viewpoint of the observer. This point is located in the direction of the longitudinal axis of the figure, very close to the image plane. Watching the image from such a hidden position, a human skull, the symbol of a spiritual message, emerges from this seemingly not representative form. It was only in 1873, over three hundred years after painting this image, when this object was defined as an anamorphosis. There is an interpretation of a painted skull as the author's signature hidden in the pun-like image. A skull was also present in Dintevile's coat of arms.

In his comprehensive study *Perspektywa malarska* ("Painting perspective"), Professor Kazimierz Bartel describes the painting by *Hans Holbein* in the following way:

> *About 26 years younger than Dörer, Hans Holbein left one work, among others, which is particularly interesting from the perspective position: "The Ambassadors." What is intriguing in this picture is the element that represents a mysterious object, located diagonally, and supported with one part against the floor. The mystery is solved only when the picture is watched from the left side in the length direction of the mysterious object, keeping the eye very close to the picture. It turns out that there is a strongly anaformic image of the human skull, created – perhaps – by reflecting it in a concave cylindrical mirror. This is an example of the influence of the type of observation on the content of visual sensation.*

The author of this description uses the term *anaform* that should be considered in as synonymous with the notion *anamorph* in this case. In the light of the geometrical considerations provided in this study, the assumption that the deformation is due to the reflection in the concave mirror and, therefore, that it is a reflective anamorphosis, may be clarified and defined as a planar anamorphosis, which does not require the use of mirrors during the construction of image distortion or its visualisation.

Another known anamorphosis is a portrait of King Edward VI by William Scrots (Figs. 5 and 6) as a flat surface anamorph.

Fig. 5. William Scrots, 1546, Edward VI, oil on panel. **Flat surface** anamorph

Fig. 6. Visualisation

In 1546, Hans Holbein's student, William Scrots, painted a portrait of an English duke Edward VI in a planar anamorphosis (Fig. 5) on wood, using the oil technique. The author puts a strongly deformed head of a boy on the panoramic landscape. When looking at the picture from the right side through the tiny hole cut in the frame specifically for this purpose, the viewer sees an undeformed portrait of the prince "coming out" from the frames and from the picture's plane (Fig. 6).

The procedure for the creation of anamorphs ceased to be a mystery in the course of time. However, these were mainly flat surface anamorphoses, the visualisation of which only required looking at them from a certain direction. The content conveyed by the artists through anamorphosis was then largely erotic, philosophical, and theological, with their readings reserved for insiders who knew the direction of observation of the way of visualisation, as well as those whose location even forced the possibility of reading an undeformed image. Emmanuel Mignam (Figs. 7 and 8) painted a large fresco on the arcade wall of the monastery of the Holy Trinity on the Hill in Rome, imposing the restoration direction of its hidden content for the viewers passing the arcade, locating on the arcade axis. Serving as a decoration of one of the walls of the monastery cloisters, it is a huge composition with a length of 20 m and a height of 3.5 m. A life-size figure of St. Francis (Fig. 8), the founder of the Order of Friars Minor in Rome, is shown in the image. It is probably the only anamorphic fresco preserved to this day. The viewer passing the corridor is surprised by the reality of the image viewed, especially given the fact that the figure seems to emerge from the wall, disturbing the corridor's perspective. The upcoming observer can notice a greater detail of the work and be surprised by its different content again. The habit of the saint now becomes a landscape full of wind fallen trees, cliffs, hills covered in trees, strolling people, and the boat floating on the lake.

In the first half of the 17th century, anamorphic images restored with the use of various mirrors appeared in Europe. The main themes of these compositions based on a mirror anamorph, widespread on both sides of the Alps up to England, were camouflaged portraits,

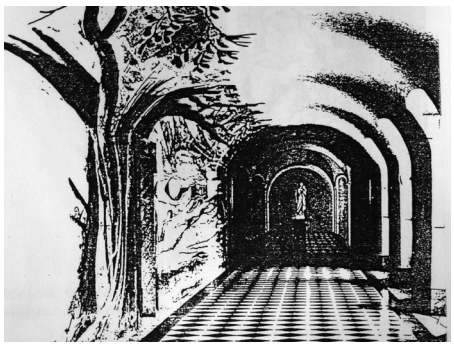

Fig. 7. Emmanuel Maignan, an anamorphic fresco, 1642, the view from the visualisation direction. Assembling **a flat planar anamorph with a planar cylindrical anamorph**

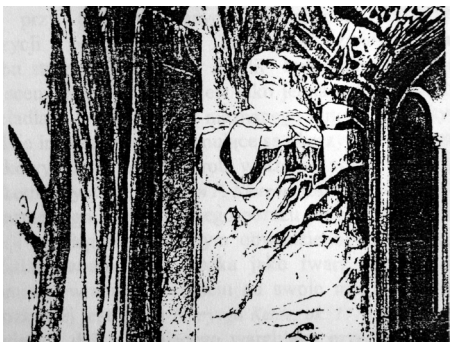

Fig. 8. Visualised part of E. Maignan's fresco – the figure of St. Francis

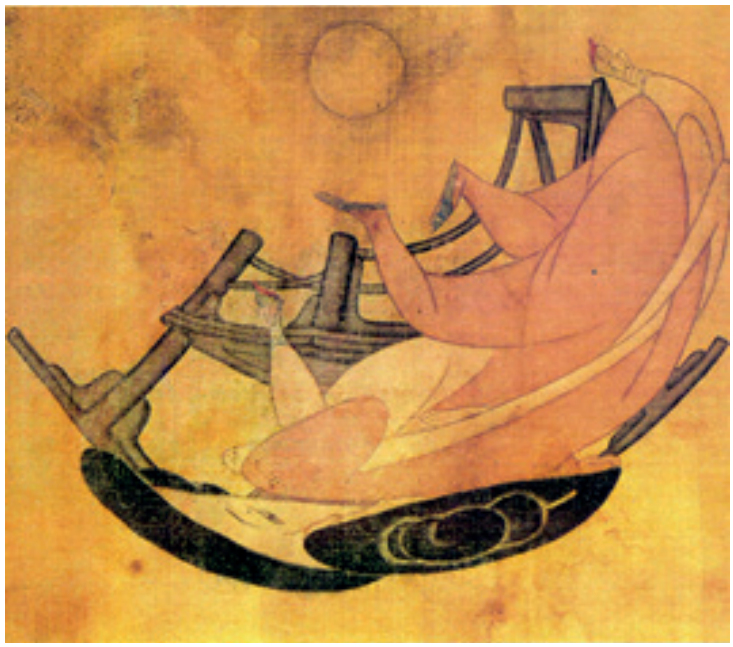

Fig. 9. China, 16th century, author unknown, reflective cylindrical convex anamorph of a sexually explicit content

Fig. 10. Jean F. Niceron, 17th century, a conical anamorphosis *The Girl with a Bird on a Wire*

images of saints, and biblical scenes. A 16th-century Chinese mirror anamorphosis of an erotic content, made by an unknown author (Fig. 9), is known as one of the oldest images of this kind.

Anamorphic images restored with conical mirrors are particularly interesting and fascinating. Such an image appears to be torn apart, astonishing us with its surprising composition (Fig. 10) Jean F. Niceron *The Girl with a Bird on a Wire*, 17th century. The visualisation of this anamorphic image is presented in its centre. Fuzzy contours, stretched around the perimeter of the image, are reflected in a field close to the top of the cone as the girl's face. The absurdly twisted arms go back into place in the reflection.

An example of a pyramidal anamorph (Fig. 11) is the work of *Henry Kettle, oil on panel, 1770–80, Leyde, History Museum.* In the pyramid with mirrored walls, there are four especially composed facial images, each reflecting in one wall, building one undeformed play portrait for the viewer looking from above.

In the 17th century, the age of the treatises, essays and anamorphic offices, the themes of compositions also included gardens, cities, and the whole of nature. In Western Europe, oil paintings by renowned masters were often converted in the reflection of cylindrical or conical mirrors. 18th-century works of unknown authors are an example of transmitting religious and symbolic contents. In the 19th century, anamorphosis moved away from the metaphysical motif and became mainly a technique, a skill, and an artistic perversion, while the intellectual overtones were moved away.

Fig. 11. Henry Kettle, 18th century, a pyramidal anamorphosis *The Portrait of a Man*

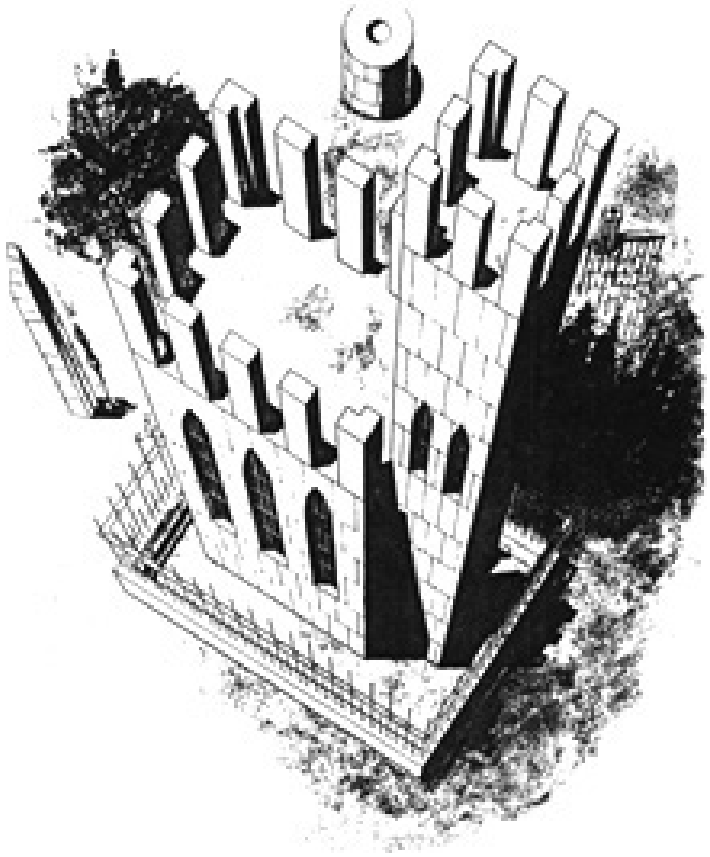

Fig. 12. *The Castle* – a planar anamorphosis, 1870, author unknown

A return to the magical and metaphysical context of mystery occurred in the era of Romanticism. A work by an anonymous Dutch author from 1870 shows the castle shown diagrammatically in a planar anamorphosis. The unusual characteristics of anamorphosis were used in a special way here. The properly viewed composition seems to rise from a two-dimensional surface of paper (Fig. 12).

In his paper entitled *Demon de l'Analogie* (1975), Roland Barthes states that analogy is a curse of artists, who are trying to oppose it in two ways: either by faithful reproduction (hyperrealism) or by creating **anamorphisms** through deformation according to strict rules.

4. Examples of anamorphs created today

Nowadays, there are examples indicating the maintenance of other practical function of anamorphosis. First of all, the group of surface anamorphoses includes applicable planar anamorphic images. A wide range of horizontal road signs can be identified as typical examples of modern planar anamorphoses. (Fig. 13 and 14).

Generally, in a public space, planar anamorphs appear on city squares. They are more or less successful paintings, which, viewed from a certain point, enable the viewer to see an attractive image. The selected examples of anamorphs created in the urban or rural space are presented below.

Example 1. An anamorphic image of a cycling path pictogram – defined as a surface planar anamorph in the classification.

Fig. 13. Surface anamorph (photo by A. Zdziarski)

Fig. 14. Visualised anamorph (photo by A. Zdziarski)

Example 2. A planar anamorph on the market in Wieliczka (Figs. 15 and 16) made by Ryszard Paprocki – defined as a surface planar anamorph in the classification.

Fig. 15. Surface anamorph (photo by M. Jonak)

Fig. 16. Visualised anamorph (photo by M. Jonak)

Example 3. A planar anamorph at the dam in Czorsztyn.

An image entitled *Moc Żywiołów* ("Power of the Elements") was created by Ryszard Paprocki and Zbigniew Wojkowy at the top pedestrian part of the dam in Niedzica. Viewed from a certain point, this large painting (measuring 34 m in length) gives the opportunity to see a flowing river, a waterfall and raging whirlpools (Fig. 17), as well as a hydro-technical detail – a turbine. (Figs. 18 and 19).

Fig. 17. The painting on the dam in Czorsztyn, a planar anamorph (source: www.niedzica.pl)

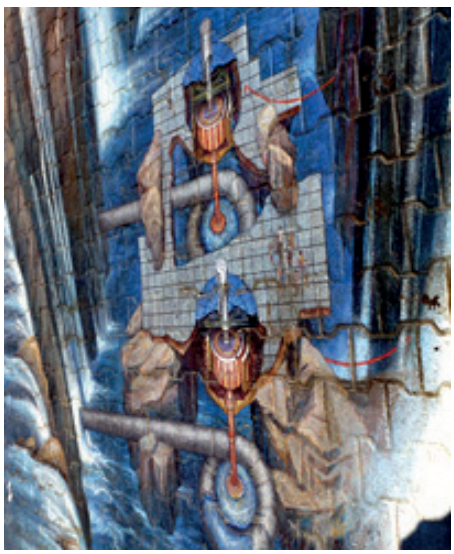

Fig. 18. A turbine on the painting in Czorsztyn. Surface anamorph

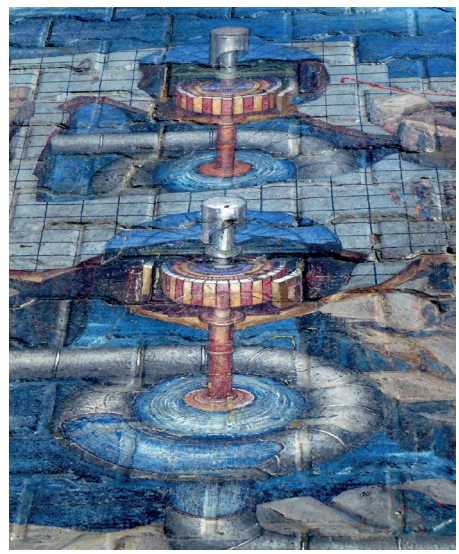

Fig. 19. Visualisation of the anamorph from Fig. 18

Example 4. Many examples of anamorphs created by architects or artists using conventional means, depicting various technical objects, e.g. a groin vault – Figs. 6 and 7) can be identified.

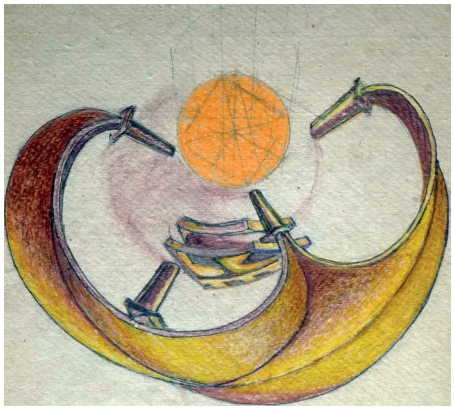

Fig. 20. Groin vault – a reflective cylindrical anamorphosis (by A. Zdziarski)

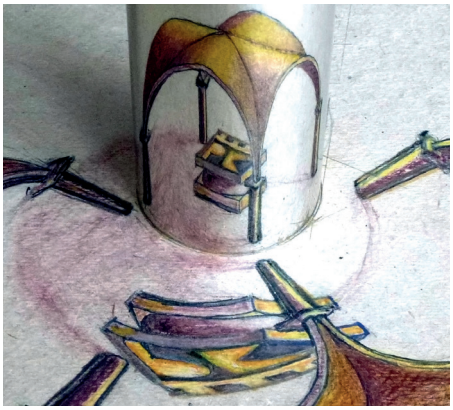

Fig. 21. Visualisation of the anamorph from Fig. 20

Tedious and monotonous construction of anamorphs inspired researchers to seek the opportunities for its mechanical assistance. Hence, A. Zdziarski came up with an idea of a prototype apparatus allowing the mechanisation of drawing operations with the help of a device called a pentagraph. The apparatus consists of eight arms connected appropriately with either rotary or rotary-sliding joints. Based on the geometric scheme (Fig. 21), see [7], the apparatus allows to set the anamorph A^{a1} of a desired designed point A^{a} (Figs. 22 and 23). The apparatus was developed for the reflective cylindrical anamorph type.

Example 5. An anamorph created using a pentagraph

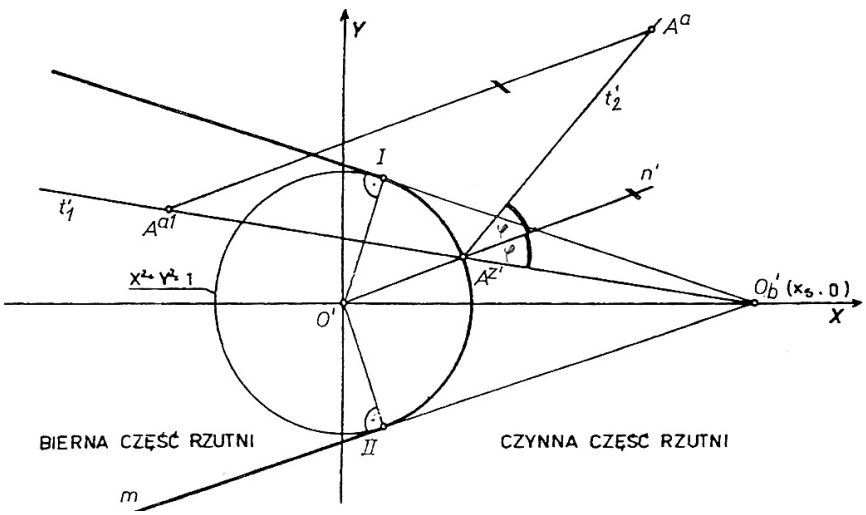

Fig. 22. A diagrammatical method of transformation

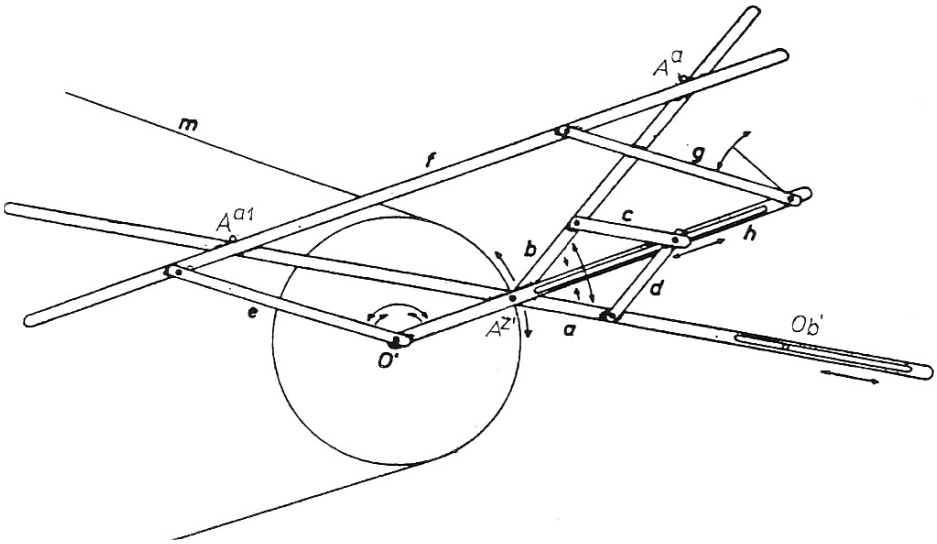

Fig. 23. Schematic diagram of the tool

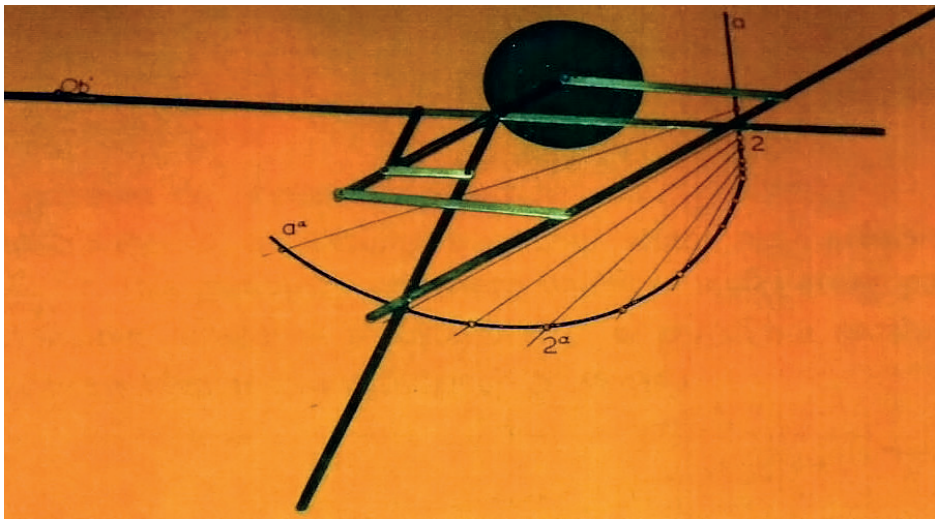

Fig. 24. A prototype of an apparatus for the mechanical determination of the anamorphic images

5. Examples of anamorphs created digitally with a visual intervention

As already mentioned, the authors deal with the digital method using MS Excel [10]. Two examples of a reflective cylindrical anamorph and a reflective conical anamorph from the convex group created on prototypical mirrors are presented below.

Visual effects were achieved by means of colour and graphical objects.

Example 6. A digitally created reflective cylindrical anamorph – MS Excel – defined as a reflective cylindrical convex anamorph in the classification.

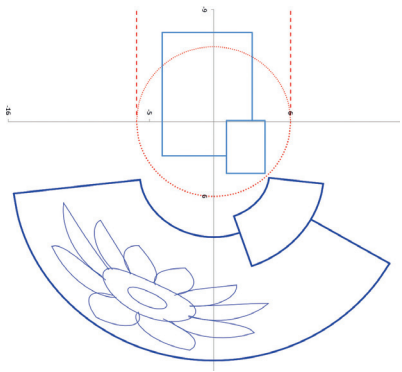

Fig. 25. *The Sunflower*, a reflective cylindrical anamorph. Digitally generated anamorph template

Fig. 26. *The Sunflower* – anamorph visualisation after a visual intervention

Example 7. A digitally created reflective conical anamorph – MS Excel – defined as a reflective conical convex anamorph in the classification.

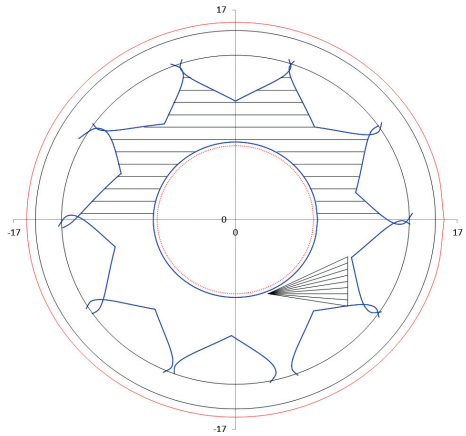

Fig. 27. *The Sunflower*, a reflective conical anamorph. Digitally generated template

Fig. 28. *The Sunflower* – anamorph visualisation after a visual intervention

6. Conclusion

The idea of anamorphism is the "destruction" of the object – the real image – and its presentation in an abstract and unclear form in order to read it properly by viewing it in a certain way or using a special mirror.

Anamorphic compositions contain the whole mechanism of illusion, pathos of abstraction and philosophy of artificially created reality. Anamorphosis is a rebus on the drawing plane. At the very beginning, skills and ways of drawing anamorphs were considered to be a kind of fun and a great mastery.

References

[1] Leeman F., Elffers J., Schuyt M., *Hidden Images: Games of perception, anamorphic art, illusion*, 1st Edition, New York 1976.

[2] Baltrušaitis J., *Anamorfozy albo Thaumaturgus opticus*: *Deformation Nets for the Reflective Conical Anamorphoses*, Wydawnictwo słowo/obraz terytoria, Gdańsk 2009.

[3] Du Breuil La Pere, *La perspective pratique*, Paris 1649.

[4] Niceron, J.-F., *La perspective curieuse ou magie artificelle des effets merveilleux*, Paris 1638.

[5] Roubaudi C., *Traité de géométrie descriptive*, Masson et Cie, Éditeurs, Paris 1948.

[6] Zdziarski A., *Classification and Nomenclature of anamorphic Images*, The Journal Biuletyn of Polish Society For Geometry and Engineering Graphics, Vol. 15, December 2005.

[7] Zdziarski A., Pałka A., *Limaçon of Pascal as an Anamorphic Image of a Circle*, The Journal Biuletyn of Polish Society For Geometry and Engineering Graphics, Vol. 22, June 2011.

[8] Zdziarski A., *Obrazy anamorficzne w metamorfozie przestrzeni miejskiej. Metamorfozy przestrzeni*, Idea Treść Forma, Vol. II, edited by F. Górski, M. Łaskarzewska-Średzińska, Fundacja Wydziału Architektury Politechniki Warszawskiej, Warszawa 2013.

[9] Zdziarski A., Jonak M., *Cylindrical anamorphic images – a digital method of transformation*, Technical Transactions, Vol. 10-A/2015.

TECHNICAL TRANSACTIONS 1/2017
CZASOPISMO TECHNICZNE 1/2017
CHEMISTRY
DOI: 10.4467/2353737XCT.17.003.6100

Grzegorz Kurowski (kurowski@chemia.pk.edu.pl)
Otmar Vogt
Jan Ogonowski
Institute of Organic Chemistry and Technology, Faculty of Chemical Engineering and Technology, Cracow University of Technology

Active ingredients in paint strippers

Substancje aktywne w preparatach do usuwania powłok lakierniczych

Abstract

The papers presents the study on the application of acetals as active ingredients in paint strippers. The formulation was prepared and the ability to wrinkling of the shell was rated. The ability to wrinkling of the shell was rated by examining the force required to detachment the coating.

Keywords: paint stripper, active ingredients, acetals

Streszczenie

W artykule przedstawiono badania dotyczące zastosowania acetali jako substancji aktywnych w preparatach do usuwania powłok lakierniczych. Sporządzono preparaty oraz oceniono ich zdolność do odspajania powłoki. Zdolność do odspajania powłoki oceniano badając siłę potrzebną do oderwania powłoki.

Słowa kluczowe: preparaty do usuwania powłok lakierniczych, substancje aktywne, acetale

1. Introduction

Since the Council of the European Union has banned the use of methylene chloride in paint removers [1], it was necessary to find substances, which are able to replace this compound. Currently, active ingredients that are used include compounds, such as N-methylpyrrolidone [2–6] and benzyl alcohol [7–12] as well as alkylene carbonates, such as propylene carbonate or ethylene carbonate [13–15]. Furthermore, carboxylic acid esters are also used. In patents, benzoic acid methyl ester [16] as well as methyl esters of dicarboxylic acids, such as succinic acid, glutaric acid and adipic acid [17–19], are described. Moreover we can use such esters like: ethyl acetate, butyl acetate, ethyl 3-ethoxypropionate and 1-methoxy-2-propyl acetate. However, the most preferred is ethyl 3-ethoxypropionate [20, 21]. The patents also describe such compounds as alkyl derivatives of carboxylic acid amides, dicarboxylic acid and hydroxycarboxylic acids [22], alkoxylated aromatic alcohols [23, 34].

Research on this topic is also being conducted at the Institute of Organic Chemistry and Technology of the Department of Chemical Engineering and Technology at the Cracow University of Technology. In our research, we study the usefulness of acetals as active ingredients.

The topic of this study was to check the influence of different active substances from the group of acetals on the ability to remove the coating. For comparison, we used the most commonly used active ingredients (N-methylpyrrolidone and benzyl alcohol).

2. Materials and methods

2.1. The paint removers

In the study, paint removers based on the author's recipe were used. The way of their preparation was different for the used active ingredient. For the study, we used substances with a different partition coefficient (logP). Due to the used different active ingredients, we used preparations in two forms - gel and emulsion.

In the study, the following substances were used: N-methylpyrrolidone (logP –0.40), dimethoxymethane (logP –0.26), dioxolane (logP –0.06), benzyl alcohol (logP 1.03), diethoxyethane (logP 1.14), cyclohexanone ethylene ketal (logP 1.35), benzaldehyde ethylene acetal (logP 1.63), dipropoxyethane (logP 2.21), dibutoxyethane (logP 3.27).

2.2. Preparations in gel form

Dioxolane and N-methylpyrrolidone were used in the gel preparation as active ingredients.

Table 1. The composition of the gel preparation

Substance	Composition [% wt.]
Active ingredient	42.2
Adduct	14.0
Water	14.0
Frakol	13.5
Ester solvent	6.7
Modisurf Clarity	4.8
Methocel	4.8

2.3. Preparations in emulsion form

Table 2. The composition of the emulsion preparation

Substance	Composition [% wt.]
Active ingredient	45.6
Methyl esters of rapeseed oil	13.6
Hydrogen peroxide	13.6
Candelila wax	9.1
Ester solvent	6.8
Frakol	6.8
Tween 40	2.9
Glycerol monostearate	1.6

Dimethoxymethane, dioxolane, benzyl alcohol, diethoxyethane, cyclohexanone ethylene ketal, benzaldehyde ethylene acetal, dipropoxyethane, dibutoxyethane were used in the emulsion preparation as active ingredients.

2.4. Plates

In the study, we used five types of plates. Two plates (blue, white) were delivered by Fiat Auto Poland Company in Tychy. The blue plate was painted with solvent-based acrylic paint. The white plate was painted with waterborne acrylic paint. The other two plates (green and brown) were painted with melamine formaldehyde paints. The last plate (epoxy) was painted with epoxy paint. The three last paints are used for roof covering.

2.5. The study of coating detachment

The paint remover was applied on the plate. In each case, the formulation was applied to the surface of 9 ± 0.3 cm^2. Due to the next steps of the procedure, we adopted a uniform square shape for the area of application of the preparation. The preparation was left on the surface for 24 hours. After this time, the preparation was removed and the effect on the surface was rated. A metal badge with an area of 9 ± 0.3 cm^2 was glued next to the coating. The glue was left for 48 hours to dry completely. After this time, the force required to detach the coating was measured. The measurement was performed on Zwick 1445 apparatus intended for testing the strength of materials. In the study, a constant crosshead speed of 50 mm/min was applied.

3. Results and discussion

3.1. Results of study of the interaction on the coating

In the case of the green plate, all active ingredients caused wrinkling of the shell. A similar situation took place in the case of the brown plate. An exception was diethoxyethane, which did not cause wrinkling of the shell. A different situation occurred in the case of the blue, white and epoxy plates. In those cases, wrinkling of the shell caused only dioxolane (emulsion). The wrinkling of the shell also caused dimethoxymethane, but only in the case of the blue plate. In the case of the epoxy plate, wrinkling of the shell also caused the preparation with benzyl alcohol. In other cases, the preparation did not cause any wrinkling of the shell.

3.2. Results of coating detachment study

In the case of the blue plate, we can see a reduction of the force needed to detach the coating that treated the preparation compared to the coating that did not treat the preparation. The average force required to pull-of the coating, which did not treat the preparation, is 216 N. However, not all layers of the coating are detached. The detachment of all layers of the coating was possible after the action on the coating formulations containing dioxolane (gel), diethoxyethane and benzaldehyde ethylene acetal. The force required to pull-of the coating is 158 N for dioxolane, 182 N for diethoxyethane and 136 N for benzaldehyde ethylene acetal. The preparations with cyclohexanone ethylene ketal and dibutoxyethane caused softening of the shell. It makes it possible to detach the coating of the silver layer with an average force of 148 N for cyclohexanone ethylene ketal and 121 N for dibutoxyethane.

Comparing the results with the properties of the compound (partition coefficient of o/w logP), we can see that, with an increase of the partition coefficient, the susceptibility to wrinkling of the shell is lower. The preparations containing dioxolane (logP –0.06) and

dimethoxymethane (logP –0.26) caused wrinkling of the shell. The preparations containing diethoxyethane (logP 1.14) and benzaldehyde ethylene acetal (logP 1.63) caused softening of the shell. This makes it possible to detach all layers of the coating. The preparations containing dipropoxyethane (logP 2.21) and dibutoxyethane (logP 3.27) also caused softening of the shell, but this makes possible to detach only one layer of the coating.

Blue plate

Table 3. Results of coating detachment study for the blue plate

Active ingredient	Force		Comments
	kPa	N	
–	246.1	216.0	A part of the coating was detached
Dimethoxymethane	The coating was wrinkled		
Dioxolane (gel)	176.2	158.6	All layers of the coating were detached
Dioxolane (emulsion)	The coating was wrinkled		
Diethoxyethane	209.5	182.2	All layers of the coating were detached
Cyclohexanone ethylene ketal	159.0	147.9	All layers of the coating were partially detached
Benzaldehyde ethylene acetal	146.6	136.4	All layers of the coating were detached
Dipropoxyethane	147.9	133.1	Coating intact
Dibutoxyethane	139.5	121.4	Coating was detached to the silver layer

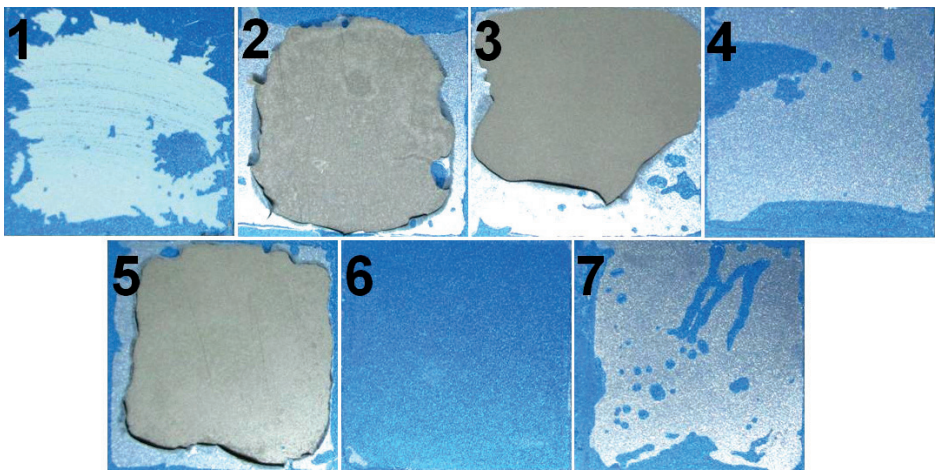

Fig. 1. The plate after study of coating detachment; 1 – reference sample, plate treated the preparation with 2 – dioxolane (gel), 3 – diethoxyethane, 4 – cyclohexanone ethylene ketal, 5 – benzaldehyde ethylene acetal, 6 – dipropoxyethane, 7 – dibutoxyethane

White plate

Table 4. Results of coating detachment study for the white plate

Active ingredient	Force		Comments
	kPa	N	
–	269.0	242.1	Coating intact
N-methylpyrrolidone	226.4	197.0	The first layer of the coating was detached
Dimethoxymethane	162.3	151.0	All layers of the coating were detached
Dioxolane (gel)	306.3	284.9	Coating intact
Dioxolane (emulsion)	The coating was wrinkled		
Benzyl alcohol	152.9	142.2	All layers of the coating were detached
Diethoxyethane	63.0	56.6	All layers of the coating were detached
Cyclohexanone ethylene ketal	243.5	226.4	All layers of the coating were detached
Benzaldehyde ethylene acetal	358.2	333.1	All layers of the coating were partially detached
Dipropoxyethane	155.7	140.2	Coating intact
Dibutoxyethane	209.8	195.2	Coating intact

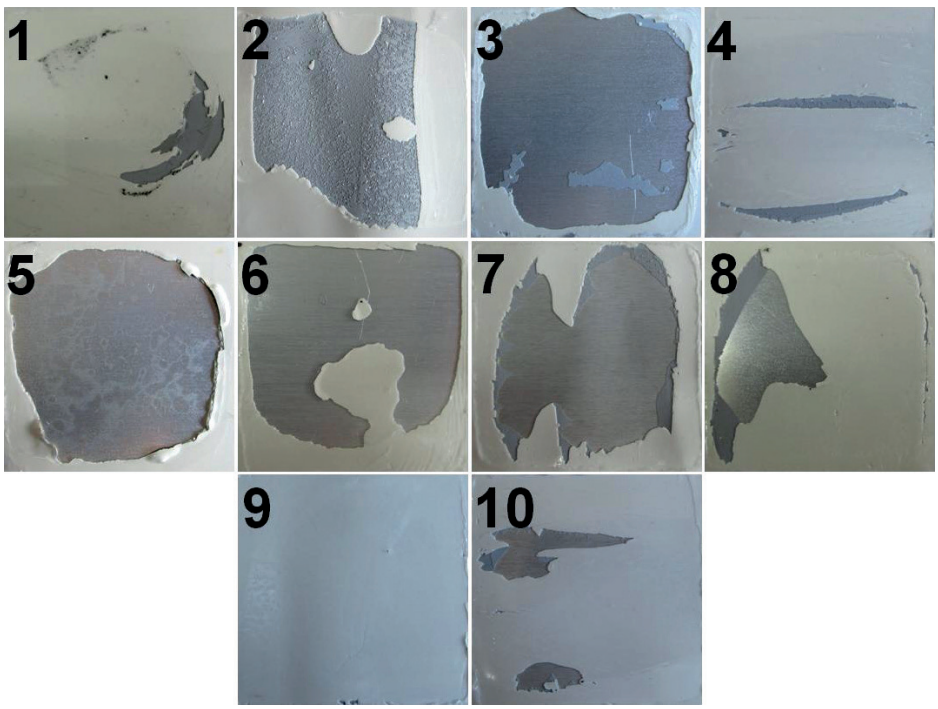

Fig. 2. The plate after study of coating detachment; 1 – reference sample, plate treated the preparation with 2 – N-methylpyrrolidone, 3 – dimethoxymethane 4 – dioxolane (gel), 5 – benzyl alcohol 6 – diethoxyethane, 7 – cyclohexanone ethylene ketal, 8 – benzaldehyde ethylene acetal, 9 – ipropoxyethane, 10 – dibutoxyethane

In the case of the white plate only, dioxolane (emulsion) caused wrinkling of the shell. In four causes, the activity caused softening of the shell, making the detachment of the coating possible. We can see that, with increasing logP, the force, which is needed to detach the coating, increases from 151 N for dimethoxymethane (logP –0.26) to 333 N for benzaldehyde ethylene acetal (logP 1.63). The exception is diethoxyethane. For this compound, the force needed to detach the coating is 56.6 N. A further increase of logP makes the preparation not soften the coating. In this case, the adhesion forces of the paint to the base are stronger than the adhesion forces of the glue to the coating. Therefore, we cannot detach the whole shell, but only small fragments. Such a situation took place in the case of the reference sample and the sample with dipropoxyethane and dibutoxyethane.

Green plate

In the case of the green plate, all substances caused a significant reduction of the forces required to detach the coating. Only the preparation with N-methylpyrrolidone did not cause a reduction of the forces required to detach the coating. However, it softened the coating, making it possible to remove all of the top layer.

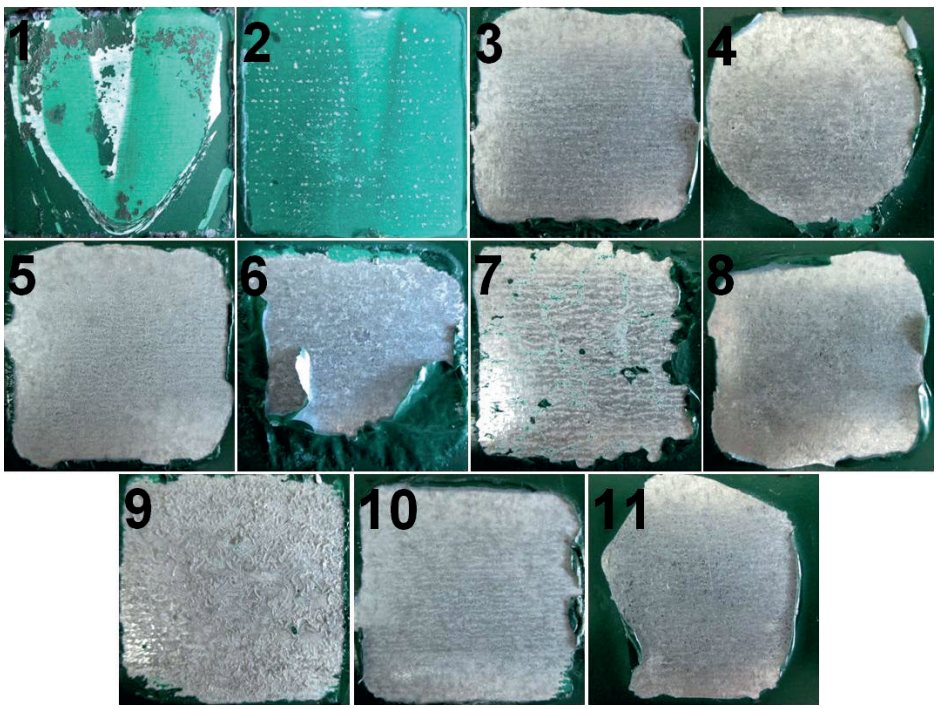

Fig. 3. The plate after study of coating detachment; 1 – reference sample, plate treated the preparation with 2 – N-methylpyrrolidone, 3 – dimethoxymethane 4 – dioxolane (gel), 5 – dioxolane (emulsion), 6 – benzyl alcohol 7 – diethoxyethane, 8 – cyclohexanone ethylene ketal, 9 – benzaldehyde ethylene acetal, 10 – dipropoxyethane, 11 – dibutoxyethane

In this case, regardless of the partition coefficient, the substances caused wrinkling of the shell. The only exception is N-methylpyrrolidone. In its case, despite a low value of partition coefficient, it did not cause wrinkling of the shell.

Table 5. Results of coating detachment study for the green plate

Active ingredient	Force		Comments
	kPa	N	
–	513.7	446.8	A part of the coating was detached
N-methylpyrrolidone	567.4	510.7	The first layer of the coating was detached
Dimethoxymethane	37.3	33.5	The coating was wrinkled
Dioxolane (gel)	139.1	121.0	The coating was wrinkled
Dioxolane (emulsion)	66.0	60.2	The coating was wrinkled
Benzyl alcohol	89.1	77.5	The coating was wrinkled
Diethoxyethane	120.8	108.7	The coating was wrinkled
Cyclohexanone ethylene ketal	32.2	30.0	The coating was wrinkled
Benzaldehyde ethylene acetal	66.5	56.4	The coating was wrinkled
Dipropoxyethane	60.0	54.0	The coating was wrinkled
Dibutoxyethane	58.8	54.7	The coating was wrinkled

Brown plate

Table 6. Results of coating detachment study for the brown plate

Active ingredient	Force		Comments
	kPa	N	
-	507.4	456.6	A part of the coating was detached
N-methylpyrrolidone	754.5	679.0	The first layer of the coating was detached
Dimethoxymethane	-	-	The coating was wrinkled
Dioxolane (gel)	392.9	353.6	The coating was wrinkled
Dioxolane (emulsion)	169.0	152.1	The coating was wrinkled
Benzyl alcohol	8.3	7.4	The coating was wrinkled
Diethoxyethane	305.8	275.2	The coating was wrinkled
Cyclohexanone ethylene ketal	83.4	77.5	The coating was wrinkled
Benzaldehyde ethylene acetal	37.4	34.8	The coating was wrinkled
Dipropoxyethane	268.3	241.4	The coating was wrinkled
Dibutoxyethane	173.1	155.8	The coating was wrinkled

The same situation as in the green plate occurred in the case of the brown plate. We can see a decreasing force required to detach the coating, from 465 N for the reference sample, to 7.4 N for benzyl alcohol. The exception is a test in which the coating was treated with the preparation containing N-methylpyrrolidone. In this case, the coating was not wrinkled. However, it softened the coating, making it possible to remove all of the top layer.

Similar in this case, regardless of the partition coefficient, the substances caused wrinkling of the shell. As a result, the force required to detach the coating was reduced. The only exception is N-methylpyrrolidone. In its case, despite a low value of partition coefficient, it did not cause wrinkling of the shell.

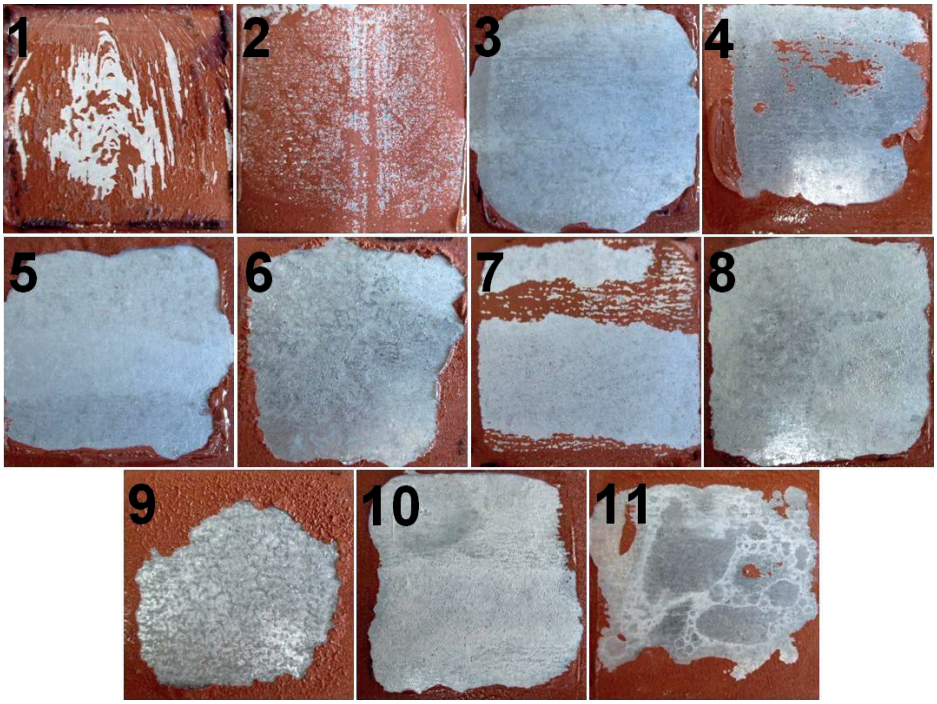

Fig. 4. The plate after study of coating detachment; 1 – reference sample, plate treated the preparation with 2 – N-methylpyrrolidone, 3 – dimethoxymethane 4 – dioxolane (gel), 5 – dioxolane (emulsion), 6 – benzyl alcohol 7 – diethoxyethane, 8 – cyclohexanone ethylene ketal, 9 – benzaldehyde ethylene acetal, 10 – dipropoxyethane, 11 – dibutoxyethane

Epoxy plate

Table 7. Results of coating detachment study for the epoxy plate

Active ingredient	Force		Comments
	kPa	N	
–	650.7	605.1	A part of the coating was detached
N-methylpyrrolidone	194.6	181.0	A small part of the coating was detached
Dimethoxymethane	63.0	52.9	A part of the coating was detached
Dioxolane (gel)	249.6	224.6	A part of the coating was detached
Dioxolane (emulsion)	The coating was wrinkled		
Benzyl alcohol	The coating was wrinkled		
Diethoxyethane	599.9	521.9	A part of the coating was detached
Cyclohexanone ethylene ketal	249.3	224.2	A part of the coating was detached
Benzaldehyde ethylene acetal	506.2	439.4	A part of the coating was detached
Dipropoxyethane	411.0	369.9	A part of the coating was detached
Dibutoxyethane	204.9	190.6	A part of the coating was detached

In case of epoxy plate only dioxolane and benzyl alcohol caused wrinkling of the shell. In other cause substances caused softening of the shell. Thereby the force needed to detachment of the coating was less than in the case of coating didn't treat the preparation. In this case, we also can see that with increasing logP, the ability to wrinkling of the shell is decreased. However, this is not as pronounced as in the case of acrylic coatings.

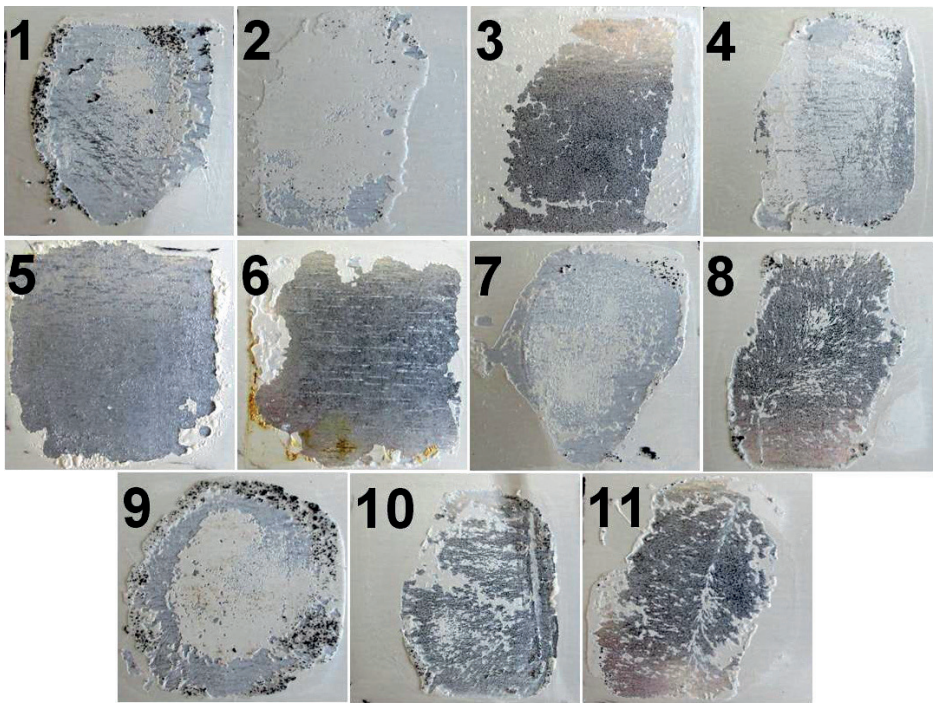

Fig. 5. The plate after study of coating detachment; 1 – reference sample, plate treated the preparation with 2 – N-methylpyrrolidone, 3 – dimethoxymethane 4 - dioxolane (gel), 5 – dioxolane (emulsion), 6 – benzyl alcohol 7 – diethoxyethane, 8 – cyclohexanone ethylene ketal, 9 – benzaldehyde ethylene acetal, 10 – dipropoxyethane, 11 – dibutoxyethane

4. Conclusions

All the used active substances caused softening or wrinkling of the shell. The best results were obtained on plates painted with melamine-formaldehyde paint. In the case of the green and brown plates, most of the test substances caused wrinkling of the shell. Thereby, the force needed to detach the coating was significantly lower than in the case of the reference sample. The exception is N-methylpyrrolidone, which did not cause wrinkling of the shell in any of the cases. In the case of the plate with acrylic (blue and white) and epoxy coating, only dioxolane caused wrinkling of the shell. In the case of the blue plate, wrinkling of the shell was also caused by dimethoxymethane. In other cases, we observed softening of the coating. Additionally, we can see that, with an increase of the partition coefficient, the ability of wrinkling the shell is lower. The study shows that dioxolane and dimethoxymethane are the best substances to replace methylene chloride.

References

[1] Decyzja Parlamentu Europejskiego i Rady zmieniająca dyrektywę Rady 76/769/EWG w zakresie ograniczeń we wprowadzaniu do obrotu i stosowaniu niektórych substancji i preparatów niebezpiecznych (dichlorometan).
[2] Patent no. US7087566, Dennis E Shireman, Paint removing composition, 08.08.2006.
[3] Patent no. US5932530, Georges Radu, Shizuo Maruyama, N-methylpyrrolidone, dimethyl ester and terpene-containing, paint removing composition, 03.08.1999.
[4] Patent no. US20060229220, Charles L Hawes, Dennis E Shireman, Color changing paint removing composition, 12.10.2006.
[5] Patent no. US6923873, Daniel Pageau, Elizabeth Marcu, David Aston, Paint stripping composition and method of using the same, 02.08.2005.
[6] Patent no. CA 2331439, Daniel Pageau, Elizabeth Marcu, David Aston, Paint stripping composition and method of using the same, 19.01.2001.
[7] Patent no. WO2008/142562, European Patent EP2152816A1, Biodegradable ecological paint remover, Michael Brailsford, 27.11.2008.
[8] Patent no. US2010326479, Michael Brailsford, Simon Mark Dormon, Paint remover, 30.12.2010.
[9] Patent no. US20050026799, Marvin Detar, Frederick Connelly, Water-based paint stripper, 03.02.2005.
[10] Patent no. US2010/0326479, Michael Brailsford, Simon Mark, Dormon, Paint remover, 30.12.2010.
[11] Australian Patent Application 2007902248, Michael Brailsford, Biodegradable ecological paint remover, 30.04.2007.
[12] Patent no. WO2006/071194, Anna Samuelsson, Agent to remove paint, lacquer, glue, plastic or similar from objects and use of it, 06.07.2006.
[13] Patent no. US6548464, James R Machac, Jr., Edward Chung-Yit Nieh, Susan A. Woodrum, Edward T Marquis, Pains stripper for aircraft and other multicoat systems, 15.04.2003.
[14] Patent no. US7485608, Daniel Perlman, pH-buffered alkylene carbonate nail polish and paint remover, 03.03.2009.
[15] Patent no. US20060058208, Mark Ventura, Steven Bolkan, Raymond F Ashley, Paint & Ink remover two-phase system, 16.03.2006.
[16] Patent no. US6417149, Gerald Wojcik, Paint stripping composition and process containing methyl benzoate and formic acid, 09.07.2002.
[17] Patent no. US6624222, Paul E Kestyn, Augustin T Chen, Hong Zhao, Environmentally safe paint stripper emulsion, 23.08.2003.
[18] Patent no. US6790891, Paul E Kestyn, Augustin T Chen, Hong Zhao, Environmentally safe paint stripper, 14.08.2004.
[19] Patent no. WO2010/084159, European Patent EP2384359A1, Stripping composition, Arnaud Bourdette, Jean-Emile Zanetto, Patrick Lasnet de Lanty, 29.07.2010.
[20] Patent no. US6159915, James R Machac, Jr, Edward T Marquis, Susan A. Woodrum, Katty Darragas, Paint and coating remover, 12.12.2000.

[21] Patent no. US6395103, James R Machac, Jr, Edward T Marquis, Susan A. Woodrum, Degreasing compositions, 28.05.2002.
[22] Patent no. EP2345702, Ramon Valls, Joaquin Bigorra Llosas, Elisabet Graupera, Javier Raya, Paint and coating remover compositions, 20.07.2011.
[23] Patent no. US7482316, Neil R Wilson, Michael A Murphy, Jr., Water-based flushing solution for paint and other coatings, 27.01.2009.
[24] Patent no. EP1918322A1, Kathryn Ellen Foster, Michael Scott Ciemiega, Paint stripper with corrosion inhibitor for aluminum, 31.10.2007.

TECHNICAL TRANSACTIONS 1/2017
CZASOPISMO TECHNICZNE 1/2017
CIVIL ENGINEERING
DOI: 10.4467/2353737XCT.17.004.6101

Alicja Kowalska-Koczwara (alicja.kowalska.koczwara@gmail.com)
Krzysztof Stypuła
Institute of Structural Mechanics, Faculty of Civil Engineering, Cracow University of Technology

A COMPARATIVE ANALYSIS OF TWO METHODS FOR DETERMINING THE INFLUENCE OF VIBRATIONS ON PEOPLE IN BUILDINGS

ANALIZA PORÓWNAWCZA DWÓCH METOD OKREŚLANIA WPŁYWU DRGAŃ NA LUDZI W BUDYNKACH

Abstract

Different methodologies for the assessment of the influence of vibrations on people residing in buildings can be found in international standards. There are two dominant methods of assessment: the analysis of the RMS values in 1/3 octave bands and vibration dose VDV. In this article, these two methods of assessing the influence of vibration on humans are compared, not only on the basis of standard formulas but also on a real example. The influence of transport vibrations (busses, trams, trucks) on humans residing in traditional, masonry buildings was analysed. Conclusions resulting from a comparative analysis of the two methods of evaluation were formed.

Keywords: passive perception of vibration, vibration dose, RMS analysis, 'in-situ' measurements, transport vibrations

Streszczenie

W normach światowych można znaleźć różne metodyki służące ocenie wpływu drgań na ludzi przebywających w budynkach. Dominują dwie metody ewaluacji: analiza RMS w pasmach 1/3 oktawowych oraz dawka (doza) wibracji VDV. W niniejszym artykule obydwie metody oceny wpływu drgań na ludzi zostały porównane nie tylko na podstawie zapisów normowych, ale także na konkretnym przykładzie. Analizie poddano wpływ drgań komunikacyjnych (przejazd autobusu, tramwaju, samochodu ciężarowego) na ludzi w budynku wykonanym w technologii tradycyjnej, murowanej. Sformułowano wnioski, które wynikają z analizy porównawczej dwóch metod ewaluacyjnych.

Słowa kluczowe: bierny odbiór drgań, dawka wibracji, analiza RMS, pomiary „in-situ", drgania komunikacyjne

1. Introduction

People residing in buildings are often exposed to dynamic influences, especially those of paraseismic origin. More and more dense urban building brings paraseismic vibration sources, mainly transport vibration sources, closer to buildings. The intensity of these dynamic influences increases because of much higher numbers of road users and much faster trains. In the diagnosis and design of buildings, there is a growing need to take into account these influences by analysing the ability to provide the necessary vibration comfort for residents. Vibration comfort cannot be exceeded. There are three main methods to assess vibration comfort:

a) corrected value – in which the assessment parameter is the acceleration (velocity) of vibration corrected across the whole frequency range;
b) *RMS* values - spectrum (frequency structure) of the effective value of acceleration (velocity) of vibration in 1/3 octave band;
c) *VDV* vibration dose – probability of complaints.

The corrected value (present in standards [1, 3]) is determined by measuring the vibration at the location where it is perceived by humans using correction by means of a correction filter. The measurement information is expressed by one number. This number is compared with the corresponding value of providing the necessary vibrational comfort to people in the building. The application of the corrected value in the evaluation of vibration influence on people is relatively small. The frequency and degree to which the reduction of vibration should be introduced in order to ensure people the necessary vibration comfort cannot be determined on the basis of the corrected value – the researcher only knows whether or not the comfort level is exceeded. For these reasons, the corrected value will not be analysed later in this study – is becoming less common in international studies.

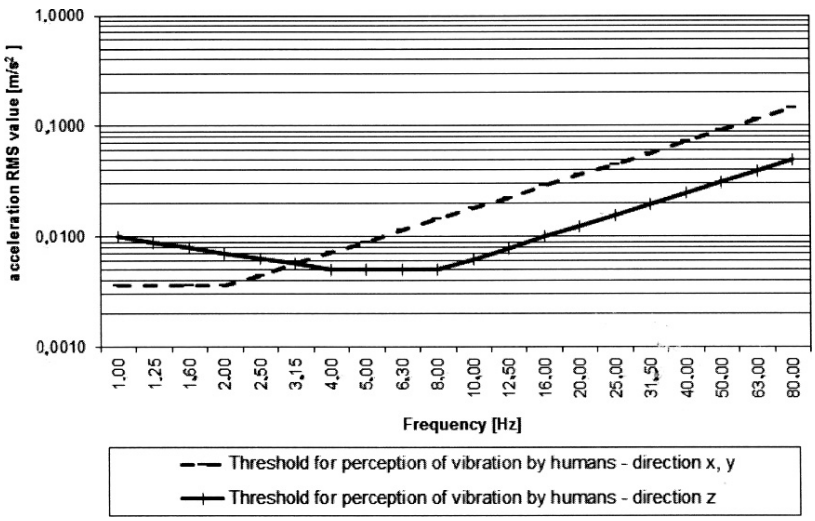

Fig. 1. Basic lines corresponding to the threshold for perception of vibration by humans (according to ISO 2631-2 [4] or Polish standard PN-88 / B-02171 [1])

The basic method of evaluation in the world is *RMS* – this evaluation parameter is adopted, for example, in standards [1, 4, 5] and used by many researchers [e.g. 6–9]. From this method of evaluation, we can receive information concerning not only whether or not the comfort level is exceeded, but also within which frequency band any exceedance has occurred. This information can be obtained by comparing the frequency structure of the measured frequency curve with the corresponding frequency providing the necessary comfort of vibration to people in the building. Comfort level, what was written earlier, should not be exceeded. Sometimes, in the experts opinion, it tends to not exceed the threshold for perception of vibration. The threshold for the perception of vibration in both horizontal and vertical directions is shown in Fig. 1.

The basic levels for determining the level of vibration comfort are shown in Fig. 1. To identify lines that represent the vibration comfort threshold for the perception of vibration, lines should be multiplied by the appropriate value of factor 'n' (see Table 3 acc. [1]). This 'n' factor depends on:

- the purpose of the room in the building (*e.g.* operating theatres, precision laboratories, hospitals, apartments, residential rooms, offices, classrooms, workshops, factories etc.);
- the time of the occurrence of the vibration (daytime or night-time);
- the nature of vibrations and the frequency of their occurrence (continual or sporadic vibrations).

Sometimes, investors have stricter regulations then just conformity to accepted comfort levels or remaining within the thresholds of the perception of vibration by humans. For example, in the regulations of the Warsaw Metro, the value of the human vibration perceptivity ratio (named in Polish: WODL) should not exceed 0.85. The WODL ratio (in English, the human vibration perceptivity ratio – HVPR), proposed by K. Stypuła [10], is the measure of vibration perception by people. It is the maximum ratio of the acceleration *RMS* value obtained from the analysis to the acceleration *RMS* value equivalent to the threshold for the perception of vibration by humans (in the same 1/3 octave band) chosen from each 1/3 octave band (formula 1).

$$WODL = \max\left(\frac{aRMS}{a_z}\right) \tag{1}$$

where:
aRMS – acceleration *RMS* value obtained from analysis;
a_z – acceleration *RMS* value equivalent to the threshold for the perception of vibration in a z-direction in the same 1/3 octave band as in *aRMS*.

This factor is very useful; however, because the graph adopts a logarithmic scale, it is often difficult to read by how much the threshold has been exceeded, or even if it has been exceeded at all (see Fig. 2).

The third of the applied parameters of the characteristics of vibration allows the effect of vibration on the inhabitants of buildings to be analysed by reference to the full-time assessment of the impact of vibration. The introduction of a value defined as the vibrations dose for the assessment of the influence of vibration on people allows the assessment of vibrations

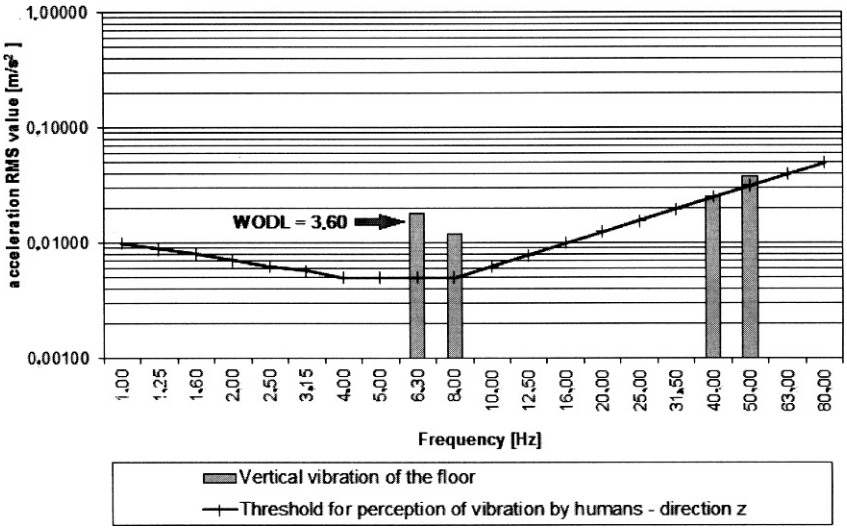

Fig. 2. Determination of human vibration perceptivity ratio (WODL)

of varying duration and repetition (continuous, intermittent, impulse). Vibrations are considered during the entire period of human exposure to vibration. In standard [2], vibration dose is denoted as *VDV* and expressed in [m/s^{1,75}] – this is given by the formula:

$$VDV = \left\{ \int_0^t \left[a_w(t) \right]^4 dt \right\}^{1/4} \tag{2}$$

where:
$a_w(t)$ – frequency-weighted acceleration;
T – duration of measurement.

The fourth power vibration dose method is more sensitive to peaks than the *RMS* method and this is why *VDV* is mostly used in shock analysis [11, 12]. In standard [4], the *VDV* method is defined as an additional method in cases when the crest factor is higher than 9. While in British Standard [2], *VDV* is the only method of evaluation. *RMS* method is also used in design see, for example, [10, 13].

The value of the vibration dose (VDV) determined from the above formula is compared with the values given in standards [2, 4]. In table 1, the three levels of probability of complains are given according to standards [2, 4].

Table 1. Criteria for assessing the influence of vibrations depending on the value *VDV* [m/s^{1,75}]

Place	Low probability of adverse comments	Adverse comments possible	Adverse comments probable
Residential buildings – 16h day	0.2–0.4	0.4–0.8	0.8–1.6
Residential buildings – 8h night	0.13	0.26	0.51

As can be seen from the above table, the value of *VDV* gives an answer for the question: if there will be any complaints from residents. The aspect of complaints is important for investor. *VDV* gives no information about the degree to which the occurring vibrations influence people. Unfortunately, nothing is known about which frequency must be reduced; this is why this method is not good for design and is only used as an additional method in the ISO standard.

2. Description of the analysed building

The building selected for analysis is located in Warsaw near two kinematic excitation sources:

- a road with heavy traffic located about 20m from the building;
- a tramway located about 30m from the building (distance measured from the railhead).

It is building with residential premises and offices. This is a five-storey building built using traditional brick technology that is typical in Poland (see Fig. 3) with a longitudinal arrangement of load-bearing walls.

Fig. 3. View of the facade from the east

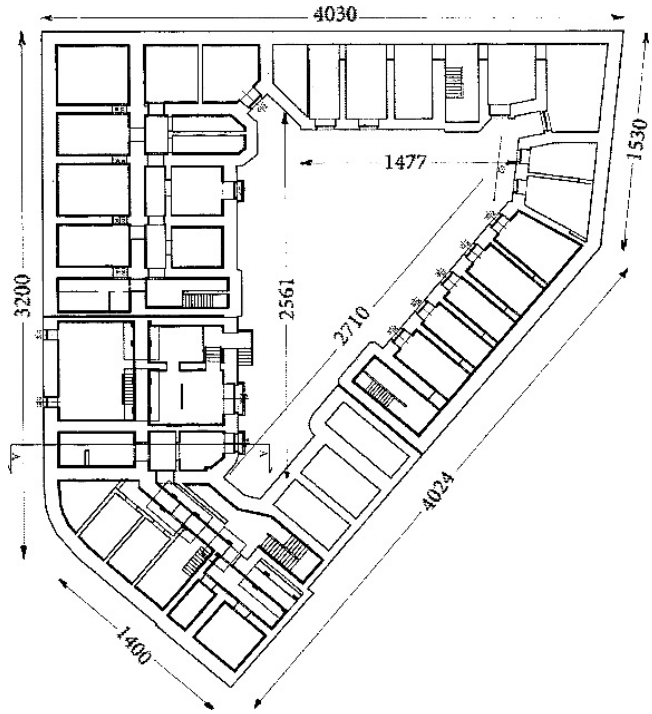

Fig. 4. Horizontal plan of building basement

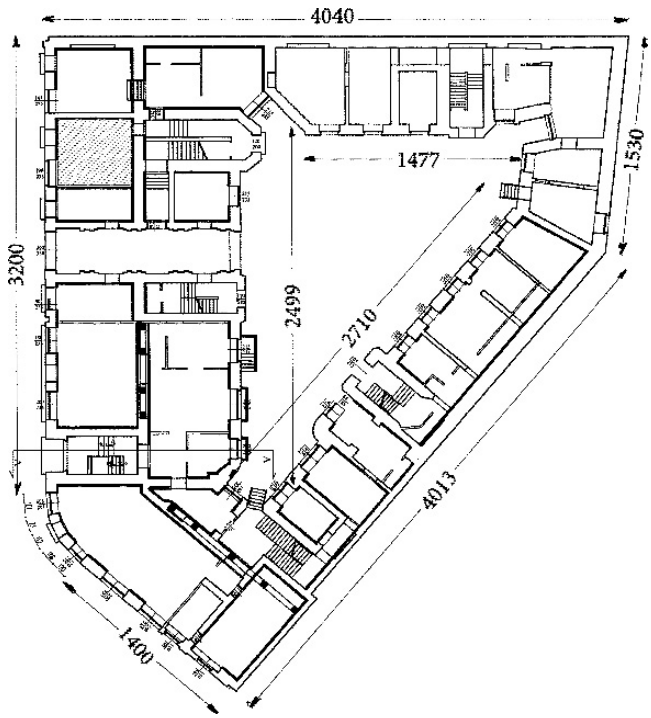

Fig. 5. Horizontal plan of the ground floor

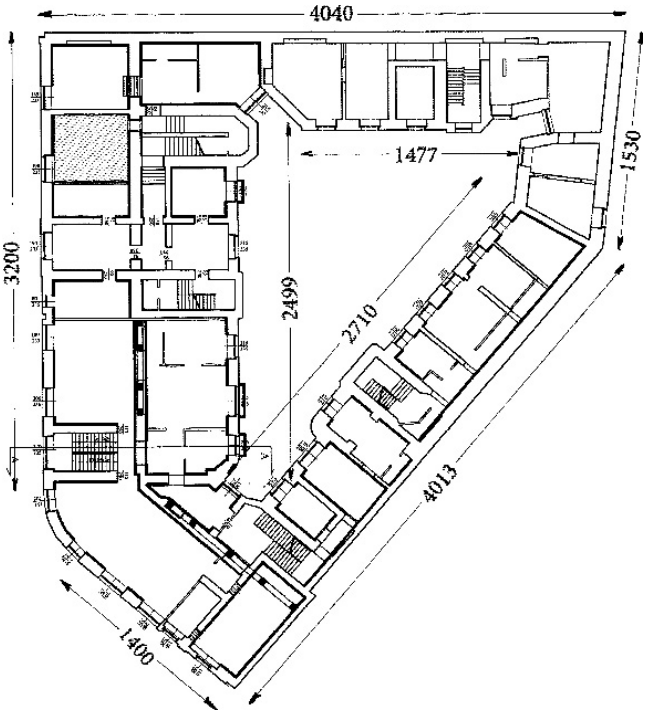

Fig. 6. Horizontal plan of the repeatable floor

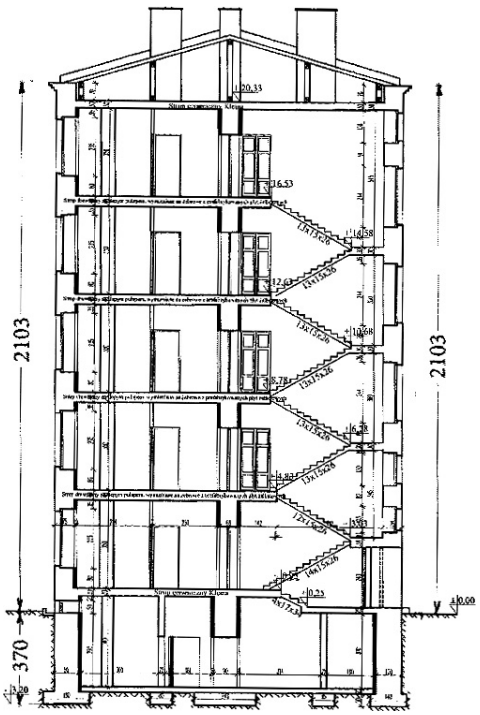

Fig. 7. Cross-section of the building

Horizontal floor plans and vertical cross-section of the building are given in Figs. 4–7.

3. Results of analysis

In accordance with section C.4 of standard [2], by possessing a registered signal that has not been weighted by weighting functions *Wb* (for the vertical direction) and *Wg* (for the horizontal direction), it is possible to calculate the estimated value of the *VDV* according to the formula:

$$eVDV = 1{,}4 \cdot a(t)_{RMS} \cdot t^{0{,}25} \tag{3}$$

where:

$a(t)_{RMS}$ – *RMS* value weighted by weighting functions *Wb* and *Wg* according to the appropriate direction;

t – the total duration of vibrations.

Five vibrograms from the measurement point 17z located in the middle of the ceiling on the fourth floor (see Fig. 8) were used for analysis. Measurements at this point were carried out in a vertical direction.

The excitation sources during these five measurements were: tram passing (three measurements); bus passing (one measurement); heavy truck passing (one measurement). An example of a registered signal is presented in Fig. 9 – this represents the passage of a tram on the nearest tram track.

RMS of registered signal was made. *RMS* analysis of the signal presented in Fig. 9 is shown in Fig. 10.

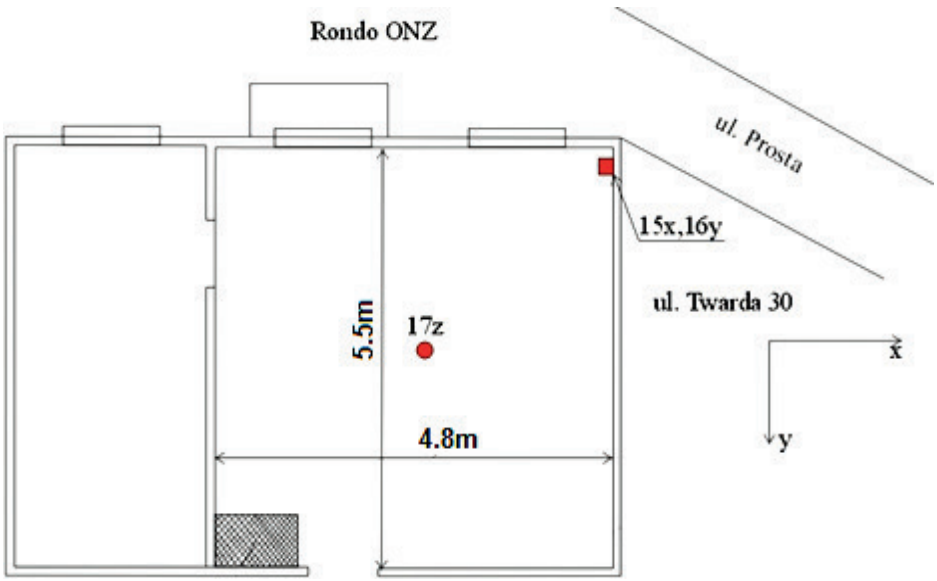

Fig. 8. Location of measurement points

As can be seen in the above figure, according to standard [1], the threshold for the perception of vibration is exceeded, while the comfort level during night and day time is not exceeded.

From signal presented in Fig. 9, the e*VDV* value was then determined. The obtained e*VDV* value is 0.3 which means that (acc. Table 1) there is a low possibility of complaints during the daytime but complains are possible during the night. Similar analyses were made for the other four measurements and the results are listed in Table 2.

Some events can be noticed from the above Table. In almost all cases, analyses made using *RMS* and *VDV* yield similar results – only in the fifth measurement are they

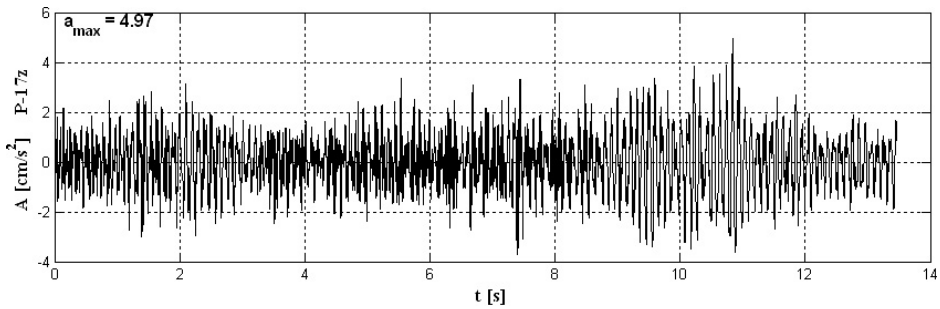

Fig. 9. The registered signal caused by tram passage

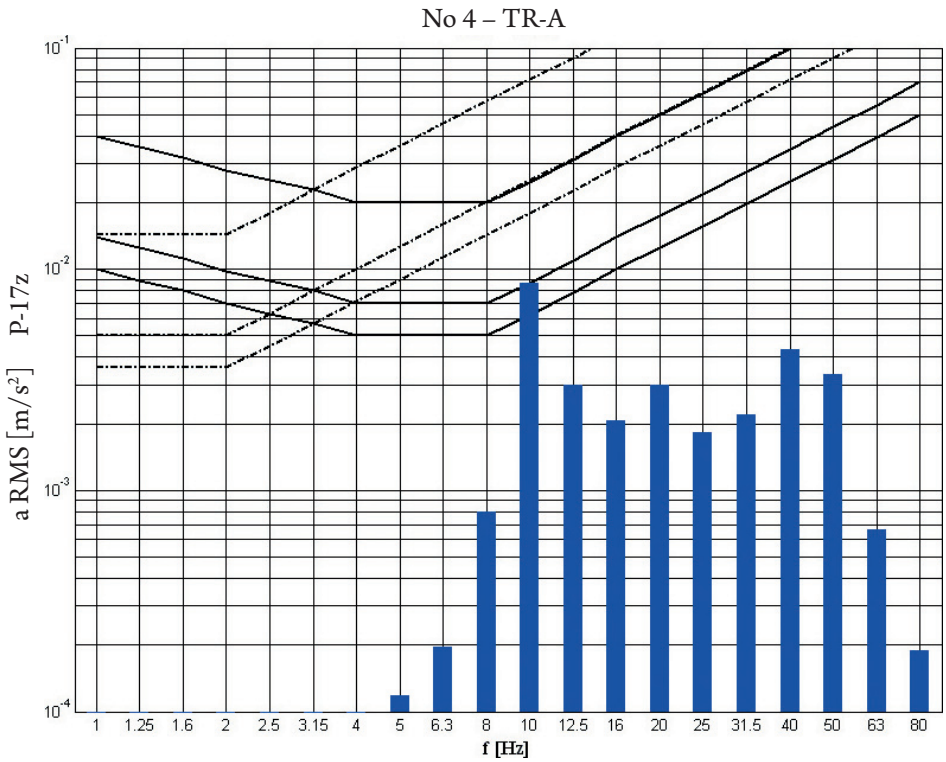

Fig. 10. *RMS* analysis of registered signal

significantly different. *RMS* analysis info*RMS* about the effects of vibrations on people while *VDV* analysis provides information about the probabilities of complaints from residents.

Table 2. Results of comparative analysis

Measurement No.	Source of vibration	RMS analysis			eVDV analysis	
		WODL	f [Hz]	comment	VDV value [m/s^{1,75}]	comment
1	Bus	1.57	10	Exceedance of comfort level during night	0.404	complains possible during daytime and very probable during the night
2	Tram	1.39	10	Exceedance of perception threshold of vibration but comfort levels not exceeded	0.300	complains possible during night-time
3	Heavy truck	0.89	10	Perception threshold not exceeded	0.180	Low possibility of complaints
4	Two trams	1.39	10	Exceedance of perception threshold of vibration but comfort levels not exceeded	0.390	complaints possible during night-time
5	Tram	0.68	10	Perception threshold not exceeded	0.313	complaints possible during night-time

To check the sensitivity of *VDV* analysis on the number of different events per day, formula 4 was used:

$$VDV_{day/night} = \left(\sum_{n=1}^{n=N} VDV^4 \right)^{0,25} \tag{4}$$

Occurrences of forty-three tram passages were simulated with *VDV* values varying from 0.1 to 0.4 during the daytime. The VDV_{day} was determined from the above formula and is 0.781– this means that complaints are possible. It was assumed that eighteen events of tram

passages occurred during the night-time with *VDV* values varying from 0.1 to 0.4. In such cases, the VDV_{night} is 0.615 which means that complaints are very probable. As can be seen, *VDV* analysis is very sensitive to number of events occurring during the day or in the night.

4. Conclusions

In this paper, a comparative analysis of two different methods of assessment of the vibration influence on humans was made. Both methods, *RMS* and *VDV*, are contained in the ISO standard [4] – the *RMS* method is defined as the main method and *VDV* as an additional method.

According to the results of analysis, it can be seen that the *RMS* method gives much more information about the vibrations and provides an answer not only on the exceedance of perception thresholds or comfort levels, but also in which frequency band the exceedance occurred. Therefore, *RMS* is a much more appropriate choice to provide information to consider in the design of structures. However, it should be noticed that the *RMS* method takes into account the time of influence of vibration on humans only by using the "n" factor while the *VDV* method takes the time itself by including time in the scope of integration. This is why the *VDV* method is more sensitive *to* different events that can occur during the daytime or at night.

The results of analysis of single events made using both methods are similar. There are some differences but not to the extent that could be expected. For the whole day or night, the *VDV* method is much restrictive. But it should be noted that the *RMS* method is concerned with the vibration influence on humans while the *VDV* values inform about the probability of complaints (low, more possible, probable) but do not provide a precise numerical value of probability.

It seems that a good direction for the evaluation method is the option contained in ISO standard [4] in which for crest factors greater than nine, more than one method of the evaluation of vibration influence on humans should be used and both main and additional methods should be reported.

References

[1] PN-88/B-02171 Evaluation of vibrations influence on people in buildings, 1988, Polish Standard [in Polish].

[2] BS 6472-1:2008 Guide to evaluation of human exposure to vibration in buildings, Part 1: Vibration sources other than blasting, 2008, British Standard.

[3] DIN 4150-2 Structural vibration, Part 2: Human exposure to vibration in buildings, 1999, German Standard.

[4] ISO 2631-2 Guide to the evaluation of human exposure to whole body vibration. Part 2 – Vibration in buildings, 2003, International Organization for Standardization.

[5] ISO 10137 Bases for design of structures – Serviceability of buildings and walkways against vibration, 2007, International Organization for Standardization
[6] Tamura Y., Kawana S., Nakamura O., Kanda J., Nakatà S., *Evaluation perception of wind-induced vibration in buildings*, Structures & Buildings, 159, 2006, 1–11.
[7] Kwok K.C.S., Hitchcock P.A., Burton M.D., *Perception of vibration and occupant comfort in wind-excited tall buildings*, Journal of Wind Engineering and Industrial Aerodynamics, Vol. 97, Issues 7–8, September–October 2009, 368–380.
[8] Waddington D.C, Woodcock J., Peris E., Condie J., Sica G., Moorhouse A.T., Steele A., *Human response to vibration in residential environments*, J. Acoust. Soc. Am. 135,82, 2014.
[9] Marioka M., Griffin M.J., *Difference thresholds for intensity perception of whole-body vertical vibration: Effect of frequency and magnitude*, J. Acoust. Soc. Am. 107 (1), January 2000, 620–624.
[10] Kawecki J., Stypuła K., *Zapewnienie komfortu wibracyjnego ludziom w budynkach narażonych na oddziaływania komunikacyjne (Ensuring vibrational comfort for people in buildings exposed for transport impact)* (in Polish), Wyd. Politechnika Krakowska, Kraków 2013.
[11] Mansfield N.J., Holmlund P., Lundstrom R., *Comparison of subjective responses to vibration and shock with standard analysis methods and absorbed power*, Journal of Sound and Vibration, 2000, 230(3), 477–491.
[12] Gaspar C.M.R., Santosda Silva J.G., Costa-Neves L.F., *Multimode, Vibration control of building steel–concrete composite floors submitted to human rhythmic activities*, Computers and Structures 165, 2016, 107–122.
[13] Kawecki J., Kozioł K., Stypuła K., *Wpływ konstrukcji obudowy tunelu metra na prognozowany odbiór drgań przez ludzi przebywających w pobliskim budynku* (*Influence of Metro Tunnel Structure on Prognosed Vibrations received by People Staying in Nearly Building*), (in Polish), Czasopismo Techniczne, Vol.3-B/2010, 51–58.

TECHNICAL TRANSACTIONS 1/2017
CZASOPISMO TECHNICZNE 1/2017
CIVIL ENGINEERING
DOI: 10.4467/2353737XCT.17.005.6102

Krystyna Kuźniar
Institute of Technology, Faculty of Mathematics, Physics and Technical Science, Pedagogical University of Cracow

Tadeusz Tatara (ttatara@pk.edu.pl)
Institute of Structural Mechanics, Faculty of Civil Engineering, Cracow University of Technology

Simple models for determination of the differences of ground and building foundation response spectra in LGC region

Proste modele do wyznaczania różnic w spektrach odpowiedzi od drgań gruntu i drgań fundamentów budynków w LGOM

Abstract

The paper deals with the transmission of mine-induced vibrations in the LGC region from the ground to the foundations of typical buildings. The simple, easy-to-use models have been proposed for the determination of the differences (relations) between ground and foundation acceleration response spectra. Experimentally obtained acceleration response spectra from vibrations occurring simultaneously on the ground near the building and the building foundation were the basis for the verification of the accuracy of the proposed models.

Keywords: mining tremors, transmission of ground vibrations to building foundation, response spectra transmission

Streszczenie

Praca dotyczy przekazywania drgań pochodzenia górniczego w LGOM z gruntu na fundamenty typowych budynków. Zaproponowano proste, wygodne w stosowaniu, modele do wyznaczania różnic (relacji) w przyśpieszeniowych spektrach odpowiedzi od drgań gruntu i drgań fundamentów budynków. Weryfikacji dokładności proponowanych modeli dokonano, bazując na przyśpieszeniowych spektrach odpowiedzi od uzyskanych eksperymentalnie, jednocześnie mierzonych drgań gruntu obok budynków i fundamentów budynków.

Słowa kluczowe: wstrząsy górnicze, przekazywanie drgań z gruntu na fundament budynku, transmisja spektrów odpowiedzi

1. Introduction

Surface vibrations originating from mining rockbursts belong to the most intense, so-called paraseismic vibrations. Their random occurrence is one of the features of this type of vibrations, which causes significant problems in the analysis. Additional difficulties in assessing and forecasting the effect of mining related vibrations on buildings result from dynamic soil-structure interaction (SSI), including the significant differences that can be observed between simultaneously recorded free-field motion near the building and building foundation vibrations [5, 8, 12, 13, 18]. However, very often in practice, vibration measurements are conducted only on free-field (e.g. at the design stage of the building), while the use of building foundation vibrations allows for a more accurate assessment of the harmfulness of vibrations for the buildings [11]. Therefore, it is necessary to assess and predict the transmission of free-field motion to the building foundations. In the paper [2], response spectra of surface vibrations recorded in three mining areas of the Upper Silesian Coalfield (USC) were also established, indicating that the local ground properties may have a significant impact on the shape of the standard spectra.

In the works referring to the experimental examination of the soil-structure interaction, a comparison of the maximum values of ground motion near the building and the building foundation vibrations, recorded simultaneously, is often made in order to evaluate the transmission of free-field motion to the building foundations. This very simple way in the case of mining-related vibrations was used in e.g. [6, 8, 17].

A comparison of the curves of response spectra, obtained on the basis of mining origin vibrations, recorded simultaneously on the free-field near the buildings and on the building foundations, allows for a more advanced analysis of vibration transmission from the ground to the building foundations [5, 7, 13, 18]. A modification of this method, involving a calculation of the Ratio of Response Spectra (*RRS*), with respect to the free-field and the building foundation vibrations caused by rockbursts, is proposed in [9]. Such a method of assessing the SSI is commonly used for vibrations caused by earthquakes [3, 4, 16]. Simple approximate models for practical uses in the evaluation of the transmission of seismic vibrations from the ground to the building foundation are proposed in [3, 14–16]. The suitability (accuracy) of these models, proposed in the literature for vibrations of seismic origin, in the case of vibrations due to rockbursts in the Legnica-Głogów Copper District (LGC), was analysed in [10].

The paper proposes similar, simple empirical models in order to determine the differences (relationship) in acceleration response spectra, calculated on the basis of the free-field and building foundation vibrations, prepared for use in conditions of the LGC region. Separate models were established for the dimensionless acceleration response spectra (β) – model $RRS(\beta)$, and dimensional spectra (S_a) - model $RRS(S_a)$. Variants of the model were designed for use regardless of the type of building (universal models), as well as models intended for use separately in each of the groups of typical residential buildings in the mining region: low-, medium- and high-rise. All of the proposed models are based on the acceleration response spectra obtained using experimentally recorded free-field and building foundation vibrations in the LGC region.

2. Characteristics of experimental data

The work deals with the transmission of mining-related vibrations in the LGC region from the free-field to the building foundations. The analysed buildings can be treated as typical residential buildings in the mining region and as buildings that are representative in their classes. These are: low-rise, one-family, two-storey, masonry dwelling house (N); medium-rise, typical prefabricated (large-block), multiple-segment, five-storey building (S) and high-rise prefabricated (large-plate), two-segment, twelve-storey building (W). All of the considered buildings have basements and are founded on continuous footings. They are situated within a residential complex, at a short distance from each other. The free-field stations are located approximately 5 m from the N, S and W buildings in order to eliminate the influence of buildings' vibrations on the vibrations of the ground points. The epicentral distances of measurement stations N, S and W fluctuated between 913–1224, 614–1430 and 938–1163 m, respectively.

Rockbursts with energies of at least 10^6 J, which generated free-field vibrations, characterised by the measured maximum values of acceleration equal to at least 0.1 m/s^2, were the sources of vibrations.

Simultaneously measured pairs of acceleration records of horizontal vibrations of the free-field vibrations next to the building (a few meters from the building) and the building foundation vibrations (parallel to the transverse and the longitudinal axis of the building respectively) are taken into account in the case of each of the hundreds of considered mining rockbursts. The number of measured pairs of acceleration records of the free-field and the building foundation vibrations considered in the studies is as follows: in the case of N-type building – 111, in the case of the building S – 205, and for the W-type building – 181. The installed measuring equipment records the vibrations in the frequency range from 0.5 Hz to 100 Hz, and the maximum acceleration range is 3 m/s^2.

Dimensionless and dimensional acceleration response spectra (β and S_a respectively) have been calculated using the above-mentioned vibration records. A fraction of critical damping ξ was adopted to be equal to 3%, according to the experimental studies of damping of the considered types of buildings [1]. It can be stated that the response spectra calculated using the free-field and the building foundation records differ considerably, which is the result of a dynamic SSI.

For each pair of response spectra (ground - building foundation), corresponding ratios $RRS(\beta)$ for the dimensionless acceleration response spectra (β) and $RRS(S_a)$ for dimensional acceleration response spectra (Sa) are calculated according to formulae (1) and (2).

$$RRS(\beta) = \frac{\beta_f}{\beta_g} \tag{1}$$

$$RRS(S_a) = \frac{S_{af}}{S_{ag}} \tag{2}$$

where:

$RRS(\beta)$, $RRS(S_a)$ – the ratio describing the transmission of response spectra from the ground to the foundation of the building, in the case of dimensionless and dimensional spectra respectively,

β_f, S_{af} – dimensionless and dimensional acceleration response spectrum from building foundation vibrations,

β_g, S_{ag} – dimensionless and dimensional acceleration response spectrum from free-field vibrations near the building.

Using the ratios *RRS* for particular rockbursts, averaged relationships (*RRS*) were computed for all pairs of the vibrations recorded on the free-field and on the foundations of the buildings N, S and W as well as the averaged relations *RRS* for the considered types of buildings.

Averaged ratios $RRS(\beta)$ and $RRS(S_a)$, determined on the basis of the acceleration records of the free-field and buildings foundations for all types of the considered buildings, are shown in Fig. 1. On the other hand, Fig. 2 contains averaged ratios $RRS(\beta)$ and $RRS(S_a)$ prepared separately for buildings corresponding to the classes of low-rise buildings (N), medium-rise buildings (S) and high-rise buildings (W).

It is visible that the average graphs $RRS(\beta)$ corresponding to the dimensionless response spectra (β) differ from the corresponding average curves $RRS(S_a)$, which were prepared on the basis of the dimensional response spectra (S_a). This observation applies to both the average relations *RRS* for all pairs of the ground-foundation determined in the case of all buildings of type N, S and W, as well as separately for each of the considered types of buildings (N, S, W). The values of the average relations $RRS(S_a)$ are significantly smaller (especially in the range of the lower frequencies) than the corresponding values of the $RRS(\beta)$. Therefore, there is clearly a greater reduction of ordinates of response spectra Sa compared with the response spectra β [9].

It is also observed that the averaged curves of the *RRS*, prepared separately in the cases of buildings of different types (N, S, W), are different. This applies to both the relations of $RRS(\beta)$ and $RRS(S_a)$ [9].

It is evident that for frequencies higher than 15 Hz, the relations *RRS* are practically constant for all variants of *RRS* shown in Fig. 1 and Fig. 2.

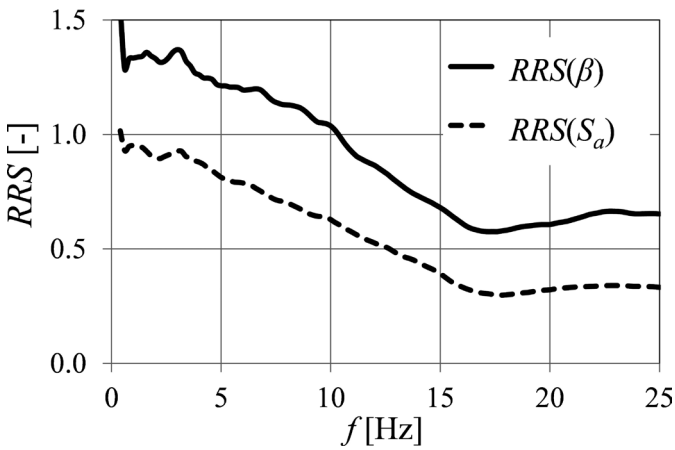

Fig. 1. Averaged relations RRS(β) and RRS(Sa) determined on the basis of vibration acceleration records on free-field near the buildings and foundations vibrations for all types of buildings

Moreover, *RRS* curves shown in Fig. 1 and Fig. 2 confirm the phenomenon that is observed in the dynamic SSI – buildings of all considered types "operate as a low pass filter", and so in the transmission of vibrations from the free-field to the building foundation, dampen vibrations of the ground with higher frequencies [9].

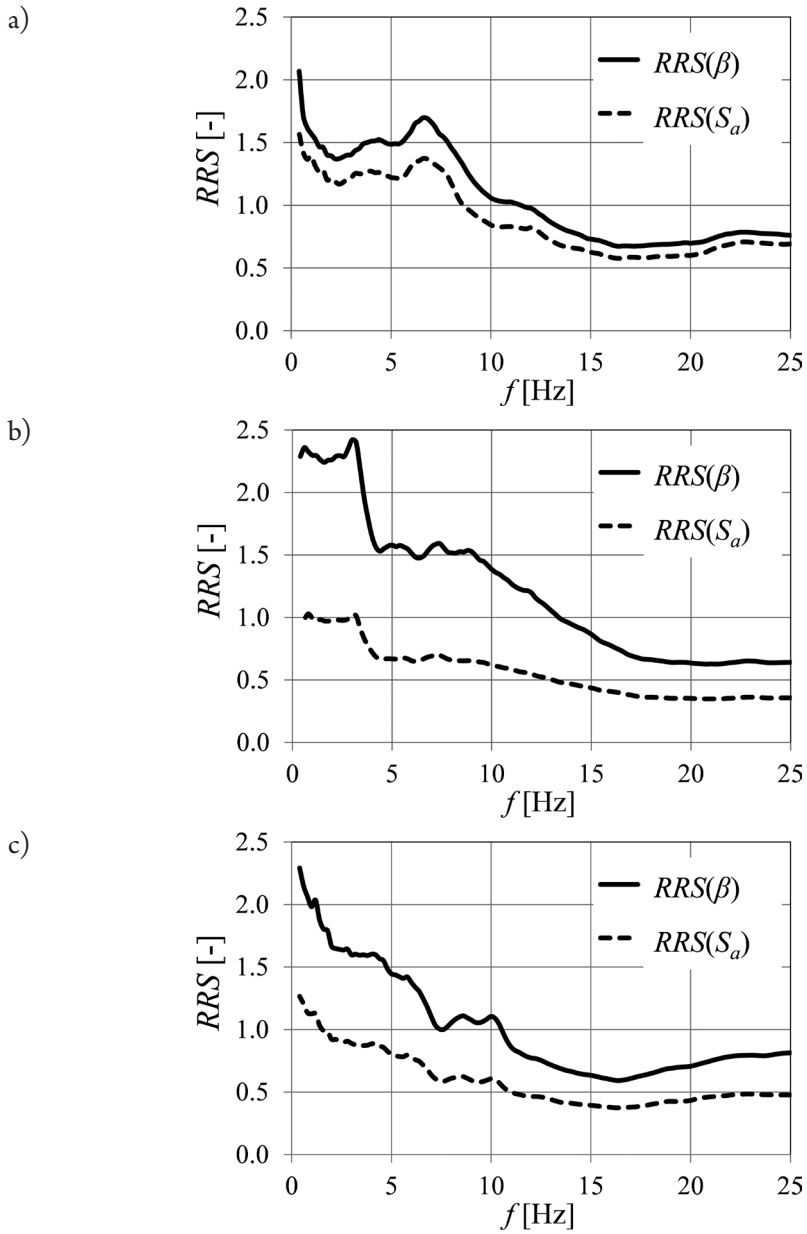

Fig. 2. Averaged relations RRS(β) and RRS(Sa) determined on the basis of vibration acceleration records on free-field and foundation vibration for building: a) low-rise (type N), b) medium-rise (type S), c) high-rise (type W)

3. Empirical transmission models of the response spectra from the free-field to the buildings foundations

In [10], the suitability (accuracy) of simple approximate transmission models of the response spectra from the ground to the building foundations was analysed, which in the literature are proposed for earthquake vibrations [3, 14–16], in application to the vibrations originating from rockbursts in the Legnica-Głogów Copper District (LGC). It can be found that the application of these models (i.e. models designed for taking into account the phenomenon of dynamic SSI in the case of earthquakes) to the prognosis of acceleration response spectra originating from the building foundation vibrations on the basis of appropriate response spectra from free-field motion in the case of rockbursts in the LGC region, results in a relatively high inaccuracy of prediction [10].

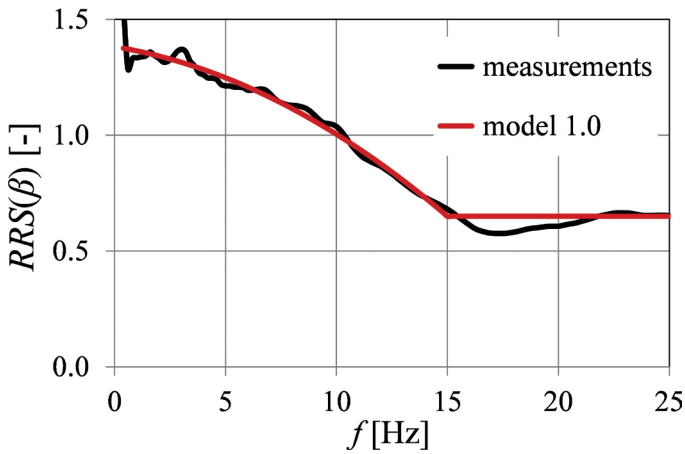

Fig. 3. Averaged relation RRS(β) determined on the basis of vibration acceleration records on free-field and buildings foundations of all types and for model 1.0

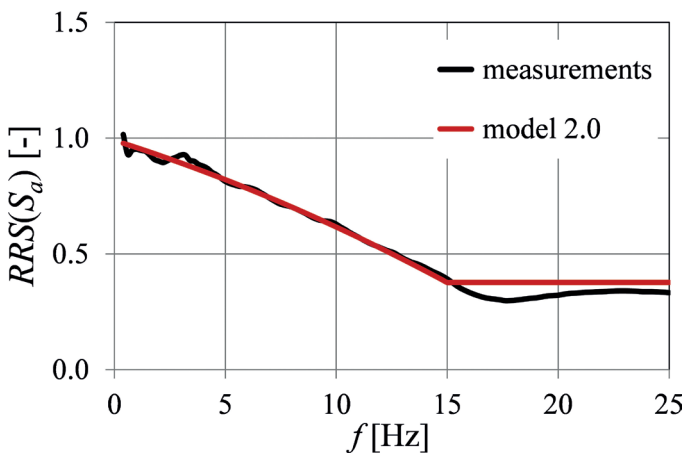

Fig. 4. Averaged relation RRS(Sa) determined on the basis of vibration acceleration records on free-field and buildings foundations of all types and for model 2.0

a)

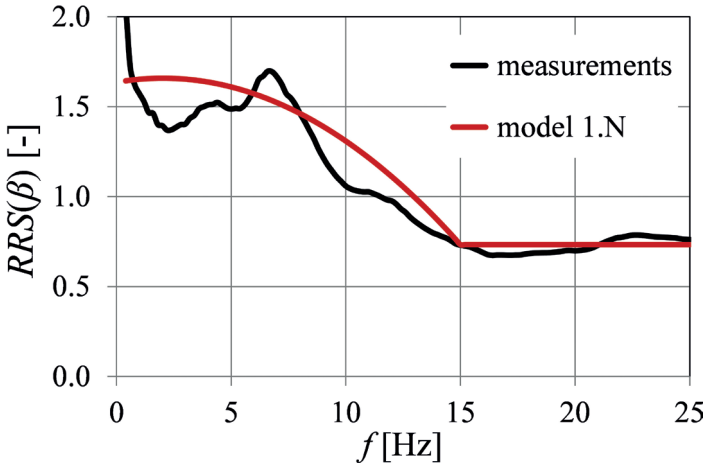

b)

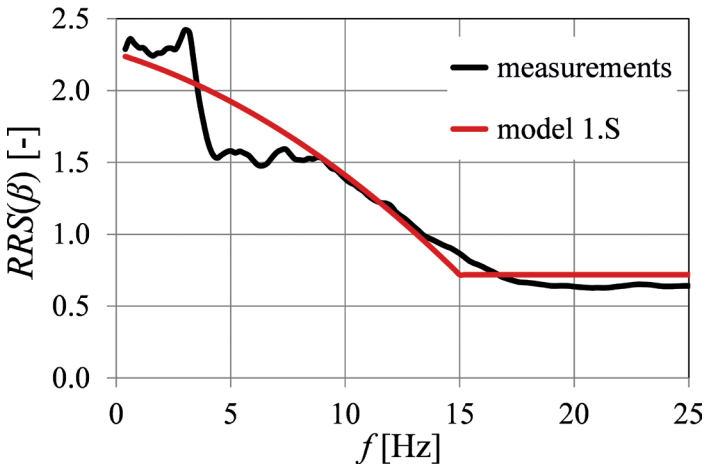

c)

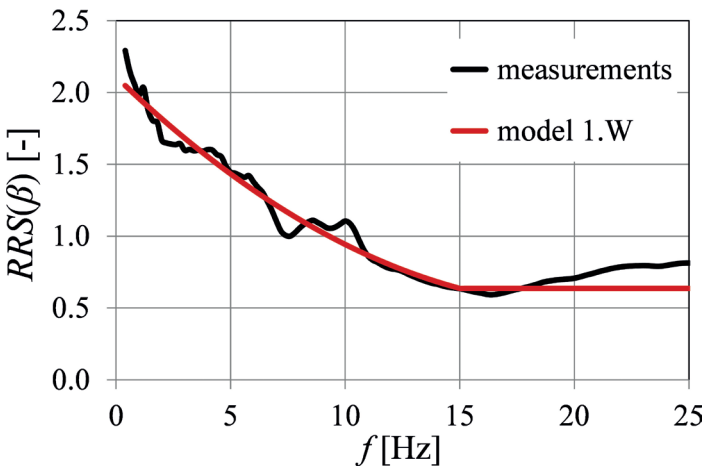

Fig. 5. Averaged relations RRS(β) determined on the basis of vibration acceleration records on free-field and buildings foundations vibrations and the proposed models for buildings: a) low-rise (type N), b) medium-rise (type S), c) high-rise (type W)

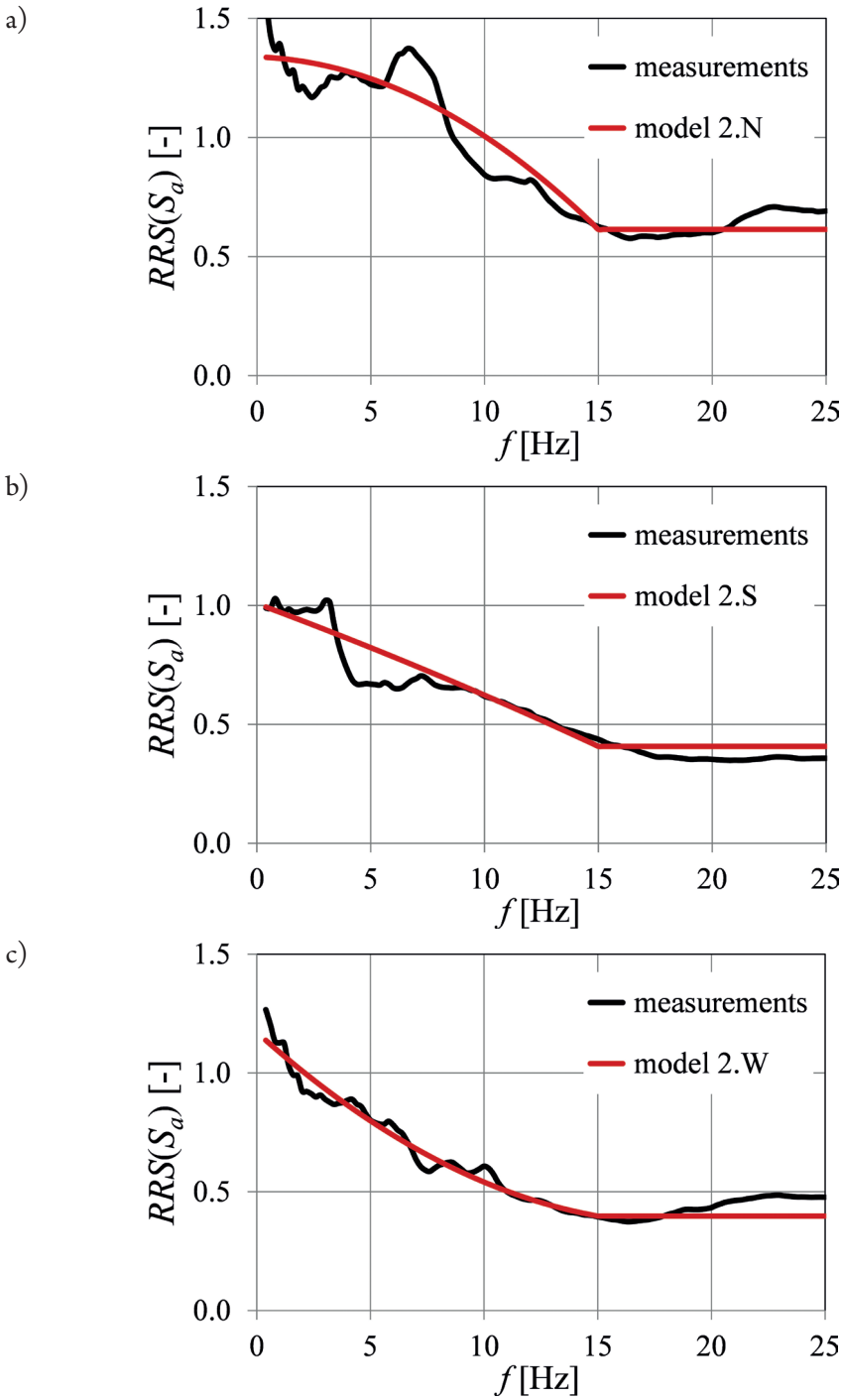

Fig. 6. Averaged relations RRS(S_a) determined on the basis of vibration acceleration records on free-field and buildings foundations vibrations and the proposed models for buildings: a) low-rise (type N), b) medium-rise (type S), c) high-rise (type W)

This paper proposes similar, simple, empirical models in order to determine the differences (relations) in the response spectra from the ground and the building foundation vibrations, prepared with the intention of using them in the LGC region conditions. These models are nearing match position to the nature of rockbursts originating vibrations and the characteristics of substrate in the LGC region.

Separate models were constructed for the dimensionless acceleration response spectra (β) – models $RRS(\beta)$, and dimensional spectra (S_a) – models $RRS(S_a)$.

Variants of the models have been developed for use regardless of the type of building ("universal" models), which are denoted as: model 1.0 for $RRS(\beta)$ and model 2.0 for $RRS(S_a)$.

Also, models intended for use separately in each of the groups of common residential buildings in this mining region: low-rise (N), medium-rise (S) and high-rise (W), have been alternatively treated. They have been denoted consecutively as: model 1.N, model 1.S and model 1.W in the case of modelling of the transmission of non-dimensional spectra (β), and model 2.N, model 2.S and model 2.W in the case of dimensional spectra (S_a) transmission.

A graphical illustration of the above-mentioned models is shown in the red line in Figs. 3–6, and their equations are given in Table 1 and Table 2.

It is worth mentioning that all the proposed models are based on the acceleration response spectra from vibration records measured during dynamic investigations in the free-field situation near the buildings and building foundations in the LGC region.

Table 1. The equations of the proposed models of empirical relation $RRS(\beta)$ for use in the cases of dimensionless response spectra β

Model	Application	Equations of the models	
		f < 15 Hz	f ≥ 15 Hz
1.0	buildings of the type N, S, W	$-0.0022f^2 - 0.0158f + 1.3822$	0.650
1.N	buildings of the type N	$-0.0055f^2 + 0.0223f + 1.6362$	0.733
1.S	buildings of the type S	$-0.0036f^2 - 0.0486f + 2.2577$	0.719
1.W	buildings of the type W	$0.0037f^2 - 0.1537f + 2.1100$	0.637

Table 2. The equations of the proposed models of empirical relation $RRS(S_a)$ for use in the cases of response spectra S_a

Model	Application	Equations of the models	
		f < 15 Hz	f ≥ 15 Hz
2.0	buildings of the type N, S, W	$-0.0007f^2 - 0.0304f + 0.9903$	0.377
2.N	buildings of the type N	$-0.0030f^2 - 0.0033f + 1.3386$	0.614
2.S	buildings of the type S	$-0.0003f^2 - 0.0355f + 1.0078$	0.408
2.W	buildings of the type W	$0.0023f^2 - 0.0861f + 1.1720$	0.398

4. Results of the calculations with the use of proposed models

Fig. 3 compares the averaged relation $RRS(\beta)$, determined on the basis of acceleration vibration records measured on the free-field near the buildings and on the building foundations of all types with the graph for model 1.0. On the other hand, separately averaged relations $RRS(\beta)$ in the cases of buildings type N, type S and type W, and graphs of appropriate models proposed for separate use for each type of the buildings are compared in Fig. 5. A similar comparison corresponding to the average relations $RRS(S_a)$ and graphs for the model 2.0, model 2.N, model 2.S, and model 2.W, is given in Fig. 4 and Fig. 6.

The accuracy of the proposed models for use as a potential tool for the prediction of differences in the free-field and the building foundation mining-related vibrations was assessed using the Pearson correlation coefficient and average values of relative errors.

Table 3 presents the average values of relative errors of the prediction of the average relations $RRS(\beta)$ using the proposed models as well as the corresponding linear Pearson correlation coefficients. Similar results relating to the average relations $RRS(Sa)$ are shown in Table 4.

In both tables, the results are given separately for the whole considered range of vibration frequencies ($f \leq 25$ Hz) and for the range of relatively low frequencies of particular importance from a practical point of view ($f \leq 15$ Hz).

A very good fit of models constructed for use in the cases of different types of buildings during the transmission of the dimensionless spectra (β) as well as the dimensional spectra (S_a) is visible. However, also the use of "universal" models (model 1.0, model 2.0) allows to predict the average values of $RRS(\beta)$ and $RRS(S_a)$ with satisfactory accuracy. These applications relate to the whole frequency range and, separately, relatively low frequency range. Moreover, in all the proposed variants of models, the adoption of a constant value *RRS* for frequencies exceeding 15Hz simplifies the structures of the models without loss of their accuracy.

Table 3. Pearson correlation coefficients and average values of relative errors of $RRS(\beta)$ obtained using the proposed empirical models in relation to the results of experimental research

Type of building	Model	Pearson correlation coefficients [-]		Average values of relative errors [%]	
		$f \leq 15$ Hz	$f \leq 25$ Hz	$f \leq 15$ Hz	$f \leq 25$ Hz
N	1.0	0.902	0.955	12.0	13.3
	1.N	0.913	0.957	9.2	11.7
S	1.0	0.909	0.964	28.5	18.8
	1.S	0.918	0.967	8.8	9.5
W	1.0	0.936	0.926	13.1	12.3
	1.W	0.983	0.980	4.8	7.6
N, S, W	1.0	0.989	0.993	1.9	3.3

Table 4. Pearson correlation coefficients and average values of relative errors of $RRS(S_a)$ obtained using the proposed empirical models in relation to the results of experimental research

Type of building	Model	Pearson correlation coefficients [-]		Average values of relative errors [%]	
		$f \leq 15$ Hz	$f \leq 25$ Hz	$f \leq 15$ Hz	$f \leq 25$ Hz
N	2.0	0.919	0.956	33.4	36.2
	2.N	0.932	0.957	7.9	7.4
S	2.0	0.915	0.963	8.1	7.2
	2.S	0.923	0.965	6.8	8.9
W	2.0	0.957	0.942	7.6	9.8
	2.W	0.985	0.981	3.7	6.4
N, S, W	2.0	0.997	0.995	15.3	7.1

5. Conclusions

The study presents empirical models for the evaluation of the differences (relations) in the acceleration response spectra originating from the free-field and the building foundations vibrations. These models have been prepared for use in the case of mining rockbursts in the Legnica-Głogów Copper District.

In practice, the proposed simple, approximate models can be used for prediction of the response spectra from the building foundation vibrations on the basis of response spectra from the free-field motion near the buildings.

The form of the developed models can be treated as the preliminary base proposal. The objective of further attempts of models' modification would be the construction of a common model for different types of buildings, but taking into account the information about the differences in their structure, and therefore also their dynamic properties.

References

[1] Ciesielski R., Kuźniar K., Maciag E., Tatara T., *Damping of vibration in precast buildings with bearing concrete walls*, Arch. Civ. Eng., Vol. 41, 3, 1995, 329–341.

[2] Czerwionka L., Tatara T., *Wzorcowe spektra odpowiedzi z wybranych obszarów GZW (Standard response spectra from chosen mining regions at Upper Silesian Coalfield)*, (in Polish), Czasopismo Techniczne, Vol. 2-B/2007, 11–18.

[3] FEMA 440, *Improvement of Nonlinear Static Seismic Analysis Procedures*, ATC-55 Project, 2005.

[4] Kim S., Stewart J.P., *Kinematic soil-structure interaction from strong motion recordings*, Journal Geotechnical and Geoenvironmental Engineering, Vol. 129, 4, 2003, 323–335.
[5] Kuźniar K., *Analiza drgań budynków ścianowych o średniej wysokości podlegających wstrząsom górniczym z wykorzystaniem sieci neuronowych (Analysis of vibrations of medium-height buildings with load bearing walls subjected to mining tremors using neural networks)*, (in Polish), Monografia 310, Inżynieria Lądowa, Wyd. Politechnika Krakowska, Kraków 2004.
[6] Kuźniar K., *Zastosowanie sieci neuronowych w prognozowaniu przekazywania drgań pochodzenia górniczego z gruntu na fundament budynku (Application of neural networks for the prediction of mine-induced vibrations transmission from the ground to building foundation)*, (in Polish), Inżynieria i Budownictwo, Vol. 1, 2014, 43–47.
[7] Kuźniar K., Maciąg E., Tatara T., *Acceleration response spectra from mining tremors*, First European Conference on Earthquake Engineering and Seismology (ECEES), Geneva 2006, Switzerland, Abstract Book, 466–467 (full paper on CD).
[8] Kuźniar K., Tatara T., *Przekazywanie drgań od wstrząsów górniczych z gruntu na fundamenty budynków różnego typu (Influence of building type on the transmission of mine-induced vibrations from the ground to building fundaments)*, (in Polish), Przegląd Górniczy, Vol. 6, 2014, 30–34.
[9] Kuźniar K., Tatara T., *Wpływ typu budynku na transmisję spektrów odpowiedzi od drgań górniczych z gruntu na fundamenty (The influence of building type on the transmission of response spectra of vibrations induced by mining tremors from the ground to building foundations)*, (in Polish), Przegląd Górniczy, Vol. 10, 2015, 31–36.
[10] Kuźniar K., Tatara T., *Zastosowanie przybliżonych modeli SSI w przypadku wstrząsów górniczych (Application of approximate SSI models in case of mining tremors)*, (in Polish), Przegląd Górniczy, Vol. 10, 2015, 25–30.
[11] Maciąg E., *Ocena szkodliwości drgań budynków od wstrząsów górniczych na podstawie drgań ich fundamentów czy drgań gruntu (Evaluation of harmfulness of mining tremors for buildings based on their foundations or free-field vibrations?)*, (in Polish), Inżynieria i Budownictwo, 12, 2005, 670-677.
[12] Maciąg E., *Interakcja układu budynek-podłoże gruntowe w świetle doświadczalnego badania drgań parasejsmicznych (Subsoil-building interaction due to the impact of paraseismic vibrations)*, (in Polish), Inżynieria Morska i Geotechnika, 4, 2006, 240–250.
[13] Maciąg E., Kuźniar K., Tatara T., *Spektra odpowiedzi drgań gruntu i fundamentów budynków od wstrząsów górniczych w LGOM Response spectra of ground and foundations of buildings vibrations caused by mining tremors in LGOM)*, (in Polish), [in:] K. Stypuła (ed.), *Aktualne problemy wpływów sejsmicznych i parasejsmicznych na budowle (Current problems of influence of seismic and paraseismic on buildings)*, Vol. II, *Badania wstrząsów górniczych i drgań komunikacyjnych (The investigation of mining tremors and communication vibrations)*, Monografia 477/2, Seria Inżynieria Lądowa, Wydawnictwo PK, Kraków 2015, 39-66.
[14] Mikami, A., Stewart, J.P., Kamiyama, M., *Effects of time series analysis protocols on transfer functions calculated from earthquake accelerograms*, Soil Dynamics and Earthquake Engineering, Vol. 28, 9, 2008, 695–706.

[15] Mylonakis G., Nikolaou S., Gazetas G., *Footings under seismic loading: Analysis and design issues with emphasis on bridge foundations*, Soil Dynamics and Earthquake Engineering, Vol. 48, 26, 2006, 824–853.
[16] NIST GCR 12-917-21, *Soil-Structure Interaction for Building Structures, prepared by NEHRP Consultants Joint Venture (a partnership of the Applied Technology Council and the Consortium of Universities for Research in Earthquake Engineering)*, 2012.
[17] Tatara T., *Działanie drgań powierzchniowych wywołanych wstrząsami górniczymi na niską tradycyjną zabudowę mieszkalną (An influence of surface mining-related vibration on low-rise buildings)*, (in Polish), Zeszyty Naukowe Politechniki Krakowskiej, seria Inżynieria Lądowa, Vol. 74, Kraków 2002.
[18] Tatara T., *Odporność dynamiczna obiektów budowlanych w warunkach wstrząsów górniczych (Dynamic resistance of buildings in mining tremors conditions)*, (in Polish), Wyd. Politechniki Krakowskiej, Kraków 2012.

TECHNICAL TRANSACTIONS 1/2017
CZASOPISMO TECHNICZNE 1/2017
CIVIL ENGINEERING
DOI: 10.4467/2353737XCT.17.006.6103

Łukasz Łukaszewski (llukaszewski@pk.edu.pl)
Institute of Building Materials and Structures, Faculty of Civil Engineering, Cracow University of Technology

The laser scanning in the digitization process of relictually preserved architectural details

Skaning laserowy w procesie digitalizacji reliktowo zachowanych detali architektonicznych

Abstract

Protection of cultural heritage in recent times is of a very important significance. The priority task is to secure the existing facilities in such a way that they can now and in the future serve as a representations of the areas and be a treasure house of knowledge for both current and future generations. Through the development of new technologies and applying them by maintenance staff and those working to protect the national heritage, digitization has become widespread. Photogrammetry and laser scanning proved to be useful tools in a non-invasive process of heritage digitizing. In the article the author describes the process of creating a three-dimensional model of an architectural detail, the model of "acanthus leaf" which is the final product of the study. The methodology described by the author outlines the problems occurring during the measurement and subsequent data processing stages. The final product is an important database, useful when creating the reconstruction and renovation of similar facilities.

Keywords: cloud points, digitizing, 3D model, relic, reconstruction, laser scanning, virtual cave

Streszczenie

Ochrona dziedzictwa kulturowego w aktualnych czasach ma bardzo ważne znaczenie. Priorytetowym jej zadaniem jest zabezpieczenie istniejących obiektów w taki sposób, aby mogły one teraz i w przyszłości pełnić funkcję reprezentacyjną danych obszarów oraz być skarbnicą wiedzy dla aktualnych i przyszłych pokoleń. Poprzez rozwój nowych technologii i zastosowanie ich przez konserwatorów oraz osoby zajmujące się ochroną dziedzictwa narodowego cyfryzacja stała się powszechna. Fotogrametria oraz skaning laserowy okazały się przydatnymi narzędziami w nieinwazyjnym procesie digitalizowania dziedzictwa narodowego. W artykule autor opisuje proces tworzenia trójwymiarowego modelu wybranego detalu architektonicznego, modelu „liścia akantu", który jest produktem finalnym badania. Metodologia opisana przez autora przedstawia problemy występujące podczas wykonywania pomiaru i w kolejnych etapach obróbki danych. Produkt finalny jest ważną bazą danych, przydatną podczas tworzenia rekonstrukcji i renowacji podobnych obiektów.

Słowa kluczowe: chmura punktów, digitalizacja, model 3D, relikt, rekonstrukcja, skaning laserowy, wirtualna jaskinia

1. Introduction

A digitalization of relictually preserved architectural details resulted in the creation of a new branch of science based on promotion of knowledge and history. By creating interactive databases and then making them available on the Internet (via network) they provided an opportunity to conduct research on given objects to researchers from around the world. Thanks to the further verification of written sources and creating 3D models we can deeper and easier interpret and understand tested subjects. Three-dimensional reconstructions of movable and immovable monuments made in various academic as well as in scientific and research centers, despite the use of different methods and various degrees of advanced computer technology, are based on the principles of *the Charter of London* [1]. Most projects made by means of a laser scanner – both geodetic and triangulate – may also be used in museology and promoting knowledge for the purposes of popular scientific studies.

When the virtual reality (VR) [2] technology was developed, it has been fully absorbed by the field of cultural heritage for different purposes. Securing, protecting and reconstructing relictually preserved details required accurate and consistent approaches of behavior, analysis, and monitoring of their integrity for future generations. The documentation presented in numerical form of CAD and digital one was stored in the form of raster and vector files. Fast development of software also meant that printing the paper documentation has become a digital copy of the studies, of a much smaller utility value than the digital form [3].

Computer methods, apart from changing the form of the classic documentation have led to the emergence of new forms of documentation previously impossible to share or use. There appeared the possibility of relatively easy development of interactive, spatial presentation of objects and the use of digital, photogrammetric, semi-finished products as a source of metric information about the product. BIM technology development has also contributed to a simpler and broader use of the products generated from point clouds and with TIN grids widely used in reconstructing, architectural details by using 3D printers and interactive caves.

This article presents a methodology that can be used in a wide range of digitization and restoration work.

2. Methodology

2.1. Equipment used

In order to create an interactive 3D model of the "acanthus leaf" the author used the following equipment and specialized software:

A triangulation scanner with a matrix of 10 MPx by Smarttech company,
A program enabling scanner support Mesh3Dx64,
A program for joining, editing point clouds Geomagic Studio 2014 x64,
A program for processing TIN model Autodesk 3ds Max Design 2015,
A program for publications Adobe Acrobat 3D PDF.

2.2. Measuring the object

The first step to create a virtual model was a correct location of the object in relation to the scanner (Fig. 1). Through a complicated geometry of an object scanning process was repeatedly carried out for 45 times since the stereoscopic positioning

Fig. 1. Image of object measurement and positioning of the scanner

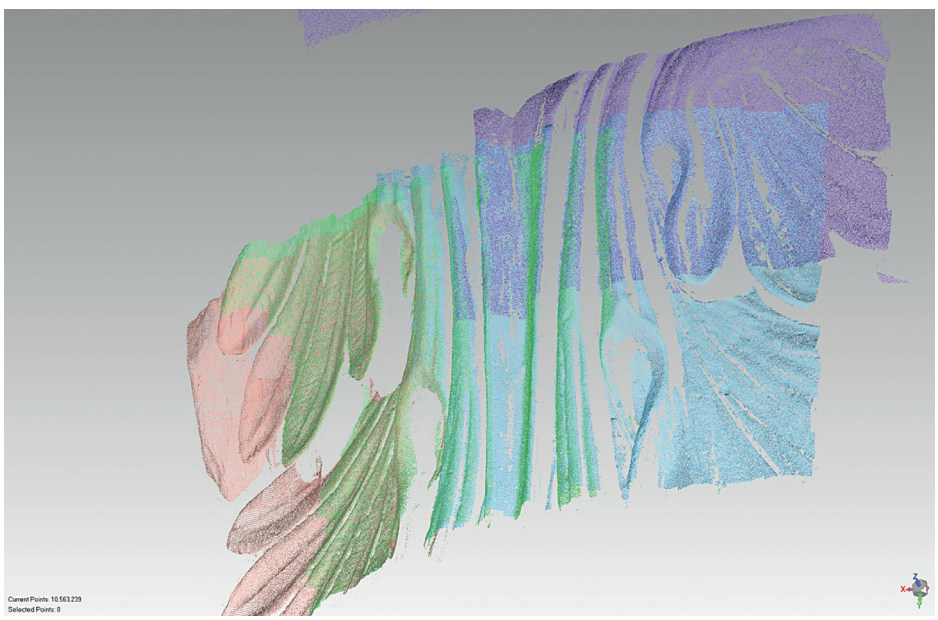

Fig. 2. Measuring divergences. Resulting from the geometry of the object

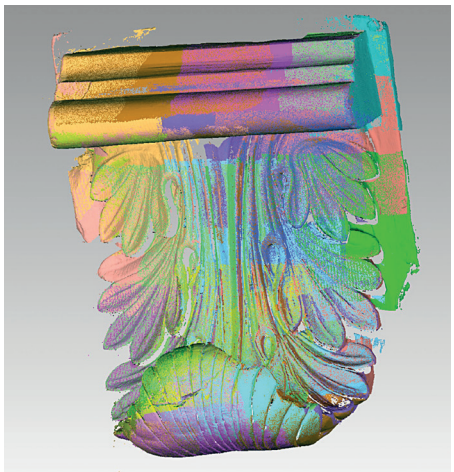

Fig. 3. The combined point clouds

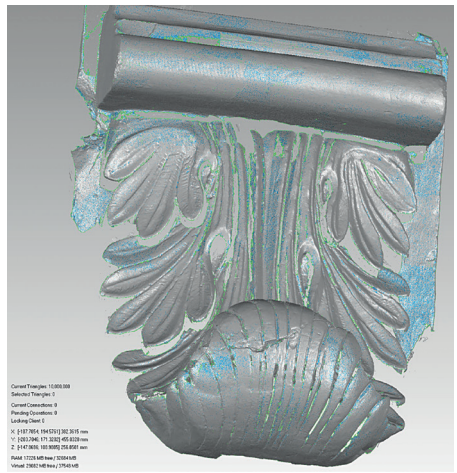

Fig. 4. The generated TIN grid

of the measuring elements in the scanner resulted in inaccuracies in the individual measurements (Fig. 2).

After obtaining point clouds, their appropriate number was selected and there were 35 elements left to easily combine in A sequence in the program of Geomagic Studio 2014 x64. After cleaning, generated clouds were arranged and a cloud numbering 66 941 225 pts. was obtained (Fig. 3).

The next step in the process of generating a 3D model was to create a grid TIN (Fig. 4) allowing easy correlations with other environmental graphic programs. Then in the program 3ds Max Design a finished product was rendered already with the applied texture. The finished product was made available in 3D PDF format.

Table 1. A table containing the most important parameters of the study performed

Scanner type	Triangulation , white light, **166 point** on 1 mm^2	
Scanner volume	200 (mm) x 300 (mm) x 150 (mm)	
Number of completed scans	45	–
Number of used scans	35	66 941 225 pts.
Number of generated triangles	10 000 000	
Time of measurment	3 h	
The duration of data processing	5 h	

2.3. Problems encountered during the test

During the measurement with triangulation scanner and data processing the author noted that there may be problems in the process of creating an interactive 3D model.

During the research we should pay attention to:

- adequate light put on the tested object,

- the expected accuracy of the tested object in order to edit the cloud point where possible at a later stage,
- after each scan, check the quality and range of information of your interest,
- try to combine and analyze the scans done up to date so that after leaving the site of research one would not discover that something is missing or badly scanned,
- pay attention to metal surfaces and highly polished ones as some scanners do not read such surfaces,
- when connecting individual cloud points of measurement, pay attention to the redundant elements and emerging "noise",
- if necessary, take advantage of the program enabling cleaning point clouds to reduce their numbers,
- the ability to generate TIN grids by selecting the appropriate function:
  - with rounded transitions between vertices,
  - with sharp transitions between vertices.

3. Conclusions

To summarize you can draw conclusions from the digitization process of national heritage relics:

Fig. 5. Database of relics details digitized in 3D [7]

Fig. 6. The virtual presentation of the usage of digitized details [7]

1) effectiveness and time spent to scan and execution of the entire 3D model is relatively faster and easier compared to traditional methods of documenting relics [4]. Through the process of digitization you can create an interactive database of architectural details used in further research projects [5–7] (Fig. 5).
2) the possibility of spreading science with the development of cyber-technology, which streamlines the process of researching and non-invasive exploring of test items. It is worth to quote the words of Professor Andrzej Kadłuczka: "(...) the CAD environment can be applied to the needs of archiving and data processing about the object, and then for modeling its spatial reconstruction, verification without restric-

tions and without harming the material substance (...)" [1]. Professor Karel Pavelka: „(...) reconstruction possibilities based on close-range photogrammetry in an image based modeling form or professional laser scanning and 3D printing using rapid prototyping technology. Thanks to low-cost and easy-to-use technology we are able to produce scaled 3D virtual models or real prints, which can be included with objects in any virtual museum (…)" [8].

3) the measurements form the basis for future analysis and comparison of measurements made in other technologies which will enable to verify the usability of the tools used in the process of digitization.

References

[1] Kadłuczka A., *Rekonstrukcja architektoniczna – realne czy wirtualne modelowanie rzeczywistości historycznej?*, Doktryny i Realizacje Konserwatorskie w Świetle Doświadczeń Krakowskich Ostatnich 30 lat, WAM, Kraków 2011, 209–223.

[2] Bruno F., Bruno S., De Sensi G., Luchi M., Mancuso S., Muzzupappa M., *From 3D reconstruction to virtual realisty: A complete methodology of digital archeological exhibition*, Journal of Cultural Heritage, Vol. 11, 2010, 42–49.

[3] Boroń A., Rzonca A., Wróbel A., *Metody fotogrametrii cyfrowej i skanowania laserowego w inwentaryzacji zabytków*, Roczniki Geometryki, Vol. V, Issue 8, 2007, 129–140.

[4] Markiewicz M., *Cyfrowe techniki dokumentacji zabytków ruchomych na przykładzie halsztackiej ceramiki malowanej z Domasławia, gm. Kobiarzyce, Digitalizacja Dziedzictwa Archeologicznego – wybrane zagadnienia*, Uniwersytet Kardynała Stefana Wyszyńskiego w Warszawie, Lublin 2011, 158–172.

[5] Pires H., Ortiz P., Marques P., Sanchez H., *Close-range Lase Scanning Applied to Archeological Artifacts Documentation. Virtual Reconstruction of an XVIth Century Ceramic Pot*, The 7th International Symphosium on Virtual Reality, Archaeology and Cultural Heritage VAST, 2006.

[6] Luis Lerma J., Muir C., *Evaluating the 3D documentation of an early Christian upringht stone withc carvings from Scotlande witch multiples images*, Journal of Archaeological Science, Vol. 46, 2014, 311–318.

[7] De Luca L., *Methods, formalism and tool for the semantic-based surveying and representation of architectural heritage*, Societe Italian di Fotogrammetria e Topgrafia 2011, online: 15.12.2011.

[8] Pavelka K., Sedina J., Faltynova M., Matouskova E., *Documentation, 3D modeling and replication of archaeological artifacts*, Processdings of the international Multidisciplinary Scientific GeoConferences SGEM, 2015, Vol. 4, 109–116.

TECHNICAL TRANSACTIONS 1/2017
CZASOPISMO TECHNICZNE 1/2017
CIVIL ENGINEERING
DOI: 10.4467/2353737XCT.17.007.6104

Krzysztof Stypuła
Tadeusz Tatara (ttatara@pk.edu.pl)
Institute of Structural Mechanics, Faculty of Civil Engineering, Cracow University of Technology

Vibrations of free-field and building caused by passages of the Pendolino train

Drgania gruntu i budynku wzbudzane przejazdami pociągu Pendolino

Abstract

The objective of the paper was to conduct dynamic measurements of free-field vibrations in three profiles and establish decay relations of propagating vibrations. The sources of vibrations were passages of the Pendolino train with dedicated speeds from 40 to 293 km/h. In each profile, soil properties tests were carried out. Based on the data for a few selected speeds of the Pendolino train's passages, the Vibration Reduction Coefficients (VRC) were determined at selected points. The paper is also focused on the analysis of vibrations of the selected one-storey masonry residential building located in the vicinity of one of the profiles and their evaluation of the harmfulness on the building structure using standard scales of dynamic influence.

Keywords: free-field vibrations, dynamic investigation, speed of passage of a train, building vibrations, harmfulness of vibrations

Streszczenie

W pracy przedstawiono wyniki analiz pomiarów drgań gruntu w trzech profilach oraz podano zależności tłumienia propagujących się w gruncie drgań, których źródłem były przejazdy pociągu Pendolino z dedykowanymi prędkościami 40–293 km/h. W każdym profilu określono właściwości gruntu. Na podstawie danych pomiarowych wyznaczono współczynniki redukcji drgań w wybranych punktach. W pracy przedstawiono także wyniki analiz pomierzonych drgań murowego, jednopiętrowego budynku mieszkalnego zlokalizowanego w sąsiedztwie jednego z profili pomiarowych prowadzonych pod kątem oceny ich szkodliwości na konstrukcję budynku. W ocenach wykorzystano normowe Skale Wpływów Dynamicznych.

Słowa kluczowe: wstrząsy górnicze, przekazywanie drgań z gruntu na fundament budynku, transmisja spektrów odpowiedzi

1. Introduction

In countries where high-speed lines operate, free-field vibrations generated by passing trains at speeds of 250 km/h and more are of particular concern due to the impact of vibrations on neighbouring buildings and people inside them. Confirmation of the need for research in this area can be found in Council Directive 96/48/EC of 23 July 1996 concerning the interoperability of the trans-European high-speed rail system. Annex III of the Directive, which contains the essential requirements given in section 2.6.2, concerning the protection of the environment, mentions the following: Operation of the trans-European high-speed rail system must not cause a level of ground vibrations, which is unacceptable for the immediate environment in the vicinity of the infrastructure and in a normal state of maintenance. Results of studies conducted in different countries published in (e.g. [1–3]) are not always comparable because of differences in the structures of trains and surface rail, the differences in soil conditions, and finally due to local differences of the buildings' construction receiving the vibration. Therefore, also in Poland, after purchasing the Pendolino trains, it was decided that test drives need to be performed within the test framework of vibration generated by the passing train (Fig. 1). The study refers to a portion of the vibration measurements made at the turn of November and December 2013 by accredited Laboratory of Distortion and Vibration Research within the Structural Mechanics Institute at the Cracow University of Technology.

Fig. 1. The Pendolino train on the track at the site of the testing research

2. Research of propagation of free-field vibrations

One of the tests was to study the propagation of free-field vibration during the trial runs of the Pendolino trains on the Central Railway route (CMK) connecting the Upper Silesian Industrial Region with the Warsaw agglomeration, near the town of Przyłęk located between Psary and Góra Włodowska in three selected sections of measurement. The source of vibration excitation was the passages of the Pendolino train with dedicated speeds. During the tests, acceleration of the horizontal components (x, y) and the vertical component (z) of free-field vibrations were measured. The direction of the x is perpendicular to the railway track. Soil conditions in selected sections of the measurement were recognised before measuring free-field vibrations. Soil conditions are essential for the propagation of communication vibrations. Such vibrations depend on their

source and the nature of the medium transferring them to the surroundings. In each measuring section, soil properties were investigated at two locations (at the foot of the railway embankment and at the distance of 20 m) located adjacent to the points of measurement of free-field vibrations.

In the first section, free-field vibrations caused by 20 passages of the Pendolino running along the railway track A at the dedicated speeds of 40–270 km/h were recorded. Figure 2a and 2b show the locations of measuring points and sensors in the first monitoring section

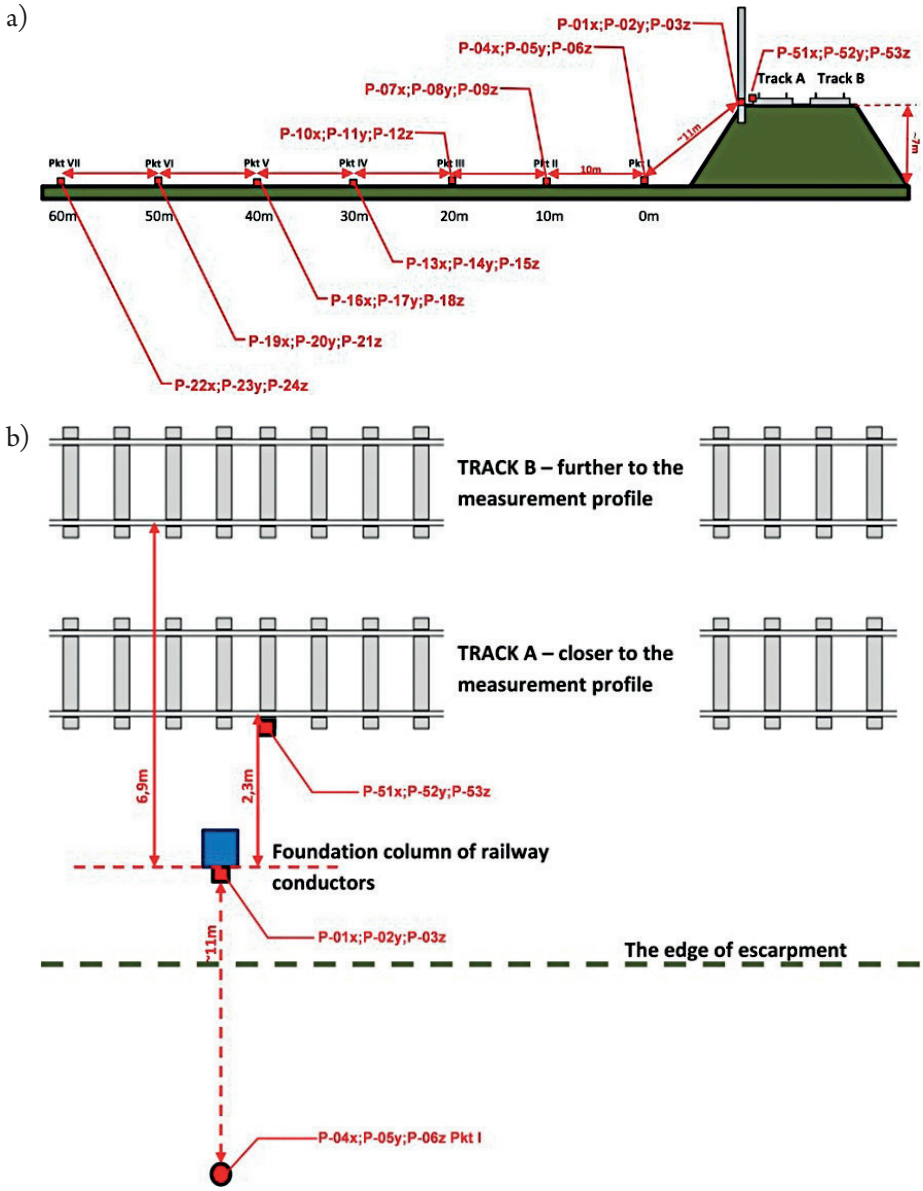

Fig. 2. Distribution of points and sensors in the first measuring profile (kilometre 177–10) on the embankment and its vicinity

(kilometre 177-10) on the embankment and its vicinity. The measurement profile in this location is situated about 5.5 m below the railway track. In this section, the railway line runs along the embankment by extensive morphological reduction. In this section, the ground is layered. In the first ground profile under a thin layer of humus land is natural coarse, non-cohesive sands, sandy silt changing with depth to sands with gravels. In some locations, single dusty inter-beddings were also drilled. The water level has been drilled to at a depth of 1.08 m below the ground surface. Medium sand layer with a dash of coarse and fine sand occurs at about 2.7 m below the surface in the medium-compacted state. In this profile there, is a clear vadose zone with a thickness of approx. 0.9–1.0 m demarcated by the underground water level; the saturation zone is located 1.4 m below the surface.

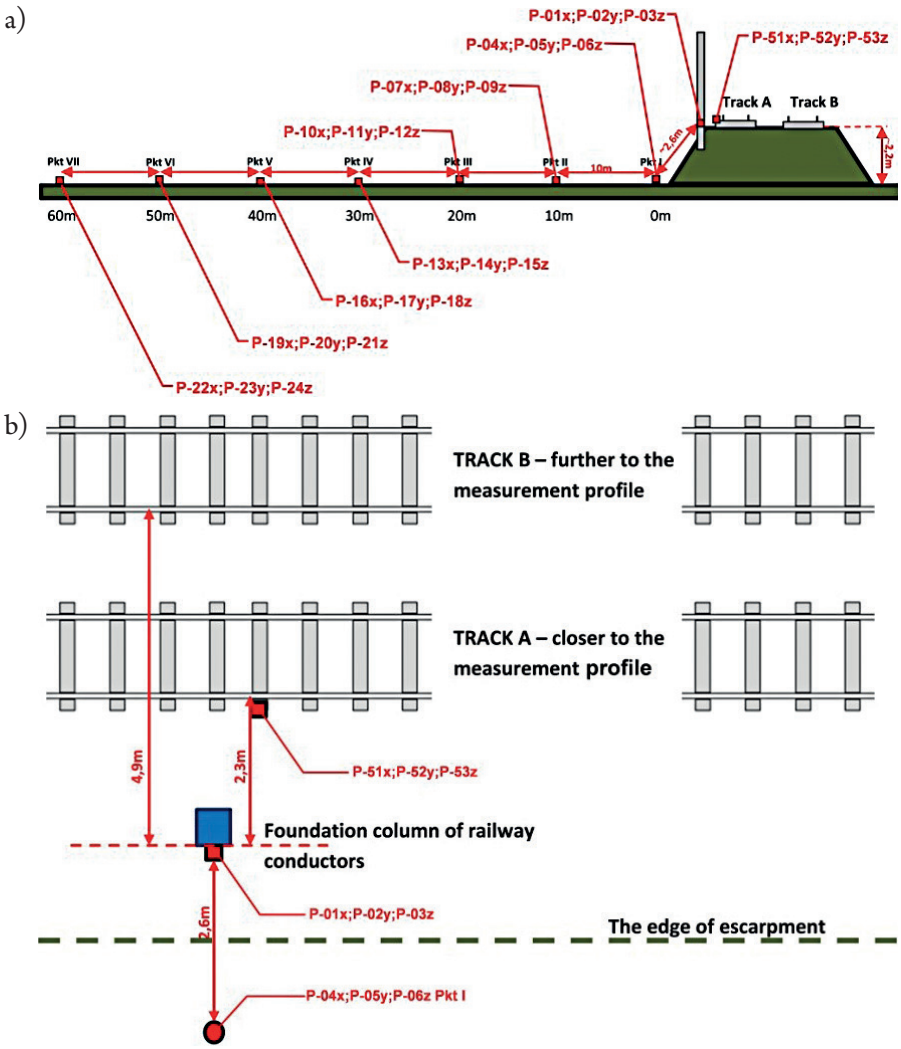

Fig. 3. Distribution of points and sensors in the second measuring profile (kilometre 180-9) on the embankment and its vicinity

In the second section, free-field vibrations, due to 21 passages of the Pendolino running along the railway track A at the dedicated speeds of 40–293 km/h, were recorded. Figure 3a and 3b show the distribution of points and gauges in the measuring section (kilometre 180-9) on the embankment and its vicinity, respectively. Geological studies indicate that this section has a simple geological structure; the substrate is layered with a thin layer of humus and natural soils underneath. The profile is dominated by lithographic layers consisting of sandy, coarse-grained (non-cohesive) sands, medium sand with an additive of fine and coarse sand. This profile has also inter-beddings of fine-grained soils (cohesive), dust and sandy dust. Groundwater has not been drilled in this profile. Therefore, the profile is in the vadose zone.

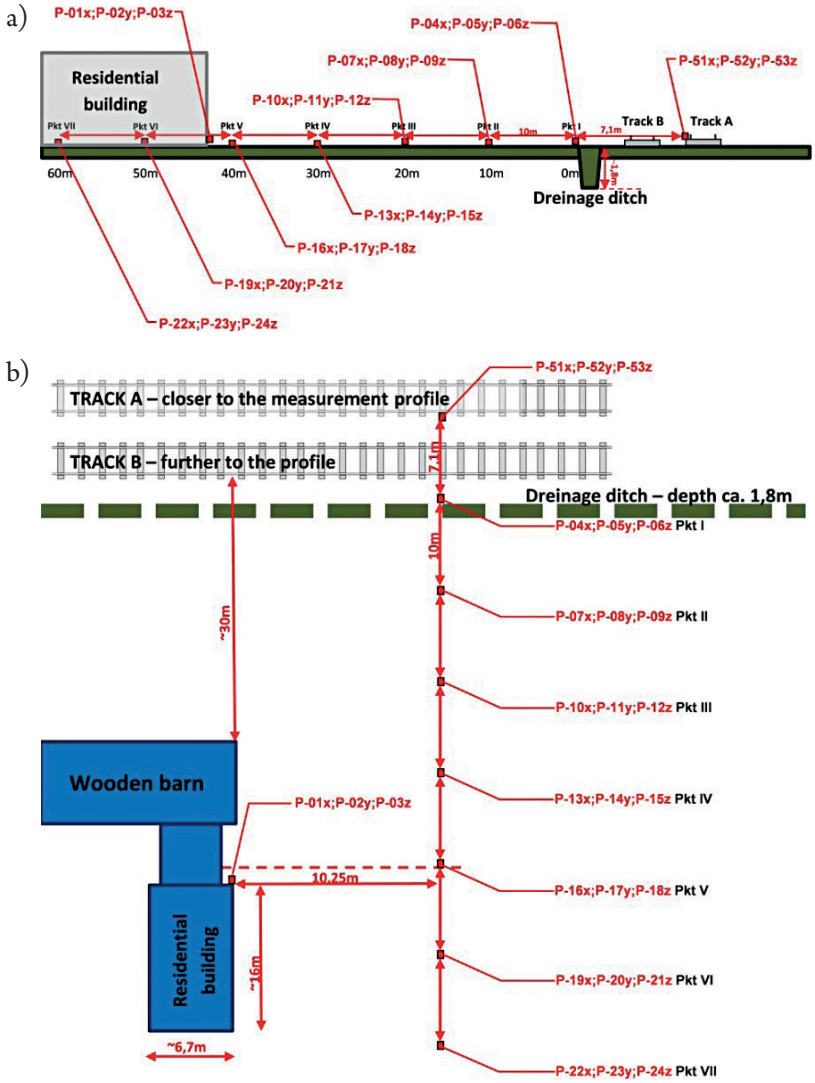

Fig. 4. Distribution of points and sensors in the second measuring profile (kilometre 180-9) on the embankment and its vicinity

In the last, third section, free-field vibrations as well as building vibrations indicated by 27 passages of the Pendolino train running along track A, with dedicated speeds of 40–250 km/h, were recorded. Figure 4a and 4b show the distribution of measuring points, accelerometers in this cross section (kilometre 177-6) and on selected residential building. It should be noted that, during tests along the third measurement section, track A was farther away in relation to the adopted cross-section. On the basis of geological studies, it was found that the substrate is layered. The soil profile under a thin layer of humus (approx. 0,1 m) in the track area consists of a thin layer of anthropogenic soil – not buildable with a thickness of approx. 0.70 m. Farther from the track, there are natural soils. A slab of soft rock, which consists of chalk marl, was drilled at a depth of about 0.8 meters below ground level. The maximum values of the horizontal components *x*, *y*, and the vertical component of the vibration acceleration caused by passage of the Pendolino train for allocated speeds in the analysed measurement sections are shown as an example in Tables 1, 2 and 3. An analysis of all measurement data showed that the highest values of the vibration acceleration of horizontal vibration components are present in the *x*-direction, i.e. perpendicular to the direction of the passages of the trains.

Table 1. Summary of maximum acceleration values of the horizontal components *x* and *y* and the vertical component *z*, cm/s^2 in the profile No. 1 for selected measuring points

Speed, km/h	Point No. 1			Point No. 3			Point No. 5			Point No. 7		
	P-04*x*	P-05*y*	P-06*z*	P-10*x*	P-11*y*	P-12*z*	P-16*x*	P-17*y*	P-18*z*	P-22*x*	P-23*y*	P-24*z*
40	3.16	1.95	1.97	1.46	1.53	0.64	1.60	1.26	0.72	0.73	0.68	0.27
80	6.20	3.25	3.59	2.76	3.06	1.46	2.41	2.14	0.99	1.60	1.20	0.57
120	7.38	9.35	6.25	5.51	5.19	2.52	4.36	4.70	1.50	2.71	3.37	1.14
135	13.55	9.27	7.43	6.81	6.90	3.12	6.20	8.16	2.23	3.69	3.32	1.23
160	11.57	10.84	7.93	7.12	7.03	3.71	7.19	5.48	2.81	4.16	3.79	2.03
180	19.13	9.10	10.36	9.91	9.41	3.91	6.08	7.48	2.57	4.09	4.54	2.27
200	18.15	13.40	11.60	7.42	9.34	4.97	7.76	8.27	3.95	5.63	4.47	1.93
220	13.99	11.50	10.35	9.31	9.76	5.91	9.35	9.09	3.76	4.33	5.13	2.66
240	16.50	27.48	14.70	10.71	8.60	5.93	7.04	7.23	5.78	5.43	5.39	2.78
250	17.52	16.96	11.35	9.49	8.66	5.77	7.75	7.59	4.99	5.74	4.30	2.22
270	19.88	20.32	15.03	10.99	7.58	6.62	10.04	8.37	4.47	6.75	5.14	3.58

A comparison of the maximum value of the horizontal components x (a_{xmax}) and y (a_{ymax}) listed in Tables 1–3 showed that in the overwhelming number of cases a_{xmax} values were greater than the a_{ymax} values. In turn, the maximum values of the vertical component (a_{zmax}) were generally smaller than the maximum values of the horizontal component a_{xmax}. Based on the data from Tables 1–3, for some chosen speeds of the Pendolino train, passages vibration reduction coefficients were determined at selected points (20 m and 60 m from the bottom of the escarpment). The values of the vibration reduction coefficients for each component of the vibration were calculated as the ratio of the maximum value of the measured vibration acceleration at the starting point profile to the maximum value of the measured vibration acceleration at a given distance. Table 4 and Table 5 summarise the calculated values for vibration reduction coefficients for the three components of vibration acceleration respectively 20 and 60 m from the bottom of the escarpment.

Table 2. Summary of maximum acceleration values of the horizontal components x and y and the vertical component z, cm/s^2 in the profile No. 2 for selected measuring points

Speed, km/h	Point No. 1			Point No. 3			Point No. 5			Point No. 7		
	P-04x	P-05y	P-06z	P-10x	P-11y	P-12z	P-16x	P-17y	P-18z	P-22x	P-23y	P-24z
40	60.04	27.95	25.36	2.96	2.78	2.37	3.73	3.22	3.09	0.35	0.35	0.50
80	50.41	25.98	23.49	3.72	2.01	2.23	1.44	1.57	0.98	0.66	0.43	0.61
120	81.11	33.80	31.37	4.92	3.53	4.13	2.24	2.74	1.62	0.99	0.90	1.14
160	68.88	59.59	48.05	10.74	6.62	5.80	5.27	5.74	2.74	1.34	0.92	1.28
180	49.76	40.61	29.93	6.09	4.01	3.96	2.44	2.38	1.63	0.96	0.61	0.88
200	186.10	134.80	57.94	9.89	5.45	7.13	7.27	8.11	4.62	1.72	1.52	2.03
250	107.44	98.55	75.26	18.92	12.25	7.31	9.29	5.42	5.09	2.36	2.03	2.22
260	195.98	128.91	62.79	14.58	7.46	8.38	8.17	6.42	4.99	2.36	2.36	2.69
270	179.32	123.43	79.55	22.50	13.54	9.02	8.16	7.45	6.74	3.23	2.45	3.12
275	236.96	117.71	88.30	12.42	9.50	8.74	7.15	7.40	6.29	3.41	2.39	4.20
280	172.81	119.20	69.20	21.93	16.58	8.38	8.82	7.69	6.68	3.15	2.13	2.87
293	241.50	114.38	87.39	13.24	7.49	9.01	6.93	6.95	6.19	3.67	2.23	2.88

Table 3. Summary of maximum acceleration values of the horizontal components *x* and *y* and the vertical component *z*, cm/s^2 in the profile No. 3 for selected measuring points

Speed, km/h	Point No. 1			Point No. 3			Point No. 5			Point No. 7		
	P-04*x*	P-05*y*	P-06*z*	P-10*x*	P-11*y*	P-12*z*	P-16*x*	P-17*y*	P-18*z*	P-22*x*	P-23*y*	P-24*z*
40	46.67	29.73	14.36	0.87	0.56	0.58	0.33	0.41	0.25	0.43	0.49	0.20
80	84.07	39.02	16.70	1.35	1.02	1.78	1.13	1.16	0.64	0.72	0.63	0.36
120	153.07	56.55	33.33	1.79	1.66	1.96	0.77	0.70	0.70	0.96	1.06	0.51
160	262.22	137.42	43.22	2.47	2.66	1.76	1.30	1.48	1.23	1.62	1.83	0.94
180	177.03	134.06	36.08	2.90	2.42	2.03	1.35	1.59	1.92	2.84	2.26	1.01
200	187.08	86.43	39.99	3.56	5.24	2.77	1.39	2.81	1.97	2.68	2.36	1.14
230	235.29	108.71	54.46	5.33	4.19	3.37	1.85	3.26	2.10	2.83	2.79	1.71
250	182.39	113.26	52.58	25.09	25.90	24.14	1.85	3.25	2.15	3.28	2.76	1.73

Table 4. The values of the vibration reduction coefficient 20 meters from the starting point of the measuring profile

Speed, km/h	Profile No. 1			Profile No. 2			Profile No. 3		
	x	*y*	*z*	*x*	*y*	*z*	*x*	*y*	*z*
160	1.6	1.5	2.1	6.4	9.0	8.3	106.2	51.6	24.6
250	1.8	2.0	2.0	5.7	8.0	10.3	7.3	4.4	2.2
270	1.8	2.7	2.3	8.0	9.0	8.8	-	-	-
293	-	-	-	18.2	15.3	9.7	-	-	-

Table 5. The values of the vibration reduction coefficient 60 meters from the starting point of the measuring profile

Speed, km/h	Profile No. 1			Profile No. 2			Profile No. 3		
	x	*y*	*z*	*x*	*y*	*z*	*x*	*y*	*z*
160	2.8	2.9	3.9	51.4	64.2	37.5	161.9	75.1	46.0
250	3.1	3.9	5.1	45.5	48.5	33.9	55.6	41.0	30.4
270	2.9	4.0	4.2	55.5	50.4	25.5	-	-	-
293	-	-	-	65.8	51.3	22.5	-	-	-

The analysis of the data given in Tables 1–3 and values of reduction coefficients of maximum components of vibration acceleration (see Tables 4 and 5) revealed a decrease of the maximum values of a_{xmax}, a_{ymax} and a_{zmax} with the distance. A significant effect of soil conditions on the values of the vibration reduction coefficients was also noted. Considerably lower values of vibration reduction coefficient were obtained in case of all three considered directions at hydrated profile No. 1. For example Figure 5, 6 and 7 show the change of the maximum value of the horizontal component x ground vibrations, respectively in the profile 1, 2 and 3 for some passages of the Pendolino train with dedicated speeds.

Figures 5–7 also show the exponential dependences of the maximum value of the horizontal component x of ground acceleration versus the speed of the Pendolino train, trend lines and correlation coefficients R^2. An analysis of the dependences presented in Figures 5–7 showed that the maximum values of the horizontal component (x) of ground vibrations across all measurement profiles decrease with increasing distance from the source of vibration. Similar results were obtained for the horizontal component (y) and the vertical component (z) of vibration acceleration. For example, correlation coefficient R^2 for the

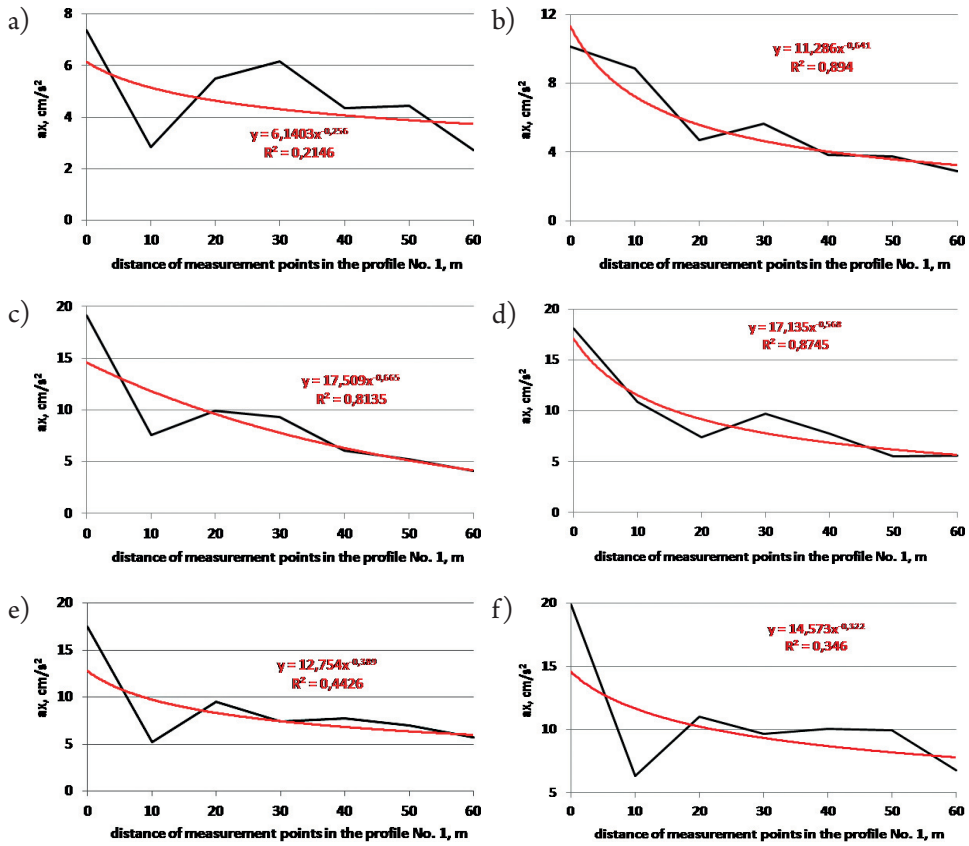

Fig. 5. The maximum value of the horizontal component (x) of free-field acceleration versus the change of distance – profile No. 1, the speed of a train: a) $v = 120$ km/h, b) $v = 160$ km/h, c) $v = 180$ km/h, d) $v = 200$ km/h, e) $v = 250$ km/h, f) $v = 270$ km/h

exponential function between the maximum values of ground acceleration vibrations and distances from the vibration source in profile No. 2 were between 0.95–0.99. Slightly smaller values of R^2 appeared in the measuring profile No. 3 (0.84–0.895), which may be the result of the profile shape (occurrence of a drainage ditch). In profile No. 1, passages of the Pendolino train at speeds of 120, 250 and 270 km/h caused low values of coefficient R^2, respectively 0.21, 0.44 and 0.35 – cf. Figure 5a, e and f. It can be associated with retention of the ground water at a very low level and rehydration of the substrate.

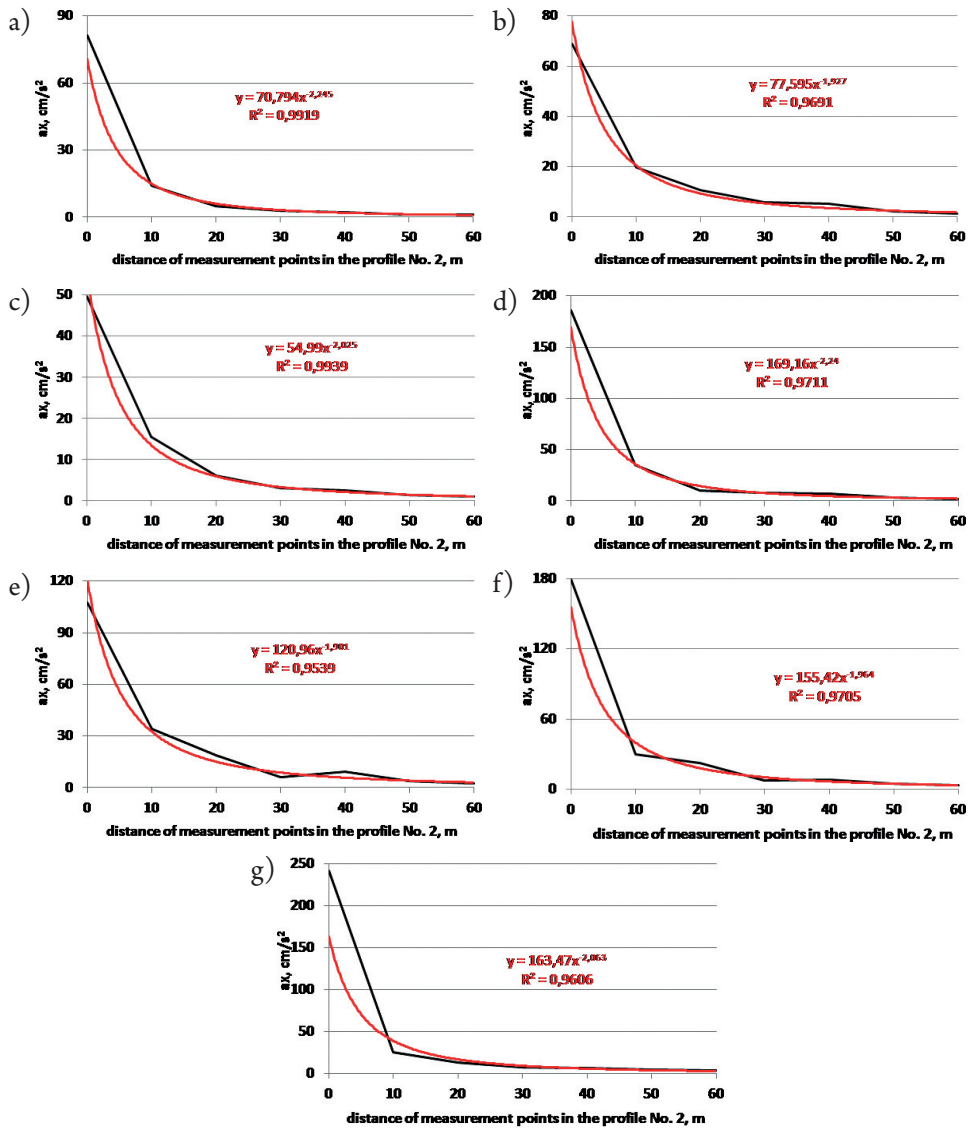

Fig. 6. The maximum value of the horizontal component (x) of free-field acceleration versus the change of distance – profile No. 2, the speed of a train: a) v = 120 km/h, b) v = 160 km/h, c) v = 180 km/h, d) v = 200 km/h, e) v = 250 km/h, f) v = 270 km/h, g) v = 293 km/h

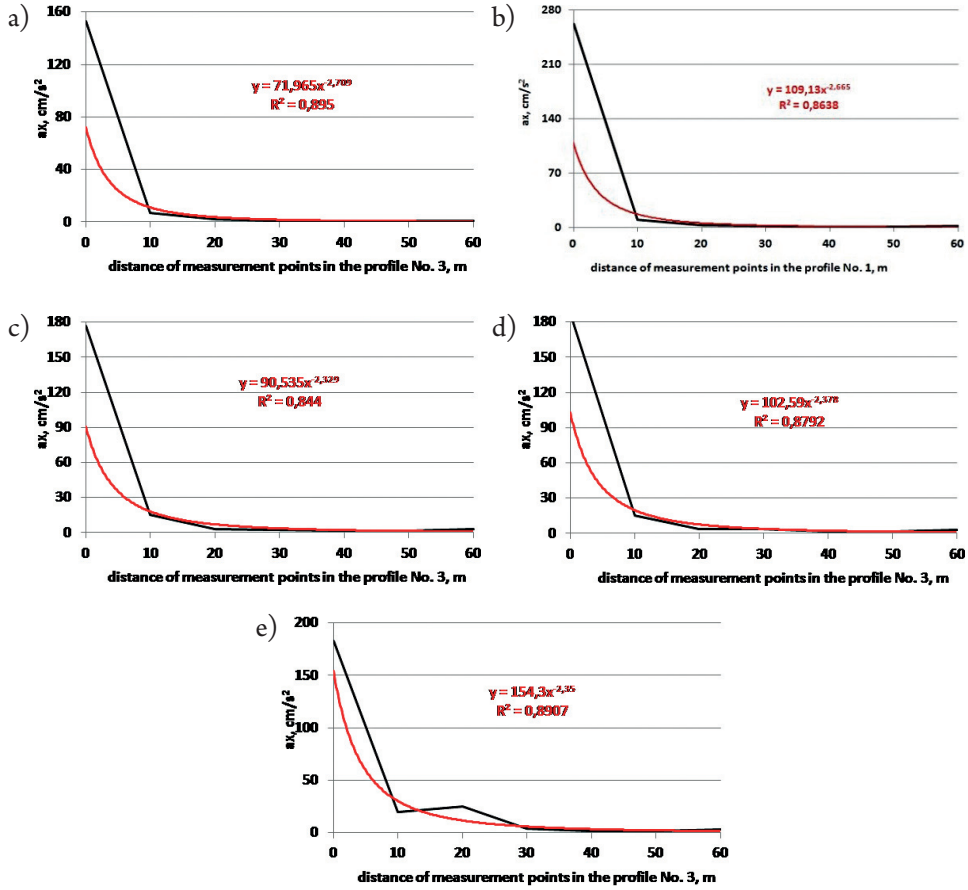

Fig. 7. The maximum value of the horizontal component (x) of free-field acceleration versus the change of istance – profile No. 3, the speed of a train: a) v = 120 km/h, b) v = 160 km/h, c) v = 180 km/h, d) v = 200 km/h, e) v = 250 km/h

Using measurement data contained in Tables 1–3, an attempt to determine the relationship between the maximum values of horizontal and vertical components of free-field vibrations and the speed of the Pendolino passages was made. For example, Figures 8a–g show the change in the value of the horizontal (x) component of free-field vibration acceleration in profile No. 3 as a function of the Pendolino train speeds. Figures 8a–g also show a trend-line of the proposed function of maximum values of the horizontal x component of free-field vibrations as a function of the Pendolino train speeds and correlation coefficient R^2. Depending on the analysis presented in Figures 8a–g, it follows that the maximum values of the horizontal (x) component of free-field vibrations rose with an increase of the Pendolino train speeds. Similar dependencies were obtained for the horizontal component (y) and vertical (z) of free-field vibrations. For example, the correlation coefficient R^2 values for the proposed relationship between the maximum values of free-field vibrations in the profile No. 3 (measurement points No. 1–7), and the speed of passages, range from 0.47–0.96 – cf. Figures 8a–g. An analysis

of the data contained in Tables 1–3 implies that the relationships between maximum values of free-field vibrations and the Pendolino train speeds are variable. In most of the measuring points in the assumed measurement profiles, there is a linear trend of increasing maximum values of free-field vibrations together with the Pendolino train speeds.

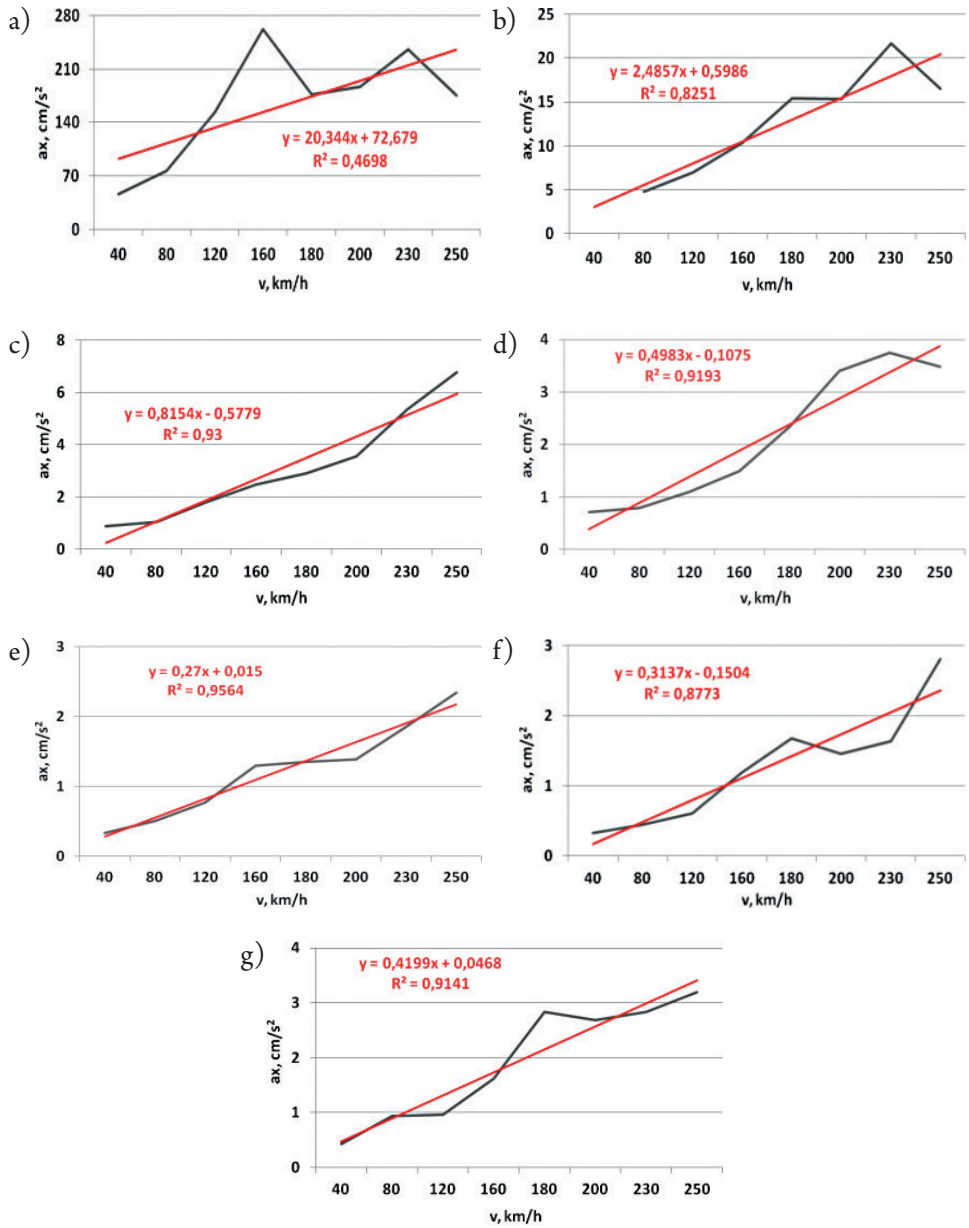

Fig. 8. Change the value of the horizontal component (x) of free-field acceleration in a) p. 1, b) p. 2, c) p. 3, d) p. 4, e) p. 5, f) p. 6, g) p. 7, profile No. 3 as a function of the Pendolino speeds

3. Research of the vibration of the selected building

The second part of the dynamic investigation refers to measuring the vibration of the dwelling building, situated at a distance of 49 m from the track along which the train was moving. The place where the study was conducted is a flat area where classical bedding layer is arranged. The investigated building is a low-rise, one-family, one-storey, masonry dwelling house with plan dimensions of 6.7 m x 16.0 m. Building vibration acceleration was measured at a ground level in order to determine the kinematic loads to which the building is subjected when the trains are passing near the building. The kinematic loads are also usable for evaluating the impact of these vibrations on the building structure using SWD scales from the Polish standard [4].

Figures 10 to 11 show an example of building vibrations due to the Pendolino passages at a speed equal to 250 km/h.

The most adverse results of the influence analysis of the horizontal components of vibration on the building during the passage of the Pendolino train at a speed of 250 km/h are given in Figure 12a and 12b. The presented results indicate that the measured vibrations of the building are classified as non-appreciable for its construction because the peak values of vibration accelerations in all 1/3 octave frequency bands are below the bottom of the curve that determines the appreciable threshold of vibrations through the structure of the building (according to the SWD-II scale from PN-85/B-02170 standard [4]).

Fig. 9. View of the investigated building

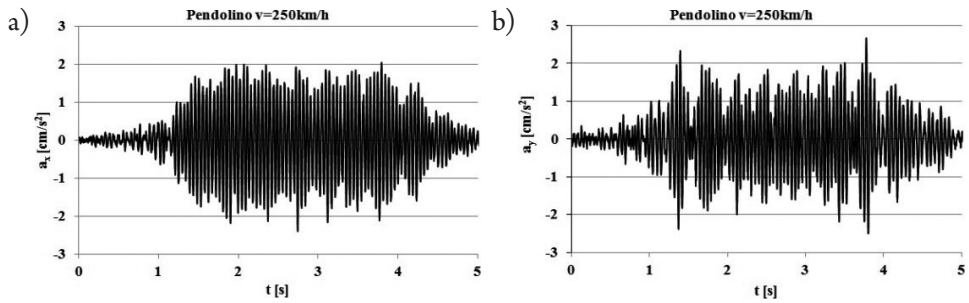

Fig. 10. The horizontal components of the vibration of the building at ground level recorded during the Pendolino passage at a speed of 250 km/h: a) component *x*, b) component *y*

For the comparison, Figure 13a and 13b show the results of the analysis of the impact of horizontal components (x, y) of vibrations for the building caused by passenger train with a speed of 160 km/h. The level of impact of these vibrations is not appreciable for the structure of the building and is about three times lower in relation to the listed in Figure 12a and 12b, which concerns the results of the analysis of the vibration impact on building generated by passage of the Pendolino train with a speed of 250 km/h.

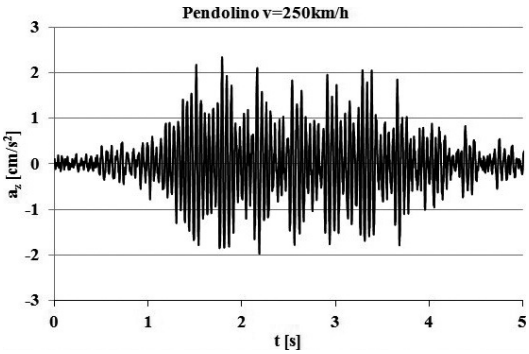

Fig. 11. The vertical z component of the vibration of the building at ground level recorded during the Pendolino passage at a speed of 250 km/h

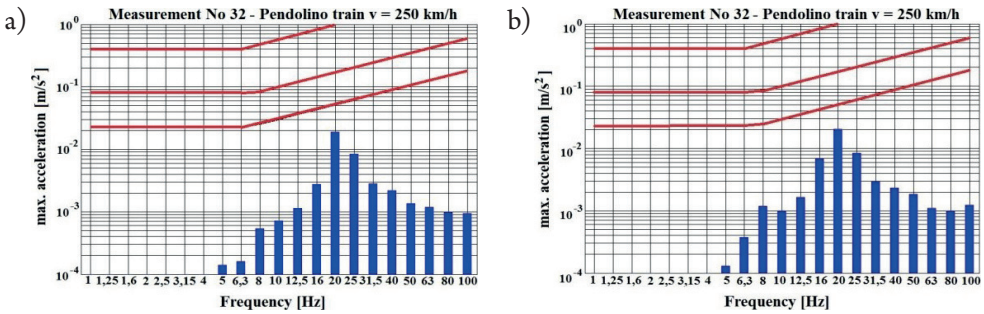

Fig. 12. The most adverse results of influence of vibrations caused by passing of the Pendolino train on the masonry structure of the building: a) component x, b) component y (measurement No. 32 – 30.11.2013)

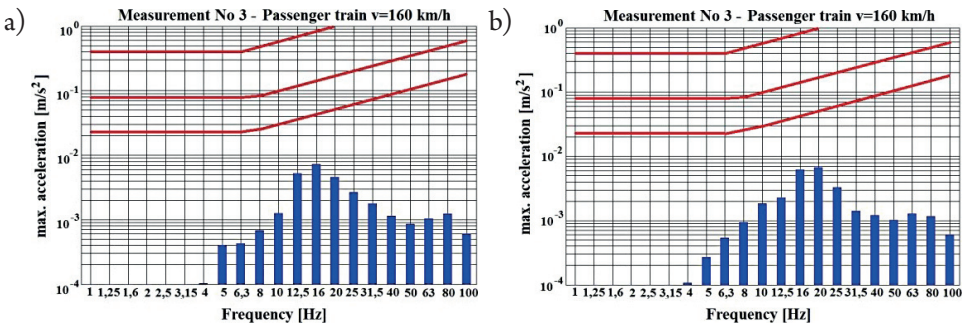

Fig. 13. The most adverse results of influence of vibrations caused by passing of the passenger train on the masonry structure of the building: a) component x, b) component y (measurement No. 32 – 30.11.2013.)

4. Conclusions

When drawing conclusions from the research results presented above, it should be remembered that they relate to the specific water – soil conditions in place where the vibrations were recorded and the particular type of building structure receiving vibrations.

On the basis of measurements of free-field vibrations, in three selected profiles of measurement, caused by passages of the Pendolino train and the results of the analysis of these vibrations, a relationship between the maximum values of the components of the vibration acceleration and the speed of the train can be noticed.

In the individual measuring points, generally the greater the speed of the train, the higher the value of the maximum acceleration values; there is also the impact of ground conditions on the propagation of vibrations. On the basis of an analysis of the measurement data, the exponential decay functions of maximum horizontal (x and y), and the vertical (z) component of the free-field measuring vibrations in three profiles versus dedicated speeds of the Pendolino train were adopted.

Vibrations of the building generated by passages of the Pendolino train are classified as non-appreciable for the structure of the building. The reason for this is e.g. the distance of the building from the railway track. The influence of vibrations on the building due to the passages of the Pendolino train was three times higher than during the passages of trains with conventional speed.

These conclusions cannot be generalised uncritically because they concern the specific surface as well as soil – water conditions at the profile of the measurements. However, they indicate that, in the future, vibrations of buildings (and hence the people in the buildings) caused by passages of the Pendolino trains may have a higher influence than it had during conventional train crossings. Hence, the result is the need to expand the area of research of dynamic influences of the high-speed line. It is therefore necessary to elaborate and implement a comprehensive research program referring to the measurement of building vibrations generated by passages of high-speed trains, including buildings at a smaller distances than permitted by the Railway Regulations. These studies should also address the impact of vibrations on humans; account should be taken of the different types of buildings as well as various geotechnical conditions on the road of the propagation of vibrations.

The results of such comprehensive research (performed on selected profiles) should be the basis for the elaboration of environmental impact assessments and design work associated with high-speed railway program in Poland in terms of influence of vibrations on the environment and design concerning vibro-isolation.

References

[1] Madshus C., Bessason B., Harvik L., *Prediction model for low frequency vibration from high speed railways on soft ground*, Journal of Sound and Vibration, Vol. 193(1), 1996, 195–203.

[2] Metrikine A.V., Vostrukhov A.V., Vrouwenvelder A.C.W.M., *Drag experienced by a high-speed train due to excitation of ground vibrations*, International Journal of Solids and Structures, Vol. 38 (48), 2001, 8851–8868.
[3] Schillemans L., *Impact of sound and vibration of the North-South high-speed railway connection through the city of Antwerp Belgium*, Journal of Sound and Vibration, Vol. 267 (3), 2003, 637–649.
[4] PN-85/B-02170, Evaluation of the harmfulness of building vibrations due to ground motion (in Polish).

TECHNICAL TRANSACTIONS 1/2017
CZASOPISMO TECHNICZNE 1/2017
ELECTRICAL ENGINEERING
DOI: 10.4467/2353737XCT.17.008.6105

Maciej Siwczyński
Marcin Jaraczewski (jaracz@pk.edu.pl)
Department of Electrical and Computer Engineering, Cracow University of Technology

Digital filters: hermitian, antihermitian, unitary and their applications

Filtry cyfrowe: hermitowski, antyhermitowski, unitarny i ich zastosowania

Abstract

The paper presents the relation between the three types of noncausal digital filters: unitary, Hermitian and antihermitian filters. A decomposition has been made of a causal filter into a Hermitian and unitary filter cascade, and the use of this decomposition to calculate the electric power quality of receivers has been highlighted. Reference has also been made to the analogy between the set of unitary filters and the unit circle in the Gaussian plane.

Keywords: unitary and Hermitian digital filters, operators, convolution

Streszczenie

W artykule podano związek między trzema typami nieprzyczynowych filtrów cyfrowych: filtrami unitarnymi, hermitowskimi i antyhermitowskimi. Dokonano też rozkładu filtru przyczynowego na kaskadę filtru hermitowskiego i unitarnego, oraz zwrócono uwagę na zastosowanie tego rozkładu do jakościowo-energetycznej oceny odbiorników energii elektrycznej. Nawiązano też do analogii zbioru filtrów unitarnych i okręgu jednostkowego na płaszczyźnie Gaussa.

Słowa kluczowe: unitarne i hermitowskie filtry cyfrowe, operatory, splot

1. Introduction

A digital filter is a transducer of a signal $\{x_n\}_{n=-\infty}^{\infty}$ that operates according to the convolution operator rules

$$(Ax)_n = \sum_m A_m x_{n-m} \qquad n,m \in (-\infty,\infty)$$

The digital filter identifier is a string of weights $\{A_n\}_{n=-\infty}^{\infty}$ or its 'z' form

$$A(z) = \sum_n A_n z^n$$

where:

$$A_n = \frac{1}{n!}\left[\frac{d^n A(z)}{dz^n}\right]_{z=0} \qquad \text{for n} \geq 0$$

$$A_n = \frac{1}{2\pi j}\oint A(z)\,d(\ln z) \qquad \text{for n} < 0$$

the integral is taken over the unit circle. In this way, the digital filter has two equivalent identifiers

$$A(z) \leftrightarrow \{A_n\}$$

For the two filters $A(z)$ and $B(z)$ the Borel theorem of convolution takes place:

$$A(z)B(z) \leftrightarrow \sum_m A_m x_{n-m} \doteqdot \{A_n\} * (B_n)$$

The filter is called causal (past) if

$$A_n = 0 \qquad \text{for } n < 0$$

The filter A^* is coupled to A if for any two signals x and y it meets the equation

$$(Ax,y) = (x,A^* y)$$

where the dot product of signals or filters is defined as

$$(A,B) = \sum_{n=-\infty}^{\infty} A_n B_n \text{ or } (A,B) = \sum_{n=0}^{N-1} A_n B_n$$

for signals or filters respectively and infinite or finite time support (in particular N-periodic).

For a digital filter realizing convolution-type operator it holds that

$$A^*_n = A_{-n} \leftrightarrow A^*(z) = A\left(z^{-1}\right)$$

The filter is called Hermitian if $A^* = A$, i.e. when

$$A_{-n} = A_n \leftrightarrow A\left(z^{-1}\right) = A(z)$$

and Antihermitian if $A^* = -A$, i.e. when

$$A_{-n} = -A_n \leftrightarrow A\left(z^{-1}\right) = -A(z)$$

The filter is stable if and only if

$$\sum_{n=-\infty}^{\infty} |A_n| < \infty \leftrightarrow |A(z)| < \infty \text{ for } z\text{: } |z| \leq 1$$

1.1. N-periodic Filter

An N-periodic filter is defined by the formula:

$$\tilde{A}_n = A_n + \sum_{p=1}^{\infty} \left(A_{n+pN} + A_{n-pN} \right) \qquad n \in \{0,1,...,N-1\}$$

It holds that $\tilde{A}^*_n = \tilde{A}_{N-n}$ for $n \in \{0,1,...,N-1\}$

In particular

$$\tilde{A}_n = A_n + \sum_{p=1}^{\infty} \left(A_{n+pN} \right)$$

for the causal filter

$$\tilde{A}_n = A_n + \sum_{p=1}^{\infty} \left(A_{pN+n} + A_{pN-n} \right)$$

for the Hermitian filter

$$\tilde{A}_n = A_n + \sum_{p=1}^{\infty} \left(A_{pN+n} - A_{pN-n} \right) \text{ for } n \in \{0,1,...,N-1\}$$

for the antihermitian filter.

A periodic filter operates on the N-periodic input signal $\{x_n\}_{n=0}^{N-1}$ according to the cyclic convolution operator

$$\left(\tilde{A}x\right)_n = \sum_{m=0}^{n} \tilde{A}_{n-m} x_m + \sum_{m=n+1}^{N-1} \tilde{A}_{n-m+N} x_m \quad \text{for } n \in \{0,1,...,N-1\}$$

2. Functional filters

The functional filter is defined as a digital filter formed from the digital filter A using some transforming function

$$f : A \to f(A)$$

Commonly it is assumed that both A and $f(A)$ are causal filters. The following notation is also assumed:

$$\left\{\left(f(A)\right)_n\right\} \leftrightarrow \left(f(A)(z)\right) = \sum_n \left(f(A)\right)_n z^n = f\left(\sum_n A_n z^n\right)$$

Thus the first two weights of the filter can easily be determined

$$\left(f(A)\right)_0 = f\left(A_0\right) \qquad \left(f(A)\right)_1 = \left[\frac{df(A)}{dA}\right]_{z=0} A_1$$

Further, the weight of the function filter can be determined directly according to the formula

$$\left(f(A)\right)_n = \frac{1}{n!}\left[\frac{d^n f(A)(z)}{dz^n}\right]_{z=0}$$

However, it seems scarcely useful due to the presence of the composite function. Often it is better to use a recursive method, which is more effective for some function $f(A)$. More about the functional filters can be found in [6]. In this paper two important functional filters are used: $f(A) = \sqrt{A}$ (the square root filter) and $f(A) = A^{-1}$ (the inverse filter).

The square root filter meets the convolution equation:

$$\sum_{m=0}^{n} \left(\sqrt{A}\right)_{n-m} \left(\sqrt{A}\right)_m = A_n$$

Thus a recursive formula can be derived

$$\left(\sqrt{A}\right)_n = \frac{A_n}{2\sqrt{A_0}} - \frac{1}{2\sqrt{A_0}} \sum_{m=0}^{n-1} \left(\sqrt{A}\right)_{n-m} \left(\sqrt{A}\right)_m \tag{1}$$

for $n = 2, 3, ...$

$$\left(\sqrt{A}\right)_0 = \sqrt{A_0}\,, \quad \left(\sqrt{A}\right)_1 = \frac{A_1}{2\sqrt{A_0}}$$

The inverse-filter weights can also be determined by the convolution equation

$$\sum_{m=0}^{n}\left(A^{-1}\right)_{n-m}A_m = I_n \doteqdot \begin{cases} 1 & n=0 \\ 0 & n\neq 0 \end{cases}$$

its solution is also a recursive formula

$$\left(A^{-1}\right)_n = -\left(A_0\right)^{-1}\sum_{m=1}^{n}\left(A^{-1}\right)_{n-m}A_m \quad \text{for } n=2,3,\ldots \tag{2}$$

$$\left(A^{-1}\right)_0 = -\left(A_0\right)^{-1}$$

For example, the weight of the digital filter of impedance *Z*, which is the inverse operator of an electrical two-terminal circuit *Y* admittance, is determined by the recursive formula

$$z_n = -z_0\sum_{m=1}^{n}z_{n-m}y_m\,,\ z_0 = \left(y_0\right)^{-1}$$

The function filter is analytical over the conjugation operation only if $\left[f(A)\right]^* = f\left(A^*\right)$. It is not difficult to prove that this condition is met for any function having the Taylor expansion form with respect to *A*, and that the inverse function to the analytic one over the inverse operation also fulfils this condition. Thus, in particular

$$\left(\sqrt{A}\right)^* = \sqrt{A^*} \text{ and } \left(A^{-1}\right)^* = \left(A^*\right)^{-1}$$

2.1. Hermitian, antihermitian and unitary filters

The weights representing the convolution-type filters are listed below:

$H^* = H$	$H_{-n} = H_n$	Hermitian	(equal)	
$A^* = -A$	$A_{-n} = -A_n$	antihermitian	(reverse)	(3)
$U^* = U^{-1}$	$U_{-n} = (U^{-1})_n$	unitary	(inverse)	

It is worth noting that the unitary filter is a generalization of a complex number over the unit circle. Just as with any digital filter, the unitary filter can be decomposed into the sum of Hermitian and antihermitian filters

$$U = H + A \text{ ie. } \mathrm{U^*} = \mathrm{H} - \mathrm{A} \tag{4}$$

thus

$$H = \frac{1}{2}\left(U + U^*\right) = \frac{1}{2}\left(U + U^{-1}\right) \tag{5}$$

$$A = \frac{1}{2}\left(U - U^*\right) = \frac{1}{2}\left(U - U^{-1}\right)$$

Hence (convolution filters commute!)

$$(H+A)(H-A)=H^2-A^2=1 \tag{6}$$

using the general composition formula of filters *A* with conjugated B

$$\left(AB^*\right)_n=\sum_m A_{n+m}B_m \tag{7}$$

it is obtained successively:

$$\left(H^2\right)_n=\sum_m H_{n+m}H_m$$

$$\left(A^2\right)_n=-\sum_m A_{n+m}A_m$$

$$\left(UU^*\right)_n=\sum_m U_{n+m}U_m=I_n \qquad m\in(-\infty,\infty)$$

It is also easy to obtain the following expression for the dot products and filter norms:

$$(H,A)=\left(A^*H,I\right)=\left(A^*,H^*\right)=-(H,A)=0$$

Thus *H* and *A* are orthogonal filters.
In addition:

$$\|U\|^2=(U,U)=\left(U^*U,I\right)=(I,I)=I$$

$$\|H\|^2=(H,\mathrm{H})=\frac{1}{4}\left(U+U^*,\mathrm{U}+\mathrm{U}^*\right)=\frac{1}{2}\left(1+\left(U^2,I\right)\right) \tag{8}$$

$$\|A\|^2=(A,\mathrm{A})=\frac{1}{4}\left(U-U^*,\mathrm{U}-\mathrm{U}^*\right)=\frac{1}{2}\left(1-\left(U^2,I\right)\right) \tag{9}$$

therefore

$$\|H\|^2+\|A\|^2=1 \tag{10}$$

3. 'Pole' decomposition of causal filter Y

The logic diagram can be written as follows:

$$
\begin{array}{lll}
Y^{*}=HU^{-1} & H^{2}=YY^{*} & \left(H^{2}\right)_{n}=\sum_{m=0}^{\infty}Y_{n+m}Y_{m} \\
\uparrow & & \\
\boxed{Y=HU} \longrightarrow & U^{2}=YZ^{*} & \left(U^{2}\right)_{n}=\sum_{m=0}^{\infty}Y_{n+m}Z_{m} \\
\downarrow & & \\
Y^{-1}=Z=H^{-1}U^{-1} & U^{-2}=ZY & \left(U^{-2}\right)_{n}=\sum_{m=0}^{\infty}Z_{n+m}Y_{m}
\end{array}
$$

$$Z^{*}=H^{-1}U$$

thus

$$
\begin{array}{lll}
H=\sqrt{Y}\left(\sqrt{Y}\right)^{*} & & H_{n}=\sum_{m=0}^{\infty}\left(\sqrt{Y}\right)_{n+m}\left(\sqrt{Y}\right)_{m} \\
U=\sqrt{Y}\left(\sqrt{Z}\right)^{*} & \longrightarrow & U_{n}=\sum_{m=0}^{\infty}\left(\sqrt{Y}\right)_{n+m}\left(\sqrt{Z}\right)_{m} \\
U^{-1}=\sqrt{Z}\left(\sqrt{Y}\right)^{*} & & U_{n}^{-1}=\sum_{m=0}^{\infty}\left(\sqrt{Z}\right)_{n+m}\left(\sqrt{Y}\right)_{m}
\end{array}
\tag{11}
$$

A square-root-causal filter is used in the above formulas.

Combining equation (8), (9) (11) we obtain

$$\left(U^{2},I\right)=\left(Z^{*}Y,I\right)=\left(Y,Z\right) \tag{12}$$

and then

$$\left\|H\right\|^{2}=1+\frac{1}{2}\sum_{n=1}^{\infty}Y_{n}Z_{n} \tag{13}$$

$$\left\|A\right\|^{2}=-\frac{1}{2}\sum_{n=1}^{\infty}Y_{n}Z_{n} \tag{14}$$

The (6) is a hyperbolic relation. If *H, A* operators have the meaning of real numbers and the identity *I* operator the meaning of the ordinary number equals one then in the *H, A* coordinates this relation will be a hyperbole equation with asymptotes of $A=\pm H$ (Fig.1).

A comparison between the operator relation (6) and the hyperbole equation is presented below:

$$\sum_{m}H_{n+m}H_{m}-\left(-\sum_{m}A_{n+m}A_{m}\right)=\begin{cases}1 & n=0\\ 0 & n\neq 0\end{cases} \tag{15}$$

$$H^{2}-A^{2}=1 \tag{16}$$

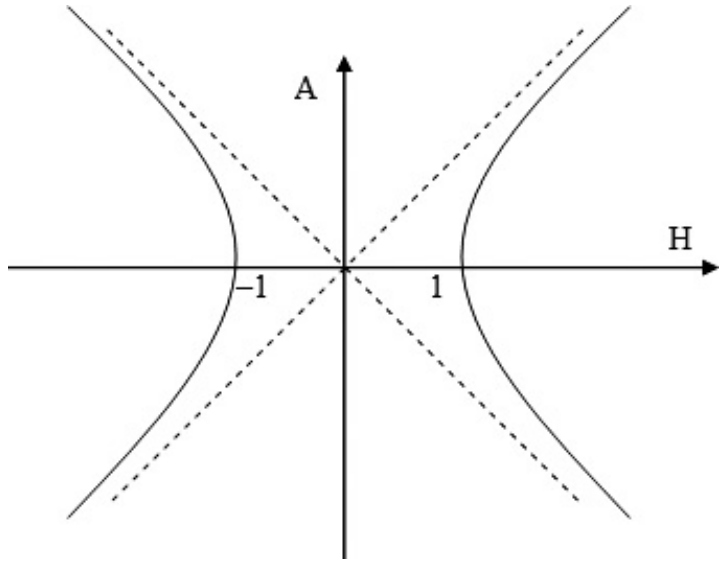

Fig. 1. A hyperbole in real-number coordinates of the equation $H^2 - A^2 = 1$ that corresponds to the operator relation (6)

It is also worth noting that for $n = 0$ the relation (15) becomes

$$\sum_m H_m^2 + \sum_m A_m^2 = 1$$

which coincides with the Pythagorean condition (10).

The Hermitian, antihermitian and unitary filters operate on signal $\{x_n\}_{n=-\infty}^{\infty}$ according to the convolution formulas

$$(Hx)_n = H_0 x_n + \sum_{m=1}^{n} H_m \left(x_{n-m} + x_{n+m}\right) \tag{17}$$

$$(Ax)_n = \sum_{m=1}^{n} A_m \left(x_{n-m} - x_{n+m}\right) \tag{18}$$

$$(Ux)_n = U_0 x_n + \sum_{m=1}^{n} \left(U_m x_{n-m} + \left(U^{-1}\right)_m x_{n+m}\right) \tag{19}$$

The weights of the periodic filters have been calculated using the following formulas (the first two were presented in the introduction):

$$\tilde{H}_n = H_n + \sum_{p=1}^{\infty} \left(H_{pN+n} + H_{pN-n}\right) \tag{20}$$

$$\tilde{A}_n = A_n + \sum_{p=1}^{\infty} \left(A_{pN+n} - A_{pN-n}\right) \tag{21}$$

$$\tilde{U}_n = U_n + \sum_{p=1}^{\infty}\left(U_{pN+n} + U_{pN-n}\right) \text{ for } n \in \{0,1,...,N-1\} \tag{22}$$

The periodic filter operates on a periodic input signal $\{x_n\}_{n=0}^{N-1}$ according to (common to *H, A and U* operators) the periodic convolution formula:

$$\left(\tilde{G}_x\right)_n = \sum_{m=0}^{n} x_m \tilde{G}_{n-m} + \sum_{m=n+1}^{N-1} x_m \tilde{G}_{n-m+N} \tag{23}$$

Unitary filter can also have the exponential form

$$U = e^{\phi} = \sum_{n=0}^{n} \frac{\phi^n}{n!} \quad : \quad \phi^* = -\phi \tag{24}$$

Any power of the ϕ operation, used in the series, can be determined with the recursive convolution formula:

$$\left(\phi^{p+1}\right)_n = \phi^p \phi$$

which has the following implementation

$$\left(\phi^{p+1}\right)_n = \sum_m \left(\phi^p\right)_{n-m} \phi_m = \sum_{m=1}^{\infty}\left[\left(\phi^p\right)_{n-m} + \left(\phi^p\right)_{n+m}\right]\phi_m \tag{25}$$

for $n = 2, 3, ...$

Then the components of the decomposition (4) can be interpreted as

$$H = ch(\phi) = \sum_{n=0}^{\infty} \frac{\phi^{2n}}{(2n)!}; \qquad A = sh(\phi) = \sum_{n=0}^{\infty} \frac{\phi^{2n+1}}{(2n+1)!} \tag{26}$$

thus

$$e^{\phi} = ch(\phi) + sh(\phi) \rightarrow ch(\phi) = \frac{1}{2}\left(e^{\phi} + e^{-\phi}\right);\ sh(\phi) = \frac{1}{2}\left(e^{\phi} - e^{-\phi}\right) \tag{27}$$

Formulas (6) and (10) take then the form in which the first formula is analogous to the well-known hyperbolic function in the common "numerical" theory:

$$ch(\phi)^2 - sh(\phi)^2 = I \tag{28}$$

$$\left\|ch(\phi)\right\|^2 + \left\|sh(\phi)\right\|^2 = 1 \tag{29}$$

From (24) it also follows that the relation between the *U* operator and the Euler's number 'e' is

$$e^I = e^I \rightarrow \left(e^I\right)_n = e\begin{cases}1\\0\end{cases} = \begin{cases}e & n=0\\0 & n\neq 0\end{cases} \tag{30}$$

4. Conclusion

The decomposition of a unitary convolution operator into the Hermitian and antihermitian operators presented in the article (4) is a significant generalization in digital filter theory of Euler's famous formula:

$$e^{j\phi} = ch(j\phi) + sh(j\phi)$$

where ϕ– real number, $j = \sqrt{-1}$
commonly used for complex numbers.

The unitary digital filter-operator itself corresponds to a complex number in the Gauss plane over the unit circle. On the other hand the decomposition (11), i.e. $Y = HU$ is an extension on digital filters of the ordinary admittance of the complex two-terminal circuit decomposition into a module and an argument, hence the name "pole decomposition", while the decomposition

$$Y = H\left(ch(\phi) + sh(\phi)\right)$$

is an operational generalization of the decomposition form of that complex admittance into a conductance and a susceptance:

$Y = |Y|\left(ch(j\phi) + sh(j\phi)\right)$, $|Y| > 0$, ϕ – real numbers

The formula (14) in the form of a negative half of the incomplete scalar product of the two causal mutually-inverse digital filters of an impedance and an admittance may be of practical significance. It is a counterpart of the susceptance measure of a digital receiver and thus it is an indicator of harmful reactive power of that receiver.

This allows, in particular, to make a comparative evaluation of the i-th receiver in relation to the others connected in parallel by simply calculating the fraction

$$\frac{\|sh\phi\|_i^2}{\sum_n \|sh\phi\|_n^2}$$

It is obvious that the "pure resistance" receiver impedance corresponds to the digital filter:

$$z = z_0 I \rightarrow y = y_0 I \ : \ z_0 y_0 = 1$$

and finally combining expressions the following beautiful theorem can be formulated

$$\|sh(\phi)\| = 0 \leftrightarrow \begin{matrix} (Y,Z) = 1 \\ YZ = I \end{matrix}$$

which we can rewrite using digital filters weights in the following form

$$\sum_{n=-\infty}^{\infty}\left[\left(sh\phi\right)_n\right]^2=1\leftrightarrow\begin{array}{l}\sum_{n=0}^{\infty}Y_nZ_n=1\\ \sum_{m=0}^{n}Y_{n-m}Z_m=I_n=\begin{cases}1 & n=0\\ 0 & n\neq 0\end{cases}\end{array}$$

5. Calculation example

The evaluation of the reactive power factor $\|sh\phi\|^2$ of the wave-impedance operator:

$$\hat{z}=\sqrt{\frac{a-z}{b-z}};\qquad a>1,\quad b>1$$

Since it is an integral-derivative operator of order ½ its inversion has the form:

$$y=\sqrt{\frac{b-z}{a-z}}$$

The time samples of the above operators are given by a power series expansion with respect to the variable 'z' [1, 2, 4, 5]

$$\hat{z}_n=\sqrt{\frac{a}{b}}a^{-n}\alpha_n;\qquad y_n=\sqrt{\frac{b}{a}}a^{-n}\beta_n;\quad n=0,1,2,\ldots$$

$$\alpha_n=\sum_{m=0}^{n}\left(\frac{a}{b}\right)^m k_{n-m}h_m;\qquad \beta_n=\sum_{m=0}^{n}\left(\frac{a}{b}\right)^m h_{n-m}k_m$$

Where $\{k_n\}$, $\{h_n\}$ – the universal sequences determined by the formulas:

$$k_m=-\frac{1}{2}\frac{1}{4}\frac{3}{6}\frac{5}{8}\ldots\frac{2m-3}{2m}\qquad\text{derivative}$$

$$h_m=-\frac{1}{2}\frac{3}{4}\frac{5}{6}\frac{7}{8}\ldots\frac{2m-1}{2m}\qquad\text{integral}$$

while $k_0=h_0=1$

Therefore, the reactive power factor is obtained from:

$$\|\sinh\phi\|^2=-\frac{1}{2}\sum_{m=1}^{\infty}y_m\hat{z}_m=-\frac{1}{2}\sum_{m=1}^{\infty}a^{-2m}\alpha_m\beta_m$$

Let us take into account the first two terms of this expansion and set $x = a/b$, the first component is positive

$$\frac{1}{8}a^{-2}\left(x-1\right)^2=\frac{1}{8}\left(\frac{a-b}{ab}\right)^2$$

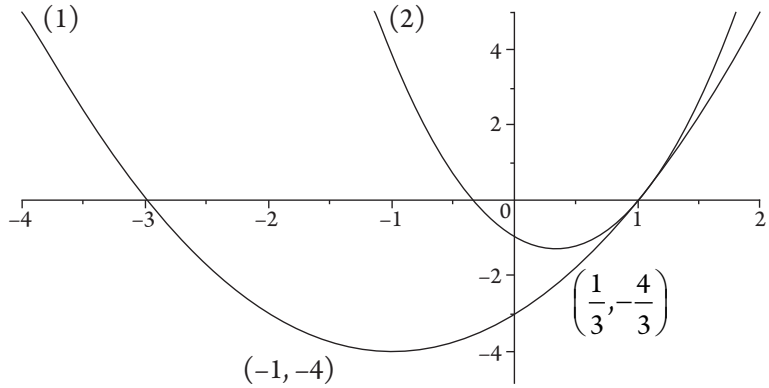

Fig. 2. Graph of the two factors of the second-order series expansion term of the reactive power factor $||\mathrm{sh}\phi||^2$

and the second is:

$$\frac{1}{2}a^{-4}\frac{1}{64}\left(3x^2\overset{(1)}{-}2x-1\right)\left(x^2\overset{(2)}{+}2x-3\right)$$

Figure 2 shows that the second term of the series expansion (as a product of 1 and 2) is also positive, therefore the reactive power factor of the wave impedance is a positive function.

References

[1] Atici F.M., *A Transform Method in Discrete Fractional Calculus*, International Journal of Difference Equations (IJDE), Vol. 2, No. 2, 2007, 165–176.

[2] Yan Lia, Hu Shengb, YangQuan Chen, *Analytical impulse response of a fractional second order filter and its impulse response invariant discretization*, ELSEVIER Signal Processing, Vol. 91, Issue 3, March 2011, 498–507.

[3] Siwczyński M., *Rozkłady: prąd aktywny, prąd rozrzutu, prąd bierny w dziedzinie czasu dyskretnego*, Przegląd Elektrotechniczny, 7/2010, 338–341.

[4] Siwczyński M., Drwal A., Żaba S., *Zastosowanie filtrów cyfrowych rzędu ułamkowego typu wykładniczego do analizy układów o parametrach rozłożonych*, Przegląd Elektrotechniczny, 2/2012, 184–190.

[5] Siwczyński M., *Postać wykładnicza i hiperboliczna operatora bądź sygnału okresowego w dziedzinie czasu – zastosowania w teorii mocy*, Przegląd Elektrotechniczny, 6/2012, 194–197.

[6] Siwczyński M., Drwal A., Żaba S., *The digital function filters-algorythms and applications*, Bull, Polish Accademy of Science, 2013.

TECHNICAL TRANSACTIONS 1/2017
CZASOPISMO TECHNICZNE 1/2017
ENVIRONMENTAL ENGINEERING
DOI: 10.4467/2353737XCT.17.009.6106

Dóra Csizmadia (dora.csizmadia@campus.tu-berlin.de)
Ina Säumel
Department of Ecology, Technical University of Berlin
Lauranne Pille
Kinga Szilágyi
Péter István Balogh
Department of Garden and Open Space Design, Szent István Universitiy

Water sensitive design potentials in Paris, Berlin, and Budapest revisited

Analiza potencjału rozwiązań wrażliwych na wodę w Paryżu, Berlinie i Budapeszcie

Abstract

Impacts of extreme weather events are increasing due to ongoing climate change. Floods in the urban areas not just damage properties but also threat human life. Coping with these challenges in metropolises of old Europe is difficult as the ex-istent building structures and combined rainwater and sewage systems originating from the 19th century. We compare three old European capital cities (Berlin, Budapest and Paris) regarding rainwater management concepts. We identify important spatial land use types of blue-green infrastructure and corresponding measures for the implementation towards a more water sensitive management by using the case study approach.

Keywords: urban rainwater management, sustainable planning, european metropolises

Streszczenie

Obecnie, w rezultacie postępującej zmiany klimatu, obserwuje się coraz więcej skutków ekstremalnych zjawisk pogodowych. Podtopienia w obszarach miejskich prowadzą nie tylko do szkód materialnych, ale też zagrażają ludzkiemu życiu. W europejskich metropoliach problem ten stanowi prawdziwe wyzwanie, ponieważ znajdujące się tam budowle i sieci kanalizacji burzowej i sanitarnej wybudowano jeszcze w XIX wieku. W artykule porównano trzy europejskie stolice (Berlin, Budapeszt i Paryż) pod względem zastosowanych tam rozwiązań dotyczących zagospodarowania wody deszczowej. Zidentyfikowano istotne sposoby zagospodarowania przestrzennego zielonej infrastruktury oraz odpowiednie środki zorientowane na zarządzanie wrażliwe na wodę na podstawie analizy przypadku

Słowa kluczowe: zagospodarowanie wody deszczowej, zrównoważone planowanie, europejskie metropolie

1. Introduction

The frequencies and duration of stormwater events and floods are increasing in Central Europe (e.g. Fig. 1). Socio-economic impacts are projected to increase by two hundred percent (Alferi et al. 2015) [1]. Floods in vulnerable and densely populated urban areas not just damage properties but also threat human life. In our ongoing urbanized world, these threats affect more people in the future, as urban dwellers will likely account for 86 per cent of the population in 2050 [2].

The old European metropolises have a similar historical and structural development and a common heirship of traditional water infrastructure. This traditional water infrastructures are unlikely to adapt to the increasingly unpredictable extreme weather events [3], imply tremendous operation and maintenance costs, and contradict sustainable use of resources and possible ecological and aesthetical advantages of integrating blue infrastructure into the urban life.

The Water Sensitive City approach aims on a more sustainable water management and includes normative values regarding environment repair and protection, supply security, flood control, public health, amenity, livability and economic sustainability and thus includes aspects beyond the traditional functions of water supply, draining and sewage [6]. The integration of green and blue urban infrastructure (e.g. Blue-Green City Approaches, Lundy & Wade, 2011; Rozos et al., 2013; Lawson et al., 2014) will also fostering multifunctionality and sustainability of urban infrastructure. Up to date certain efforts have been done to implement an alternative approach on urban water services in new built up areas whereas the transformation of existing

Fig. 1. The summer flood 2013 of Danube River caused costs of over ten Mio. Euro for Budapest, Hungary [4]. At 17th of August 2013 96 mm of rain fall within one hour– an amount equivalent to the average of one month. Consequently, the canal system could not cope with the runoff and on some streets flow more than one meter high water.[5]

housing areas remains understudied. Thus, in this paper we compare three old European capital cities (Berlin, Budapest and Paris) regarding water relevant natural features, existing urban structure and rainwater management concepts. We identify important spatial land use types of blue-green infrastructure and corresponding measures for the implementation towards a more water sensitive city. We analyzed geographical information, land use maps, and other cartographic data. Successfully implemented methods and measures will be identified from city development plans, water strategies, climate adaptation plans and from the KURAS database (see www.kuras-projekt.de). The measures will be illustrated with realized projects from our focus cities. Finally we attempt to define a set of potential strategies and measures for Budapest, which could be used in order to foster transition from the existing towards a more sustainable rainwater management system in the capital of Hungary.

Sustainable urban stormwater management (SUWM) appeared in Europe at first in the 80ies often related to brownfields and poor water quality. New draining solutions and restored retention basins reduced costs through using of smaller diameter drainage pipes [7]. Nowadays sustainable measures takes part of planning principles in European countries. Especially the European Water Framework Directive fostered the implementation of laws, directives and supporting programs towards a more sustainable water management. Metropolises, which are substantial affected in extreme weather events and rising see level (e.g. Copenhagen or Rotterdam) creates long-range climate adaptation plans or water city plans with complex measurements for the next decades.

2. Results

2.1. Natural and structural features relevant for water infrastructure

Climate, geology and hydrology determine basically the natural features of an area and thus frame conditions of blue-green infrastructure. Table 1 summarizes relevant features. In general, the cities show similarities in major climatic parameters and also in the riverside location. Special soil types of floodplains with good permeability are dominating. Some city specific features modify the main character.

Table 1. Water relevant natural features of three old European capital cities (Berlin, Budapest and Paris)[1]

	PARIS	BERLIN	BUDAPEST
Climate	oceanic	oceanic-continental	continental
Annual precipitation	641 mm	581 mm	533 mm
Area	105 km^2	525 km^2	892 km^2
Population	2,2 mio	3,5 mio	1,7 mio

[1] Data sources: Institut national de la statistique et des études économiques; Amt für Statistik Brandenburg; Központi Statisztikai Hivatal.

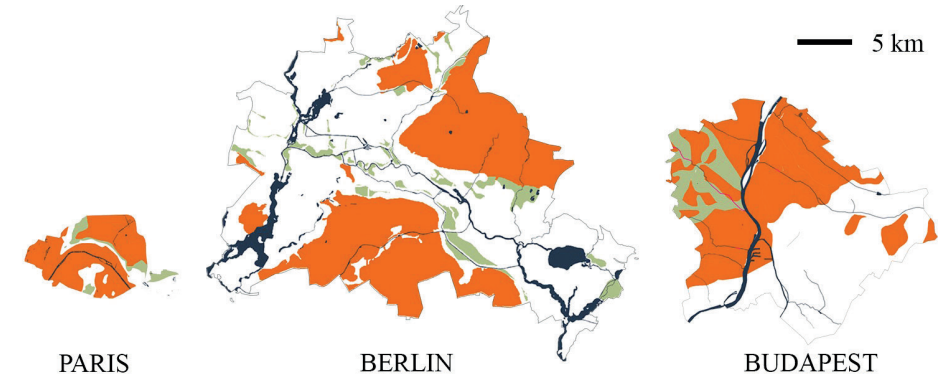

Fig. 2. Soil types of Paris, Berlin and Budapest

Paris with large, evenly dispersed annual precipitation and narrow temperature range has the most balanced climate [8]. The main river Seine of the city´s blue infrastructure has highly changeable water level which threatens the city permanently with flooding. Infiltration of rain is often obstructed by watertight soil such as claim or granite (Fig. 2).

The big city renovations of 19th centuries turned the blue infrastructure into simple constructed utilities. Many creeks were canalized and carried under the earth. The creek Biévre had been completely underdrained. Thus, a revitalization of water courses towards nature near riverbanks appear ambitious.

Berlin´s climate is a transition between oceanic and continental climate with warm temperate, massive humidity and colder summers [9] Numerous lakes, canals and rivers of Berlin help to cool the city and buffer the changes of water level. The Berlin rivers (Spree, Havel and Dahme) have a low water volume, the water surface is large. Berlin is dominated by sand and turf soil, high groundwater level implies limits for infiltration in many parts of the city.

Budapest is situated easternmost – summer droughts with 35°C are increasing. The city similarly to Paris is dominated by one big river, the Danube. The Danube has fifteen times bigger water volume, than the all main rivers of Berlin together, but the water surface is just third. The east side of the city has mostly permeable soil types as sand and gravel, the western Buda side is mainly constructed on limestone

Climate change will strongly affect climate of European metropolises. Main effects will be expectedly similar in the three cities: distribution of precipitation will be shifted from summer to winter, summer droughts will enhance frequency of heat waves and extreme weather events will cause bigger surface runoff [10].

The structure of old European Metropolis had been developed till the middle of 19th century in a similar way and was supplemented or modified during the last century (Fig. 3).

Hausmann´s renovation formed Paris into a looser structure, but the density of historical tenement housing dominates as 2.2 mio inhabitants live in an area that is fifth of Budapest. In some places of the old city structure just the street trees can help the vaporization and infiltration. In the dense structure of Paris there are few possibilities for rainwater infiltration.

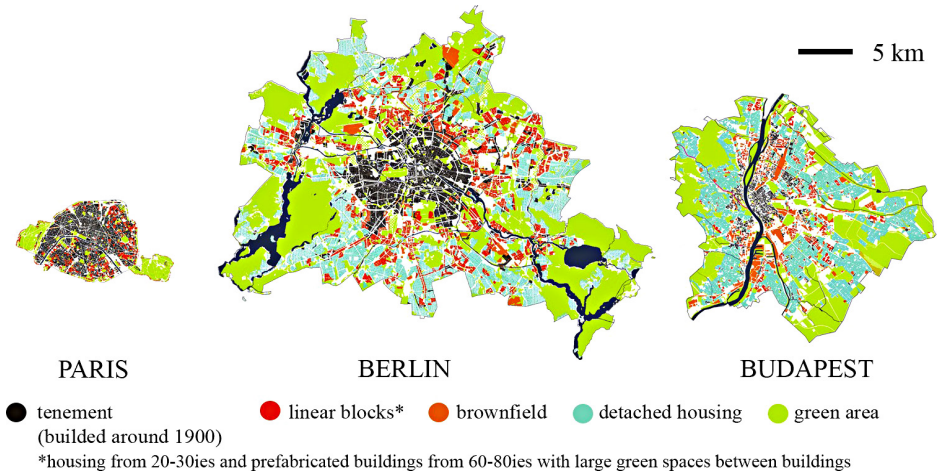

Fig. 3. Land use types of Paris, Berlin and Budapest

The combined sewage system transports the stormwater into the river increasing the flood wave. Heat island effect is also a common challenge in the city: the temperature difference between Paris and the outer suburbs is able to reach over 8°C difference at night [11].

Berlin´s building inventory suffered in World War II huge damages – the historical city center was mainly perished. Today's city structure is loose, 44% of the urban surface is green area and City center is characterized by a high proportion of new buildings. Berlin has some special housing types with high green area ratio: linear blocks of 20-30ies and the 50-60ies (Zeilenbau) and prefabricated buildings from 60-80ies (Plattenbau and Großsiedlungen) are surrounded by extended green areas in common use. Away from the center the most common type is low density housing with private gardens. Built-in areas are connected with a multifunctional network of creeks, rivers, lakes, canals, green corridors and recreational areas. This blue-green grid turns Berlin into a green and livable city. Budapest's compact city center with tenement is framed by looser zones of prefabricated building estates and low density housing. Parks of the inner city and the larger green areas near to the city border are poorly connected. In the last 20 years the green area ratio of Budapest has been decreased 4% [12]. The city structure lacks of green ways which could provide ecological transfer zones and healthy recreational areas for the citizens.

As the analysis of city structures shows, while Berlin has a large similarity in younger housing types to Budapest, Paris can be used as an example to cope with flooding and challenges of dense tenement housing.

2.2. Best Practise toward a new water infrastructure for old European metropolises

Paris synthetized goals and measures of sustainable water management in the urban water strategy **"Livre Bleu"** (Blue Book) to cope the challenges of climate change. The main measures selected as part of this policy are the improving of evaporation, infiltration

of rainwater and restricted flow rejection in the network [11]. Implementation are reviewed by instruments as city gardens, small green areas, green roofs, and the lake "Lac Inférieur". Small sized city gardens and pocket parks have a great importance for recreation and cooling in the dense tenement housing of Paris. These green islands are supplemented with numerous small green areas such as swales along pedestrian ways. However lack of green space is partially compensated by the use of planters and rooftop vegetable gardens – a frequent and beloved type of green roofs in Paris. Riverside projects in Paris can be hardly implementing due to the lack of space and the traffic routes along the river. Local government tries to find nevertheless new connections between the Seine and the city: inźthe project named "Paris Plages" the wharfs are closed for the weekend for traffic and opened for the citizens as a promenade [13] (Fig. 4). The "Lac Inférieur" is a retention pond of the place Colombie integrated into the historical park Bois de Bolougne. A wetland between lake and road was constructed to protect the highly sensitive aquatic environment of the lake from the direct polluted runoff of neigbouring streets.

Fig. 4. Project Paris-Plages [13]

Fig. 5. Visualization of the project "Panke 2015" [14]

Development and climate adaptation plan of Berlin focuses on the action zones of historical city center and watercourses. Street trees, permeable pavement, green roofs and green walls are defined as most relevant measures in the historical districts. Pedestrian ways and parking lots are huge potential infiltration surfaces – Berlin's typical micro cube stone pavement can infiltrate more rainwater as grass. Applicability of green roofs and green walls depends mainly on building structure [10]. Ecological pilot project **Block 103 Kreuzberg** was one of the first experiments for transformation existing housing into an energy and water efficient, climate friendly environment. Green area ratio was increased from 2% to 39% with measures as court greening, green roofs, green walls. Rainwater collection permitted graywater reuse for irrigation and toilet flushing [15].

Improving of water quality is an important goal of the city since two decades. Emission reduction and riverside restorations helped to reach such a betterment for today, that newest city concept **"Flussbad Berlin"** is considering to transform the banks of the Spree River and Spree Canal into a bath area and new meeting place for urban society [16]. Water quality is however just one required factor of a diverse biocoenosis. Revitalisation project of creek Panke aims the restoration of natural meandering river form and configuration of new habitats and flood zones (Fig. 5) The naturalized stretches with widened and meandering river section and new river forks make step stones for species of flora and fauna [14].

The **Park Am Gleisdreieck** was constructed with the transformation of a former marshaling yard partly as green area compensation for dense building development of Potsdamer Platz. Larger paved areas are permeable and the stormwater goes from the ways to the grass surfaces. The park has a special area with temporary water filled swales and hills, where children and young people can experience nature [17]. The larger green areas between linear blocks permit the application of SUWM measures such as swales, rain gardens or retention ponds. Building structure is ideal for green roofs and green walls. Some tree species are unequal to the increasing summer droughts. Gradual change of plants into climate adaptive species is therefore an important goal of the city [10].

The concept of SUWM has appeared only recently in urban planning practice of Hungary, nevertheless several projects have been realized within the last ten years used the approach of water sensitive planning. An early example from the 90ies was the radical **reconstruction of the district Ferencváros.** Demolition of numerous building annexes resulted an airier tenement structure with large gardens inside the blocks.[18] **Rehabilitation of the Károly-körút**, a section of the small boulevard, created a new broad grass stripe, two tree rows and more fountains to improve the microclimate in the hearth of the city [19] (Fig. 6). Revitalisation of Kopaszi dam in 2007 was the first big successful riverside project. Cleaning the bank of the former harbor bay and forming surroundings into a multifunctional green space turned the area into one of the most popular public parks of the city [20] (Fig. 7).

Fig. 6. Rehabilitation of Károly-körút [21]

Fig. 7. Kopaszi-dam [20]

Revealing priority action fields, we took a closer examination on urban structure of Budapest (Fig. 8). 47% of the city surface is covered by plants, two-thirds made up of forests and field lands [12]. In the built-in area most green spaces can be found on private house grounds. This research is engaged in transitioning of public urban areas, doesn't examine therefore the three aforementioned categories (forests, fields and private gardens).

We classified **5 action zones** of sustainable urban rainwater management according to their different use, features and spatial position, illustrated on the Figure 9.

Historical **tenement housing** with combined sewage system has the biggest lack of green spaces and impervious surfaces – often not just the streets and squares but also the courtyards are totally paved. These surfaces are mainly covered with low albedo asphalt,

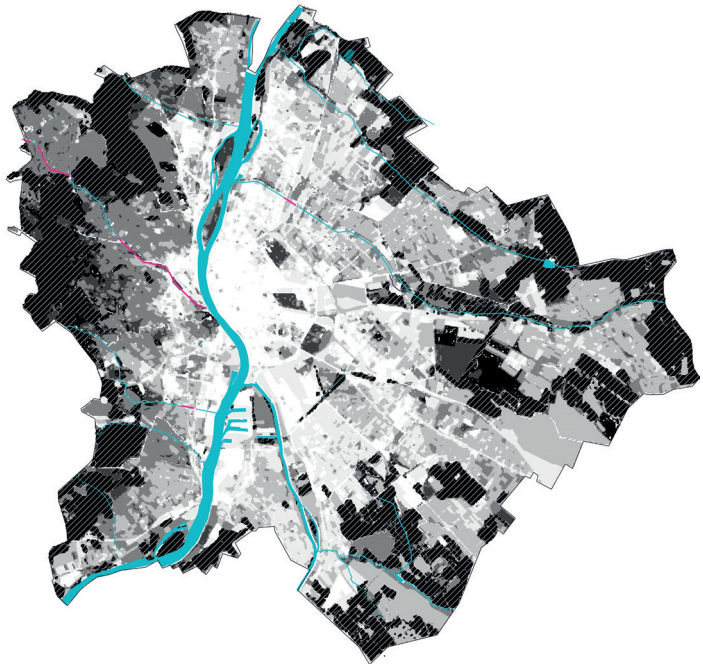

Fig. 8. Green intensity analysis of Budapest [22]

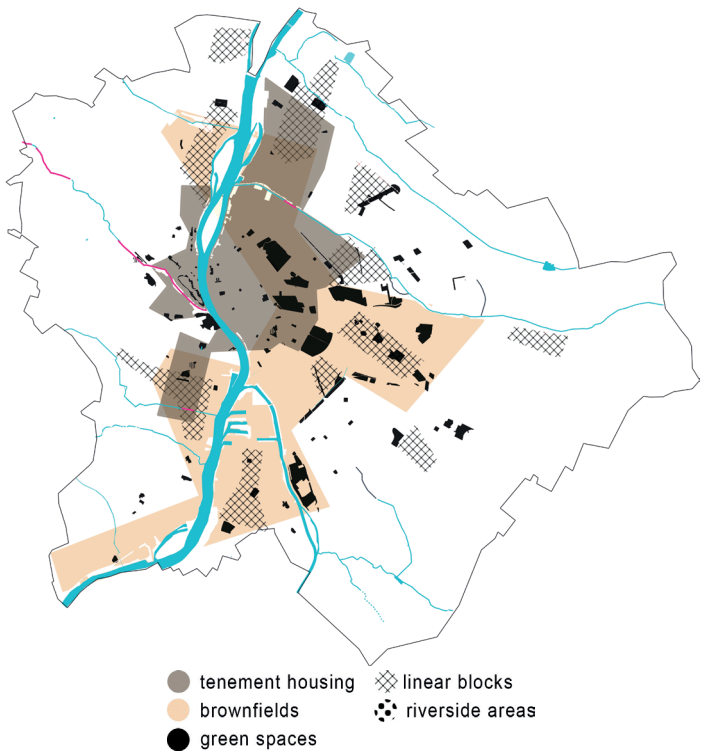

Fig. 9. The five action zones of SWUM

which causes fast runoff and amplifies urban heat island effect. Historical facades permit limited application of green roofs and green facades. A new tree line demands therefore Tree planting costs oftentimes multiple as a usual green space establishment because of the dense underground public utility system.

Linear blocks in extended public green space are represented by prefabricated modernist buildings of 60-80ies (Plattenbau) and social realist linear and perimeter blocks of the 50ies. The grounds are owned and generally maintained by the local government and used as a public park with good plant condition. Building structure favors for green roofs and green facades.

There are mainly two big possibilities for larger extension of retention areas in the old city structure. **Brownfield areas** cover more than 1200 ha in Budapest [23]. These ancient industrial and railway areas intersected with riverside zones (e.g. the Csepel Island or the Rákosrendezö marshalling yard) are particularly valuable for blue infrastructure development. **Riverside areas** along the Danube and smaller creeks can provide new green connections. Canalization of watercourses prohibited the direct contact with the city. Along the rivers flooding zones are built-up in many places, but outside of the city center river a natural riverbed revitalization is still possible [24].

The performance of **public parks** in the blue-green infrastructure is strongly influenced by the plant condition. Condition of less drought-tolerant species decays year by year – application of adaptive species and retention of rainwater or infiltration into the groundwater has an essential importance to retain ecosystem services. In contrast with Paris and Berlin Budapest has a lack of small city gardens and linear green spaces, which would have an important role in urban recreation and also in decentralized rainwater management in the dense urban structure.

3. Conclusion

Climate change and the heritage of old urban structure rise common challenges for the European metropolises. Different spatial situations of extent housing need adopted planning solutions. Best practice and realized projects shows broad possibilities of acting.

Most challenging areas are city centers with dense tenement housing. Application of permeable pavement, green roofs and green walls allowing for the traditional facades and roof-forms would provide reduced runoff and higher evaporation. Surrounding of 20th linear or prefabricated block buildings are suitable for even for measures with larger area demand like swales, retention ponds or rain gardens. Brownfields and riverside areas have the highest potential for new green space establishment and can also provide important linear elements of the blue-green infrastructure. Preserving of green space condition needs nevertheless providing good maintenance and the plant use adoption to the climate change.

Old European metropolises was designed to exploit the natural sources – transitioning extent housing into a water sensitive city needs radically new approaches and customized smart solutions. Our mentality has to be changed from consuming into adopting – the blue-green infrastructure is our tool for cheaper, safer and more livable cities.

References

[1] Alfieri L., Feyen L., Dottori F., Bianchi A., *Ensemble flood risk assessment in Europe under high end climate scenarios*, Global Environmental Change, 35, 2015, 199–212.

[2] UN Department of Economic and Social Affairs, *World Urbanization Prospects. The 2011 Revision*, ST/ESA/SER.A/322, UN Department of Economic and Social Affairs, 2012.

[3] Wilderer P.A., *Applying sustainable water management concepts in rural and urban areas: some thoughts about reasons, means and needs*, Water Sci. Technol. J. Int. Assoc. Water Pollut. Res., 49 (7), 2004, 8–16.

[4] Tenczer G., *index.hu*, http://index.hu/belfold/budapest/2013/06/12/3_2_milliardos_kart_okozott_budapesten_az_arviz/ (access: 24.11.2015).

[5] *BudapestCity.org*, http://budapestcity.org/02-tortenet/2013-arviz/index-hu.htm (access: 29.10.2015).

[6] Brown R.R. et al., *Transitioning to Water Sensitive Cities: Historical, Current and Future Transition States*, 11th International Conference on Urban Drainage, 2008.

[7] Geiger W.F. et al., *Neue Wege für das Regenwasser: Handbuch zum Rückhalt und zur Versickerung von Regenwasser in Baugebieten*, Oldenbourg, 2009.

[8] *Institut national de la statistique et des études économiques*, http://www.insee.fr/fr/themes/comparateur.asp?codgeo=DEP-75 (access: 03.05.2016).

[9] http://koeppen-geiger.vu-wien.ac.at/ (access: 02.05.2016).

[10] *Senatsverwaltung für Stadtentwicklung Abt. I – Stadt- und Freiraumplanung: Stadtentwicklungsplan Klima*, Senatsverwaltung für Stadtentwicklung und Umweltschutz, 2011.

[11] Mairie de Paris, *Le Livre Bleu*, 2012.

[12] BFVT Kft. et al., *Budapest környezeti állapotértékelése 2014*, Budapest Főváros Önkormányzatának Főpolgármesteri Hivatala Városüzemeltetési Főosztály, 2014.

[13] Kim S., *Paris-Plages: artificial beaches open along the Seine*, The Telegraph, 15:27.

[14] Wolter A., *Panke 2015 – Ein Bach wird naturnah*, Senatsverwaltung für Gesundheit, Umwelt und Verbraucherschutz, 2009.

[15] S.T.E.R.N. GmbH, *Modellvorhaben Block 103 – Endbericht zu den Investitionen und zur Begleitforschung*, 2015/2121, Adalbertstraße 95 A 10999 Berlin: FHXB Friedrichshain-Kreuzberg Museum, 1993.

[16] *Berliner Zeitung*, http://www.berliner-zeitung.de/berlin/baden-in-der-spree-warum-berlin-immer-noch-kein-flussbad-hat-22833132 (access: 27.03.2016).

[17] http://www.stadtentwicklung.berlin.de/umwelt/stadtgruen/gruenanlagen/de/gruenanlagen_plaetze/kreuzberg/gleisdreieck/index.shtml (access: 13.04.2016).

[18] Zettisch F., *Középsö ferencvárosi rehabilitáció*, Ferencvárosi Kal., 2006, 12–15.

[19] *Budapest Portál*, http://budapest.hu/Lapok/Budapest-Sz%C3%ADve-hivatalosan-is-%C3%A1tadt%C3%A1k-a-K%C3%A1roly-k%C3%B6rutat-%C3%A9s-a-M%C3%A1rcius-15.-teret.aspx (access: 18.04.2016).

[20] Salgó B. et al., *epiteszforum.hu*, http://epiteszforum.hu/park-a-gaton (access: 12.01.2016).

[21] Origo, http://www.origo.hu/foto/20110912-elkeszult-a-karoly-korut-felujitasa.html (access: 05.05.2016).
[22] *Pro Verde. Budapest zöldfelületi-rendszerének fejlesztési koncepciója és programja*, Budapest, 2006.
[23] Budapest Főváros Főpolgármesteri Hivatal, *Barnamezős területek fejlesztése tematikus fejlesztési program*, 2014.
[24] Budapest Főváros Önkormányzat, *Budapest Duna menti területeinek fejlesztési tanulmányterve*, 2013.

TECHNICAL TRANSACTIONS 1/2017
CZASOPISMO TECHNICZNE 1/2017
ENVIRONMENTAL ENGINEERING
DOI: 10.4467/2353737XCT.17.010.6107

Raja-Louisa Mitchell (raja-louisa.mitchell@tu-berlin.de)
Paul Uwe Thamsen
Chair of Fluid System Dynamics, Department of Fluid Dynamics and Technical Acoustics, Technische Universität Berlin

Michel Gunkel
Jan Waschnewski
Berliner Wasserbetriebe, Berlin, Germany

Investigations into wastewater composition focusing on nonwoven wet wipes

Badanie składu ścieków ze szczególnym uwzględnieniem chusteczek nawilżanych z włókniny

Abstract

This paper summarizes the problems caused for wastewater systems by changing wastewater composition, especially the increasing use of nonwoven wet wipes and their disposal via the toilet. The nonwoven wet wipes do not disintegrate in the sewer system as paper-based toilet does, but accumulate to large agglomerations that can block the system and clog pumps. This not only reduces the operational safety and stability of the wastewater system, but also costs the operator a lot of money. The paper introduces an approach to estimate the composition of wastewater and presents first results for the city of Berlin.

Keywords: wastewater composition, solids, wet wipes, clogging

Streszczenie

W artykule omówiono problemy występujące w sieciach kanalizacyjnych związane ze zmieniającym się składem ścieków, a zwłaszcza obecnością w ściekach chusteczek nawilżanych z włókniny wrzucanych do toalety. Chusteczki nawilżane wykonane z włókniny nie rozpadają się w kanalizacji tak jak papier toaletowy, ale tworzą skupiska, które mogą powodować niedrożność instalacji i rur, zagrażając bezpieczeństwu i stabilności eksploatacji sieci kanalizacyjnej i zwiększając koszty eksploatacyjne ponoszone przez operatora. W artykule przedstawiono metodę analizy składu ścieków i pierwsze wyniki uzyskane podczas badań przeprowadzonych w Berlinie.

Słowa kluczowe: skład ścieków, ciała stałe, chusteczki nawilżane, niedrożność

1. Introduction

1.1. Project KURAS – Concepts for urban stormwater management and wastewater systems

Urban water infrastructures are increasingly facing challenges resulting from climate change and demographic developments. Using Berlin as an example, the project KURAS (concepts for urban stormwater management and wastewater systems), which is supported by the Federal German Ministry for Education and Research, aims at demonstrating how future wastewater disposal, water quality, urban climate, and quality of life in the city can be improved through intelligently combined stormwater and wastewater management. The project consists of a network of partners from research, industry and public authorities as well as one public utility responsible for drinking water supply and wastewater disposal.

The KURAS project focusses on two main research areas: *Stormwater management* and *wastewater systems*.

Based on specific selection criteria (population, type of sewer system, pumping station etc.), the Berlin district Wilmersdorf (~260,000 inhabitants and 40,000 m^3 dry weather flow) was chosen as a model area for the focus *wastewater system* (shown in Figure 1). The wastewater in Wilmersdorf is collected partly in a combined sewer system and partly in a separate sewer system. This means measures in both sewer system types can be examined. The model area belongs to the catchment area of the main wastewater pumping station Wilmersdorf, which pumps the greatest part of the wastewater to the wastewater treatment plant (WWTP) Ruhleben.

The focus in the research area wastewater systems lies on operational and constructive measures in the sewage network to counter problems resulting from overload and underload in the system, using the model area Wilmersdorf as an example. Expected changes in demography, water consumption and climate until 2050 were defined for the model area, as they can result in an increase or reduction of the extent and frequency of overload and underload in the wastewater system.

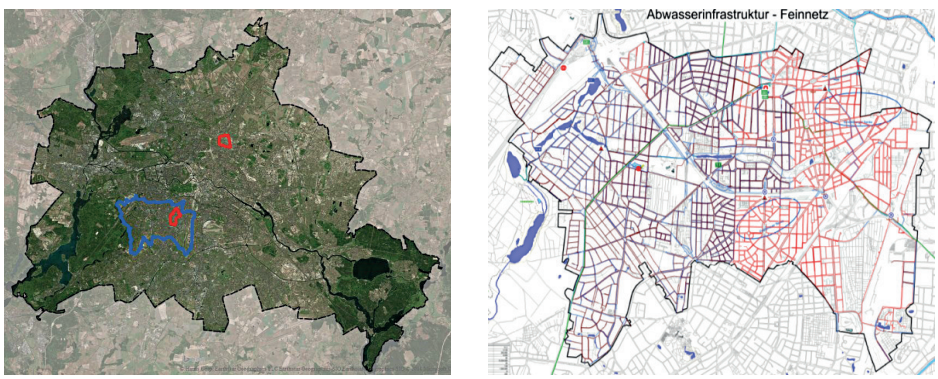

Fig. 1. Left: City of Berlin with the model catchment area "Wilmersdorf", used in the project KURAS, depicted in blue outline. Right: Detailed map of model area "Wilmesdorf" showing the sewers

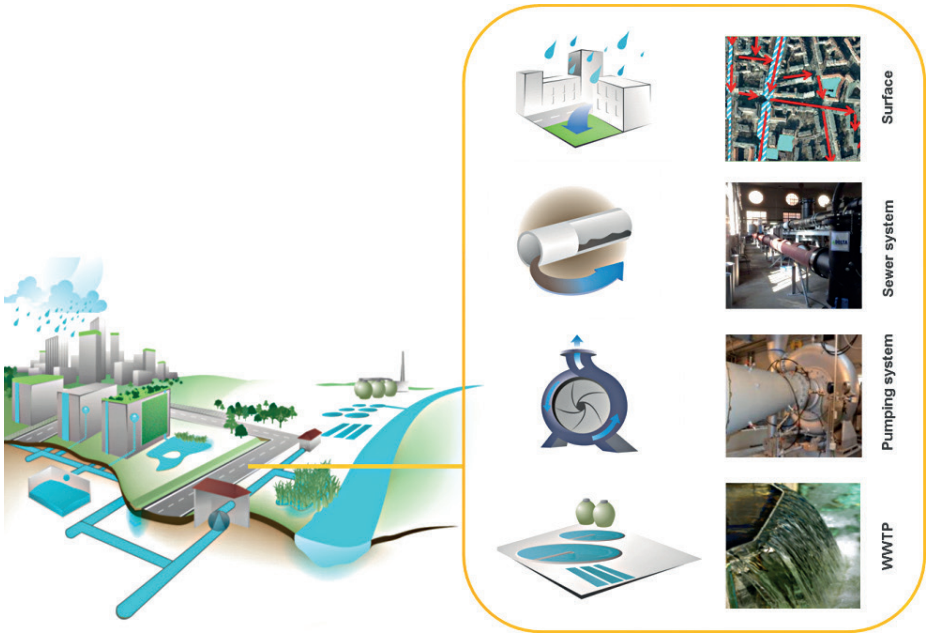

Fig. 2. Research focus areas in KURAS [picture: KURAS]

To systematically examine and identify the most effective measures for the sewage network (from the discharger to the WWTP) the system was divided into four research clusters: Surface, sewers, pumping system and wastewater treatment plant (as seen in Figure 2).

Currently, there are two main challenges confronting operators of wastewater systems. On the one hand, the growing gap between overload in the system due to extreme weather events and underload due to generally reduced wastewater amounts makes it hard to handle the large variations in flow. On the other hand, the use of toilets for the disposal of various products increasingly leads to problems in the wastewater system (e.g. blockages). Both challenges are explored in the research project KURAS. This paper will present an approach to investigate the composition of the solid fraction of wastewater, thereby providing valuable information for the operation of the wastewater infrastructure, especially the pumping systems.

1.2. Wastewater composition

The characteristic wastewater composition is well described from a chemical point of view. However, from a physical point of view, a description of wastewater, or its solid components, is lacking. To date, no description or standardisation regarding the physical properties of wastewater exists, let alone an approximation of the amount, type and composition of flushed products in the wastewater.

Nonetheless, wastewater operators throughout the world have seen a change in wastewater composition over the last years, due to a growing amount of wet wipes in the wastewater (some examples: [1–4]). These disposable wipes (baby wipes, cosmetic wipes and wet toilet paper wipes, examples are shown in Figure 3) are made of synthetic nonwoven textiles

and thus do not tear or disintegrate in the sewer system as toilet paper does. This means they can become knotted during the wastewater transport to form large conglomerates of textile materials which can cause system blockage, clogging and operational problems in the wastewater system. Sydney Water, e.g., removed about 1 million kilograms of wet wipes from its wastewater systems over the past two years [1].

On the one hand this disrupts operation and reduces the operational stability of the whole wastewater system. On the other hand, these blockages are a growing expense factor for wastewater operators (New York City, e.g., claims that more than $18 million have been spent during the past five years to remedy wipe-related problems in their 14 wastewater treatment plants [2]).

This problem has been discussed in the media in recent years, as the literature shows ([1–4]) but has hardly been researched scientifically yet. Due to this, scientific literature is still greatly lacking. An example are Karadagli et al. and Eren et al. [5, 6, 7] who researched the physical disintegration of wet wipes in the sewer system.

Fig. 3. Examples for wet wipes (wet toilet paper wipes, baby wipes, cosmetic wipes, hand wipes)

2. Methods

In Berlin, wet wipes are increasingly found in the wastewater system, too, for example in the sewers, in the layer of scum in the pump suction chambers and in the pumps themselves. For this reason, together with the Berliner Wasserbetriebe (the Berlin water utilities) the Department of Fluid System Dynamics at TU Berlin conducted a series of field studies in the KURAS model area Wilmersdorf to better assess the nature and amount of flushed materials.

Fig. 4. Impressions of wet wipes in the Berlin sewer system [pictures from TUB-FSD and BWB]

2.1. Field measurements

An extensive field measurement campaign was designed and samples were collected at two points (combined sewer system) within the KURAS model area Wilmersdorf.

To gain a representative overview of the constituents per m^3 wastewater, composite samples of wastewater (~2.8 m^3) were taken three times a day (morning, noon and afternoon) with a suction vehicle. Flaps on the nozzle of the suction hose ensured that all of the incoming wastewater was collected. The samples remained in the suction vehicle until the end of the day, so that the total mixed sample amounted to 8.3 m^3 (8.3 m^3 is the total volume of the suction vehicle). The total sample was then discharged into the sewer through a basket screen (mesh size ~ 5 mm^2). The basket screen retained all the solids contained in 8.3 m^3 wastewater. The solids were weighed and then a random grab sample was extracted from the total solids. The constituents of the random sample were analysed by a textile laboratory. Figure 5 and Figure 6 show the process of sampling.

In total 13 composite samples were collected over the course of one year, whereof 12 samples could be analysed using their weight in comparison to the total weight of the sample (one sample was not weighed in total. Therefore for this sample it was only possible to determine a percentage distribution of the different fractions, but not determine the specific weights). A more extensive measuring campaign with a greater amount of samples would have given a broader picture. However, due to financial and scheduling conflicts, the measuring campaign could not be continued in the project. A possible continuation is planned for the future.

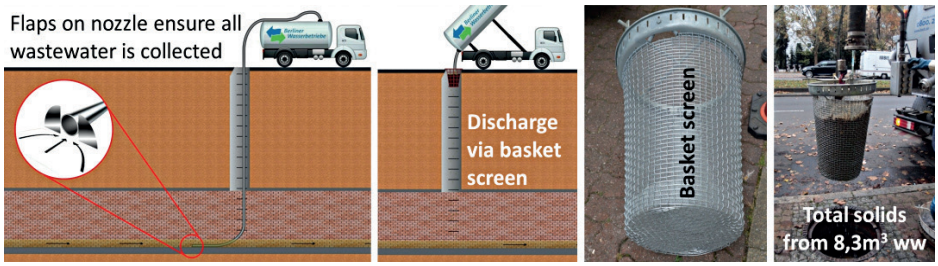

Fig. 5. From left to right: Wastewater being collected with the suction vehicle, wastewater being discharged into the sewers through the basket screen, basket screen, basket screen with solids captured from 8.3 m^3 of wastewater

Fig. 6. From left to right: Suction vehicle, wastewater being discharged into the basket screen, basket screen retaining the solid

The textile laboratory dried the samples and determined the dry weight of the total sample and each specific fraction (after separating the fractions by hand). The following fractions (dry weight) were analysed: plastics (foils and other plastics), textiles (fibres, threads, areas, nonwovens (drylaid nonwovens and spunbound nonwovens), composite materials, knitted fabrics, woven fabrics), paper (lumps, strands and areas), wood/leaves, rest (e.g. hair. cigarette butts etc.). Sediments were also analysed, however, as they are not in the focus of this investigation (they don't have the potential to clog pumps or screens), they were disregarded. An overview of the analysed fractions with their respective subcateogires is given in Table 1.

Table 1. Solid fractions anaylsed by the textile laboratory (with respective subcategories)

<table>
<tr><td colspan="6">Textiles</td><td colspan="3">Paper</td><td colspan="2">Plastics</td><td rowspan="6">Wood. leaves</td><td rowspan="6">Rest</td></tr>
<tr><td colspan="6">Fibres</td><td rowspan="5">Lumps</td><td rowspan="5">Strands</td><td rowspan="5">Areas</td><td rowspan="5">Foils</td><td rowspan="5">Others</td></tr>
<tr><td colspan="6">Threads</td></tr>
<tr><td colspan="6">Areas</td></tr>
<tr><td colspan="2">Nonwovens</td><td rowspan="2">Composite materials</td><td rowspan="2">Knitted fabrics</td><td rowspan="2">Woven fabrics</td></tr>
<tr><td>Dry-laid</td><td>Spun-bound</td></tr>
</table>

3. Initial results

The composition of the solids in the wastewater varies much more than initially thought. The samples were taken from May 2014 to June 2015 (not in the very cold winter months),

always on Mondays. It was expected that the solid fractions would be somewhat similar (due to same day of the week and same time of day of sampling), perhaps varying with the weather (rain events) and annual seasons. However, the compisition of the solids differed strongly and no correlation with weather or seasons could be inferred. Figure 7 shows the specific amount of solids for the 12 samples found per m^3 wastewater, divided into the analysed fractions (plastics, textiles, paper, wood/leaves and rest). The total amount of solids varies from 57.7 g/m^3 to 1109.3 g/m^3, with an average total amount of solids of 319 g/m^3 wastewater (as seen in Figure 8). The composition of the total solids (the amount of the individual fractions) also varies strongly. Paper (this fraction also includes wetlaid nonwoven fabrics, e.g. kitchen roll), is the fraction which has the largest range (from 0 g/m^3 to 886 g/m^3). The textiles, which were in the focus of this investigation, also show a large range, varying from 0 g/m^3 to 155 g/m^3.

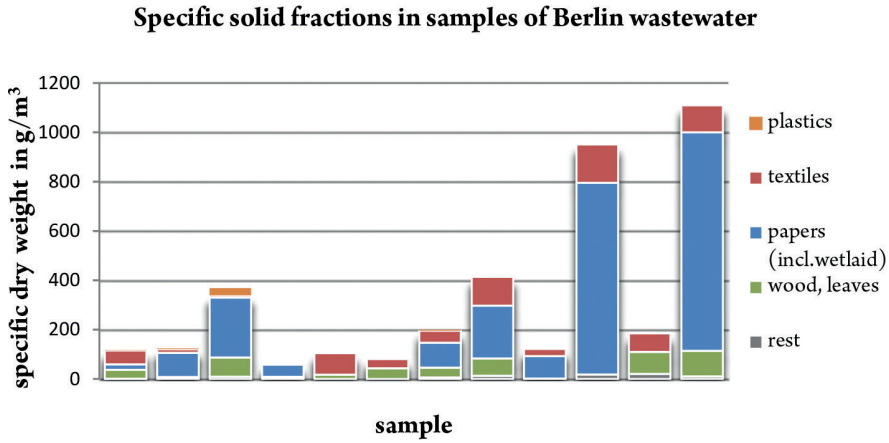

Fig. 7. Specific amount of solids per m^3 wastewater in samples of Berlin wastewater (based on 12 samples from two wastewater catchment areas. sampled from May 2014 to June 2015).

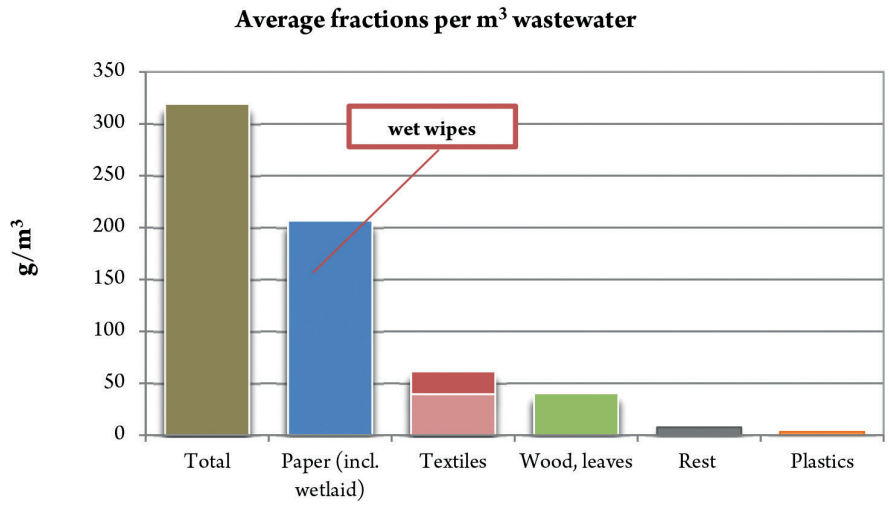

Fig. 8. Average fractions of solids per m^3 wastewater (based on 12 samples from two wastewater catchment areas, sampled from May 2014 to June 2015).

Figure 8 shows the average fractions of solids to be found in one m^3 of wastewater. As can be seen in Figure 7, it is hard to determine a meaningful average, as the total amount of samples is very small and the individual samples differ so much (and partly do not follow a clear normal distribution). Nonetheless, for the purpose of getting an idea of wastewater physical constituents, average values were calculated. Based on the existing samples, analyses and type of catchment (combined sewer system in residential urban area), it can be stated that on average one m^3 wastewater has a total amount of 319 g of solids per m^3 wastewater. These total solids are made up of 207 g of paper per m^3, 62 g of textiles per m^3 (of which 40 g are nonwoven wet wipes), 40 g of wood and leaves per m^3, 7.5 g of rests (e.g. cigarette butts or hair) and, finally, the smallest fraction are the plastics with an average of 3 g/m^3 wastewater.

Figure 9 shows the average percentage distributions of the solids. As can be seen, paper makes up the largest fraction with 45%, followed by the textile fraction (33%), the wood/ /leaves fraction (18%), the rests (3%) and finally the plastics with 1%. While paper is the largest fraction, it can be seen that the textiles are a relevant fraction as they make up a third of total wastewater solids. In the textile fraction, the nonwoven wet wipes make up the largest share (14% of total solids), followed by fibres (10% of total solids), composite materials, e.g. tampons or incontinence articles (8% of total solids) and finally threads with 1% of total solids.

A hotspot for pump clogging material to collect, is the layer of scum in suction chambers of pumping stations. After the routine flushing of the suction chamber (in most large Berlin pumping stations, e.g., at least once a day), this layer is broken up and the concentrated floating solids (paper, textiles) have to be pumped away. To get an impression of the solids collected in the layer of scum, a random sample was taken and analysed. The composition of this sample is pictured in Figure 10. As only one sample was taken in one pumping station, no general conclusions regarding the composition of the scum layer can be made. However, this example can be used to illustrate the possible constituents. As expected, the scum layer

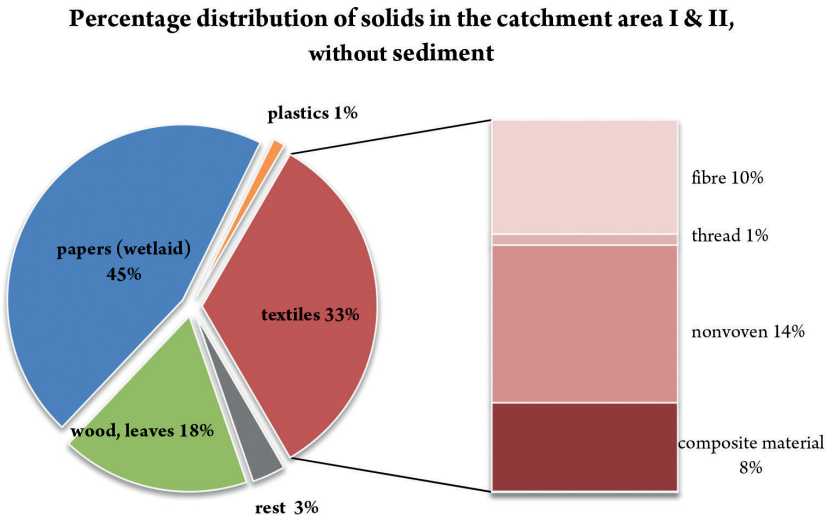

Fig. 9. Percentage distribution of solids (based on 12 samples from two wastewater catchment areas, sampled from May 2014 to June 2015)

comprises only floating solids. Paper made up the largest fraction (76%), which was mostly due to large amounts of wetlaid nonwovens (i.e. household kitchen roll), which is a paper, but not as soluble and readily degradable as toilet paper. Aside from minor amounts of plastic (1%) and some rests (1.8%), the textiles made up the remaining solids (21%). This textile portion was made up of 11% composite materials (e.g. incontinence articles, pictured in Figure 11), 8% nonwoven wet wipes (different sizes and types, e.g. spunbound nonwovens and drylaid nonwovens, examples shown in Figure 11), as well as minor amounts of other fabrics.

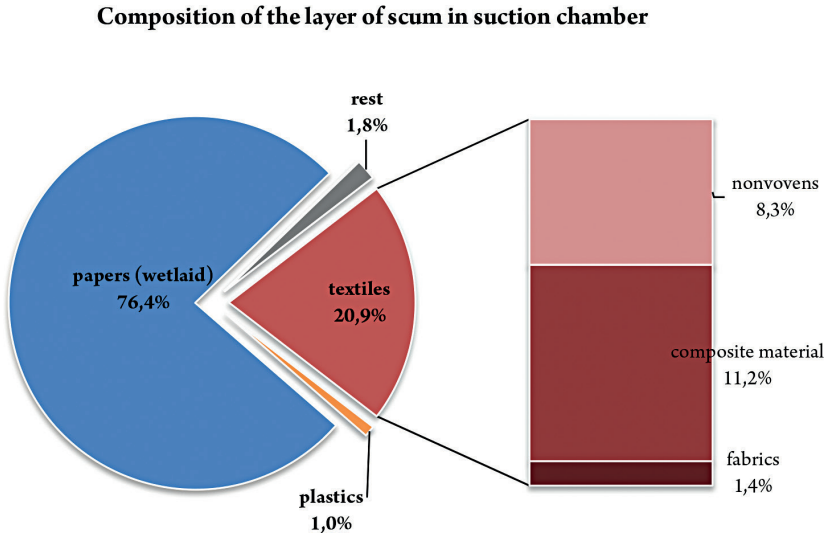

Fig. 10. Composition of the scum layer in a suction chambr of a pumping station (based on one random sample)

Fig. 11. Example constituents of scum layer in pumping station (based on one random sample), from top left to bottom right: paper lumps (paper), incontinence articles (composite materials), gauze (composite materials), wet wipes (different types, category nonwovens)

4. Conclusions

Based on the present data, it could be shown that textiles, and among them the wet wipes, which are currently causing so many problems in the wastewater system, are definitely a relevant category of wastewater solids. To be able to draw more general conclusions, further samples will be taken and analysed.

Furthermore it could be shown that the amount and composition of solids in wastewater vary immensely. To be able to correlate influencing factors with the wastewater solids, further field measurements are necessary.

4.1. Outlook

The field measurement campaign will be continued to collect further data. In addition to further samples taken from the sewers directly, "system hotspots" will be sampled. These include suction chambers of pumping stations, the screenings of wastewater treatment plants and the material clogging the pumps. This will give an insight into which wastewater constituents are the most damaging for our wastewater systems.

The presented results were established within the project KURAS, mainly funded by the German Ministry of Education and Research (BMBF) in the framework of the FONA (Research for Sustainable Development) initiative. The partners' contributions to the project's progress and various inputs to the paper are highly appreciated.

References

[1] Radulova L., *The 500 tonnes of putrid WET WIPES choking our cities' sewers... and comfort-loving MEN are to blame because they like the 'softer feel' in the bathroom*, http://www.dailymail.co.uk/news/article-3129319/Pictured-500-tonnes-putrid-piles-WET-WIPES-choking-cities-sewers-s-comfort-loving-MEN-blame-like-softer-feel-bathroom.html (access: 23.04.2016).

[2] Flegenheimer M., *Wet Wipes Box Says Flush. New York's Sewer System Says Don't...*, The New York Times, http://www.nytimes.com/2015/03/15/nyregion/the-wet-wipes-box-says-flush-but-the-new-york-city-sewer-system-says-dont.html?_r=1 (access: 23.04.2016).

[3] Bjorkman M., *Disposable Wipes Threaten Wastewater Systems*, Pumps & Systems, Issue September 2015.

[4] DWA, *Feuchttücher*, KA Betriebsinfo, Issue 01.2016, 2428–2434.

[5] Karadagli F., Rittman B. et al., *Effect of Turbulence on the Disintegration Rate of Flushable Consumer Products*, Water Environment Research, Issue May 2012.

[6] Karadagli F., Rittman B. et al., *Development of a Mathematical Model for Physical Disintegration of Flushable Consumer Products in Wastewater*, Water Environment Research, 81(5):459-65, June 2009.

[7] Eren B. et al., *Physical Disintegration of Toilet Papers in Wastewater Systems:Experimental Analysis and Mathematical Modeling*, Environ. Sci. Technol., 46, 2870–2876, January 2012.

TECHNICAL TRANSACTIONS 1/2017
CZASOPISMO TECHNICZNE 1/2017
ENVIRONMENTAL ENGINEERING
DOI: 10.4467/2353737XCT.17.011.6108

Daniel Venghaus (daniel.venghaus@tu-berlin.de)
Matthias Barjenbruch
Institute of Civil Engineering, Departement of Urban Water Management, Technische Universität Berlin

Microplastics in urban water management

Mikroplastiki a miejska gospodarka wodna

Abstract

The paper is discussing microplastics in the effluent of wastewater treatment plants and other discharges from urban areas. The aim of the discussion is to expose the challenges related to sampling and detecting plastic particles in treated wastewater. The different types of microplastics and a rough estimation of the amount of plastic which could end up in the aquatic environment is given. The work is based on a literature review of microplastic particles in treated wastewater and discusses their consequences on the aquatic ecosystem.

Keywords: microplastic, particle, sample, analytic

Streszczenie

W artykule omówiono problem obecności mikroplastików w cieczach odpływających z oczyszczalni ścieków i w innych cieczach pochodzących z obszarów miejskich w celu ujawnienia trudności związanych z pobieraniem próbek i wykrywaniem cząsteczek plastiku w ściekach. Określono różne rodzaje mikroplastików oraz szacowaną ilość plastiku, który może znajdować się w środowisku wodnym. Przeprowadzone prace oparto na przeglądzie piśmiennictwa na temat obecności mikrocząsteczek plastiku w ściekach i omówiono jej skutki dla ekosystemu wodnego.

Słowa kluczowe: mikroplastik, cząsteczka, próbka, analiza

1. Introduction

When Charles Goodyear randomly identified the process of vulcanization in 1839 the development of synthetic materials took its course. Later in the 1940's after nylon was introduced, plastics processing was practiced in mass production. [1, 2] In 2014 more than 311 mill. t of plastics where produced worldwide [3]. Germany produced 18.5 mill. t in 2015 out of this amount 12.8 mill. t where exported. Additionally, 9.3 mill. t where imported. This results in an overall plastic consumption of 15 mill. t in Germany. From this amount, 2.94 mill. t where mainly used in branches of gluten, fibers, vanish and 12.06 mill t in branches of packaging (35.2%), construction (22.7%) and automotive engineering (10.5%). Other branches and electronics, agriculture, households medicine and furniture use 31.6 %. This consumption results in about 3.7 mill. t of plastic waste in Germany. 53% of the plastic waste is utilized for energy and 46% for recycling. About 1% (0.04 mill. t) ends up on dumpsites [4]. Data on plastic littering is actually not available [5].

2. Basic Information about plastics

The most commonly used plastics are polyethylene (PE), polypropylene (PP), polyvinyl-chloride (PVC), polystyrene (PS) and polyethylenterephthalat (PET), which represent about 90% of the global plastic production [6]. Table 1 offers a survey of the attributes, the production volume and the possible uses of plastics.

Table 1. Attributes, production volume and the possible uses of plastics [7]

Sort	Abbreviation	Density [g/cm³]	% of the production volume	Possible uses
low-density polyethylen	PE-LD	0.91– 0.93	21	carrier bag, straw, bottle
high-density polyethylen	PE-HD	0.94	17	can, pipe
polypropylene	PP	0.83– 0.85	24	bottle top
polystyrene	PS	1.05	6	electronic casing, thermal insulation material, packaging
polyethylenterephthalat	PET	1.37	7	bottles
polyvinyl chloride	PVC	1.38	19	foil, pipe

It is shown that a large part of the produced plastic is used in different products and processes in all different ranges of application. Consequentially one big challenge is to define the pathways of plastics and microplastics which end up in the aquatic environment and to balance them.

3. Microplastics

Beside the subdividing particles in macro- and mesoplastics, the Marine Strategy Framework Directive (2008/56/EG) describes particles < 5 mm as microplastics [8].

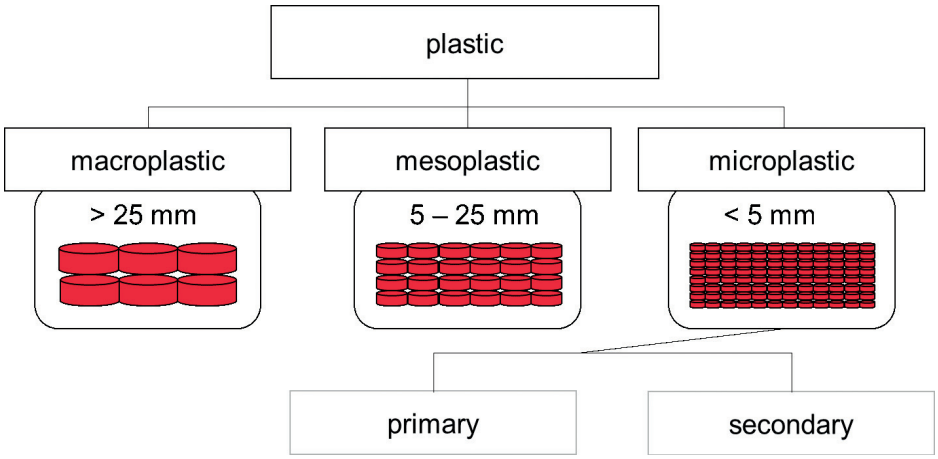

Fig. 1. Classification of plastic in the aquatic environment [8]

Microplastics occur in the aquatic environment as primary and secondary micropastic particles. Primary microplastic describes industrial defined and produced particles. They include for example pellets, which are used as basic material in the production of plastic products. [9] Another application is to use the microbeads as filler for cosmetics or as abrasives in toothpaste and peeling. To estimate the emission of microplastics from domestic wastewater the TU Berlin conducted panel tests. A group of customers (approx. 20 people) documented the usage and the volume of all critical products. For these tests primary microplastics from shampoo (Fig. 2a), peeling (Fig. 2b) and toothpaste (Fig. 2c) were separated and balanced out. The proportions of the particles are shown in Figure 2.

For the input of microplastics raised by the named products from domestic wastewater an amount of approximately 7.5 g/(person · a) was determined [10].

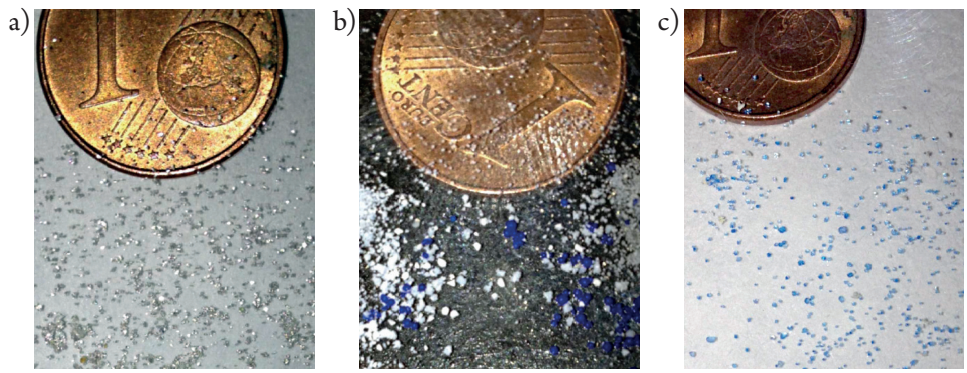

Fig. 2. Microplastics from shampoo (a), peeling (b), toothpaste (c) [10]

a) b)

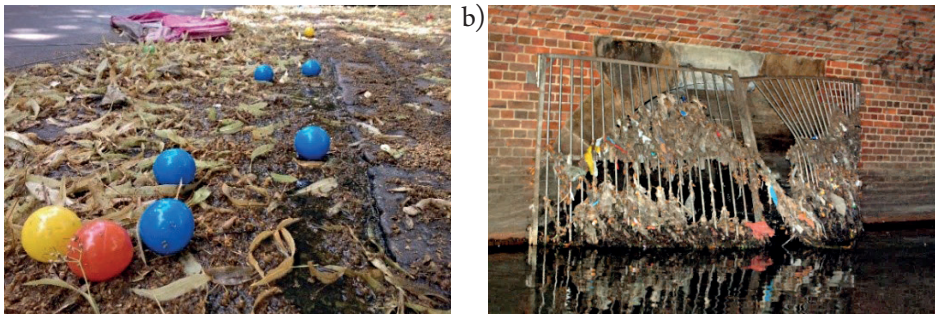

Fig. 3. Plastic in rainwater runoff (a) and mixed sewage water (b) in Berlin

Secondary microplastic describes fragments or fibers which rise by biological, chemical or physical degradation of sizeable particles [9]. Consequently, microplasticparticles occur in different size, form and colour. Figure 3 shows macroplastics in the effluent of rainwater runoff (Fig. 3a) and in a mixed sewage water system (Fig. 3b) which could end up as grinded microplastics in the aquatic environment.

4. Microplastics in the aquatic environment

Plastic debris in the aquatic ecosystem amount to 80% of the total waste [11]. Because of its low density and its durability plastic is transported over wide distance by the rivers and the wind [12] so that it has been found on isolated islands, the Arctic and Antarctic zone [13]. Two big garbage patches developed in the North Pacific and the North Atlantic Ocean. The great Pacific garbage patch, which was discoverded in 1997 is approximatly as big as central Europe and it is estimated to contain 1 million plastic particles and parts per square kilometer [11]. Except for the garbage patches, microplastics are urbiquitary in the aquatic environment, which has been indicated in scientific studies in the recent past [14, 6].The plastic debris in the oceans increased to 80% from land [7, 15]. A reasonable part is transported by rivers to the oceans however only a few studies have been conducted [16, 17].

The consequences of the urbiquitary plastic load on the aquatic ecosystem is diverse; in comparison to natural flotsam such as wood; the plastic parts and particles can act as carriers, which can transport attached organisms over wide distances far away from their geographical origin. The introduced organisms may suppress the native species and influence or change the ecosystem [18].

In 2012 an interaction between plastic debris in the ocean was registered with 663 marine animal species, this discribes an increase of 40% in comparison to the year 1997. In more than 50% of the cases living organism become entangled to the debris or they absorb them. Meanwhile, different kinds, forms and sizes of plastic particles are found meanwhile in stomachs of mammals, fishes and birds [19].

Planktivorus animals ingest microplastics with their nourishment beside microplastics was verified in shrimps, which absorbed zooplankton with microplastics [20] and in mussels which transferred microplastics to crabs [21].

In this manner microplastics could enter the food chain and spread in the food web [22, 23, 24]. Absorbed microplastics can have different effects. Experiments with mussels showed that microplastics accumulate in the mussel and cause inflammatory changes of the cells [11]. Especially because the experiment was performed under conditions with high microplastic concentrations. It is yet to be verified up to what extend the results are transferable in the environment [5].

Often non - digestible plastic particles are not excreted, so that the animals starve with stuffed stomach. Sharp edged particles may harm the mucosa of the animals. In addition to the mechanical characteristics microplastic particles may transport harmful substances like plasticizer or adsorbed persistant substances. They possibly escape from the plastic in the alimentary canal and have an effect on the organism. Some of them are carcinogenic or mutagenic or they can affect the hormonal balance [11].

Currently, coherent toxicology methods for the evaluation of microplastics (especially for particles with few µm) are missing.

5. Microplastics in Urban Water Management

Figure 4 indicates that the different pathways of microplastics are complex although a balancing of the pathways has not been performed so far. Decreasing microplastic particle concentrations have been verified over the treatment stations of a wastewater treatment plant (WWTP) and in the ocean [25]. The plastic tyre wear particles are assumed to be

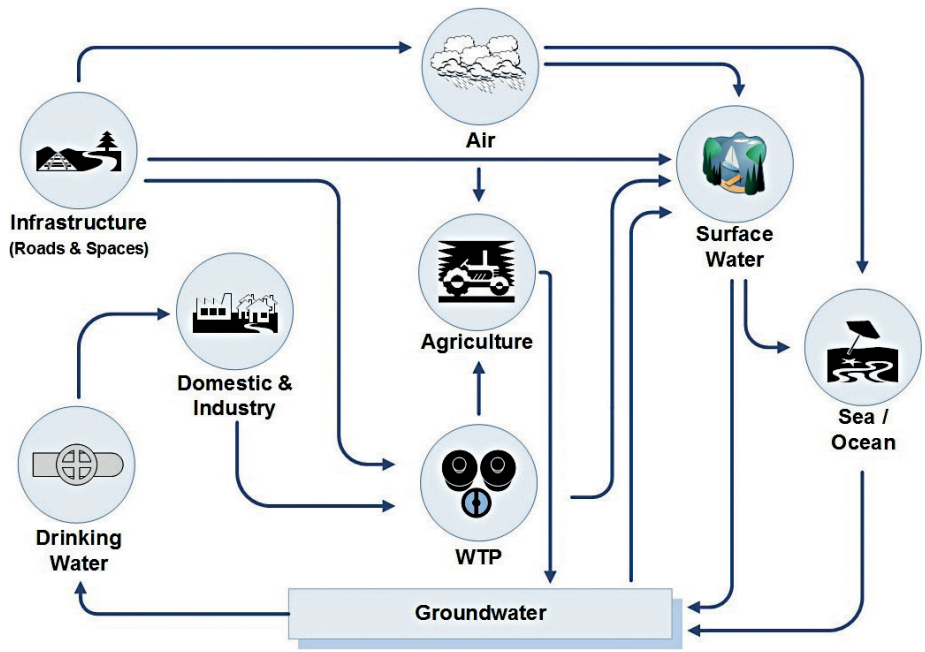

Fig. 4. Pathways of microplastics in the aquatic environent

a part of the fine particulate matter and the rain water runoff. Furthermore, the consumption of private households and the usage in industrial production processes may contribute microplastic particles to the aquatic environment.

In urban water management microplastics can get to the aquatic environment through the following pathways in principal :

1. If microplastics are not restrained sufficiently in wastewater treatment
2. By combined wastewater overflow
3. By discharging rainwater runoff

Currently, only a few studies about the microplastic exposure and –removal in WWTP are available. New studies in Finnland, Germany, Russia, Austria, Sweden and USA found different quantities of microplastics in the purification process of the WWTP. The results differ widely in terms of validity and resilience, because different techniques of sampling, preparation and analytical equipment was used as shown in Table 2.

Table 2. Microplastics at the effluent of wastewater treatment plants (WWTP) [25, 26, 27, 28, 29, 30]

Location	Sample volume	Sampling equipment	Particle / l	Analytical equipment
WWTP in Finland [25]	2–285 l	filtertube: Ø= 60 mm mesh size: 20 µm, 100 µm, 200 µm	8.6 ± 2,5 particles 4.9 ± 1,4 fibres	optical microscope
12 WWTPs in Germany [26]	390–1000 l	sieve with mesh size: 500 µm stainless steel candle filter with mesh size: 10 µm	0.077–0.712 (8.85 l) (particles < 500 µm) 0–0.052 (particles > 500 µm) 0.098–4.808 (fibers)	optical microscope, ATR – FTIR* micro – FTIR
WWTP in Russia [27]	8 l	filtertube: Ø= 60 mm mesh size: 20 µm,100 µm, 300 µm	16 fibrous 7 synthetic 125 black	optical microscope
WWTP in Austria [28]	20000 l	sieve batch with 3 sieves mesh size: 63 µm, 630 µm, 5 mm	Less than 0.001 (particles > 63 µm)	optical microscope
WWTP in Sweden [29]	1000 l	filter holder/net: Ø= 80 m mesh size: 300µm	3.75 ± 1.25 fragments 0.5 ± 0.5 flakes 4 ± 0.58 fibers (particles ≥ 300 µm)	optical microscope, ATR – FTIR
7 WWTPs in USA [30]	189000– –95700000 l	stack of 3 (4) sieves mesh size: (20µm), 45 µm, 180 µm, 400 µm surface skimmer with mesh size: 125 µm	0 particles 0 fibers $(3.12*10^{-7}–2.43*10^{-6})$ particles skimmed	optical microscope FTIR

*ATR-FTIR: Attenuated Total Reflectance- Fourier Transformed Infrared

The studies refer to sample volumes of WWTP -effluent from 2 up to 9570000 l, the filtration process is performed with mesh size from 10 µm up to 5 mm and for taking the samples measuring cups are taken as well as different pumps at the same time [25, 26, 27, 28, 29, 30]. Mintening et al. reveals that the method for taking the samples as well as the preparation of the samples may affect the contamination of the sample with microplastics by the atmosphere and laboratory equipment significantly. Fourier Transformed Infrared (FTIR) is widely prefered for analysing microplastic particles. It allows for the determination of the type of plastic after the sample has been prepared [26]. The number of particles can be counted whereas the mass can not be determined because the FTIR focuses on the material.

To estimate the weight percent of microplastics which may summed up in the effluent of WWTP the following contemplation is made:

The particles are spherical, have an average size of 1000 µm and consist of mostly utilized plastic PE. From the maximum concentration of 0.712 pcs/l, which is described for the German WWTPs in Table 2, results a weight percent of microplastics of 0.34 mgTSS/l.

Making an assumption that 12 mg TSS/l is the average mass of suspended solids at the effluent of a WWTP, the plastic fraction would sum up at least 3% and could be neglected related to the mass. However, a distribution of the particle size does not exist.

A benchmark for technologies of advanced wastewater treatment with the focus on microplastics has not been formulated yet. In an first measurement Mintening et al. 2014 determined for the final filtration, where cloth filtration media is installed, a reduction of 97% of microplastics. In the whole purification process of the WWTP in Russia, Talvitie et al. determined a quantity reduction of 96% for microplastics and for the whole purificaton process of the Swedish WWTP Magnusson et al. determined a reduction of 99,9% for the American WWTPs Carr et al. suggests that the effluent discharges of microplastics are minimal. Current studies emanate from significant amounts of microplastic particles remaining in the sluge [26, 29].There is a further need of research for this fraction to get verifiable results. Concerning the entry from combined wastewater overflow and discharged rainwater runoff currently there is no data available. In addition, for raw sewage any valid concentrations are identified so that the degree of degradation for microplastics can just be estimated.

6. Conclusions

The first studies about microplastics in wastwater treatment plans suggest that the restrained grade of microplastic particles during the purification process is considerable.

To evaluate the particles at the effluent of a WWTP as a basis of deciding whether or not to implement advanced wastewater treatment is mainly depending on the ecological relevance of the particles (size, mass, number, etc.) which is not fully clarified.

Technical solutions for the effluent of WWTPs and for combined wastewater overflow, could be the istallation of additional processes like for example micro sives, cloth filtration and sand filtration, which separate particles, specificly microplastics. In terms of this technologies, high performance webs and the cloth filtration media are promising solutions.

To separate microplastics form rainwater runoff decentralized systems could be implemented in road gullys at relevant sites. The different technics are currently evaluated in practical investigations (-OEMP- Optimized materials and processes for the separation of microplastic form the water cycle, BMBF-funded).

Plastics and microplastics will be preserved in the environment for many years, therefore systematic studies in the field of urban water management are reasonable and the municipality, the industry, the research and the citizen/consumer are requested to collaborate.

References

[1] Strong A.B., *Plastics: Materials and Processing*, 3 edition, Prentice Hall, New Jersey 2006.

[2] Braun D., *Kleine Geschichte der Kunststoffe,* Carl Hanser Verlag, München 2013.

[3] Statista, *Weltweite und europäische Produktionsmenge von Kunststoff in den Jahren 1950 bis 2014 (in Millionen Tonnen)*, http://de.statista.com/statistik/daten/studie/167099/umfrage/weltproduktion-von-kunststoff-seit-1950/ (access: 18.04.2016).

[4] Consultic Marketing & Industrieberatung GmbH 63755 Alzenau Germany, *Produktion, Verarbeitung und Verwertung von Kunststoffen in Deutschland 2015 – Kurzfassung*, http://www.plasticseurope.de/Document/studie-zu-produktion-verarbeitung-und-verwertung-von-kunststoffen-in-deutschland-2013---kurzfassung.aspx?FolID=2 (access: 25.11.2016).

[5] Bannick C.G., Brand K., Jekel M., König F., Miklos D., Rechenberg B., *Kunststoffe in der Umwelt*, article in Korrespondenz Abwasser, vol. 62 (1), 2015, 34–39.

[6] Sul J., Costa M., *The present and future of microplastic pollution in the marine environment*, Environmental Pollution, 185, 2014, 352–364.

[7] Andrady A.L., *Microplastics in the marine environment*, Marine Pollution Bulletin, 62, No. 8, 2011, 596–1605.

[8] Essel R., Engel L., Carus M., Ahrens R.H., *Quellen für Mikroplastik mit Relevanz für den Meeresschutz in Deutschland*, Text 63/2015 UBA, http://www.umweltbundesamt.de/publikationen/quellen-fuer-mikroplastik-relevanz-fuer-den (access: 18.04.2016).

[9] Hidalgo-Ruz V., Gutow L., Thompson R.C., Thiel M., *Microplastics in the Marine Environment: A Review of the Methods Used for Identifcation and Quantifcation*, Environmental Science & Technology, 46, No. 6, 2012, 3060–3075.

[10] Feller L., *Bilanzierung von Mikroplastik in Haushaltsabwasser,* Bachelor Thesis im bachelor degree course civil engineering at the department Siedlungswasserwirtschaft at the TU Berlin, release 25.02.2015, first supervisor: Barjenbruch Matthias, second supervisor Venghaus Daniel.

[11] Holm P., Schulz G., Athanasopulu K., *Meeresverschmutzung der neuen Art: Mikroplastik - ein unsichtbarer Störnfried*, Biologie unserer Zeit, 43, No. 1, 2013, 27–33.

[12] Hammer J., Kraak M.H., Parsons J.R., *Plastics in the marine environment: The dark side of a modern gift*, Reviews of Environmental Contamination and Toxicology, 220, 2012, 1–44.

[13] Lubbadeh J., *Der junge Mann und das Meer*, Technology Review, No. 7, 2014, 26–33.
[14] Cole M., Lindeque P., Halsband C., Galloway T.S., *Microplastics as contaminants in the marine environment: A review*, Marine Pollution Bulletin, 62 , No. 12, 2011, 2588–2597.
[15] Wagner M., Scherer C., Alvarez-Muñoz D., Brennholt N., Bourrain X., Buchinger S., Fries E., Grosbois C., Klasmeier J., Marti T., Rodriguez-Mozaz S., Urbatzka R., Vethaak A., Winther-Nielsen M., Reifferscheid G., *Microplastics in freshwater ecosystems: What we know and what we need to know*, Environmental Sciences Europe, 26, 12, 2014, DOI:10.1186/s12302-014-0012-7.
[16] Moore C.J., Lattin G.L., Zellers A.F., *Quantity and type of plastic debris flowing from two urban rivers to coastal waters and beaches of Southern California*, Journal of Integrated Coastal Zone Management, 11, No. 1, 2011, 65–73.
[17] Rech S., Macaya-Caquilpán V., Pantoja J.F., Rivadeneira M.M., Jofre Madariaga D., Thiel M., *Rivers as a source of marine litter. A study from the SE Pacific*, Marine Pollution Bulletin, 82, No. 1-2, 2014, 66–75.
[18] Gregory M.R., *Environmental implications of plastic debris in marine settings – entanglement, ingestion, smothering, hangers-on, hitch-hiking and alien invasions*, Philosophical Transactions of the Royal Society, B: Biological Sciences, 364, 2009, 2013–2025.
[19] Umweltbundesamt, *Auswirkungen von Meeresmüll.*, http://www.umweltbundesamt.de/sites/default/files/medien/419/dokumente/auswirkungen_von_meeresmuell.pdf, Version: 2013 (access: 18.04.2016).
[20] Setälä O., Fleming-Lehtinen V., Lehtiniemi M., *Ingestion and transfer of microplastics in the planktonic food web*, Environmental Pollution, 185, 2014, 77–83.
[21] Farell P., Nelson K., *Trophic level transfer of microplastic: Mytilus edulis (L.) to Carcinus maenas (L.)*, Environmental. Pollution, 177, 2013, 1–3.
[22] Wright S.L., Thompson R.C., Galloway T.S., *The physical impacts of microplastics on marine organisms: A review*, Environmental Pollution, 178, 2013, 483–492.
[23] Miranda D.d.A., de Carvalho-Souza G.F., *Are we eating plastic-ingesting fish?*, Marine Pollution Bulletin, 103, 2016, 109–114.
[24] Rochman C.M., Tahir A., Williams S.L., Baxa D.V., Lam R., Miller J.T., Teh F.C., Werorilangi S., Teh S.J., *Anthropogenic debris in seafood: Plastic debris and fibers from textiles in fish and bivalves sold for human consumption*, Scientific Reports, 5, 14340, 2015, DOI:10.1038/srep14340.
[25] Talvitie J., Heinonen M., Paakkonen J.P., Vahtera E., Mikola A., Setala O., Vahala R., *Do wastewater treatment plants act as a potential point source of microplastics? Preliminary study in the coastal Gulf of Finland, Baltic Sea*, Water Science Technologie, 72(9), 2015, 1495–1504, DOI:10.2166/wst.2015.360.
[26] Mintening S., Int-Veen I., Löder M., Gerdts G., *Mikroplastik in ausgewählten Kläranlagen des Oldenburgisch Ostfriesischen Wasserverbandes (OOWV) in Niedersachsen. Probenanalyse mittels Mikro-FTIR Spektroskopie. Abschlussbericht*, http://www.awi.de/fileadmin/user_upload/News/Press_Releases/2014/4_Quartal/Mikroplastik_Klaeranlagen/Abschlussbericht_Mikroplastik_in_Klaeranlagen.pdf (access: 18.04.2016).

[27] Talvitie J., Heinonen M., *HELCOM 2014 – Base project 2012-2014: Preliminary study on synthetic microfibers and particles at a municipal wastewater treatment plant*, http://www.helcom.fi/Lists/Publications/Microplastics at a municipal waste water treatment plant.pdf (access: 18.04.2016).
[28] Kreuzinger N., *Mikroplastik in der aquatischen Umwelt. Die Rolle der Kläranlage*, presentation of the Technischen Universität Wien, Institut für Wassergüte, Ressourcenmanagement und Abfallwirtschaft, Wien 2014.
[29] Magnuson K., Norén F., *Screening of microplastic particles in and down-stream a wastewater treatment plant*, http://www.diva-portal.org/smash/get/diva2:773505/FULLTEXT01.pdf (access: 18.04.2016).
[30] Carr S.A., Liu J., Tesoro A.G., *Transport and fate of microplastic particles in wastewater treatment plants*, Water Research, 91, 2016, 174–182, http://dx.doi.org/10.1016/j.atres.2016.01.002.

TECHNICAL TRANSACTIONS 1/2017
CZASOPISMO TECHNICZNE 1/2017
MATHEMATICS
DOI: 10.4467/2353737XCT.17.012.6109

Ludwik Byszewski (lbyszews@pk.edu.pl)
Institute of Mathematics, Faculty of Physics, Mathematics and Computer Science, Cracow University of Technology

An abstract nonlocal functional-differential second order evolution problem

Abstrakcyjne nielokalne funkcjonalno-różniczkowe ewolucyjne zagadnienie rzędu drugiego

Abstract

The aim of the paper is to prove two theorems on the existence and uniqueness of mild and classical solutions of a semilinear functional-differential evolution second order equation together with nonlocal conditions. The theory of strongly continuous cosine families of linear operators in a Banach space is applied. The paper is based on publications [1–9] and is a generalization of paper [6].

Keywords: nonlocal, second order, functional-differential, evolution problem, Banach space

Streszczenie

W artykule udowodniono dwa twierdzenia o istnieniu i jednoznaczności całkowych i klasycznych rozwiązań semiliniowego funkcjonalno-różniczkowego zagadnienia ewolucyjnego rzędu drugiego z warunkami nielokalnymi. W tym celu zastosowano teorię rodziny cosinus liniowych operatorów w przestrzeni Banacha. Artykuł bazuje na publikacjach [1–9] i jest pewnym uogólnieniem publikacji [6].

Słowa kluczowe: nielokalne, rzędu drugiego, funkcjonalno-różniczkowe, zagadnienie ewolucyjne, przestrzeń Banacha

1. Introduction

In this paper, we consider the abstract nonlocal semilinear functional-differential second order Cauchy problem

$$u''(t)=Au(t)+f(t,u(t),u(a(t)),u'(t)),\ t\in(0,T], \tag{1}$$

$$u(0)=x_0, \tag{2}$$

$$u'(0)+\sum_{i=1}^{p}h_iu(t_i)=x_1, \tag{3}$$

where A is a linear operator from a real Banach space X into itself, $u:[0,T]\to X$, $f:[0,T]\times X^3\to X$, $a:[0,T]\to[0,T]$, $x_0,x_1\in X$, $h_i\in\mathbb{R}$ $(i=1,2,...,p)$ and $0<t_1<t_2<...<t_p\le T$.

We prove two theorems on the existence and uniqueness of mild and classical solutions of problem (1)–(3). For this purpose we apply the theory of strongly continuous cosine families of linear operators in a Banach space. We also apply the Banach contraction theorem and the Bochenek theorem (see Theorem 1.1 in this paper).

Let A be the same linear operator as in (1). We will need the following assumption:

Assumption (A_1). Operator A is the infinitesimal generator of a strongly continuous cosine family $\{C(t):t\in\mathbb{R}\}$ of bounded linear operators from X into itself.

Recall that the infinitesimal generator of a strongly continuous cosine family $C(t)$ is the operator $A:X\supset D(A)\to X$ defined by

$$Ax:=\frac{d^2}{dt^2}C(t)x\big|_{t=0},\ x\in D(A),$$

where

$$D(A):=\{x\in X:\ C(t)x \text{ is of class } C^2 \text{ with respect to } t\}.$$

Let

$$E:=\{x\in X:\ C(t)x \text{ is of class } C^1 \text{ with respect to } t\}.$$

The associated sine family $\{S(t):t\in\mathbb{R}\}$ is defined by

$$S(t)x:=\int_0^t C(s)x\,ds,\ x\in X,\ t\in\mathbb{R}.$$

From Assumption (A_1) it follows (see [9]) that there are constants $M\ge1$ and $\omega\ge0$ such that

$$\|C(t)\|\le Me^{\omega|t|} \quad \text{and} \quad \|S(t)\|\le Me^{\omega|t|} \quad \text{for} \quad t\in\mathbb{R}.$$

We also will use the following assumption:

Assumption (A_2). The adjoint operator A^* is densely defined in X^* that is, $\overline{D(A^*)}=X^*$.

The paper is based on publications [1–9] and is a generalization of paper [6].

For convenience of the reader, a result obtained by J. Bochenek (see [2]) will be presented here. Let us consider the Cauchy problem

$$u''(t) = Au(t) + h(t), \quad t \in (0,T], \tag{4}$$

$$u(0) = x_0, \tag{5}$$

$$u'(0) = x_1. \tag{6}$$

A function $u : [0, T] \to X$ is said be a classical solution of the problem (4)–(6) if

(a) $$u \in C^1([0,T],X) \cap C^2((0,T],X),$$

(b) $$u(0) = x_0 \quad \text{and} \quad u'(0) = x_1,$$

(c) $$u''(t) = Au(t) + h(t) \quad \text{for} \quad t \in (0,T].$$

Theorem 1.1. *Suppose that:*
(i) *Assumptions* (A_1) *and* (A_2) *are satisfied,*
(ii) $h : [0, T] \to X$ *is Lipschitz continuous,*
(iii) $x_0 \in D(A)$ *and* $x_1 \in E$.
Then u given by the formula

$$u(t) = C(t)x_0 + S(t)x_1 + \int_0^t S(t-s)h(s)ds, \quad t \in [0,T],$$

is the unique classical solution of the problem (4)–(6).

2. Theorem on mild solutions

A function u belonging to $C^1([0, T], X)$ and satisfying the integral equation

$$u(t) = C(t)x_0 + S(t)x_1 - S(t)\left(\sum_{i=1}^{p} h_i u(t_i)\right)$$

$$+ \int_0^t S(t-s) f(s, u(s), u(a(s)), u'(s))ds, \quad t \in [0,T],$$

is said to be a mild solution of the nonlocal Cauchy problem (1)–(3).

Theorem 2.1. *Suppose that:*
(i) *Assumption* (A_1) *is satisfied,*
(ii) $a : [0, T] \to [0, T]$ *is of class* C^1 *on* $[0, T]$, $f : [0, T] \times X^3 \to X$ *is continuous with respect to the first variable* $t \in [0, T]$ *and there exists a positive constant* L_1 *such that*

$$\|f(s,z_1,z_2,z_3)-f(s,\tilde{z}_1,\tilde{z}_2,\tilde{z}_3)\|\le L_1\sum_{i=1}^{3}\|z_i-\tilde{z}_i\| \quad for \quad s\in[0,T],\ z_i,\tilde{z}_i\in X \quad (i=1,2,3),$$

(iii) $2C\left(2TL_1+\sum_{i=1}^{p}|h_i|\right)<1,$

where $C:=\sup\{\|C(t)\|+\|S(t)\|+\|S'(t)\|:t\in[0,T]\},$

(iv) $x_0\in E \quad and \quad x_1\in X.$

Then the nonlocal Cauchy problem (1)–(3) *has a unique mild solution.*

Proof. Let the operator $F:C^1([0,T].X)\to C^1([0,T],X)$ be given by

$$(Fu)(t)=C(t)x_0+S(t)x_1-S(t)\left(\sum_{i=1}^{p}h_iu(t_i)\right)$$

$$+\int_0^t S(t-s)f(s,u(s),u(a(s)),u'(s))ds,\ \ t\in[0,T].$$

Now, we shall show that F is a contraction on the Banach space $C^1([0,T],X)$ equipped with the norm

$$\|w\|_1:=\sup\{\|w(t)\|+\|w'(t)\|:t\in[0,T]\}.$$

To do this, observe that

$$\|(Fw)(t)-(F\tilde{w})(t)\|=\left\|S(t)\left(\sum_{i=1}^{p}h_i(\tilde{w}(t_i)-w(t_i))\right)\right.$$

$$\left.+\int_0^t S(t-s)(f(s,w(s),w(a(s)),w'(s))-f(s,\tilde{w}(s),\tilde{w}(a(s)),\tilde{w}'(s)))ds\right\|$$

$$\le C\left(\sum_{i=1}^{p}|h_i|\right)\|w-\tilde{w}\|_1$$

$$+\int_0^t\|S(t-s)\|L_1\left(\|w(s)-\tilde{w}(s)\|+\|w(a(s))-\tilde{w}(a(s))\|+\|w'(s)-\tilde{w}'(s)\|\right)ds$$

$$\le C\left(2TL_1+\sum_{i=1}^{p}|h_i|\right)\|w-\tilde{w}\|_1$$

and

$$\|(Fw)'(t)-(F\tilde{w})'(t)\|=\left\|S'(t)\left(\sum_{i=1}^{p}h_i(\tilde{w}(t_i)-w(t_i))\right)\right.$$

$$+\int_0^t C(t-s)(f(s,w(s),w(a(s)),w'(s))-f(s,\tilde{w}(s),\tilde{w}(a(s)),\tilde{w}'(s)))ds\Big\|$$

$$\leq C\left(\sum_{i=1}^{p}|h_i|\right)\|w-\tilde{w}\|_1$$

$$+\int_0^t \|C(t-s)\|L_1\left(\|w(s)-\tilde{w}(s)\|+\|w(a(s))-\tilde{w}(a(s))\|+\|w'(s)-\tilde{w}'(s)\|\right)ds$$

$$\leq C\left(2TL_1+\sum_{i=1}^{p}|h_i|\right)\|w-\tilde{w}\|_1, \quad t\in[0,T].$$

Consequently

$$\|Fw-F\tilde{w}\|_1 \leq 2C\left(2TL_1+\sum_{i=1}^{p}|h_i|\right)\|w-\tilde{w}\|_1 \quad \text{for} \quad w,\tilde{w}\in C^1([0,T],X).$$

Therefore, in space $C^1([0,T],X)$ there is the only one fixed point of F and this point is the mild solution of the nonlocal Cauchy problem (1)–(3). So, the proof of Theorem 2.1 is complete.

Remark 2.1. The application of a Bielecki norm in the proof of Theorem 2.1 does not give any benefit.

3. Theorem about classical solutions

A function $u:[0,T]\to X$ is said to be a classical solution to the problem (1)–(3) if

(a) $$u\in C^1([0,T],X)\cap C^2(([0,T],X),$$

(b) $$u(0)=x_0 \quad \text{and} \quad u'(0)+\sum_{i=1}^{p}h_i u(t_i)=x_1,$$

(c) $$u''(t)=Au(t)+f(t,u(t),u(a(t)),u'(t)) \quad \text{for} \quad t\in[0,T].$$

Theorem 3.1. *Suppose that:*
(i) *Assumptions* (A_1) *and* (A_2) *are satisfied, and* $a:[0,T]\to[0,T]$ *is of class* C^1 on $[0,T]$.
(ii) *There exists a positive constant* L_2 *such that*

$$\|f(s,z_1,z_2,z_3)-f(\tilde{s},\tilde{z}_1,\tilde{z}_2,\tilde{z}_3)\|\leq L_2\left(|s-\tilde{s}|+\sum_{i=1}^{3}\|z_i-\tilde{z}_i\|\right)$$

for $s,\tilde{s}\in[0,T]$, $z_i,\tilde{z}_i\in X$ $(i=1,2,3)$.

(iii) $2C\left(2TL_2+\sum_{i=1}^{p}|h_i|\right)<1.$

(iv) $x_0 \in E$ and $x_1 \in X$.

Then the nonlocal Cauchy problem (1)–(3) *has a unique mild solution u. Moreover, if*

$$x_0 \in D(A), \quad x_1 \in E \quad and \quad u(t_i) \in E \quad (i=1,2,...,p),$$

and if there exists a positive constant κ *such that*

$$\|u(a(s))-u(a(\tilde{s}))\| \le \kappa \|u(s)-u(\tilde{s})\| \quad for \quad s,\tilde{s} \in [0,T]$$

then u is the unique classical solution of nonlocal problem (1)–(3).

Proof. Since the assumptions of Theorem 2.1 are satisfied, the nonlocal Cauchy problem (1)–(3) possesses a unique mild solution which is denoted by u.

Now, we shall show that u is the classical solution of problem (1)–(3).

Firstly, we shall prove that u, $u(a(\cdot))$and $u`$ satisfy the Lipschitz condition on $[0, T]$. Let t and $t+h$ be any two points belonging to $[0, T]$. Observe that

$$u(t+h)-u(t)=C(t+h)x_0+S(t+h)x_1-S(t+h)\left(\sum_{i=1}^{p}h_i u(t_i)\right)$$

$$+\int_0^{t+h} S(t+h-s)f(s,u(s),u(a(s)),u'(s))ds$$

$$-C(t)x_0-S(t)x_1+S(t)\left(\sum_{i=1}^{p}h_i u(t_i)\right)$$

$$-\int_0^{t} S(t-s)f(s,u(s),u(a(s)),u'(s))ds.$$

Since

$$C(t)x_0+S(t)\left(x_1-\sum_{i=1}^{p}h_i u(t_i)\right)$$

is of class C^2 in $[0, T]$, there are $C_1 > 0$ and $C_2 > 0$ such that

$$\left\|\left(C(t+h)-C(t)\right)x_0+\left(S(t+h)-S(t)\right)\left(x_1-\sum_{i=1}^{p}h_i u(t_i)\right)\right\| \le C_1|h|$$

and

$$\left\|\left((C(t+h)-C(t)\right)x_0)'+\left((S(t+h)-S(t))(x_1-\sum_{i=1}^{p}h_i u(t_i)\right)'\right\| \le C_2|h|.$$

Hence

$$\|u(t+h)-u(t)\| \le C_1|h| + \Big\| \int_0^t S(s)\big(f(t+h-s,u(t+h-s),u(a(t+h-s)),u'(t+h-s))$$
$$-f(t-s,u(t-s),u(a(t-s)),u'(t-s))\big)ds\Big\|$$
$$+\Big\| \int_t^{t+h} S(s) f(t+h-s,u(t+h-s),u(a(t+h-s),u'(t+h-s))ds \Big\|$$
$$\le C_1|h| + \int_0^t Me^{\omega T} L_2\big(|h| + \|u(t+h-s)-u(t-s)\| + \|u(a(t+h-s))-u(a(t-s))\|$$
$$+\|u'(t+h-s)-u'(t-s)\|\big)ds + Me^{\omega T} N|h|,$$

where

$$N := \sup\{\|f(s,u(s),u(a(s)),u'(s))\| : s \in [0,T]\}.$$

From this we obtain

$$\|u(t+h)-u(t)\| \le C_3|h| + C_4 \int_0^t \big(\|u(s+h)-u(s)\| + \|u'(s+h)-u'(s)\|\big)ds. \tag{7}$$

Moreover, we have

$$u'(t) = \left(C(t)x_0 + S(t)\left(x_1 - \sum_{i=1}^{p} h_i u(t_i) \right) \right)' + \int_0^t C(t-s) f(s,u(s),u(a(s)),u'(s))ds.$$

From the above formula we obtain, analogously

$$\|u'(t+h)-u'(t)\| \le C_5|h| + C_6 \int_0^t \big(\|u(s+h)-u(s)\| + \|u'(s+h)-u'(s)\|\big)ds. \tag{8}$$

By inequalities (7) and (8), we get

$$\|u(t+h)-u(t)\| + \|u'(t+h)-u'(t)\|$$
$$\le C_*|h| + C_{**} \int_0^t \big(\|u(s+h)-u(s)\| + \|u'(s+h)-u'(s)\|\big)ds.$$

From Gronwall's inequality, we have

$$\|u(t+h)-u(t)\| + \|u'(t+h)-u'(t)\| \le \tilde{C}|h|, \tag{9}$$

where $\tilde{C}$ is a positive constant.

By (9), it follows that u, $u(a(\cdot))$ and u' satisfy the Lipschitz condition on $[0,T]$ with a positive constant $\tilde{C}$. This implies that the mapping

$$[0,T] \ni t \to f(t,u(t),u(a(t)),u'(t)) \in X$$

also satisfies the Lipschitz condition.

The above property of f together with the assumptions of Theorem 3.1 imply, by Theorem 1.1 and by Theorem 2.1, that the linear Cauchy problem

$$v''(t) = Av(t) + f(t, u(t), u(a(t)), u'(t)), \quad t \in [0, T],$$

$$v(0) = x_0,$$

$$v'(0) = x_1 - \sum_{i=1}^{p} h_i u(t_i)$$

has a unique classical solution v such that

$$v(t) = C(t)x_0 + S(t)\left(x_1 - \sum_{i=1}^{p} h_i u(t_i) \right)$$

$$+ \int_0^t S(t-s) f(s, u(s), u(a(s)), u'(s)) ds = u(t), \quad t \in [0, T].$$

Consequently, u is the unique classical solution of the semilinear Cauchy problem (1)–(3) and, therefore, the proof of Theorem 3.1 is complete.

References

[1] Balachandran K., Ilamaran S., *Existence and uniqueness of mild and strong solutions of a semilinear evolution equation with nonlocal conditions*, Indian J. Pure Appl. Math. 25.4, 1994, 411–418.

[2] Bochenek J., *An abstract nonlinear second order differential equation*, Ann. Polon. Math. 54.2, 1991, 155–166.

[3] Bochenek J., *Cosine operator functions and condition (F)*, Selected Problems of Mathematics, Cracow University of Technology Monographs, Anniversary Issue 6, 1995, 13–24.

[4] Bochenek J., Winiarska T., *Second order evolution equations with parameter*, Ann. Polon. Math. 59.1, 1994, 41–52.

[5] Byszewski L., *On some application of the Bochenek theorem*, Univ. Iagel. Acta. Math. 45, 2007, 147–153.

[6] Byszewski L., Winiarska T., *An abstract nonlocal second order evolution problem*, Opuscula Mathematica 32.1, 2012, 75–82.

[7] Fattorini H.O., *Ordinary differential equation in linear topological spaces*, J. Differential Equations 5, 1968, 72–105.

[8] Nagy B., *Cosine operator functions and the abstract Cauchy problem*, Periodica Math. Hungary 7, 1976, 213–217.

[9] Travis C.C., Webb G.F., *Cosine family and abstract nonlinear second order differential equations*, Acta Math. Hungar. 32, 1978, 75–96.

TECHNICAL TRANSACTIONS 1/2017
CZASOPISMO TECHNICZNE 1/2017
MATHEMATICS
DOI: 10.4467/2353737XCT.17.013.6110

Ludwik Byszewski (lbyszews@pk.edu.pl)
Institute of Mathematics, Faculty of Physics, Mathematics and Computer Science, Cracow University of Technology

Tadeusz Wacławski
Institute of Electrical Engineering and Computer Science, Faculty of Electrical and Computer Engineering, Cracow University of Technology

On the uniqueness of solutions to parabolic semilinear problems under nonlocal conditions with integrals

O jednoznaczności rozwiązań parabolicznych zagadnień z nielokalnymi warunkami z całkami

Abstract

The uniqueness of classical solutions to parabolic semilinear problems together with nonlocal initial conditions with integrals, for the operator $\sum_{i,j=1}^{n}\frac{\partial}{\partial x_i}\left(a_{ij}(x,t)\frac{\partial}{\partial x_j}\right)+c(x,t)-\frac{\partial}{\partial t}$, $x=(x_1,...,x_n)$, in the cylindrical domain $D:=D_0\times(t_0,t_0+T)\subset\Re^{n+1}$, where $t_0\in\Re$, $0<T<\infty$, are studied. The result requires that the nonlocal conditions with integrals be introduced.

Keywords: parabolic problems, semilinear equation, nonlocal initial condition with integral, cylindrical domain, uniqueness of solutions

Streszczenie

W artykule omówiono jednoznaczność klasycznych rozwiązań parabolicznych semiliniowych zagadnień z nielokalnymi początkowymi warunkami z całkami dla operatora $\sum_{i,j=1}^{n}\frac{\partial}{\partial x_i}\left(a_{ij}(x,t)\frac{\partial}{\partial x_j}\right)+c(x,t)-\frac{\partial}{\partial t}$, $x=(x_1,...,x_n)$, w walcowym obszarze $D:=D_0\times(t_0,t_0+T)\subset\Re^{n+1}$, gdzie $t_0\in\Re$, $0<T<\infty$. Wynik polega na tym, że zostały wprowadzone warunki nielokalne z całkami.

Słowa kluczowe: zagadnienia paraboliczne, równanie semiliniowe, nielokalny warunek początkowy z całką, obszar walcowy, jednoznaczność rozwiązań

1. Introduction

In this paper we prove two theorems on the uniqueness of classical solutions to parabolic semilinear problems, for the equation

$$\sum_{i,j=1}^{n}\frac{\partial}{\partial x_i}\left(a_{ij}(x,t)\frac{\partial u(x,t)}{\partial x_j}\right)+c(x,t)u(x,t)-\frac{\partial u(x,t)}{\partial t}=f(x,t,u(x,t)), \tag{1}$$

$$=f(x,t,u(x,t)),$$

$$(x,t)\in D:=D_0\times(t_0,t_0+T)\subset\Re^{n+1},$$

where $t_0\in\Re$, $0<T<\infty$. The coefficients $a_{ij}(i,j=1,...n)$, c and the function f are given. The nonlocal initial condition considered in the paper is of the form

$$u(x,t_0)+\frac{h(x)}{T}\int_{t_0}^{t_0+T}u(x,\tau)d\tau=f_0(x),\ x\in D_0,$$

where $|h(x)|\le 1$ for $x\in D_0$.

The result obtained is a continuation of the results given by Rabczuk in [5], by Chabrowski in [3], by Brandys in [1] and by the first author in [1] and [2].

In monograph [5], Rabczuk gives two uniqueness criteria for classical solutions for initial – boundary problems to the equation

$$\sum_{i=1}^{n}\frac{\partial^2 u(x,t)}{\partial x_i^2}-\frac{\partial u(x,t)}{\partial t}=f(x,t,u(x,t)),\ x\in D_0\subset\Re^n,\ t>0.$$

In paper [3], Chabrowski studies nonlocal problems for the equation

$$\sum_{i,j=1}^{n}a_{ij}(x,t)\frac{\partial^2 u(x,t)}{\partial x_i\partial x_j}+\sum_{i=1}^{n}b_i(x,t)\frac{\partial u(x,t)}{\partial x_i}+c(x,t)u(x,t)-\frac{\partial u(x,t)}{\partial t}=$$

$$=f(x,t),\ x\in D_0\subset\Re^n,\ t\in(0,T).$$

The nonlocal initial condition, considered in [3], is of the form

$$u(x,0)+\sum_i\beta_i(x)u(x,T_i)=\psi(x),\quad x\in D_0,$$

where $t_0\in(0,T)$ and was introduced in this form as the first by Chabrowski.

In publication [2], two uniqueness criteria for classical solutions for equation (1) together with the nonlocal condition $u(x,t_0)+h(x)u(x,t_0+T)=f_0(x),\ x\in D_0$, are studied.

2. Preliminaries

The notation, definitions and assumptions from this section are valid throughout this paper.

We will need the set $\Re_-:=(-\infty,0]$.

Let t_0 be a real number, $0<T<\infty$ and $x=(x_1,...,x_n)\in\Re^n$.

Define the domain (see [1] or [2])

$$D := D_0 \times (t_0, t_0 + T),$$

where D_0 is an open and bounded domain in $\Re^n$ such that the boundary ∂D_0 satisfies the following conditions:

(i) If $n \geq 2$ then ∂D_0 is a union of a finite number of surface patches of class C^1 which have no common interior points but have common boundary points.

(ii) If $n \geq 3$ then all the edges of ∂D_0 are sums of finite numbers of $(n-2)$ – dimensional surface patches of class C^1.

Assumption (A_1). a_{ij}, $\frac{\partial a_{ij}}{\partial x_s} \in C(\bar{D}, \Re)$ $(i,j,s = 1,...,n)$, where $a_{ij} = a_{ij}(x,t)$ for $(x,t) \in \bar{D}$ $(i,j = 1,...,n)$; $a_{ij}(x,t) = a_{ji}(x,t)$ for $(x,t) \in D$ $(i,j = 1,...,n)$ and $\sum_{i,j=1}^{n} a_{ij}(x,t)\lambda_i \lambda_j \geq 0$ for arbitrary $(x,t) \in$ D and $(\lambda_1, ..., \lambda_n) \in \Re^n$; $c \in C(\bar{D}, \Re_-)$.

Assumption (A_2).

(i) $f : \bar{D} \times \Re \ni (x,t,z) \rightarrow f(x,t,z) \in \Re$, $f \in C(\bar{D} \times \Re, \Re)$, $\frac{\partial f}{\partial z} \in C(\bar{D} \times \Re, \Re)$ and $\frac{\partial f(x,t,z)}{\partial z} > 0$ for $(x,t) \in \bar{D}$, $z \in \Re$;

(ii) $f_1 : \partial D_0 \times [0,T] \rightarrow \Re$;

(ii′) $k \in C(\partial D_0 \times [0,T], \Re_-)$;

(iii) $f_0 : D_0 \rightarrow \Re$.

Assumption (A_3). $h \in C(\bar{D}_0, \Re)$ and $|h(x)| \leq 1$ for $x \in D_0$.

Let $C^{2,1}(\bar{D}, \Re)$ be the space of all $w \in C(\bar{D}, \Re)$ such that $\frac{\partial w}{\partial x_i}$, $\frac{\partial^2 w}{\partial x_i \partial x_j} \in C(\bar{D}, \Re)$ for $i,j = 1, ..., n$ and $\frac{\partial w}{\partial t} \in C(\bar{D}, \Re)$.

The symbols L and P are reserved for two operators given by the formulas

$$(Lw)(x,t) := \sum_{i,j=1}^{n} \frac{\partial}{\partial x_i} \left(a_{ij}(x,t) \frac{\partial w(x,t)}{\partial x_j} \right) \tag{2}$$

and

$$(Pw)(x,t) := (Lw)(x,t) + c(x,t)w(x,t) - \frac{\partial w(x,t)}{\partial t} \tag{3}$$

for $w \in C^{2,1}(\bar{D}, \Re)$, $(x,t) \in \bar{D}$.

By n_x where $x \in \partial D_0$, we denote the interior normal to ∂D_0 at x. In short, we denote, also, n_x by n.

Let $C^{2,1}(\bar{D},\Re)$, $x \in \partial D_0$ and $t \in [t_0, t_0+T]$. The expression

$$\frac{du(x,t)}{d\upsilon(x_0,t)} := \sum_{i=1}^{n} \frac{\partial u(x_0,t)}{\partial x_i} \sum_{j=1}^{n} a_{ij}(x_0,t)\cos(n_{x_0}, x_j) \tag{4}$$

is called the transversal derivative of the function u at the point (x_0, t). If it does not lead to misunderstanding the transversal derivative $\frac{du(x,t)}{d\upsilon(x_0,t)}$ will be denoted by $\frac{d}{d\upsilon}u(x_0,t)$ or by $\frac{du}{d\upsilon_{x_0}}$.

For the given functions $a_{ij}(i,j=1,...,n)$ and c satisfying Assumption (A_1) and for the given functions f, f_1, f_0 and h satisfying Assumptions (A_2) (i)–(iii) and (A_3) the first Fourier's semilinear nonlocal problem in D consists in finding a function $u \in C^{2,1}(\bar{D},\Re)$ satisfying the equation

$$(Pu)(x,t) = f(x,t,u(x,t)) \quad \text{for} \quad (x,t) \in D, \tag{5}$$

the nonlocal initial condition

$$u(x,t_0) + \frac{h(x)}{T}\int_{t_0}^{t_0+T} u(x,\tau)d\tau = f_0(x) \quad \text{for} \quad x \in D_0 \tag{6}$$

and the boundary condition

$$u(x,t) = f_1(x,t) \quad \text{for} \quad x \in \partial D_0 \times [t_0, t_0+T]. \tag{7}$$

A function u possessing the above properties is called a solution of the first Fourier semilinear nonlocal problem (5)–(7) in D.

If condition (7) from the first Fourier semilinear nonlocal problem (5)–(7) is replaced by the condition

$$\frac{d}{d\upsilon_x}u(x,t) + k(x,t)u(x,t) = f_1(x,t) \quad \text{for} \quad x \in \partial D_0 \times [t_0, t_0+T], \tag{8}$$

where k is the given function satisfying Assumption (A_2)(ii′) then problem (5), (6) and (8) is said to be the mixed semilinear nonlocal problem in D. A function $u \in C^{2,1}(\bar{D},\Re)$ satisfying equation (5) and conditions (6), (8) is called a solution of the mixed semilinear nonlocal problem (5), (6) and (8) in D.

Assumption (A_4). For each two solutions w_1 and w_2 of problem (5)–(7) or of problem (5), (6) and (8) the following inequality

$$\left[\frac{1}{T}\int_{t_0}^{t_0+T} (w_1(x,\tau) - w_2(x,\tau))d\tau\right]^2 \le \left[w_1(x,t_0+T) - w_2(x,t_0+T)\right]^2 \quad \text{for} \quad x \in D_0$$

is satisfied.

Remark 2.1. The reason for which Assumption (A_4) is introduced is that the problems considered are nonlocal.

3. Theorems about uniqueness

In this section we shall prove two theorems about the uniqueness of solutions of parabolic semilinear problems together with nonlocal initial conditions with integrals.

Theorem 3.1. *Suppose that the coefficients $a_{ij}\,(i,j=1,...,n)$ and c of the differential equation (5) satisfy Assumption (A_1) and the functions f, f_1, f_0 and h satisfy Assumptions (A_2)(i)–(iii) and (A_3). Then the first Fourier semilinear nonlocal problem (5)–(7) admits at most one solution in D in the class of the solutions satisfying Assumption (A_4).*

Proof. Suppose that u_1 and u_2 are two solutions of problem (5)–(7) in D and let

$$v := u_1 - u_2 \quad \text{in} \quad \bar{D}. \tag{9}$$

Then the following formulas hold:

$$(Pv)(x,t) = f(x,t,u_1(x,t)) - f(x,t,u_2(x,t)) \quad \text{for} \quad (x,t) \in \bar{D}, \tag{10}$$

$$v(x,t_0) + \frac{h(x)}{T} \int_{t_0}^{t_0+T} v(x,\tau)\,d\tau = 0 \quad \text{for} \quad x \in \bar{D}_0, \tag{11}$$

$$v(x,t) = 0 \quad \text{for} \quad (x,t) \in \partial D_0 \times [t_0, t_0+T]. \tag{12}$$

From the assumption that $u_1, u_2 \in C^{2,1}(\bar{D},\Re)$, from the second and third part of Assumption (A_2)(i) and from the mean value theorem, there exists $\theta \in (0,1)$ such that

$$f(x,t,u_1(x,t)) - f(x,t,u_2(x,t)) \tag{13}$$

$$= v(x,t)\frac{\partial f(x,t,u_2(x,t) + \theta v(x,t))}{\partial z} \quad \text{for} \quad (x,t) \in \bar{D}.$$

By (13), (10), by Assumption (A_1) by (2) and (3) and by [4] (Section 17.11),

$$\int_{t_0}^{t_0+T} \left[\int_{D_0} v^2 \frac{\partial f(x,t,u_2+\theta v)}{\partial z} dx \right] dt \tag{14}$$

$$= \int_{t_0}^{t_0+T} \left[\int_{D_0} vPv\,dx \right] dt$$

$$= \int_{t_0}^{t_0+T} \left[\int_{D_0} vLv\,dx \right] dt + \int_{t_0}^{t_0+T} \left[\int_{D_0} cv^2\,dx \right] dt$$

$$-\int_{t_0}^{t_0+T}\left[\int_{D_0}\frac{\partial v}{\partial t}v\,dx\right]dt$$

$$=-\int_{t_0}^{t_0+T}\left[\int_{\partial D_0}v\sum_{i=1}^{n}\cos(n,x_i)\sum_{j=1}^{n}a_{ij}\frac{\partial v}{\partial x_j}d\sigma_x\right]dt$$

$$-\int_{t_0}^{t_0+T}\left[\int_{D_0}\sum_{i,j=1}^{n}a_{ij}\frac{\partial v}{\partial x_i}\frac{\partial v}{\partial x_j}dx\right]dt$$

$$+\int_{t_0}^{t_0+T}\left[\int_{D_0}cv^2dx\right]dt-\int_{t_0}^{t_0+T}\left[\int_{D_0}\frac{\partial v}{\partial t}v\,dx\right]dt,$$

where $d\sigma_x$ is a surface element in $\Re^n$.

From (14), (12) and from Assumption (A_1),

$$\int_{t_0}^{t_0+T}\left[\int_{D_0}v^2\frac{\partial f(x,t,u_2+\theta v)}{\partial z}dx\right]dt\le-\int_{t_0}^{t_0+T}\left[\int_{D_0}\frac{\partial v}{\partial t}v\,dx\right]dt. \tag{15}$$

Using integration by parts, it is easy to see that

$$\int_{t_0}^{t_0+T}\left[\int_{D_0}\frac{\partial v}{\partial t}v\,dx\right]dt=\frac{1}{2}\int_{D_0}v^2(x,t_0+T)dx-\frac{1}{2}\int_{D_0}v^2(x,t_0)dx. \tag{16}$$

Formulae (15) and (16) imply the inequality

$$\int_{t_0}^{t_0+T}\left[\int_{D_0}v^2\frac{\partial f(x,t,u_2+\theta v)}{\partial z}dx\right]dt \tag{17}$$

$$\le-\frac{1}{2}\int_{D_0}v^2(x,t_0+T)dx+\frac{1}{2}\int_{D_0}v^2(x,t_0)dx.$$

From (17) and (11), we have

$$\int_{t_0}^{t_0+T}\left[\int_{D_0}v^2\frac{\partial f(x,t,u_2+\theta v)}{\partial z}dx\right]dt \tag{18}$$

$$\le-\frac{1}{2}\int_{D_0}v^2(x,t_0+T)dx+\frac{1}{2}\int_{D_0}\left[\frac{h(x)}{T}\int_{t_0}^{t_0+T}v(x,\tau)d\tau\right]^2dx.$$

By (18) and Assumption (A_4),

$$\int_{t_0}^{t_0+T}\left[\int_{D_0}v^2\frac{\partial f(x,t,u_2+\theta v)}{\partial z}dx\right]dt \tag{19}$$

$$\leq -\frac{1}{2}\int_{D_0} v^2(x,t_0+T)dx+\frac{1}{2}\int_{D_0} h^2(x)\left[\frac{1}{T}\int_{t_0}^{t_0+T} v(x,\tau)d\tau\right]^2 dx$$

$$\leq -\frac{1}{2}\int_{D_0} v^2(x,t_0+T)dx+\frac{1}{2}\int_{D_0} h^2(x)v^2(x,t_0+T)dx$$

$$=-\frac{1}{2}\int_{D_0} v^2(x,t_0+T)[1-h^2(x)]dx.$$

From (19) and from Assumption (A_3) we obtain

$$\int_{t_0}^{t_0+T}\left[\int_{D_0} v^2\frac{\partial f(x,t,u_2+\theta v)}{\partial z}dx\right]dt\leq 0.$$

By the above inequality and by Assumption (A_2)(i), we obtain

$$v^2(x,t)\leq 0 \quad \text{for} \quad (x,t)\in D$$

and therefore

$$v(x,t)=0 \quad \text{for} \quad (x,t)\in D.$$

The proof of Theorem 3.1 is thereby complete.

Theorem 3.2. *Suppose that the assumptions of Theorem 3.1, concerning to the coefficients $a_{ij}(i,j=1,...,n)$, c and the functions f, f_1, f_0 and h, are satisfied and that the function k satisfies Assumption (A_2)(ii′). Then the mixed semilinear nonlocal problem (5), (6) and (8) admits at most one solution in D in the class of the solutions satisfying Assumption (A_4).*

Proof. Suppose that u_1 and u_2 are two solutions of problem (5), (6) and (8) in D, and let

$$v:=u_1-u_2 \quad \text{in} \quad \bar{D}. \tag{20}$$

Then the following formulas hold:

$$(Pv)(x,t)=f(x,t,u_1(x,t))-f(x,t,u_2(x,t)) \quad \text{for} \quad (x,t)\in\bar{D}, \tag{21}$$

$$v(x,t_0)+\frac{h(x)}{T}\int_{t_0}^{t_0+T} v(x,\tau)d\tau=0 \quad \text{for} \quad x\in\bar{D}_0, \tag{22}$$

$$\frac{d}{d\upsilon_x}v(x,t)+k(x,t)v(x,t)=0 \quad \text{for} \quad (x,t)\in\partial D_0\times[t_0,t_0,T]. \tag{23}$$

Applying a similar argument as in the proof of Theorem 3.1 and using the definition of $\frac{du}{d\upsilon_x}$ (see (4)), we have

$$\int_{t_0}^{t_0+T}\left[\int_{D_0} v^2\frac{\partial f(x,t,u_2+\theta v)}{\partial z}dx\right]dt \tag{24}$$

$$= -\int_{t_0}^{t_0+T}\left[\int_{\partial D_0} v\frac{dv}{d\upsilon}d\sigma_x\right]dt$$

$$-\int_{t_0}^{t_0+T}\left[\int_{D_0}\sum_{i,j=1}^{n}a_{i,j}\frac{\partial v}{\partial x_i}\frac{\partial v}{\partial x_j}dx\right]dt$$

$$+\int_{t_0}^{t_0+T}\left[\int_{D_0}cv^2dx\right]dt-\int_{t_0}^{t_0+T}\left[\int_{D_0}\frac{dv}{dt}vdx\right]dt.$$

From (24), (23), and as in the proof of Theorem 3.1

$$\int_{t_0}^{t_0+T}\left[\int_{D_0}v^2\frac{\partial f(x,t,u_2+\theta v)}{\partial z}dx\right]dt \tag{25}$$

$$\le\int_{t_0}^{t_0+T}\left[\int_{\partial D_0}kv^2d\sigma_x\right]dt-\frac{1}{2}\int_{D_0}v^2(x,t_0+T)[1-h^2(x)]dx.$$

By (25) and Assumptions (A_2)(ii′) and (A_3) we obtain the inequality

$$\int_{t_0}^{t_0+T}\left[\int_{D_0}v^2\frac{\partial f(x,t,u_2+\theta v)}{\partial z}dx\right]dt\le 0.$$

Consequently, as in the proof of Theorem 3.1,

$$v(x,t)=0 \quad \text{for} \quad (x,t)\in D$$

and the proof of Theorem 3.2 is complete.

4. Physical interpretation of the nonlocal condition (6)

Theorems 3.1 and 3.2 can be applied to descriptions of physical problems in heat conduction theory for which we cannot measure the temperature at the initial instant but we can measure the temperature in the form of the nonlocal condition (6).

Observe, also, that in Theorem 3.1 and 3.2, the nonlocal condition (6) considered is more general than the classical initial condition and the integral periodic condition and the integral anti-periodic condition. Namely, if the function h from condition (6) satisfies the relation

$$h(x)=0 \quad \text{for} \quad x\in D_0 \qquad \text{then condition (6) is reduced to}$$

the initial condition

$$u(x,t_0)=f_0(x) \quad \text{for} \quad x\in D_0.$$

Instead if the function h and f in (6) satisfy the conditions

$$h(x)=-1[h(x)=1] \quad \text{for} \quad x\in D_0,$$

$$f_0(x)=0 \quad \text{for} \quad x\in D_0,$$

then condition (6) is reduced, respectively, to the integral periodic [antiperiodic] initial condition:

$$u(x,t_0)=\frac{1}{T}\int_{t_0}^{t_0+T} u(x,\tau)d\tau \quad [\, u(x,t_0)=-\frac{1}{T}\int_{t_0}^{t_0+T} u(x,\tau)d\tau \,] \text{ for } x\in D_0.$$

References

[1] Brandys J., Byszewski L., *Uniqueness of solutions to inverse parabolic problems*, Comment. Math. Prace Matem. 42.1, 2002, 17–30.

[2] Byszewski L., *Uniqueness of solutions of parabolic semilinear nonlocal-boundary problems*, J. Math. Anal. Appl. 165.2, 1992, 472–478.

[3] Chabrowski J., *On nonlocal problems for parabolic equations*, Nagoya Math. J. 93, 1984, 109–131.

[4] Krzyżański M., *Partial Differential Equations of Second Order*, Vol. 1, PWN, Warszawa 1971.

[5] Rabczuk R., *Elements of Differential Inequalities*, PWN, Warszawa 1976 (in Polish).

TECHNICAL TRANSACTIONS 1/2017
CZASOPISMO TECHNICZNE 1/2017
PHYSICS
DOI: 10.4467/2353737XCT.17.014.6111

Gabriela Lewińska (glewinska@pk.edu.pl)
Jerzy Sanetra
Institute of Physics, Faculty of Physics, Mathematics and Computer Science, Cracow University of Technology

CuO/TiO_2 AND Cu_2O/TiO_2 NANOPARTICLES INFLUENCE ON PARAMETERS OF BULK HETEROJUNCTION ORGANIC SOLAR CELLS

WPŁYW NANOCZĄSTEK CuO/TiO_2 I Cu_2O/TiO_2 NA PARAMETRY ZŁĄCZ OBJĘTOŚCIOWYCH W ORGANICZNYCH OGNIWACH SŁONECZNYCH

Abstract

This publication presents a study conducted for related pyrazoloquinoline doped nanoparticles CuO/TiO_2 and Cu_2O/TiO_2. The mixtures were used as the active material for the construction of photovoltaic cells.

Keywords: photovoltaic cells, pyrazoloquinoline, efficiency, light absorbing materials

Streszczenie

W publikacji prezentujemy badania dotyczące pirazolochinolin domieszkowanych nanocząstkami CuO/TiO_2 oraz Cu_2O/TiO_2. Mieszaniny zostały zastosowane do konstrukcji ogniw fotowoltaicznych.

Słowa kluczowe: ogniwo fotowoltaiczne, pirazolochinoliny, wydajność, materiały absorbujące promieniowanie

1. Introduction

Due to rising costs and energy requirements, development of newer and newer technologies is essential. Technologies associated with silicon as well as subsequent generations and types of photovoltaic cells are constantly being developed. However, third generation cells are also developed, including organic cells, whose example we are presenting.

The organic heterojunctions have been the subject of interest of researchers since the 1950s [1]. Especially, they are environmentally friendly, cheap to operate and solar energy resources are infinite. On the other hand, the efficiency received, although still increasing, needs to be ameliorated [2]. The research we present was motivated by the objective of improving the efficiency of bulk-heterojunction solar cells.

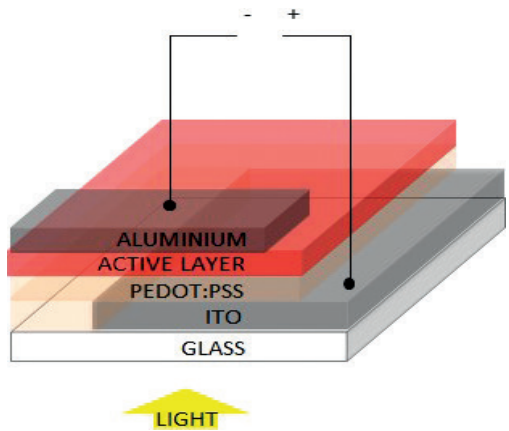

Fig. 1. The heterojunction ITO/PEDOT:PSS/active layer/Al architecture

The electrocell mechanism is customarily divided into several stages. The first step is to absorb photons with energies greater than the band gap of the material, and the exciton creation. Excitons diffuse until they achieved dissociation position, where charge separation occurs. Electric charges are transported through polymeric material to the electrodes. However, during this way may also exhibit recombination. In heterojunctions blends of two kinds of materials are used as the active layer – with a different electron affinity and ionization

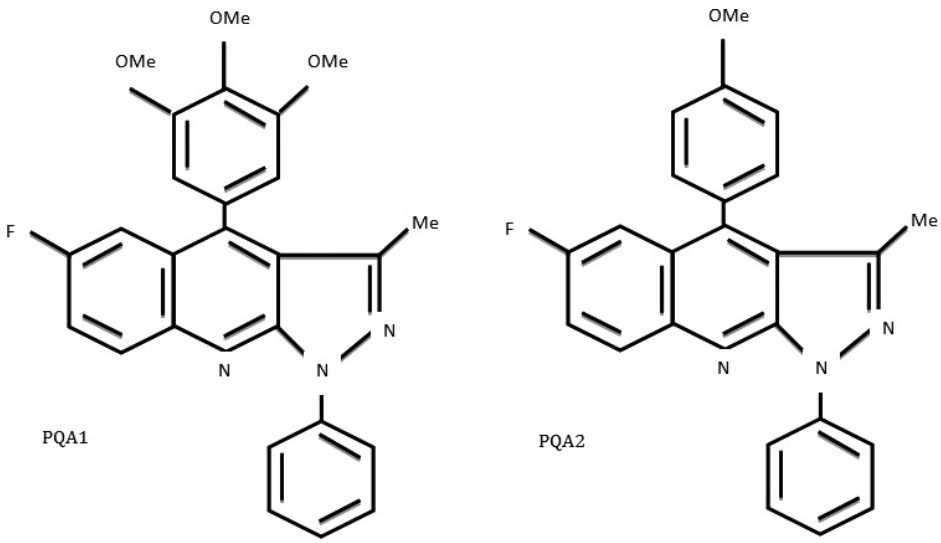

Fig. 2. Acceptor chemical formulas

potential. As a rule the electrons are attracted to the material having a greater affinity; however, a hole is attracted to the material with lower ionization potential. This type of mixture causes that the ratio of electrons in the external circuit to the number of photons entering, compared with the structure of a typical active layer, increases. Existing research indicates an increase in the absorption of the active layer doped nanoparticles [3–5], which was the motivation for research.

2. Experiment

As the active layer components pyrazoloquinolines derivatives [6–9] were used as the acceptors, (Fig. 2), poly(3-hexylthiophene-2,5-diyl), provided by Sigma Aldrich, was used as a donor. The first tests were carried out absorption measurements for compounds and mixtures. Nanoparticles were obtained by precipitation method. The composite suspension (250 cm^3) was prepared by mixing P25 powder (1 g) with $Cu(NO)_3$ (2.51 cm^3 for CuO/TiO_2 and 4.19 cm^3 for Cu_2O/TiO_2) aqueous solution (0.5 M) and deionized water. Then the suspension was sonificated for 10 minutes, finally agitated (~300 rpm). For the CuO/TiO_2 $2.5 \cdot 10^{-5}$ cm^3 (25%) ammonia solution was diluted in 50 cm^3 of deionized was instilled. The resulting $Cu(OH)_2/TiO_2$ nanocomposite was recovered after 24 h by filtration, rinsed with deionized water several times and finally dried for 12 h at 40°C in the dark.

The absorbance (Fig. 3, Fig. 4) and photoluminescence spectra (as reference was used chloroform solution) of P3HT and pyrazoloquinolines and mixtures doped with nanoparticles follow (Fig 5). The absorption maximum is observed for wavelengths, respectively: P3HT – 449 nm, PQA1 – 403 nm, PQA2 – 481 nm, for the mixture P3HT and PQA1 – 410 nm and 458 nm, for the mixture P3HT and PQA2 – 408 nm and 451 nm. Photoluminescence intensity maximum band occurs for P3HT – 401 nm, PQA1 – 489 nm, PQA2 –446 nm, for the mixture P3HT and PQA1 – 462 nm and 570 nm, for the mixture P3HT and PQA2 – 412 nm and 455 nm. As shown, the addition of nanoparticles increases the intensity of absorption, the position of the bands is, however, unchanged.

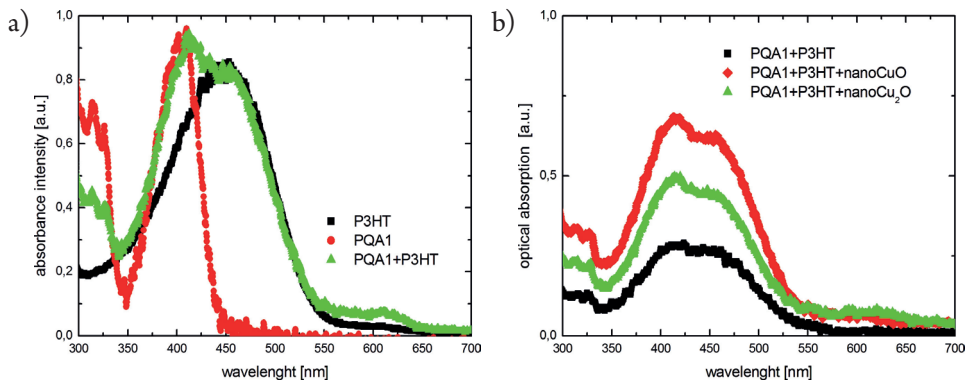

Fig. 3. Optical absorption measured in solution versus wavelength for studied systems active layers based on PQA1: a) P3HT, PQA1, mixture; b) mixture, mixture with nanoparticles CuO, mixture with nanoparticles Cu_2O

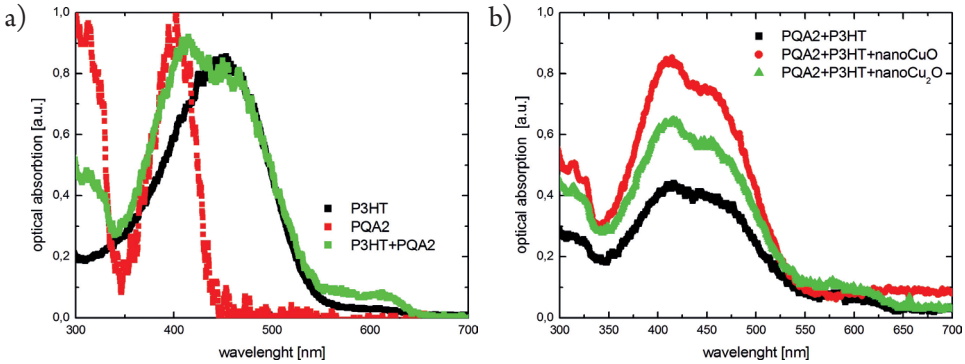

Fig. 4. Optical absorption measured in solution versus wavelength for studied systems active layers based on PQA2: a) P3HT, PQA2, mixture; b) mixture, mixture with nanoparticles CuO, mixture with nanoparticles Cu_2O

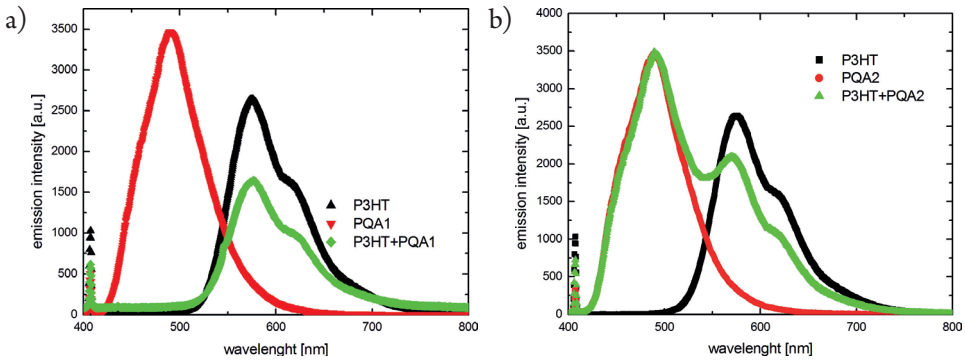

Fig. 5. Emission photoluminescence measured in solution versus wavelength: a) P3HT, PQA1 and mixture PQA1+P3HT; b) P3HT, PQA2 and mixture PQA2+P3HT. The peak in photoluminescence spectra at 405 nm corresponds to the laser

A photovoltaic cell is composed of several layers – the substrate is indium tin oxide (ITO) coated glass provided by Aldrich Chem Co. The ITO layer, forming the first electrode, is 100 nm thick, and its resistance rate is 50 om/sq. The second electrode is made of aluminium and has been received during process of deposition in a high vacuum. The PEDOT:PSS (poly(3,4-ethylendioxythiohene)-polystyrene-para-sulfonic acid) supports the transfer of holes and it is an anode buffer layer. The PEDOT:PSS and active layers were formed by spin-coating method, then followed annealing the layers in a vacuum heater.

The photocurrent density-voltage characteristics for prepared photovoltaic cells were measured with a Keithley 2400 source due to picoamperemeter. To illuminate the cells was used lamp (lamp power is approximately 1.3 mW/cm^2.

Based on experimental data, polynomial curves were fitted and the critical parameters of photovoltaic cells determined (Table 1). Parameters describing the photovoltaic cells are short current density (I_{sc}), open circuit voltage (U_{oc}) , fill factor (FF) defined as

$$FF = \frac{I_m V_m}{I_{SC} V_{OC}} \tag{1}$$

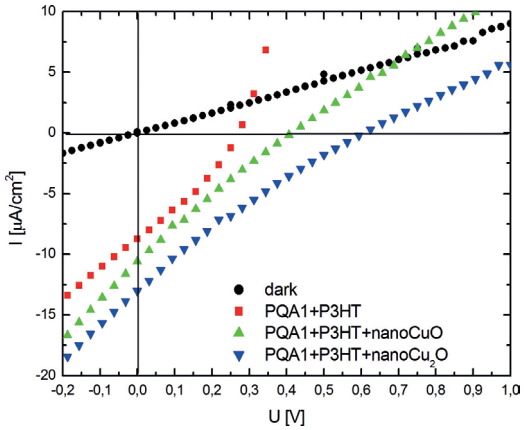

Fig. 6. Current-voltage characteristics obtained for PQA1 and P3HT mixture doped nanoparticles

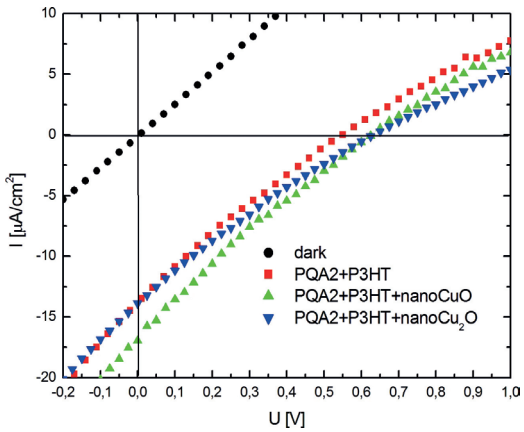

Fig. 7. Current-voltage characteristics obtained for PQA2 and P3HT mixture doped with nanoparticles

and conversion efficiency (η)

$$\eta = \frac{I_{SC} V_{OC} FF}{P_{\text{light}}} \tag{2}$$

The U_m and I_m are voltage and current of maximum power, and P_{light} is input optical power.

Table 1. Parameters describing the photovoltaic devices

	I_{SC} [μA/cm²]	Uoc[V]	FF	η [%]	R_{sh}[10⁴Ω]	R_s [10⁴Ω]
PQA1+P3HT	20.2	0.48	0.41	**0.30**	1.69	1.03
PQA1+P3HT+nanoCu_2O	4.2	0.77	0.22	**0.05**	0.11	11.7
PQA1+P3HT+nanoCuO	8.9	0.77	0.22	**0.13**	6.78	1.76
PQA2+P3HT	17.6	0.38	0.21	**0.14**	2.09	40.2
PQA2+P3HT+nano Cu_2O	16.7	0.76	0.21	**0.20**	3.13	5.67
PQA2+P3HT+nanoCuO	21.5	0.88	0.19	**0.29**	2.62	7.34

3. Summary

For all constructed cells the fill factor were comparable. Because of the similar shape of spectrum absorption studied systems (mixtures of nanoparticles have higher absorption) depends on the quantum efficiency of the exciton diffusion path or the conductivity of electric charge. The exciton diffusion path is supported by ballistic transport (observed for nanoparticles, caused by the size reduction to a size smaller than the exciton mean free path). Cells with pyrazoloquinolines have the greatest short-circuit current (ITO/PEDOT:PSS/PQA2+P3HT/Al: Isc = 20,2; μA/cm^2 ITO/PEDOT:PSS/PQA2+P3HT/Al: Isc = 17,6 μA/cm^2), while a lower open-circuit voltage. Doping nanoparticles increases the voltage (for undoped cells is twice lower). The reason for changes in efficiency in the systems must be different nanoparticles charge affinity. The relatively low fill factor is caused by the fact that the resistance R_s and R_{sh} in the same order. For PQA2 both nanoparticles improved power conversion efficiency factor. The only mixture in which no cell parameter improvements were observed is the mixture PQA1. This may be due incompatible HOMO levels of nanoparticles and pyrazoloquinolines. However, the results obtained are similar to those previously obtained [10–12] with specified base chemical compounds.

The authors thank Ph.D. Eng. Robert Socha and Ph.D. Dawid Wodka (Jerzy Haber Institute of Catalysis and Surface Chemistry Polish Academy of Sciences, Cracow) for providing the nanoparticles that were used in the work.

References

[1] Bernanose A., *Progress with Light-Emitting Polymers*, J. Chem. Phys., 1953, 50, 64.
[2] Norris D.J., Aydil E.S., *Getting Moore from Solar Cells*, Science, 2012, 625–626.
[3] Baoquan S., Eike M., Greenham N.C., Letters N., *Photovoltaic Devices Using Blends of Branched CdSe Nanoparticles and Conjugated Polymers*, 2003, 3 (7), 961–963.
[4] Woo-Jun Yoon, Kyung-Young Jung, Jiwen Liu, Thirumalai Duraisamy, Rao Revur , Teixeira F.L. , Suvankar Sengupta, Berger P.R., *Plasmon-enhanced optical absorption and photocurrent in organic bulk heterojunction photovoltaic devices using self-assembled layer of silver nanoparticle*, Solar Energy Materials and Solar Cells, Vol. 94, Issue 2, February 2010, 128–132.
[5] Kakavelakis G., Stratakis E., Kymakis E., *Aluminum nanoparticles for efficient and stable organic photovoltaics*, RSC Adv., 2013, 3, 16288–16291.
[6] Chaczatrian K., Chaczatrian G., Danel A., Tomasik P., *The synthesis of 4-aryl-1H-pyrazolo[3,4-b]quinolines by cyclization of 4-arylidenepyrazolin-5-ones with anilines*, ARKIVOC 2001, 2, 6.
[7] Araki K., Funaki J., Danel A., Tomasik P., *A facile synthesis of 4-aryl-1H-pyrazolo[3,4-b] quinolines*, Polish Journal Of Chemistry, 2004, 78, 843.
[8] Danel A., Jarosz B., Karasinski P., Sahraoui B., Armatys P., *Synthesis, photophysical and electroluminescent properties of 1,3-diphenyl-1H-benzo[g]pyrazolo[3,4-b]quinoxaline* Materials Letters, 2015, 138, 9–12.

[9] Danel A., Danel K., *Synteza niektórych azotowych układów hetero cyklicznych oraz ich zastosowanie w komórkach elektroluminescencyjnych,* Chemik, 2010, 64, 7–8, 511–522.
[10] Pokladko-Kowar M., Gondek E., Danel A., *Ogniwa fotowoltaiczne na bazie organicznych materiałów*, Technical Transactions, Vol. 1-NP/2011, 77–83.
[11] Nosidlak N., Socha R.P., Kulig E., Sanetra J., *Organic photovoltaic cells built on P3HT and 1,3,4- triphenyl 6-(9-karbazolyl)-1H pyrazolo[3,4-b]quinoline with nanoparticles*, Przegląd Elektrotechniczny, Vol. 90, No. 9/2014.
[12] Gondek E., Djaoued Y., Priya S., Balaji S., Robichaud J., Karasinski P., *Organic hybrid solar cells-Influence of ZnO nanoparticles on the photovoltaic efficiency*, Materials Letters, 2014, 131, 259–261.

TECHNICAL TRANSACTIONS 1/2017
CZASOPISMO TECHNICZNE 1/2017
PHYSICS
DOI: 10.4467/2353737XCT.17.015.6112

Andrzej Osak (aosak@ifpk.pk.edu.pl)
Institute of Physics, Faculty of Physics Mathematics and Computer Science, Cracow University of Technology

AC low frequency conductivity in PZT PFS ferroelectric ceramics

Niskoczęstotliwościowe przewodnictwo elektryczne ferroelektrycznej ceramiki PZT PFS

Abstract

Low frequency AC conductivity has been studied in ferroelectric ceramics PZT + PFS ($Pb[(Fe_{1/3}Sb_{2/3})_x Ti_y Zr_z]O_3$ with $x = 0.1$ and $y = 0.43, 0.44, 0.47$) using Fourier transformation of charging and discharging currents. The results are interpreted in terms of fractal structure of the randomly generated clusters formed by sequentially correlated hopping paths of charge carriers.

Keywords: PZT, AC conductivity, fractal structure conduction clusters

Streszczenie

W artykule przedstawiono przewodnictwo zmiennoprądowe ceramiki ferroelektrycznej PZT + PFS ($Pb[(Fe_{1/3}Sb_{2/3})_x Ti_y Zr_z]O_3$, gdzie $x = 0.1$ i $y = 0,43, 0,44, 0,47$) w zakresie ultra niskich częstotliwości obliczone na podstawie analizy Fouriera prądów polaryzacji i depolaryzacji dielektrycznej. Wyniki zostały zinterpretowane na podstawie fraktalnej struktury klasterów generowanych przez stochastyczny sekwencyjny hopping nośników ładunku.

Słowa kluczowe: PZT, przewodnictwo zmiennoprądowe, fraktalna struktura przewodzących klasterów

1. Introduction

The investigation of dielectric and electric properties in disordered solids has been the subject of a great deal of interest because of their many technical applications.

From the phase diagram of the PZT ($Pb(Zr_{1-x}Ti_x)O_3$) ferroelectric solid solution follows that in this compound the phase boundary exists which divides regions with rhombohedral and tetragonal structures [1, 2]. Recently Noheda et al. [3] reported that, within a narrow region $0.45 < x < 52$, there was a bringing monoclinic phase. This region is called the morphotropic phase boundary (MPB). It was established that in the MPB there is a progression from long range to short range structural orders leading to a stochastic disorder [4]. In the studied complex compound PZT + PFS ($Pb[(Fe_{1/3}Sb_{2/3})_x Ti_y Zr_z]O_3$ with $x+y+z=1$, $x=0.1$ and $y=0.43, 0.44, 0.47$) the crystal lattice Pb sites are partially replaced by Sb cations while the Ti sites by Zr or Fe cations. The structural studies performed for the 0.43 and 0.44 of Ti content samples established the existence of the MPB region [5]. The coexistence of rhomboedral and tetragonal phases in the MPB range as well as doping leads to structural disorder in the studied compound.

AC conductivity measurements are an important means to study deep defect centres. The alternating current (AC) conductivity of disordered solids shows a dispersive behaviour through the dependence of electrical conductivity $\sigma(\omega)$ vs. frequency ω of the form [6].

$$\sigma(\omega)=\sigma_{dc}+\sigma_p(\omega) \tag{1}$$

where σ_{dc} is the direct current (DC) conductivity and $\sigma_p(\omega)$ is the frequency dependent polarization conductivity. Polarization conductivity $\sigma_p(\omega)$ is created due to the relaxation process connected with defect centres or group of centres that develop electric dipole moments under the action of applied electric field. A strong frequency dispersion of AC conductivity follows from a broad distribution of the relaxation times [7]. The measurement of the step response function over several decades of time (up to 10^4 s) is usually used to investigate low frequency AC dielectric losses. The dielectric response in the frequency domain is described in terms of dielectric susceptibility $\chi(\omega)$ or permittivity $\varepsilon(\omega)$ functions. The dielectric properties can be equivalently expressed in terms of complex conductivity.

$$\sigma(\omega)=-i\omega\chi(\omega) \tag{2}$$

In order to convert results from the time- into frequency domain the one-side Fourier transform is commonly used.

The AC conductivity $\sigma(\omega)$ in disordered solids depends strongly on the external field frequency. At high frequency range, one observes a sublinear dependence $\sigma(\omega) \propto \omega^s$ with $0 < s < 1$, whereas at low frequency range a supralinear dependence with the power exponent $s > 1$. The cross-over from high-to low frequency range takes place at the dielectric loss peak frequency ω_c.

The AC conductivity in disordered solids has been studied in terms of hopping mechanism of charge carriers between localization sites. Many models based on relaxation caused by hopping or tunnelling of electrons, polarons or ions between equilibrium states, have been proposed [8–15] to explain the frequency and temperature dependencies of AC conductivity.

2. Theory

2.1. Rate equitation

In disordered solids the electron hopping process takes place between localized states that are statistically distributed in space and in energy. According to Miller and Abrahams [9], the electron transition probability w_{ij} between the localized states r_i and r_j depends on the tunnelling probability, proportional to $\exp(-2ar_{ij})$ and the energy difference between both sites $E_{ij} = E_i - E_j$ taking the following form

$$w_{ij} = w_0 \exp\left(-2ar_{ij} - E_{ij}/kT\right) \tag{3}$$

In this expression k is the Boltzmann contrast, T is temperature and a is localization length of the wave function ψ in a site r_i, i.e. $\psi \propto [-|r - r_i|/a]$. The transition rate is defined as the product of the site transition probability w_{ij}, occupation probability of the initial site $P_i(t)$ and non occupation probability of the final state $w_{ij} f_i (1 - f_j)$, where f is the Fermi function. The transition rate fulfils the following master equation

$$\frac{dP_i(t)}{dt} = \Sigma_j w_{ji} P_i(t) - \Sigma_i w_{ji} P_i(t) \tag{4}$$

In order to determine the conductivity we must consider the transition rate in the presence of an electric field. The electric field changes the occupation probability $P(t)$ of localized states. In the linear approximation (Ohmic conduction) Miller and Abrahams have shown that rate equation can be mapped on the impedance network. According to this treatment, the transition rate for the hopping process in the electric field may be given as the product of conductance G_{ij} and voltage V_{ij} between sites r_i and r_j. The conductance $G_{ij} = R_{ij}^{-1}$, linking each pair of sites (i, j) is

$$R_{ij}^{-1} = \left(e^2/kT\right)\gamma_{ph} \exp\left(\frac{\Delta_{ij}}{kT} + 2r_{ij}/a\right) \tag{5}$$

and the capacitance values C_i, linking each sites to the external field generator $E_0 \cos\omega t r_i$, are

$$C_i = \left(e^2/kT\right)\exp\left(-E_{i/kT}\right) \tag{6}$$

Here γ_{ph} is the phonon frequency of about 10^{12} Hz and Δ_{ij} is equal to $|E_i - E_j|$ or $|E_j|$ depending on which is greater. All energies are related to the Fermi level E_f.

2.2. Pair approximation

At high frequency, the two-site model (pair approximation) and its modification have been commonly used [8, 14, 16]. According to these models,the charge hopping takes place between nearest neighbour sites (single hopping) and it is assumed that each individual relaxation process occurs in parallel and independently of all others. The exact form of $\sigma(\omega)$ depends on details of the transition rate relations describing movement of charge carrier between a pair of sites.

In the simplest approximation only sites within kT of the Fermi level are involved in AC conduction. It is also assumed that pairs with relaxation time $\tau = 1/\omega$ make the dominant contribution to $\sigma(\omega)$ [8]. In order to obtain expression for the $\sigma(\omega)$, the product of the AC current J_{ij}, of the pair i, j and the density of pairs of the length rij must be summed to give

$$\sigma(\omega) = \sigma_{dc} + \Sigma_{i,j} n_{ij} J_{ij} \tag{7}$$

Calculating this expression at any frequency ω gives for $\sigma(\omega)$ [17]

$$\sigma(\omega) = \sigma_{dc} + 0.3 r_{\omega}^2 a \left[N\left(E_f\right) kT \right]^2 e^2 \omega / kT \tag{8}$$

where $r_{\omega} \cong a \ln(v_{ph}/\omega)$ is greater than the hopping distance. The numerical factor in Eq. (8) differs slightly from the value presented in [15].

At high frequencies, the main results of pair approximation have been confirmed, but at low frequencies discrepancies exist and a modification has been needed [17–19].

2.3. Cluster approximation

At low frequencies, during a half period of the oscillation of an external field, the carriers make multiple hopping and the pair approximation fails. Therefore, at low frequency range, hopping charge transport has been formulated in terms of random walk theory of Scher and Lax [12], cluster approach of Bötcher et al. [15] and equivalent random resistor network of Summerfield and Butcher [16]. From this treatment as well as from the computer simulation [20] it follows that, at very low frequencies, the quadratic law $\sigma(\omega) \sim \omega^2$ should be fulfilled. However, the experimental results show that the frequency exponent *s*, at very low frequencies, is subquadratic ($1 < s < 2$). By application of a low frequency electric field to a disordered system, large clusters of charge carriers with the percolation path of the fractal structure are randomly generated [19, 21]. At low frequencies, the mechanism of cluster charge transport dominates and individual relaxation process of clusters must be considered. The conductivity $\sigma(\omega)$ can be expressed as the sum of σ_{dc} and the cluster polarization conductivity $\sigma_p(\omega)$. Since the exact calculation of cluster polarization current are unavailable, therefore the simple approximation has been proposed by Hunt [17–19]. The complexity of large cluster structures composed of many percolation paths has then been replaced by a collection of chains with a resistor oriented in the direction of the applied field. Replacement of clusters by one dimensional chains was proposed by several authors [22, 23]. The polarization currents J_{NR} of chain composed of *N* resistors with resistivity *R* and *N*

capacitors with capacitance C may be expressed in the same way as in the pair approximation, if we replace R by NR, C by NC and with $\tau_N \propto N^2\tau$ to get [17, 18]

$$J_{N,R}(\omega) = \left(2/3\pi^2\right)\left(Nl^2/R\right)\left[\omega^2\tau_N^2/\left(1+\omega^2\tau_n^2\right)\right] \tag{9}$$

The total conductivity is the sum over all contributing chains [17]

$$\sigma(\omega) = \sigma_{dc} + \Sigma l_{N,R} \cdot n_{N,R} \tag{10}$$

wheren $n_{N,R}$ is the number of chains.

The statistical distribution function density of chains $n_{N,R}$ on a given cluster has been adopted from the Stauffer formula of cluster distribution in the percolation system [24]. According to this approach, AC conduction at low frequencies may be expressed as [19]

$$\sigma(\omega) = \sigma_{dc}\left\{1 + \left[A \cdot \frac{\omega}{\omega_c}\right]^{\frac{d-1}{2}} + \left[A \cdot \frac{\omega}{\omega_c}\right]^{\frac{d-1+1/\nu}{2}}\right\} \tag{11}$$

where $A = \left(\frac{T}{T_0}\right)^{1/4}$, d is the dimension of conducting system, ν is critical exponent of the correlation length $\nu = 0.9$ [24] and $T_0 = [N(E_f)a^3k]^{-1}$ with $N(E_f)$ being the density of states at the Fermi level and ω_c is the critical frequency corresponding to the onset of dispersion. It is evident that in the case of a 3D system, two different terms, one with linear $s = 1$ and the second with a supralinear frequency exponent $1 < s < 2$, contribute to the total conductivity.

3. Method and results

In the experiment, a step voltage $V(t) = V_0$ applied to a dielectric sample, generates the charging current J_d which is composed of a transient polarization current $J_p(t)$ and a steady state conduction current J_{dc}. Discharging current J_d, flowing after the removal of polarization voltage does not involve a steady state component. In the case of low polarization field (linear condition), $J_d = -J_p(t)$. Details of the experimental procedure and sample characterization are presented in [25, 26]. The AC conductivity has been calculated by taking the Fourier transformation of the transient currents $J_p(t)$. The numerical calculation of the Fourier transformation was based on a simple summation

$$J(\omega) = \Delta t \Sigma_{n=0}^{\infty} \exp(-i\omega n\Delta t) \cdot J(n\Delta t) \tag{12}$$

The summation was carried out at various periods of time with various time intervals Δt changing from $\Delta t = 1$ s to $\Delta t = 1000$ s. The charging and discharging currents were measured over a long period of time up to 10^5 s. The measurements at low temperatures were performed

down to 77 K but at higher temperatures the measurements were performed at temperatures which were lower than the Curie temperature. To eliminate the non-linear effects, the samples at low temperature were poling at field 0.2 kV/cm, and at high temperatures, at field 0.02 kV/cm. As an example, in Fig. 1 the time dependent decaying charging $J_c(t)$ and discharging currents, $J_d(t)$ for sample with $y=0.43$ are shown in log-log scale. The charging currents $J_c(t)$ were used to calculate the total AC conductivity $\sigma(\omega)$ which contains the DC component. The discharge (depolarization) current was used to calculate $\sigma(\omega)$. In Figs. 2, 3 and 4, the low frequency dependent AC conductivity for samples with $y=0.43$, 0.44 and 0.47 are presented respectively. In table I, the frequency exponent *s* are listed for the same samples. The power exponents are given for the frequencies above and below the cross-over frequency ω_c. It is evident that frequency exponent *s* depends on the sample composition and temperature. The samples with the morphotropic composition containing less Ti (with $y=0.43$ and 0.44) have a lower *s* value than those with the non-morphotropic composition (with $y=0.47$). For the frequency range $\omega << \omega_c$, the exponents is greater than one, but only slightly in the case of samples with $y=0.43$ and 0.47.

4. Discussion

1. The experimental evidence and theoretical conclusions [27–29] show that the dielectric relaxation and transport properties in perovskite structures are closely related to the oxygen vacancies. The oxygen vacancies are created by losses of oxygen from the crystal lattice during sintering at high temperature according to

$$O_O \rightleftarrows V_{\dot{O}} + 1/2O_2$$

The oxygen vacancies are positively charged with respect to the lattice and always appear single ionized at low temperature $V_O \rightleftarrows V_O^0 + e'$ or doubly ionized at high temperature $\left(V_{\dot{O}} \rightleftarrows V_{\ddot{O}} + e'\right)$. In perovskites, the energy of the first ionization of oxygen vacancies is about 0.1 eV, whereas the second energy ionization is about 1.4 eV. The thermally liberated electrons contribute to the dielectric relaxation and conduction process. In $Pb[(Fe_{1/3}Sb_{2/3})_x Ti_y Zr_z]O_3$, the Fe^{3+} ions are incorporated into the perovskite B site acting as acceptors [27]. At high sintering temperature, the trivalent Sb ions substitute the divalent Pb ions and create lead vacancies V_{Pb}.

$$Sb_2O_3 \rightleftarrows 2Sb_{\ddot{P}b} + 3O_O^x + V_{Pb}''$$

The lead vacancy V_{Pb}'' carries two excess negative charges. The oxygen vacancies existing in perovskite compound migrate around the Fe ions leading to formation of dipolar defects- $Fe'_{TiZr}V_{\ddot{O}}$ complexes. The orientation of these dipolar defects depends on V_0 location in the oxygen octahedron. A linear dielectric relaxation is connected not only with dipoles but also with potentially mobile charges (electrons, polarons or ions) The observed dielectric relaxation may originate from the Fe^{2+}/Fe^{3+} mixed valence structure of

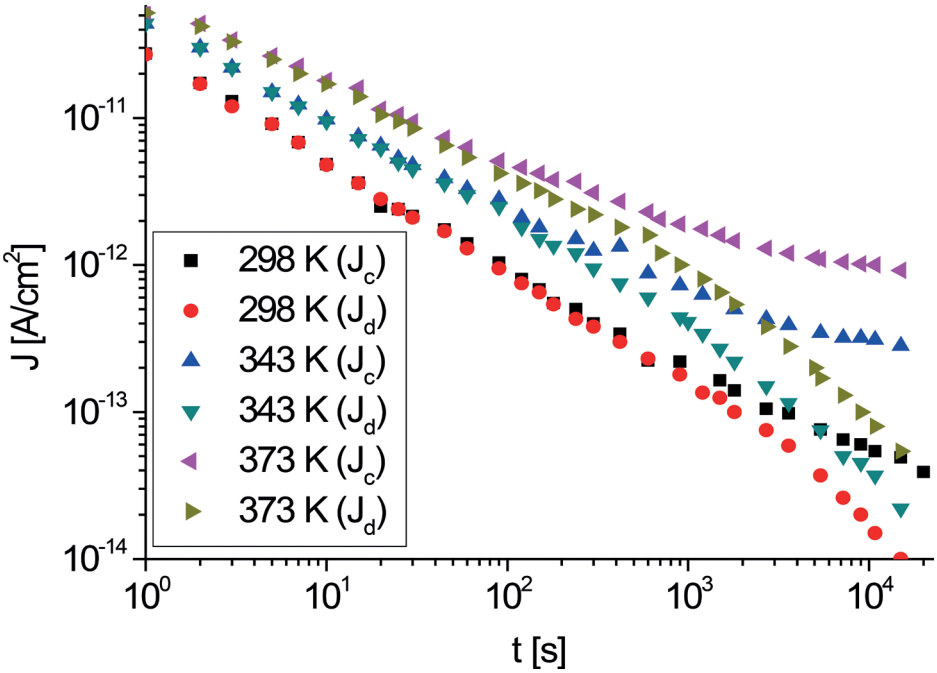

Fig. 1. Time dependence of charging $J_c(t)$ and discharging $J_d(t)$ currents for sample $y = 0.43$ measured at temperatures 298 K, 343 K, and 373 K. Poling field: 0.02 kV/cm

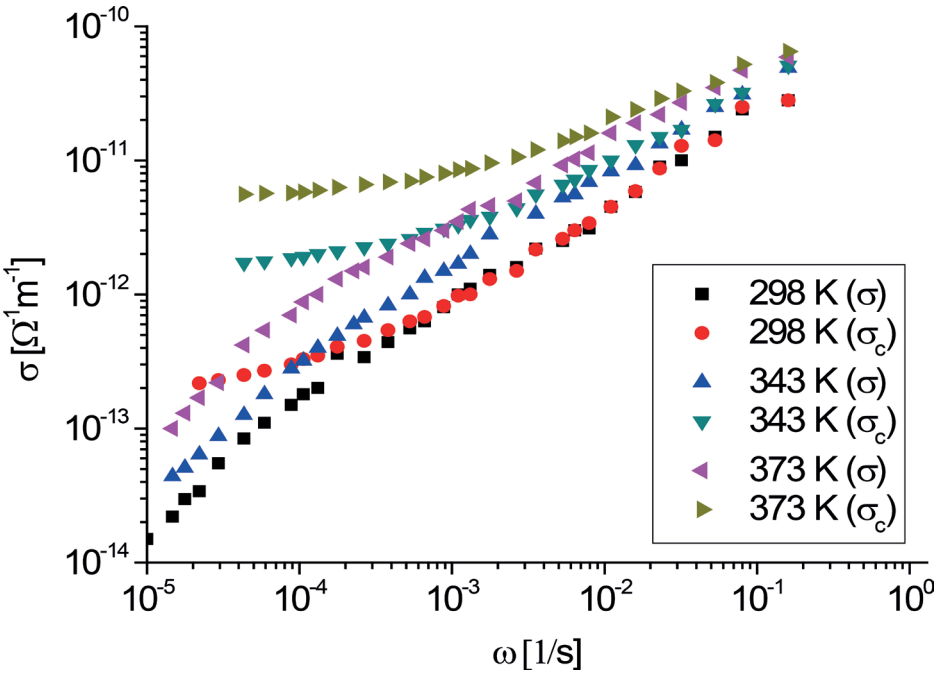

Fig. 2. The low frequency AC conductivity for sample with $y = 0.43$ at selected temperatures; $\sigma_c(\omega)$ – total AC conductivity $\sigma(\omega)$ – polarization conductivity

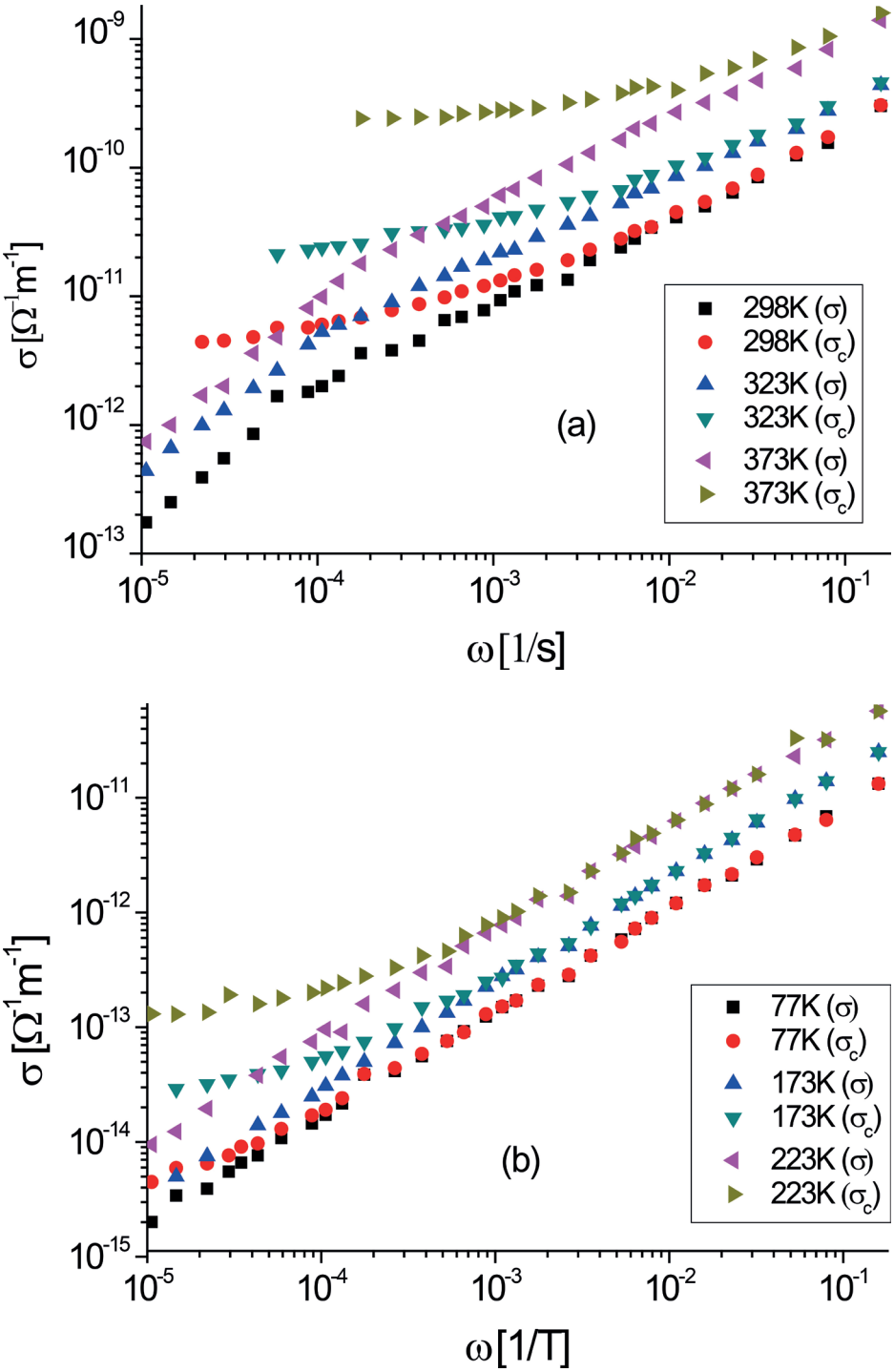

Fig. 3. The low frequency AC conductivity for sample with $y = 0.44$ at selected high (*a*) and low (*b*) temperatures

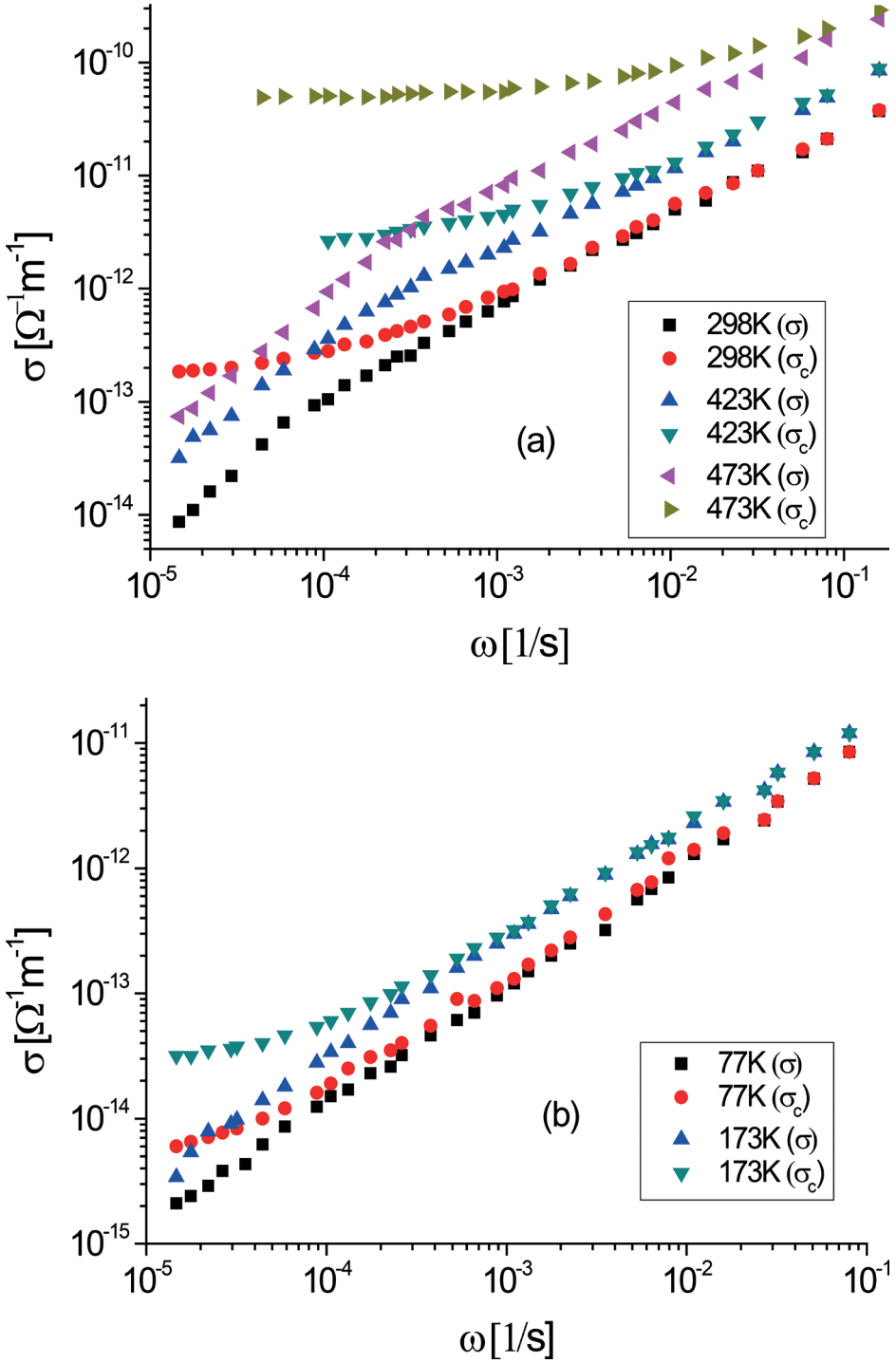

Fig. 4. The low frequency AC conductivity for sample with $y = 0.47$ at selected high (a) and low (b) temperatures

$Pb[(Fe_{1/3}Sb_{2/3})_xTi_yZr_z]O_3$. The 3d electrons in Fe^{3+} may hop to Fe^{2+} ions; the same hopping movement may take place between $Ti^{3+} \rightarrow Ti^{2+}$ and $Zr^{3+} \rightarrow Zr^{2+}$ ions. This electron hopping creates time dependent dipole moments. At higher frequencies, the carrier hopping takes place between sites separated by lower energy, whereas at lower frequencies, the energy barrier with higher energy must be over-passed. This way, the AC conductivity at higher frequencies is greater than at lower ones. At higher temperatures, the energy distribution of barriers becomes more uniform and variation of AC conductivity with frequency becomes weaker. The dielectric relaxation can be also attributed to the motion of dipoles created by the defect associate $\left(Fe'_{TiZr}V_{\ddot{O}}\right)$ under the action of an external field. In the electric field, the defect dipole can be reoriented only slightly in the field direction or may perform greater movements. In the latter case, changes in position of $V_{\ddot{O}}$ within the oxygen octahedron via hopping process will result in reorientation of the complex defect dipole. The relaxation time in this case is determined by thermally activated diffusive jumping of the oxygen vacancies. The long range movement of weakly bonded electrons gives rise to the DC conduction that can be described by the hopping mechanism. The transport of electrons from cathode to anode, contributing to the DC conduction, needs to overcome a higher potential barrier, as compared to a lower energy barrier needed to overcome a shorter displacement in the case AC conduction. Therefore the activation energy of DC conductivity is higher than the activation energy of AC conductivity.

2. The temperature dependence of the frequency exponent $s(T)$ is consistent with results of multiple hopping models [13, 20, 21]. According to these models, s should decrease with increasing temperature, as can be seen from results presented in Table I. The exponent s depends also on concentration N of localization sites. The concentration $N = 2.9 \cdot 10^{23}\,m^{-3}$ for sample with $y = 0.44$ is greater than concentration $N = 1.5 \cdot 10^{23}\,m^{-3}$ for sample with $y = 0.47$ [25]. Indeed, for all temperatures, the exponent s for sample with $y = 0.44$ is smaller than that for sample with $y = 0.47$. Moreover, the values of s are much smaller than 2, being at variance with the prediction of the cluster model [10] and computer simulation [20] yielding $s = 2$. It is evident from expression (11) that two different terms for low ω exist: one linear and the second supralinear. For three dimensional systems, $d = 3$ and $v = 0.9$ [24] and the frequency exponent equals $(d - 1 + 1/v)/2 = 1.55$.
The results presented in Table I show that the frequency exponent for all samples is less than the theoretical value 1.55. These results may suggest that the Debye-type relaxation effects play an important role. In the low temperature range, concentration of charge carriers decreases and contribution of dipolar dielectric relaxation becomes more important.

5. Conclusions

1. The presented results suggest that the frequency dependence of AC conductivity of PZT-PFS at very low frequencies $\sigma(\omega) \sim \omega^s$ may be explained in terms of fractal structure of the randomly generated clusters formed by sequentially correlated hopping paths of charge carriers (i. e. the geometry of multiple hopping).

2. Approximation of cluster current as the one-dimension collection of chain currents leads to low frequency AC conductivity expression with the frequency exponent $1<s<2$, in accordance with the experimental results.

Table 1. Values of frequency power exponents s for samples with $y = 0.43$, $y = 0.44$ and $y = 0.47$.

y	T [K]	$s(\omega<\omega_c)$	$s(\omega>\omega_c)$
$y=0.43$	298	1.38	0.62
	343	1.35	0.62
	373	1.38	0.577
$y=0.44$	298	1.37	0.62
	323	1.41	0.58
	373	1.47	0.577
	223	1.36	0.84
	173	1.31	0.43
	77	1.27	0.81
$y=0.47$	298	1.33	0.81
	423	1.31	0.70
	473	1.34	0.675
	173	1.42	0.81
	77	1.38	0.91

The author is grateful to Prof. J. Cisowski and Ph.D. W. Osak for suggestions and helpful discussion.

References

[1] Shirane G., Suzuki K., Takeda A., *Phase transition in Solid Solutions $PbZrO_3$ and $PbTiO_3$ (II) X ray study*, Journal of the Physical Society of Japan, Vol. 7, 1952, 12–18.

[2] Jaffe B., Cook W.R., *Piezoelectric Ceramic,* Academic Press, London 1971, 136.

[3] Noheda B., Cox D.E., Gonzalo J.A., Cross L.E., Park S.E., *A monoclinic ferroelectric phase in the Pb (Zr1-xTix) O_3 solid solution*, Applied Physics Letters, Vol. 74, 1999.

[4] Glazer A.M., Thomas P.A., Baba-Kishi K.Z., Pang G.K.H., Tai C.W., *Influence of short-range and long range order on the evolution of the morphotropic phase boundary of $Pb(Zr_{1-x}Ti_x)O_3$*, Physical Reviev B, Vol. 70, 184123–1–9.

[5] Osak A., Pawelczyk M., Ptak W.S., *Investigation of the structure, pyro- and piezoelectric properties of a ferroelectric ceramics of PZT+(FeSb)*, Ferroelectics, Vol. 186, 1996, 123–126.

[6] Elliot S. R., *Ac conduction in amorphous chalcogenite and pnictidesemicondactors*, Advances in Physics, Vol. 36, 1987,131–218.
[7] Jonsher A.K., *Dielectric relaxation in solids Ch. 4*, Chelsae Dielectric Press, London 1984.
[8] Pollak M. *On the Frequency Dependence of Conductivity in Amorphous Solids*, Philosophical Magazine, Vol. 23, 1971, 519–2.
[9] Miller A., Abrahams E., *Impurity Conduction at Low Concentration*, Physical Review, Vol. 120, 1960, 745–755.
[10] Ambegaokar V., Halperin B.J., Langer J.S., *Hopping Conductivity in Disordered Systems*, Physical Review B, Vol. 7, 1971, 2612–2620.
[11] Butcher P.N., *On the rate equation formulation of the hopping conductivity problem*, Journal of Physics C: Solid State Physics, Vol. 5, 1972, 1817–1829.
[12] Scher H., Lax M., *Stochastic transport in disordered solids*, Physical Review B, Vol. 7, 1973, 4491–4519.
[13] Dyre J.C., *The radom free-energy barier model for AC conduction in disordered solids*, Journal of Applied Physics, Vol. 64, 1988, 2456–2468.
[14] Pike G.E., *Ac conductivity of scandium oxide and new hopping model of conductivity*, Physical Review B, Vol. 6, 1972, 1572–1580.
[15] Böttger H.B., Bryksin V.V., Yashin G. Yu., *Cluster approximatelly in the theorry of hopping model of conductivity in disordered solids*, Journal Physics C: Solids State Physics, Vol. 12, 1979, 2797–2808.
[16] Summerfield S., Butcher P.N., *A unified equivalent-circuit approach to the theory of AC and DC hopping conductivity in disordered systems*, Journal of Physics C: Solid State Physics, Vol. 15, 1982, 7003–7016.
[17] Hunt A., *The AC conductivity of variable range hopping systems such as amorphous semiconductors,* Philosophical Magazine B, Vol. 64, 1991, 579–589.
[18] Hunt A., *The AC conductivity of the Fermi glass. A model for glassy conduction*, Solid State Communication, Vol. 80, 1991, 151–155.
[19] Hunt A., *Frequency dependent conductivity of the Fermi glass,* Journal of Physics Condensed Matter, Vol. 4, 1992, 6957–6970.
[20] Moore E.J., *Numerical studies of the AC conductivity of hopping system I. Effects of space and energy disorder*, Journal of Physics C: Solid State Physics, Vol. 7, 1974, 1840–1853.
[21] Niklassan G.A., *Fractal aspects of the dielectric response of charge carriers in disordered materials*, Journals of Applied Physics, Vol. 62, 1987, R1–14.
[22] Pollak M., Pohl H.A., *Dielectric dispersion in some polymer and polyelectrolyte. A model,* Journal Chemical Physics, Vol. 67, No. 7, 1975, 2980–2987.
[23] Skal A.S., Shklovski B.J., *Soviet Physics of Semiconductors*, Vol. 8, 1975, 1029.
[24] Stauffler D., *Introduction to Percolation Theory,* Taylor and Francis, London 1985.
[25] Osak A., Jankowska-Summara I., *Electrical transport in ferroelectric* $Pb[(Fe_{1/3}Sb_{2/3})_xTi_yZr_z]O_3$ ceramics, Phase Transitions, Vol. 82, 2009, 899–909.
[26] Osak A., *Ultra low frequency dielectric dispersion in PZT-PFS ferroelectric ceramics*, Journal of Advanced Dielectrics, Vol. 3, 2013.

[27] Erdem E., Eichel R.A., Kungl H., Hoffman M.J., Ozarowski A., van Tal J., Brunel L.C., *Characterization of (Fe_{ZrTi}-$V_O^{\cdot\cdot}$) defects dipoles in (La, Fe) codoped PZT 52.2/47.5 Piezoelectric ceramics by Multifrequency Electron Paramagnetic Resonance Spectroscopy*, IEEE Trans. Ultrasonic, Ferroelectrics, Frequency Contr. Vol. 55, 2008, 1061–1068.
[28] Chen Ang., Zhi Yu and Cross L.E., *Oxygen-vacancy low-frequency dielectric relaxation and electrical conduction in Bi:$SrTiO_3$,* Physical Review B, Vol. 62, 2000, 228–236.
[29] Marton P., Elsässer C., *Switching of a substitutional-iron/oxygen-vacancy defect complex in ferroelectric $PbTiO_3$ from first principles*, Physical Review B, Vol. 83, 2011, 020106–1–4.